ABSTRACT

Title of Dissertation:	SIMULATION OF POLYMERIC DROP DYNAMICS: EFFECT OF PHOTOPOLYMERIZATION, IMPACT VELOCITY, AND MULTI-MATERIAL COALESCENCE
	Vishal Sankar Sivasankar, Doctor of Philosophy, 2023
Dissertation directed by:	Professor Siddhartha Das, Department of Mechanical Engineering, University of Maryland.

Over the past couple of decades, additive manufacturing has emerged as one of the most promising manufacturing tools and has rightfully garnered the attention of researchers across various fields ranging from biochemistry and medicine to energy and infrastructure. Especially, direct-ink-writing methods (*e.g.*, inkjet printing, aerosol jet printing, or AJ printing, etc.) have been widely studied because of their ability to print highly complex geometries with finer resolution. In order to design a more efficient droplet-based direct ink writing system, it is essential to understand the deposition process and the post-deposition dynamics of the drop. The post-deposition drop dynamics dictate the spreading radius of the drop and hence the print resolution. Such an understanding is even more critical when there are multiple drops interacting with each other, given the fact that such interactions determine the presence/absence of surface defects in addition to determining the print resolution. Moreover, to have a holistic understanding of the post-

deposition process, it is essential to further account for the droplet solidification mechanisms (for example, through effects such as *in-situ* curing) that might interplay with multiple drop dynamics events (such as drop spreading, drop coalescence, drop impact, etc.).

In this dissertation, computation fluid dynamics (CFD) frameworks have been developed to investigate the facets dictating the post-deposition dynamics of one (or several) solidifying polymer drops, with these dynamics show-casing the different post-deposition events that are intrinsic to the droplet-based additive manufacturing processes. First, we considered a situation where the polymeric drop undergoes simultaneous spreading and photopolymerization, with the timescales of the spreading and photopolymerization events being τ_s and τ_p respectively. The findings from this work confirmed the significant impact of the ratio of timescales (τ_s and τ_p) on the thermo-fluidic-solutal dynamics of the polymeric drops. Moreover, the evolution of the curing front showed distinct behaviors as a function of the timescale ratio.

Subsequently, the effect of the interaction of multiple polymeric drops during the post-deposition event, as seen in the typical printing process, was investigated. Specifically, we studied the effect of drop impact on the coalescence dynamics of two polymeric drops of identical and different sizes. The study revealed the presence of two distinct stages of coalescence. The early-stage coalescence was found to be enhanced with an increase in the impact velocity; however, the late-stage coalescence behavior remained unaffected by the impact velocity. Further, the coalescence dynamics of polymeric drops of different materials, as witnessed in multi-jet printing, was probed. This study shed light on the mechanisms that drive the mixing process at different stages of drop coalescence.

Finally, we evaluated the effects of the *in-situ* photopolymerization on the coalescence dynamics of multiple polymeric drops deposited on a substrate. Here too the comparative values of the drop dynamics timescale and the photopolymerization became important. Our results show three-distinct regimes characterizing the bridge growth which was further validated through physics-based theoretical scaling. This study would provide key insights into the direct-ink writing process and would aid in designing parameters for polymer-based additive manufacturing and product repair.

SIMULATION OF POLYMERIC DROP DYNAMICS: EFFECT OF PHOTOPOLYMERIZATION, IMPACT VELOCITY, AND MULTI-MATERIAL COALESCENCE

by

Vishal Sankar Sivasankar

Dissertation submitted to the Faculty of the Graduate School of the

University of Maryland, College Park, in partial fulfillment

of the requirements for the degree of

Doctor of Philosophy

2023

Advisory Committee:
Professor Siddhartha Das, Chair
Professor Abhijit Dasgupta
Professor Amir Riaz
Professor Eleonora Tubaldi
Professor Peter Kofinas, Dean's Representative

© Copyright by
Vishal Sankar Sivasankar
2023

Acknowledgments

I owe my gratitude to my advisor, Dr. Siddhartha Das, for his continuous support throughout my graduate study. I am grateful for this wonderful opportunity to pursue research under his guidance. I am also grateful to him, as he has always made himself available to help and encourage me during difficult times. I would also like to thank my dissertation committee and my colleagues for their valuable input and contribution to my dissertation. I acknowledge the valuable computational support provided by the Deepthought2 High Computing Cluster at the University of Maryland.

Table of Contents

List of Figures

List of Tables

List of Abbreviations

3D/3DP	three-dimensional/ three-dimensional printing
AJ/AJP	Aerosol Jet/Aerosol Jet Printing
AM	Additive Manufacturing
CE	Coalescing end
CFD	Computational Fluid Dynamics
CIJ	Continuous inkjet
CMC	carboxymethylcellulose
CSF	Continuum Surface Force
DI	De-ionized
DIW	Direct-ink-writing
DNS	Direct Numerical Simulation
EHD	Electrohydrodynamic
FDM	Fused Deposition Melting
FGM	Functionally Graded Material
IJP	Inkjet Printing
LENS	Laser Engineered Net Shaping
LOM	Laminated Object Manufacturing
LS	Level Set
MULES	Multidimensional Universal Limiter with Explicit Solution
NCE	Non-coalescing end
OpenFOAM	Open-source Field Operation And Manipulation
PBF	Powdered Bed Fusion

PDE	Partial Differential Equation
PMMA	Polymethylmethacrylate
PVAc	Polyvinyl acetate
SLA	Stereolithography
TIJ	Thermal inkjet
TDS	Transport of Diluted Species
TPCL	Three Phase Contact Line
TPLFMMM	Two-phase laminar-flow moving mesh method
UV	ultraviolet
VOF	Volume of Fluid

Chapter 1: Background and Motivation

1.1 Overview

Additive manufacturing (AM), aided by its inherent flexibility, customizability, freedom of design, sustainability, and most importantly, the ability to manufacture complex structures and handle a wide variety of materials (including metals, metal alloys, polymers, composites, and ceramics) has emerged as one of the extremely promising manufacturing tools for diverse fields, including aerospace,[1] automation,[2] automobile,[3] biomedical,[4] construction,[5] electronics,[6] energy,[7] food sector,[8] etc.

The ever-growing demand for improved precision, complexity, and rapidly expanding arsenal of new materials has resulted in the development of many different additive manufacturing techniques. Depending on the input material type – powder, liquid, or filament – different additive manufacturing techniques have been developed to convert these primitive forms into a finished product through an additive (layer-by-layer or drop-by-drop) approach. Fundamental to the success of these different methods is a precise control of depositing drops on various types of printing surfaces as well as ensuring that we could generate solidified structures from the deposited non-solid materials. Various solidification mechanisms incorporated in the AM processes include thermal solidification,[9-11] evaporation,[12,13] sintering,[14] photopolymerization,[15] thermal curing/gelation,[16-17] etc. Some of the commonly used AM processes that employ the above-mentioned solidification mechanisms are[18]: Stereolithography (SLA), Fused Deposition Modeling (FDM), three-dimensional printing (3DP), aerosol jet printing (AJP), Selective Laser Sintering (SLS), inkjet printing (IJP), powdered bed fusion (PBF), laser engineered

net shaping (LENS), Laminated object manufacturing (LOM), syringe/extrusion printing etc.

1.2 Droplet based additive manufacturing (AM) processes

Direct-ink-writing (DIW) processes such as inkjet printing, syringe/extrusion printing, aerosol-jet (or AJ) printing, and electrohydrodynamic (EHD) jet printing, which use liquid ink (either in form of continuous jet or drops) as their input material, have been widely employed due to their ability to create complex structures with high resolution.[19] For the successful implementation of droplet-based additive manufacturing processes (such as AJ printing or inkjet printing), it is crucial to have an in-depth understanding of the dynamics of the droplets throughout its life cycle, which includes the droplet generation, droplet transportation, and the post deposition dynamics.

1.2.1 Droplet generation in droplet-based AM processes

Prior to the layer-by-layer (or drop-by-drop) printing, for the droplet-based AM processes, droplets have to be generated and their sizes have to controlled. Some of the common mechanisms developed for generating droplets include pneumatic atomization,[20] piezoelectric (ultrasonic) atomization,[21] electrohydrodynamic drop generation,[22] continuous drop generation, thermal drop generation,[23] etc. The drops generated by the atomization processes often vary in sizes. It is important to obtain more uniform distribution of drop sizes and concentration of aerosol stream (in droplet-based printing method such as the AJ printing) to avoid problems like overspray, clogging of nozzles, etc.

For instance, in the pneumatic atomization process in AJ printing, the generated aerosol stream (with droplets) is directed through a virtual impactor to: (1) reduce the droplet concentration in the aerosol stream in order to avoid clogging of nozzles and (2) reduce the variation in the droplet size distribution in order to avoid undesirable effects like overspray. Of course, the atomization process that is selected for the printing process depends on the ink material properties like viscosity, vapor pressure, surface tension, etc.[24,25]

1.2.2 Droplet transport in droplet-based AM processes

The drops generated by the atomization processes are transported from the atomization chamber (or the droplet generation location) to the substrate on which the final product is printed. The generated droplets are usually sent through a nozzle to focus the droplets to a pre-determined location on the substrate. In some processes, such as the continuous inkjet (CIJ) printing, thermal inkjet (TIJ) printing, electrohydrodynamic (EHD) printing, the droplets are actually produced at the nozzle exit.[19]

Sometimes, in addition to the focusing obtained through nozzles, external forces are applied to better focus the aerosol streams with the goal of attaining printed traces with finer resolutions. For instance, in aerosol jet printing (AJP) process, aerosol stream is focused by means of sheath gas which helps focus the drops and achieve high resolution printed traces.[26] Similarly, acoustic forces can also be employed to achieve extremely high focusing of the aerosol streams.[27]

1.2.3 Post-deposition droplet dynamics in droplet-based AM processes

For all the droplet-based AM processes, the post deposition dynamics of the drops, along with the associated solidification technique, depend on primarily on the material of the drop. The commonly employed solidification mechanisms include thermal solidification, evaporation, thermal curing/gelation, photopolymerization, sintering, etc.

1.3 Agenda of the dissertation

The main objective of this dissertation is to delve into the post-deposition aspect of the droplet based additive manufacturing (AM) process in order to obtain an in-depth understanding of the effect of the droplet dynamics on the printed traces. In these manufacturing processes, the deposited droplets undergo spreading on the printing substrate in addition to undergoing the solidification process. In this work, we especially probe the simultaneous spreading and solidification of micron sized, power-law obeying polymeric drops. These polymeric drops are solidified by means of UV light induced photopolymerization process. For that purpose, we first provide a numerical framework to capture the dynamics of single micron sized drop that undergoes simultaneous spreading and in-situ photopolymerization. Next, we probe the effect of impact velocity on the coalescence dynamics of multiple droplets of identical and non-identical materials as observed in a typical droplet-based AM process. Finally, we explore and analyze the post-deposition dynamics of simultaneous coalescence and in-situ photopolymerization process.

While understanding the droplet-based AM processes better has been the genesis of this dissertation, the findings of the different chapters of this dissertation have much wider

connotation in the realm of dynamics of polymeric, non-Newtonian, and chemically reactive droplets. For example, this thesis for the first time probes the effect of impact velocity (and the associated Weber number) in the coalescence dynamics of non-Newtonian polymeric drops. Similarly, this study investigates for the first time the spreading and coalescence of two non-identical miscible polymeric drops: such a consideration brings to the fore the role of Marangoni effects in the coalescence dynamics of the non-identical polymeric drops. Finally, this thesis expands our understanding of the dynamics of single and multiple chemically reactive drops: photopolymerization is a special type of such chemical reaction that these drops undergo and such reactions significantly influence the properties of the drops to the extent that their dynamics get massively altered.

1.4 Outline of the dissertation

Chapter 2 of this dissertation introduces the computational fluid dynamics (CFD) framework to model the thermo-fluid-solutal dynamics of the in-situ photopolymerization of the 3D printed polymeric microdroplet (a first of its kind study of the spreading behavior of chemically reactive drops undergoing photopolymerization type chemical reaction). A detailed formulation that couples the material properties and energy released during the process with the extent of polymerization, also known as degree of cure (α), is provided. A detailed analysis of the time dependent fluid velocities, temperature, and monomer concentration (degree of cure) distribution are presented. Next, the progression of the curing front over time is captured. A detailed comparison of thermo-fluid-solutal dynamics for various spreading and polymerization timescales is provided for various drop sizes.

Chapter 3 of this dissertation deals with the coalescence dynamics of micron sized, power-law obeying, polymeric drops. First, a detailed analysis of the 3D velocity field inside the coalescing droplets was provided. Subsequently, the formation of fluid bridges and the subsequent growth of the bridge during the coalescence was investigated. Next, simulation-based scaling laws for the bridge height and width growth were compared with the corresponding physics based theoretical scaling laws. A thorough analysis for various stages of coalescence for different Weber numbers (impact velocity) were presented. Finally, the effect of the fluid viscosity, and the droplet size on the coalescence dynamics were explored.

Chapter 4 of this dissertation deals with the coalescence behavior of identical sized, micrometric polymeric drops of dissimilar materials. A multiphase framework to capture the spreading and mixing of dissimilar droplets were described. A detailed analysis of the 3D velocity vectors inside the coalescing droplets was used to investigate the mechanisms that dictate the mixing of two dissimilar yet miscible liquids. Further, the non-monotonic progression of the mixing front was analyzed. Finally, a quantitative analysis of the mixing process on both the coalescing and non-coalescing ends of the drops was provided.

Chapter 5 of this dissertation provides a detailed investigation of the effect of *in-situ* photopolymerization on the coalescence dynamics of polymeric drops. First, a detailed analysis of the 3D velocity field inside the coalescing droplets for varying ratios of spreading to photopolymerization timescale was provided. Next, a quantitative analysis of the evolution of the liquid bridge growth during coalescence in the presence of in-situ photopolymerization was provided. We further provide theoretical physics-based scaling

analysis to explain the regimes of bridge growth. Later, the progression of the curing front over time was captured, which was similar to the findings from Chapter 2.

Finally, in Chapter 6, we summarize the main findings of this dissertation and identify the possible future direction of studies that may evolve from the findings of this dissertation.

Chapter 2: 3D Printed Microdroplet Curing: Unravelling the Physics of On-spot Photopolymerization*

Abstract

Droplet-based direct-write printing (one form of 3D printing) methods like inkjet printing, aerosol-jet printing (AJP) etc. have changed our ideas about bottom-up additive manufacturing. AJP is capable of 3D printing by depositing microdroplets that leads to certain benefits in 3D printing of microscale structures. Here we study the in-situ photopolymerization based curing of a microdroplet. The droplet is simultaneously spreading and curing which leads to the rise of two timescales – the spreading timescale (τ_s) and the photopolymerization timescale (τ_p). When $\tau_s << \tau_p$, the spreading occurs very fast and is independent of polymerization. If the timescales are of the same order ($\tau_s \sim \tau_p$), the spreading is significantly affected by the polymerization. For this case, a progressive increase in the viscosity of the drop during the spreading ensures a much slower spreading and also a much weaker extent of spreading (i.e., the spreading ceases at a much smaller spreading radius of the drop). This complex thermo-fluidics is eventually manifested as distinct differences in the time-dependent velocity, temperature, and curing (or equivalently, monomer concentration) profiles within the drop between the two cases.

* Contents of this chapter is published as: V. S. Sivasankar, H. S. Sachar, S. Sinha, D. R. Hines, and S. Das, "3D Printed Microdroplet Curing: Unravelling the Physics of On-spot Photopolymerization". *ACS Applied Polymer Materials*, 2(2), 966-976 (2020).

2.1 Introduction

In-situ photopolymerization of polymer-rich systems drive the fabrication of nanocomposites[28] and nanocomposite gels,[29] anisotropic particles,[30] solid-state solar cells,[31] electrodes for solar cells[32] and supercapacitors,[33] ionic-liquid-rich gel electrolyte,[34] flexible broadband mirrors,[35] gas sensors,[36,37] core-shell and hybrid nanofibers,[38] monoliths for protein separation,[39] functional biomaterial microstructures,[40] customized nanoparticles and hydrogels for various applications,[41-45] and many more. The process of 3D printing with polymer inks has been extensively employing such *in-situ* polymerization (*in-situ* curing) of deposited and spreading polymer drops and traces.[46-53] Such *in-situ* curing of the printed polymer traces significantly enhances the rate of 3D printing. The central thermofluidic issue dictating this problem is the manner in which the deposited polymer trace is simultaneously spreading and getting cured. This information will be critical to a large number of 3D printing issues such as (a) the width and the thickness of the printed trace achieved using a given printing pass, (b) the rheology of the deposited trace with which the incoming subsequent depositing mass interacts, etc.

As a close representation of this problem, we study here the spreading dynamics of a photo-curable polymer drop in the presence of UV-light-mediated *in-situ* curing or photopolymerization [see Fig. 2.1(b,d,e)]. Very recently, de Ruiter et al. had studied the spreading dynamics of thermo-responsive polymer drops.[17] Our study is different from Ref. 17 as we consider a photopolymerization process that involves a significant number of chemical reactions triggered by the light-absorption-induced heat generation, thereby necessitating the coupled solutions of the fluid flow, heat transport, and species transport equations. In addition to being an extremely intriguing fluid dynamics problem, our

problem closely mimics the situation that occurs during the Aerosol Jet Printing (AJP) of photocurable polymer drops [see Fig. 2.1(a-f)] and can also provide useful ideas on other droplet-based printing methods such as thermal bubble jet printing and inkjet printing [see Figs. 2.1(a)].[54] In the AJP process, the polymer ink, in the form of aerosolized particles, is deposited on the printing surface, as shown in Fig. 2.1(b). The deposited drop undergoes a simultaneous spreading and photopolymerization dynamics. We consider two separate cases dictated by the relative values of the spreading time scale (τ_s) and the polymerization (triggered by the *in-situ* curing) time scale (τ_p). We develop numerical simulations based on the *two-phase laminar-flow moving mesh method (TPLFMMM)* to track the coupled spreading-polymerization dynamics of the liquid drop. We first study the case where $\tau_s << \tau_p$. For this case, the drop first spreads and it polymerizes only after the spreading has completed. Therefore, the problem of spreading and polymerization are decoupled. We denote this case as Case 1. We next study the case where $\tau_s \sim \tau_p$. For this case, the spreading and the polymerization occur simultaneously. As a consequence, the spreading event manifests the effect of the progressive change in drop properties (e.g., change in viscosity, density, etc.) associated with the polymerization process. We denote this case as Case 2. We study in detail the time-dependent variation of the temperature, velocity, and concentration (of the monomer) profiles within the drop for both the cases 1 and 2. We unravel the distinct differences in the spreading dynamics for the two cases. Polymerization-induced progressive increase in the viscosity of the drop ensures that the drop spreading for case 2 is retarded as manifested by a slower increase in *r* with *time* (where *r* is the wetted radius) as well as a smaller value of r_{eq} (where r_{eq} is the equilibrium value for the wetted radius). Secondly, we study the time-dependent evolution of the

temperature within the drop. The average temperature of the drop first decreases and then increases (back to its original temperature) over time for both the cases as it spreads. Of course, the rate and the extent of this decrease and increase in the temperature is dictated by the value of τ_p. Finally, we study the variation of the curing profiles for the two cases. These curing profiles directly provide the monomer concentration profiles: a larger extent of curing implies a smaller concentration of the monomers. The smaller value of τ_p for Case 2 implies a much faster curing of the drop. Furthermore, tracking of the curing front (or the iso-monomer-concentration lines) establish a direction of the curing from the drop three-phase-contact-line to the drop center. Overall, by highlighting the effect of the interplay of spreading and *in-situ* polymerization for a polymer drop, the present paper sheds light on an important complex thermo-fluid-solutal dynamics process with applications in a plethora of disciplines ranging from additive manufacturing to fabrication of various polymer-based materials.

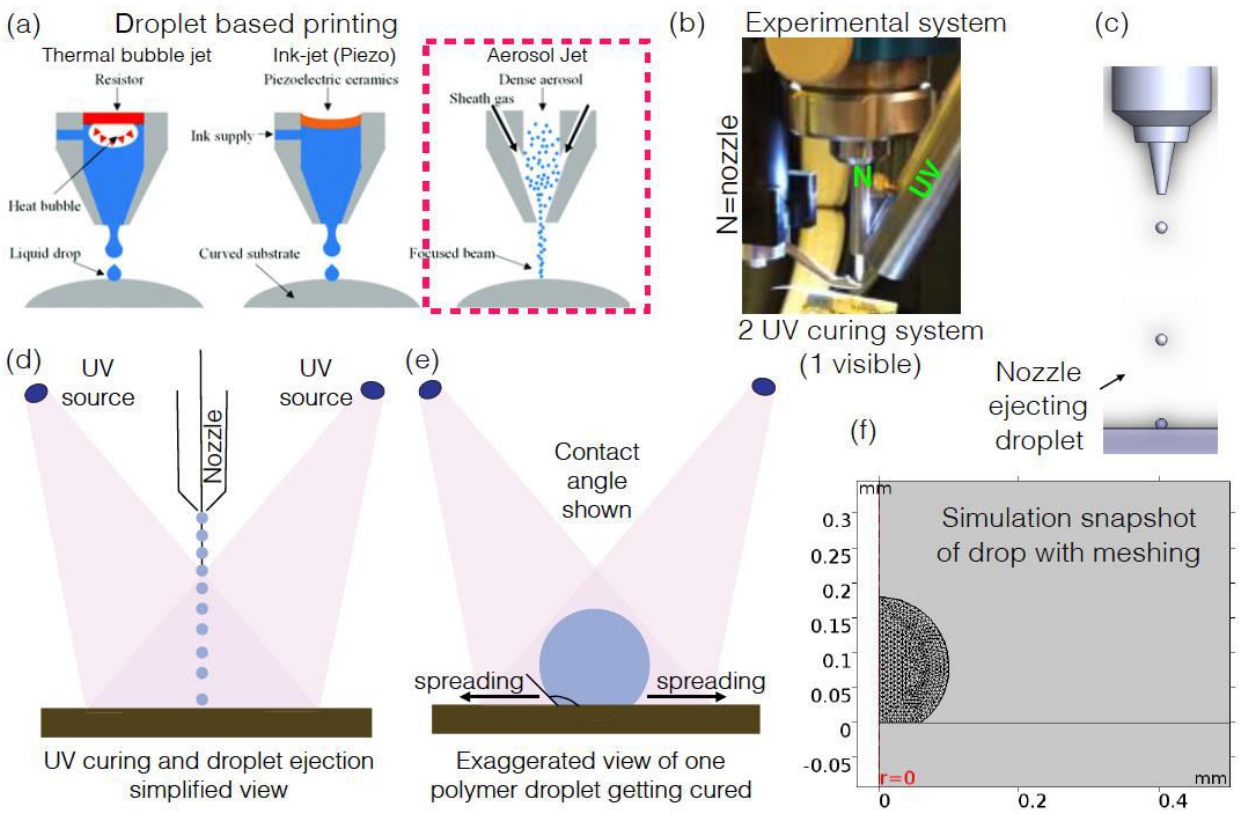

Figure 2.1: (a) Examples of droplet-based 3D-printing methods: thermal bubble jet printing, inkjet printing, and aerosol jet printing. A part of Fig. 2.1(a) has been reproduced from Ref. 54 with permission from The Royal Society of Chemistry. (b) Experimental set up showing the UV-mediated in-situ curing of the aerosol-jet printed photocurable polymer. We have employed this strategy in our previous papers to AJ print several polymer-based systems.[17,51,52] (c) A schematic showing the drops coming out from the tip of the AJ printer. (d,e) Schematic representations of the problem of drop dynamics in the presence of simultaneous spreading and photopolymerization. (f) Description of the simulation set up showing the simulation box, the simulated drop, and the meshing used for the numerical simulations. The meshing for the surrounding air and the substrate is not shown for the purpose of clarity. The dimensions of simulation box and the substrate are

3mm x 3mm and 3mm x 0.5mm, respectively. The radius of the droplet is 10μm and the initial contact angle is 135^0.

2.2 Theory and Simulations

2.2.1 Governing Equations

The simulations for the dynamics of the polymer drop are carried out using the *two-phase laminar-flow moving mesh method (TPLFMMM)*. We start with a simulation geometry as shown in Fig. 2.1(d). We use a 2D axisymmetric model of incompressible Moving mesh approach with surface tension modeling. The Moving mesh is used to capture the moving interface of the droplet that is spreading. The simulations are started from the point where the drop has touched the surface and has spread slightly. In other words, at the start of the simulation, the drop has a contact angle of 135^0. We do such a thing since we are employing the Moving Mesh method that faces difficulty to converge for cases of large deformation. By considering such a starting point for the drop, we exclude the situation of large deformations that occur at the very start of the spreading process. Under this condition, the coupled thermo-fluid-solutal dynamics of the drop is obtained by solving the following equations:

2.2.1.1 Continuity and Navier Stokes equations

The continuity and Navier Stokes equations for describing the incompressible velocity field vector $\boldsymbol{u}$ and the pressure field p in the system (the system consists of the polymer drop and the surrounding air) can be expressed as:

$$\nabla.(\boldsymbol{u}) = 0, \qquad (2.1)$$

$$\rho\frac{\partial \boldsymbol{u}}{\partial t} + \rho(\boldsymbol{u}.\boldsymbol{\nabla})(\boldsymbol{u}) = \nabla.[-pI + \mu(\nabla\boldsymbol{u} + (\nabla\boldsymbol{u})^T)] + \boldsymbol{F}. \qquad (2.2)$$

In the above equations, ρ and μ are the density and the dynamic viscosity of the fluid (either the drop or the air), $\boldsymbol{u}$ is the velocity vector, and $\boldsymbol{F}$ is the per unit volume gravitational body force. The equilibrium contact angle of the droplet with the substrate is 25^0. The interfacial surface tension between the drop and air is 0.024 N/m. Finally, the drop-air fluid-fluid interface is modeled by the following equation:

$$\boldsymbol{n}.(\boldsymbol{T_1} - \boldsymbol{T_2}) = \sigma(\nabla.\boldsymbol{n})\boldsymbol{n} - \nabla\sigma, \quad (2.2a)$$

where, T_1 and T_2 are total stress tensors in fluid 1 (drop) and 2 (air), respectively, σ is the drop-air surface tension, and $\boldsymbol{n}$ is the surface normal.

Here we solve eqs.(2.1,2.2) for two domains: 1 – polymer drop, 2- air.

The viscosity for the polymer drop is expressed as:[55]

$$\mu_1 = \mu_0 \exp(\kappa\alpha) \exp\left(\frac{U}{RT}\right), \quad (2.3)$$

where μ_0 is the apparent viscosity that can be expressed as:[56]

$$\mu_0 = m\,\dot{\gamma}^{n-1}. \quad (2.4)$$

In eq. (2.4), $\dot{\gamma}$ is the shear rate, m is the consistency coefficient, and n is the power law index. Eq.(2.4) suggests that we are considering the polymer as a shear-thinning, non-Newtonian liquid. Of course, the polymer drop is constantly undergoing photo-polymerization; therefore, its viscosity should increase as a function of the extent of polymerization. This is accounted for by the term "exp (κα)" in eq.(2.3). Here α (defined later) denotes the degree of cure; hence larger the extent of polymerization, i.e., larger the extent of cure, larger will be the value of exp (κα) (for a positive κ), or larger the value of the viscosity μ. Furthermore, in eq. (2.3), R and T denote the universal gas constant and the

absolute temperature in Kelvin. Finally, *U* in eq. (2.3) refers to the energy of activation associated with the viscous flow that characterizes the drop spreading. We consider *U* as a constant and independent of the varying (due to photopolymerization) viscosity of the drop.

The density of the polymer drop is expressed as:[57]

$$\rho_1 = (1 - \alpha)\rho_m + \alpha\,\rho_p, \qquad (2.5)$$

where ρ_m=1250 kg/m^3 is the density of the unpolymerized liquid part and ρ_p=1375 kg/m^3 is the density of the photo-polymerized solid part.

Finally, the viscosity and the density of air, μ_2 and ρ_2, respectively, are obtained from the COMSOL database and are provided in Table 2.1.

2.2.1.2 Energy equations

The heat transfer effects are modeled by solving the energy equation for the three domains (1- droplet, 2- air, 3- silica substrate):

$$\rho_1 C_{p1}\left(\frac{\partial T}{\partial t} + \boldsymbol{u}\nabla.T\right) = \nabla.(k_1\nabla T) + Q - \Delta H_r\frac{\partial c_m}{\partial t}, \qquad (2.6)$$

$$\rho_2 C_{p2}\left(\frac{\partial T}{\partial t} + \boldsymbol{u}\nabla.T\right) = \nabla.(k_2\nabla T), \qquad (2.7)$$

$$\rho_3 C_{p3}\frac{\partial T}{\partial t} = \nabla.(k_3\nabla T), \qquad (2.8)$$

where C_{pi} and k_i are respectively the specific heat capacity at constant pressure and the thermal conductivity of the material *i* (*i*=1,2,3). Furthermore, *T* is the temperature in Kelvin, c_m is the concentration of the monomer, and ΔH_r is the heat of polymerization reaction. The different parameters governing eqs. (2.1-2.8) are provided in Table 2.1.

In eq.(2.6), Q is the source term that accounts for the volumetric heating effects. It is expressed as:

$$Q = I\epsilon c_i, \quad (2.9)$$

where I is the local radiation intensity (in W/m^2), ϵ is the molar absorptivity coefficient, and c_i is the local concentration of the UV-radiation absorbing species, i.e., the initiators. I is calculated in accordance with Beer-Lambert's law as:

$$I = I_0 e^{-\int \epsilon c_i(z) dz}, \quad (2.10)$$

where I_0 is the incident radiation intensity and z is the path length of the beam through the material sample. The different parameters governing eqs. (2.1-2.10) are provided in Table 2.1.

2.2.1.3 Species Transport equations

The degree of cure α depends on the instantaneous local value of c_m [see eq.(2.17) later]. Accordingly, c_m will affect the velocity distribution given that the viscosity and the density of the polymer drop depend on α [please see eqs.(2.3,2.5)]. Also, the energy equation, in addition to being dependent on the density, directly involves terms that depend on c_m. Therefore, the problem can only be closed by an appropriate description of the monomer concentration distribution c_m. Below, we describe in detail the equations governing the distribution of c_m and the origin of these equations.

Here we are considering a free-radical chain photopolymerization process. This process generally starts with the process of initiation, in which the initiator molecule (E) absorbs a photon and yields free radical pair R° [see eq.(2.11a)]. Subsequently, the free radical reacts with a monomer molecule M_1 to form the chain-initiating species M_1° [see eq.(2.11b)].

These species react with other unreacted monomers to propagate the chain [see eqs.(2.11c-e)]. Finally, the process is terminated by either the coupling or the disproportionation or both leading to the formation of a dead polymer [see eq.(2.11f) and Ref. 58].

$$E \overset{h\upsilon}{\rightarrow} 2R^{\circ} \quad (2.11a)$$

$$R^{\circ} + M_1 \overset{k_1}{\rightarrow} M_1^{\circ} \quad (2.11b)$$

$$M_1^{\circ} + M_1 \overset{k_2}{\rightarrow} M_2^{\circ} \quad (2.11c)$$

$$M_2^{\circ} + M_1 \overset{k_3}{\rightarrow} M_3^{\circ} \quad (2.11d)$$

$$\ldots\ldots\ldots\ldots$$

$$M_n^{\circ} + M_1 \overset{k_{n+1}}{\longrightarrow} M^{\circ}_{n+1} \quad (2.11e)$$

$$M_j^{\circ} + M_k^{\circ} \overset{k_t}{\rightarrow} dead\ polymer \quad (2.11f)$$

Here $k_\alpha s$ (α=1,2,..,n) are the rate constants for the propagation reaction and k_t is the rate constant for the termination reaction (considering both coupling and/or disproportionation effect). We consider $k_1 = k_2 = ... = k_n = k_p$, which implies that the rate of reaction is independent of the chain length. Both k_p (propagation rate constant) and k_t (termination rate constant) are calculated using the Arrhenius equation, i.e.,

$$k_j = A_j e^{-E_j/RT}, \quad (2.12)$$

where E_j is the activation energy and A_j is the frequency factor of each stage j (j=p,t).

Under the condition $k_1 = k_2 = ... = k_n = k_p$, we can express the species transport equation for the monomer concentration c_m [note that here we represent the molecule of the monomer as M_1, see eq.(2.11b)] as:[58,59]

$$\frac{\partial c_m}{\partial t} + \nabla.(-D_m.\nabla \mathrm{c}_m) + \boldsymbol{u}.\nabla \mathrm{c}_m \;=\; \mathrm{R}_m, \quad (2.13)$$

where

$$\mathrm{R_m} = -k_p\, c_m \left(\frac{\Phi I_{\,abs}}{k_t}\right)^{\frac{1}{2}}. \quad (2.14)$$

In eq.(2.13), D_m is the diffusivity of the monomers. On the other hand in eq.(2.14), ϕ, which is a constant (see Table 2.1 for the value), is the quantum yield for the initiation, i.e., it represents the number of propagating chains that get initiated for every light photon that has been absorbed.[60] Also in eq.(2.14), I_{abs} is the rate of photon absorption in mol/(Ls) and can be expressed as:

$$I_{abs} = \frac{\partial I_{moles}}{\partial z} \;=\; I_{moles}\epsilon \mathrm{c}_i, \quad (2.15)$$

where I_{moles} is the intensity of light in μmol/(m^2s) and is related to the intensity I (having units of W/m^2) appearing in eqs.(2.9,2.10) through a simple conversion factor,[61] i.e., $I_{moles} = (4.57 \times 10^{-6}[\mathrm{mol/J}])I$.

Finally, the species transport equation for the initiator concentration c_i [note that here we represent the molecule of the initiator as E, see eq.(2.11a)] can be expressed as:[59]

$$\frac{\partial c_i}{\partial t} + \nabla.(-\mathrm{D}_i \nabla c_i) + \boldsymbol{u}.\nabla c_i \;=\; -\mathrm{I}_{abs} c_i, \quad (2.16)$$

where D_i is the diffusivity of the initiator.

Finally, the degree of cure α appearing in eqs.(2.3,2.5) can be expressed in terms of the instantaneous monomer concentration c_m and the initial monomer concentration c_{m0} as:

$$\alpha = \frac{c_{m0} - c_m}{c_{m0}}. \quad (2.17)$$

2.2.1.4 Initial Conditions

The initial conditions for all the velocity components are considered to be zero. The initial condition for the pressure is considered to be atmospheric pressure. The initial temperatures for the drop, the surrounding, and the substrate are T=300 K. The initial monomer concentration is c_{m0}= 2000 moles/m^3. The initial initiator concentration is c_{i0}=100 moles/m^3.

2.2.1.5 Boundary Conditions

2.2.1.5.1 Velocity and pressure boundary conditions

We employ a Navier-slip condition and a no-penetration boundary condition at the substrate.

The no-penetration boundary condition is expressed as:

$$\boldsymbol{u}.\boldsymbol{n} = 0, \quad (2.18)$$

where $\boldsymbol{n}$ is the unit normal vector to the substrate.

The Navier-slip condition is expressed as:

$$\mathbf{F_{fr}} = -\frac{\mu}{\beta}\mathbf{u}, \quad (2.19)$$

where $\mathbf{F_{fr}}$ is the friction force on the fluid based on the fluid velocity,[36,37] β is the slip length. The slip length is usually of the order of mesh size; here we take it as half of the mesh size.[64]

We employ the atmospheric pressure condition at the other two boundaries of the simulation domain [Fig. 2.1(d) shows the simulation domain].

2.2.1.5.2 Temperature boundary condition

T=300 K is maintained as the boundary condition at the top, side (right), and the bottom wall boundaries of the simulation domain [see Fig. 2.1(d)]. The bottom wall is the bottom of the finitely thick (thickness $t_{substrate}$=0.5 mm) glass substrate.

2.2.1.5.3 Concentration boundary condition

We employ a *no-flux* boundary condition at the drop-substrate and the drop-air interfaces at all times.

For all the variables, symmetry condition is employed at the left boundary (i.e., the plane passing through the drop) of the simulation domain [see Fig. 2.1(d)].

2.2.2. Simulation Procedure

The simulation considered all the equations simultanoeusly and did not unnecessarily simplify any of the equations by deleting any term. The Navier -Stokes equations are solved by using Laminar Two-Phase Flow-Moving-Mesh module of COMSOL. We use General

Partial Differential equation (PDE) module that applies volumetric heat source based on Beer-Lambert's law. The governing equations for polymerization can be implemented into COMSOL interface by using Transport of Dilute Species module (TDS). To implement the moving mesh method to track the interface, an automatic remeshing condition based on mesh quality is provided to ensure proper meshing conditions.

We provide the definition as well as the values of all the parameters used in the simulation in Table 2.1.

Parameter	**Definition**	**Value**	**Reference**
ρ_m	Density of monomer	1250 [kg/m^3]	Ref. 53
ρ_p	Density of polymer	1375 [kg/m^3]	
ρ_2	Density of air	1.164 [kg/m^3]	COMSOL Database
μ_2	Viscosity of air	20×10^{-6} [Pa.s]	COMSOL Database
m	Consistency index	2	Ref. 56
N	Power law index	0.6	
κ	a constant	2	

U	Energy of activation associated with the viscous flow	1.1 [kJ/mol]	Ref. 65
R	Universal gas constant	8.314 [J/mol/K]	COMSOL Database
σ	Surface tension of the drop/air interface	0.024 [N/m]	Ref. 26
θ	Contact angle	25^0	
ρ_3	Density of silica glass	2203 [kg/m^3]	Ref. 66
k_1	Thermal conductivity of drop	0.3 [W/m/K]	Ref. 53
k_2	Thermal conductivity of air	0.03 [W/m/K]	COMSOL Database
k_3	Thermal conductivity of silica glass	1.38 [W/m/K]	Ref. 66
C_{p1}	Heat capacity (at constant pressure) of the drop	4185 [J/kg/K]	Ref. 26
C_{p2}	Heat capacity (at constant pressure) of air	1007[J/kg/K]	COMSOL Database

C_{p3}	Heat capacity (at constant pressure) of silica	708 [J/kg/K]	Ref. 66
I_0	Incident radiation intensity	100 [mW/cm^2]	Ref. 67
ϵ	Absorption coefficient	150 [m^2/mol]	Ref. 59
c_{i0}	Initial initiator concentration	0.1 [M]	
H_r	Heat of polymerization reaction	-50 [kJ/mol]	Ref. 58
E_p	Activation energy for the propagation reaction	29.7 [kJ/mol]	
E_t	Activation energy for the termination reaction	22.2 [kJ/mol]	
A_{p1}	Frequency factor for the propagation reaction for case 1 ($\tau_s << \tau_p$)	5×10^{10} [L/mol/s]	
A_{p2}	Frequency factor for the propagation reaction for case 2 ($\tau_s \sim \tau_p$)	1.2×10^{12} [L/mol/s]	

A_t	Frequency factor for the termination reaction (identical for cases 1 and 2)	10^{11} [L/mol/s]	
D_i	Diffusivity of initiator	1e-9 [m^2/s]	Ref. 68
D_m	Diffusivity of monomer	1e-9 [m^2/s]	
c_{m0}	Initial concentration of monomer	2000 [mol/m^3]	Ref. 69
ϕ	Quantum yield	0.6	Ref. 60

Table 2.1: Definition and values of the different parameters used

2.3. Results

2.3.1 Velocity Distribution within the Drop for Case 1 for Different Time Instants

We show the velocity distributions inside the spreading drop for case 1 (i.e., where $\tau_s << \tau_p$) at different time instants in Fig. 2.2. In this paper, for a drop of a given material and size, $\tau_s = \tau_c + \tau_v = \sqrt{\frac{\rho r_0^3}{\sigma}} + \frac{\mu r_0}{\sigma}$, where τ_c and τ_v are the capillary and viscous timescales,[70] r_0 is the drop radius, σ is the air-drop surface tension (defined in Table 2.1), ρ is the drop density, and μ_0 is the apparent viscosity defined by eq.(2.4). Also, τ_p is defined as $\tau_p = \frac{1}{k_p \left(\frac{\phi I_{abs} 4.57 \times 10^{-6}}{k_t} \right)^{0.5}}$ [where k_p and k_t are defined by eq.(2.12), ϕ is defined by eq.(2.14), and I_{abs} is defined by eq.(2.15)].

Here we consider a drop of radius 0.01 mm, A_{p1} as the frequency for the propagation reaction, and all other properties defined in Table 1. For such a drop, $\tau_s \approx 1.1$ ms and $\tau_p \approx 66$ ms. As has been pointed out before, the simulation starts from the condition where the drop has already contacted the substrate and the spreading has begun. Near the starting point of the simulation (t=0.1 ms), we observe a large gradient in the velocity field within the drop with the velocity decreasing rapidly towards the substrate [see Fig. 2.2(a)]. The effect of the substrate quickly progresses away from the wall causing a rapid decrease in the velocities inside the drop away from the wall (see the velocity distribution within the drop from t=0.15 to 0.4 ms) [see Figs. 2.2(b-e)]. This progressive decrease in the velocities within the drop occurs simultanoeusly along with the spreading of the drop, eventually enforcing the drop to attain an equilibrium at 1-4 ms, i.e., around the time dictated by τ_s [see Figs. 2.2(f-h)]. Since $\tau_s << \tau_p$, the polymerization sets in after the spreading has

completed and accordingly the spreading is unaffected by the polymerization process. Therefore, we simply show the velocity distributions for $t \leq 4$ ms.

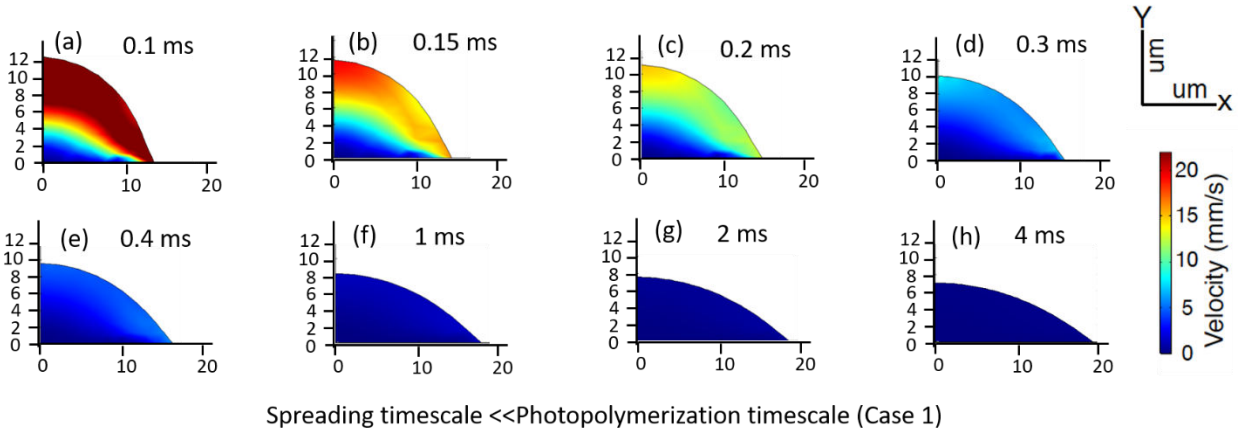

Figure 2.2 (a-h): Velocity distribution within the spreading polymer drop at different time instants for case 1 ($\tau_s << \tau_p$). Here we have $\tau_s \approx 1.1$ ms and $\tau_p \approx 66$ ms. Velocity profiles within the air have not been shown for the sake of clarity.

2.3.2 Velocity Distribution within the Drop for Case 2 for Different Time Instants

In Fig. 2.3, we show the velocity distribution within the spreading drop for case 2 (i.e., where $\tau_s \sim \tau_p$) for different time instants. Here we consider a drop of radius 0.01 mm, A_{p2} as the frequency for the propagation reaction, and all other properties defined in Table 1. Accordingly, we get $\tau_s \approx 1.1$ ms and $\tau_p \approx 3.3$ ms. Here too at the starting point of the simulation (t=0.1 ms), we observe a large gradient in the velocity field within the drop with the velocity decreasing rapidly towards the substrate [see Fig. 2.3(a)]. Similarly, this velocity gradient quickly nullifies and the velocity within the drop reaches close to uniformity (see from t=0.15 to 0.4 ms) [see Figs. 2.3(b-e)]. Here too the equilibrium is attained around 1-4 ms [see Figs. 2.3(f-h)], although the equilibrium-spreading radius is distinctly smaller than that for case 1 [see Fig. 2.4(a)]. This stems from the fact that the drop polymerizes and solidifies and hence stops spreading. Obviously, such an interplay between the spreading and the polymerization dynamics is possible since τ_s and τ_p are comparable, which is not the case for Case 1.

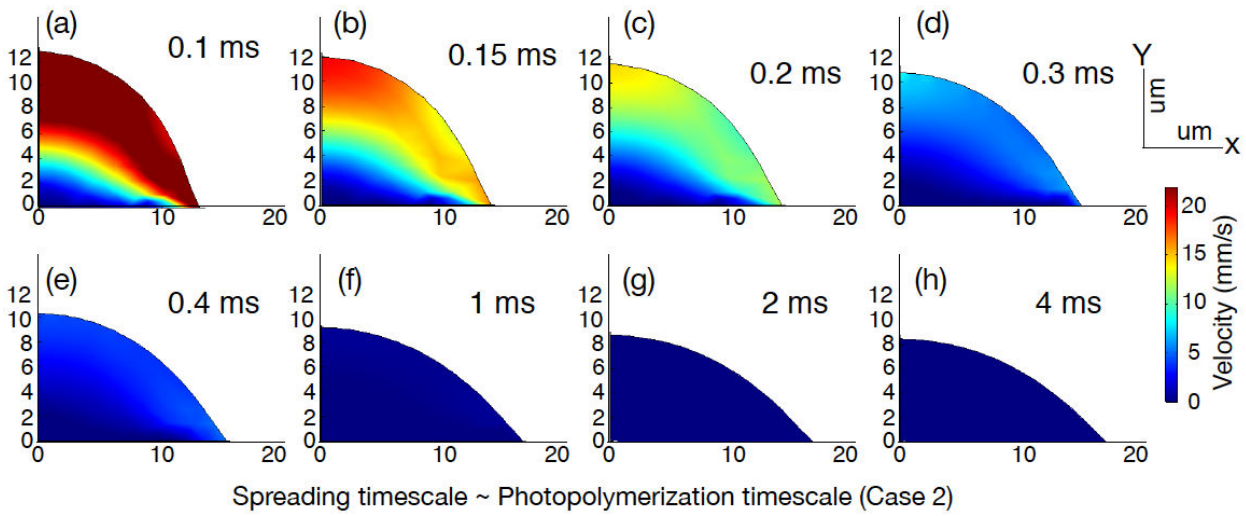

Figure 2.3 (a-h): Velocity distribution within the spreading drop at different time instants for case 2 ($\tau_s \sim \tau_p$). Here we have $\tau_s \approx 1.1$ ms and $\tau_p \approx 3.3$ ms. Velocity profiles within the air have not been shown for the sake of clarity.

2.3.3 Time Variation of the spreading radius and contact angle of the Drop for Cases 1 and 2

Fig. 2.4(a) shows the time variation of the spreading radius of the drop for the two cases. The progressively increasing viscosity of the drop for the case when the spreading and polymerization time scales are comparable (Case 2) will imply that the spreading of the drop for this case is retarded. Accordingly, the rate of spreading is slower. Furthermore, the polymerization effect ensures that the drop solidifies and hence stops to spread much sooner than the drop for case 1. Accordingly, the equilibrium radius of the drop for Case 2 is smaller than that for Case 1.

Fig. 2.4(b) shows the variation of the drop contact angle with time for the two cases. The drop contact angle for case 1 (i.e., the case where the viscosity is unaffected by the polymerization during the spreading process) decreases much faster confirming an augmented spreading rate. Furthermore, the drop for case 2, due to the polymerization-induced increased viscosity, stops to spread much earlier than the drop for case 1. Accordingly, the final equilibrium contact angle is much smaller for the drop in Case 1 as compared to the drop in Case 2.

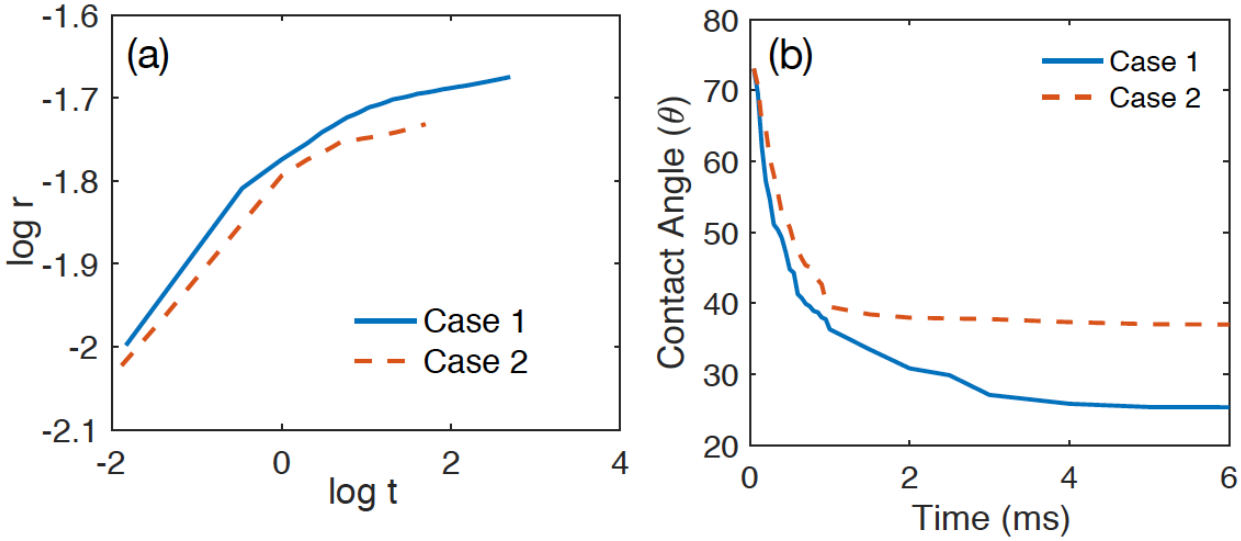

Figure 2.4: (a) Variation of the spreading radius (r) with time for the two cases. (b) Variation of the drop contact angle with time for the two cases. In (b), we intentionally show the contact angle variation starting from a finite time (t>0.2 ms). Here for case 1, we have $\tau_s << \tau_p$ ($\tau_s \approx 1.1$ ms and $\tau_p \approx 66$ ms) and for case 2, we have $\tau_s \sim \tau_p$ ($\tau_s \approx 1.1$ ms and $\tau_p \approx 3.3$ ms).

2.3.4 Temperature Distribution within the Drop for Cases 1 and 2 for different time instants

Figs. A1(a-h) and A2(a-h) in the Appendix A provide the temperature distribution within the drop for different time instants for Cases 1 and 2, respectively. At the start, the drop, the surroundings, and the glass substrate on which the drop spreads are all at 300 K. Under these conditions, the absorption of the incident UV radiation by the drop leads to a volumetric heat addition to the drop. However, the polymerization reaction itself ensures that the heat is released by the drop. The second effect overwhelms the first effect, which would suggest that polymerization process leads to an instantaneous reduction of the average drop temperature.

First, we consider Case 1 (see Fig. A1). Here τ_p being large, the rate of polymerization is weak. Accordingly, the heat loss is significantly weak and consequently one witnesses a very small decrease in the drop temperature. Given that the substrate is maintained at T=300 K, this decrease in temperature is more prominent at drop locations away from the drop-substrate interface. Also, the presence of the constant temperature of 300 K at the substrate and the fact that the rate of polymerization (and hence the rate of heat loss) is very weak, will imply that the substrate quickly increases the temperature of the parts of the drop near the substrate back to 300 K. Accordingly, the average temperature of the drop for Case 1 first decreases quickly by ~0.15 K and then starts to increase much more slowly to reach 300 K asymptotically at a time $t\sim \tau_p$. This is evident from Fig. 2.5.

A much more interesting case is that of case 2, where $\tau_s \sim \tau_p$ (see Fig. A2). Here too the effect of heat addition due to incident UV radiation is overwhelmed by the heat release due to the polymerization reaction, ensuring an overall decrease in the drop temperature. A key

difference with respect to case 1, however, is the fact that τ_p being much smaller here, the rate of polymerization is much faster. Accordingly, the rate of heat release is much faster leading to a large decrease in the temperature (~3K) within a very small time instant. This is evident from Fig. A2 (Appendix A) and Fig. 2.5. However, τ_p being small, the polymerization quickly ceases and at that point the condition of a constant wall temperature becomes dominant enforcing an increase in the drop temperature back to 300 K. Like the case 1, here too, dictated by the presence of the condition of a constant substrate temperature, both the decrease and the increase (back to 300 K) of the drop temperature is typically at drop locations away from the drop-substrate interface.

2.3.5 Variation of the average drop temperature with time for Cases 1 and 2

Fig. 2.5 provides the time variation of the average drop temperatures for cases 1 and 2. A rapid rate of polymerization for case 2 and a weak rate of polymerization for case 1 explains the rapid decrease (by as large as ~3K) and a slightly weaker increase (back to 300 K) of the average drop temperature for case 2, while a weak decrease (not more than 0.15 K) and an even weaker slow increase (back to 300 K) of the average drop temperature for case 1 (see Fig. 2.5 and its insets).

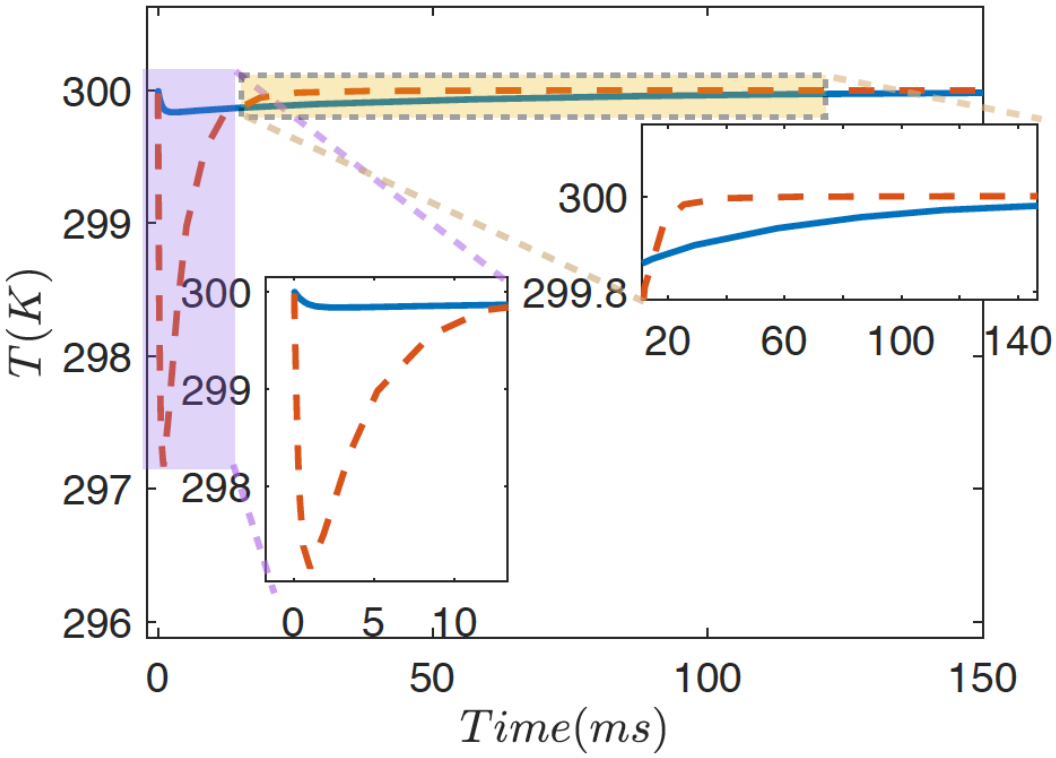

Figure 2.5: Variation of the average temperature of the drop with time for the two cases (the solid and the dashed lines represent the temperature profiles for cases 2 and 1, respectively). In the top and the bottom insets respectively, the temperature values for the two cases for intermediate and small times have been magnified.

2.3.6 Curing Profiles within the Drop for Case 1 for Different Time Instants

Figs. A3(a-h) in the Appendix A provide the curing profile α of the drop for case 1. Variation of α directly provides the variation of the monomer concentration c_m: larger α implies a smaller c_m [see eq. (2.17)]. Therefore, the curing profiles quantified in the next few figures actually reflect the corresponding variation in c_m. A value of α=1 indicates a complete curing. As expected, with time the polymer drop gets more and more cured (i.e., the monomer concentration decreases progressively due to polymerization). For case 1, τ_p ≈ 66 ms and accordingly, the drop cures over a longer time [for example, an average degree of curing of 0.7 is attained around 80 ms, see Fig. A3(e)].

Fig. 2.6(a) shows the time evolution of the curing front (corresponding to α=0.1) for case 1 elucidating the direction in which the curing progresses. One can clearly see that the curing front proceeds from the three-phase contact line of the drop towards the drop center. This stems from the fact that the TPCL is always at the highest possible temperature in system (i.e, 300 K), while the rest of the drop can have a smaller temperature due to the polymerization effect (as already discussed in Figs. A1, A2, and 5).

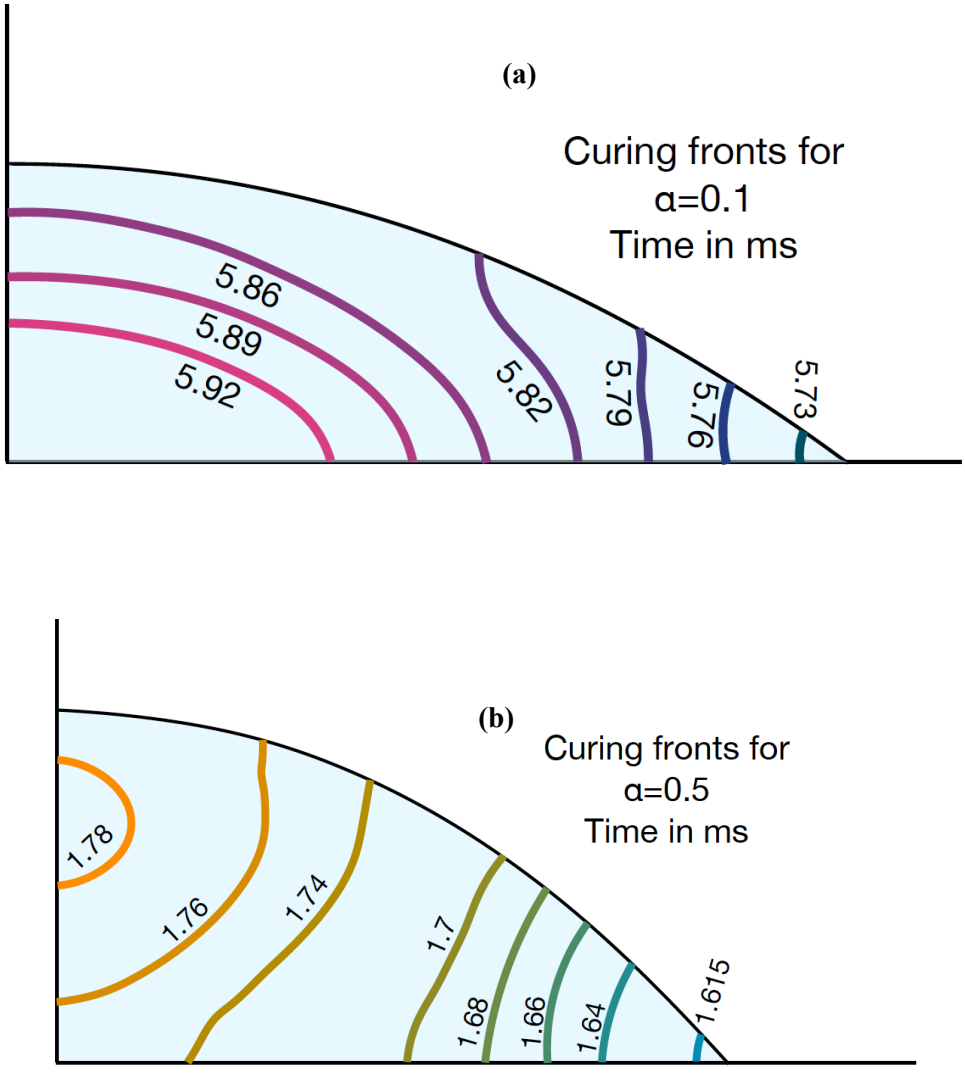

Figure 2.6: (a) Progression of the curing front (corresponding to α=0.1) for case 1. The numbers beside each front depict the corresponding times in milliseconds. The front, which is shown in green, can be also interpreted as a representation of the iso-monomer-concentration line at different time instants. (b) Progression of the curing front (corresponding to α=0.5) for case 2. The numbers beside each front depict the corresponding times in milliseconds. The front which is shown in green can be also interpreted as a representation of the iso-monomer-concentration line at different time instants.

2.3.7 Curing profiles within the drop for Case 2 for different time instants

The curing profiles within the drop for Case 2 ($\tau_s \sim \tau_p$) [see Fig. A4(a-h) in the Appendix A] are qualitatively very similar to that of case 1 (see Fig. A3) with the only exception that the curing occurs much faster since $\tau_{p,Case\ 2} \approx 3.3$ ms is much smaller than $\tau_{p,Case\ 1}$. Hence the drop is 70% cured at t=3 ms [see Fig. A4(e)], as compared to being 70% cured at t=80 ms for Case 1 [see Fig. A3(e)].

Fig. 2.6(b) shows the time evolution of the curing front (corresponding to α=0.5) for case 2 establishing that here too the curing progresses from the drop TPCL to the drop center.

2.3.8 Variation of the average drop curing profile with time for Cases 1 and 2

Fig. 2.7 provides the time variation of the average drop curing profile for Cases 1 and 2. As expected, the curing occurs much faster for Case 2 ensuring that the maximum curing (represented by a value of unity) is attained at a much smaller time. Concentration of monomers is inversely related to the degree of cure [see eq.(2.17)]; therefore, Fig. 2.7 also quantifies the decay of the monomer average concentration.

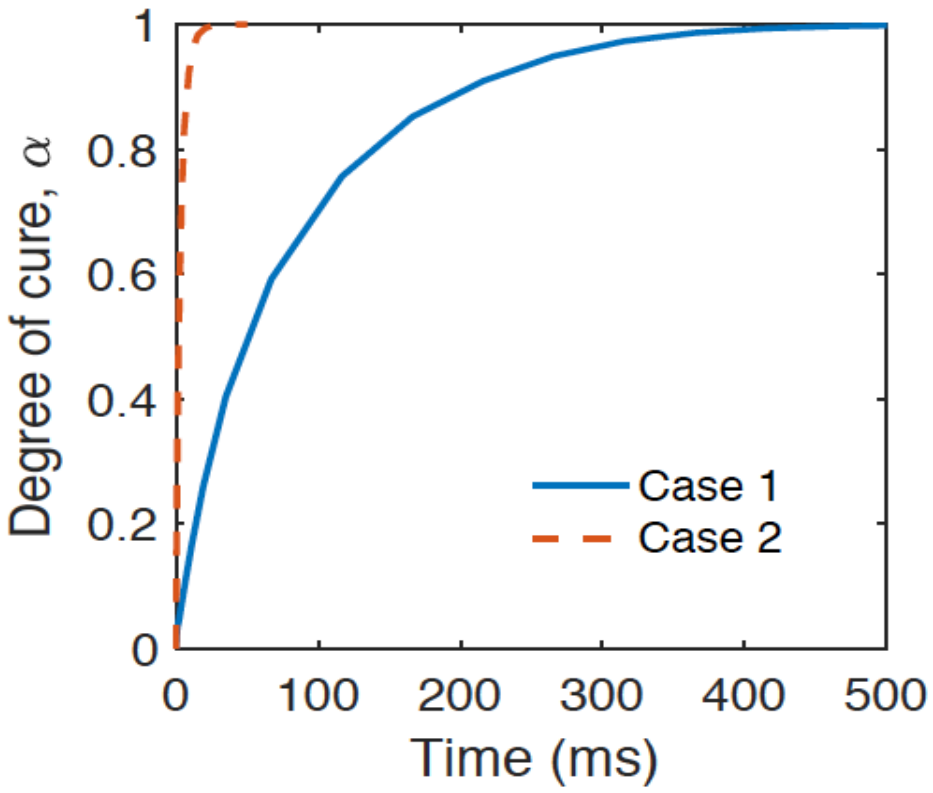

Figure 2.7: Variation of the average curing profile (quantified by the degree of polymerization) with time for the two cases.

2.3.9 Effect of the drop sizes on the drop behaviour

In order to obtain a generality in our description of the problem, we conducted simulations with more drop sizes: drops of radii 0.1 mm and 1 mm.

A key issue is that we find very similar trends depicting r/r_0-versus-t/τ_c (where r_0 is the drop radius and τ_c is the corresponding capillary time scale) for different drop sizes. For example, for case 1 for drops all the three sizes, we find $r/r_0 \sim (t/\tau_c)^{1/7}$ and $r/r_0 \sim (t/\tau_c)^{1/12}$ at smaller and larger values of t/τ_c, respectively [See Fig. 2.8(a)]. Similar r/R-vs-t/τ_c variation have been well reported experimentally for the spreading dynamics of the polymeric drops for Case 1 (i.e., when $\tau_{s<<}\tau_p$). For example, Ruijter *et al.* in their experimental study on the spreading behavior of di-n-butyl phthalate droplet established a $r \sim t^{1/7}$ and $r \sim t^{1/10}$ variation for the initial and final stages of the drop spreading.[71] On the other hand, Han *et al.* in their experimental study on the spreading behavior of polyisobutylene polymer (a power law based shear-thinning polymer) droplet established a $r \sim t^{1/7}$ and $r \sim t^{1/11}$ variation for the initial and final stages of the drop spreading.[72] For case 2 as well, we find that r/R-vs-t/τ_c shows a very similar variation [see Fig. 2.8(b)] for all the three different drop sizes.

In Fig. A5, we compare the time variation of the average drop temperature for cases 1 and 2 for the three different drop sizes. Results exhibit similar qualitative variation for a given case (case 1 or case 2) for the drops of different sizes, although the exact magnitude of the temperature drop is larger for the larger sized drops.

Finally, in Fig. A6 we compare the time variation of the average degree of cure for cases 1 and 2 for the three different drop sizes. Here too, results exhibit very similar qualitative variation for a given case (case 1 or case 2) for the drops of different sizes.

All other quantities, namely the velocity profiles, temperature distributions, curing profiles, and curing fronts are studied for these two different drop sizes (0.1 mm and 1 mm) as well. These results have been provided in Appendix A (please see Figs. A7-A22).

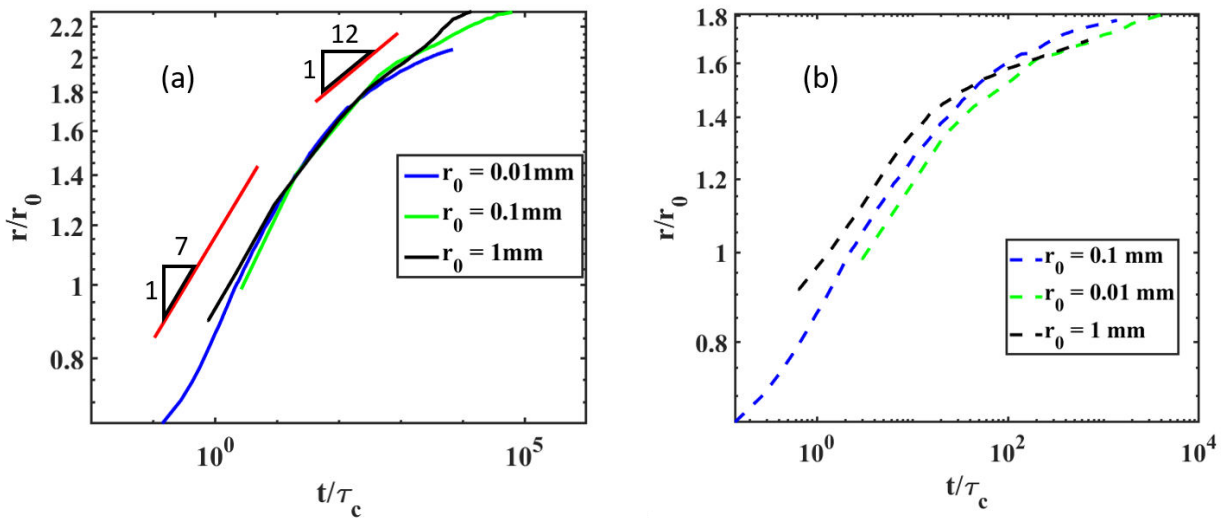

Figure 2.8: Variation of the dimensionless spreading radius (r/r_0) with the dimensionless time (t/τ_c) for (a) Case 1 and (b) Case 2. For Case 1, $r/r_0 \sim (t/\tau_c)^{1/7}$ and $r/r_0 \sim (t/\tau_c)^{1/12}$ at smaller and larger values of t/τ_c, respectively and these scaling variations are identified in the figures. Here r_0 is the drop radius and τ_c is the corresponding capillary time scale for different drop sizes. We have three values of r_0, i.e., r_0 = 1 mm, 0.1 mm, and 0.01 mm and three corresponding values of the capillary time scales (see Table A1 in Appendix A).

The values for the different characteristic timescales needed for the Figs. 8, S5, and S6 are summarized in Table A1 in the Appendix A (see the 1st paragraph of the **Results** section for the expression of these different time scales)

2.3.10 Comparison with Experimental Results

We are not aware of many studies that have probed the spreading dynamics of a photopolymerizing drop for the condition of case 2 (i.e., $\tau_s \sim \tau_p$). On the other hand, there are several experimental studies that have probed the dynamics of a photopolymerizing drop for the condition of case 1 (i.e., $\tau_s \ll \tau_p$). In Fig. 2.9, we compare our simulation results for the time variation of the spreading radius of the drop with the experimental results (all the parameters needed for the simulation are provided in Table A2). The comparison is done for the 1-mm drop of 1 wt % of carboxymethylcellulose (CMC) solution (a psuedeoplastic).[73] The necessary property information used to conduct the simulations for this material is provided in Table A2 and Refs. 74, 75. The results confirm excellent match between the simulation results and the experimental data.

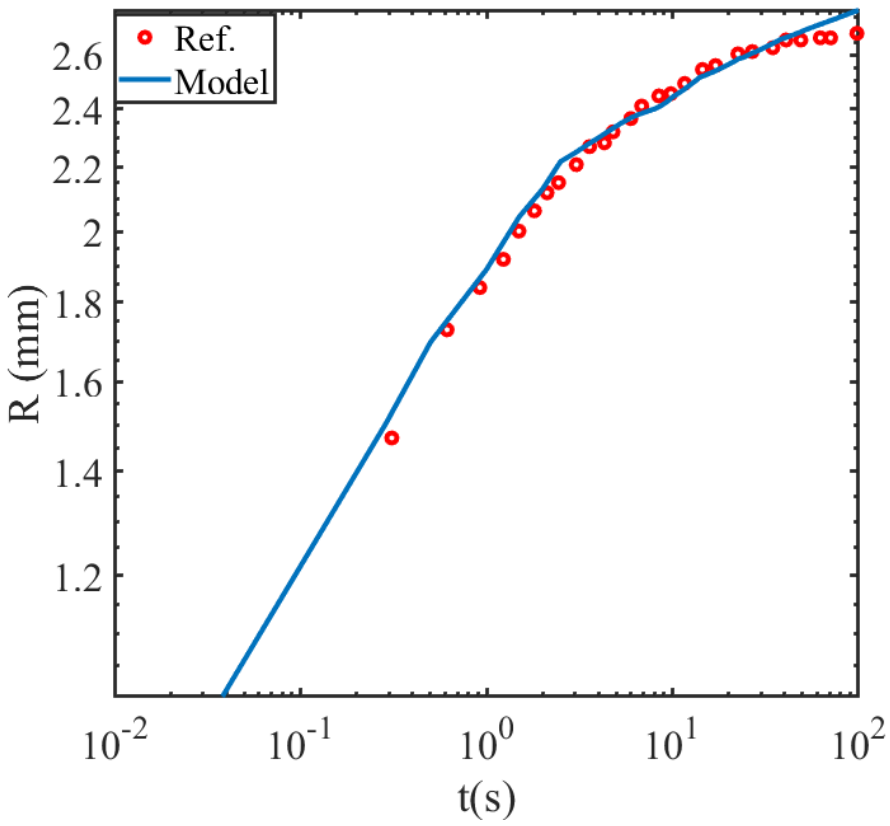

Figure 2.9: Comparison of the simulation result with experiments for the time variation of the spreading radius (R) of 1-mm drop of 1 wt % of carboxymethylcellulose (CMC) solution. The parameters needed to conduct the simulation are provided in Table A2 and those parameters that are not listed in Table A2 are identical to those listed in Table 1. For this case, τ_s= 150 ms and τ_p=1200 ms (i.e., we consider the condition of Case 1). The experimental results are obtained from Ref. 73.

2.4 Discussions

2.4.1 Relevance of the present study in the context of understanding the thermofluidics of the 3D printing processes

As elucidated in Fig. 2.1, the present study has been motivated to better understand the thermofluidics of the AJ polymer printing process, where polymer drops are deposited by the nozzle and these drops undergo simultaneous spreading and *in-situ* photopolymerization.[51,52] The present study will be useful as a starting predictor for quantifying the width of the AJ-printed traces as a function of the rheology of the polymer (dictating the corresponding photopolymerization timescale τ_p), intensity of the UV irradiation, wettability of the printing substrate with respect to the polymer drop, and the size of the polymer drops. Such a prediction will be critical in establishing a more mathematically-supported design space for the choice of the materials and conditions for AJ printing rather than simply relying on a trial and error approach.

Of course, the present thermofluidic problem will be a close representation of the deposition process of the AJ printing as long as as $\tau_d >> \tau_s, \tau_p$. Here τ_d is the deposition timescale, that characterizes the time interval between the deposition of the two drops. The condition $\tau_d >> \tau_s, \tau_p$ will imply that when a second drop comes and hits the deposited first drop, the latter has already completely spread and photopolymerized. Of course, in such a setting, the coupled spreading and photopolymerization dynamics of the second drop will need to be modelled differently since it will spread and photopolymerize on the top of the first drop and not the substrate. The situation becomes much more complicated for cases when $\tau_s < \tau_d < \tau_p$ or $\tau_d < \tau_s, \tau_p$. For these cases, the coupled spreading-photopolymerization dynamics of the first drop gets affected by the fact that before the completion of this

coupled process, the second drop will hit the first drop thereby completely altering the structure and the morphology of the spreading-photopolymerizing drop. Obviously, the present study does not capture such complicated situation where the coupled spreading-photopolymerization dynamics of the deposited polymer drop is getting affected by its interactions with the subsequently deposited drops.

While the studied problem has a close resemblance to the problem of AJ printing or *ink-jet printing,*[48,54] given the fact that these methods print by depositing materials in the form of drops, the problem will also be useful in providing insights to the thermo-fluidics of 3D printing of polymer in the presence of *in-situ* photopolymerization using methods such as *extrusion printing*.[76] For such problems too, there is a moving contact line of a polymeric material (deposited as continuous traces and not drops) undergoing photopolymerization in the presence of *in-situ* curing.

All the different multi-jet/polyjet additive manufacturing processes invariably rely upon printing photocurable polymers and rapid curing of these material by UV light. Therefore, the properties of the printed features (e.g., the thickness of the layer that is possible to deposit in one step) are directly dictated by the competition between spreading and curing. The present study provides the foundational physical basis for studying the not only the aerosol jet or inkjet process, but also such generic multi-jet/polyjet additive manufacturing processes.

Such a competition between the spreading and curing has been intelligently exploited in previous studies to develop novel 3D printed polymer architectures. Such examples include the use of (a) AJ printing to create three-dimensional pillar-like structures from acrylated urethane,[77] (b) syringe printing to fabricate free-standing and shape-memorable filament-

like structures from epoxy polymers,[78] (c) AJ printing of polymeric fillets for fabricating electrical interconnects over fillets,[51] (d) AJ printing of polymeric core for printing solenoidal inductors,[52] (e) AJ printing of polymer support for fabricating 3D printed broadband inductors,[79] etc. Therefore, the present paper can also be potentially useful for designing novel polymer architectures.

2.4.2 Possible Future Improvement of the Present Model

The overall thermofluidic modeling of the AJ printing process has been gathering great interest of late.[80-82] In our recent paper,[26] we described the fluidics problem where the size of the aerosolized ink drops interplays with the Sheath Gas and the Carrier Gas flow rates to dictate the extent of overspray in AJ printing. These calculations provide the velocities at which the drops impact the printing substrate during their deposition. In future studies, we plan to combine this deposition dynamics (or the corresponding effect of impact velocity), which will also dictate the corresponding timescale τ_d, with the coupled spreading-polymerization dynamics of the polymer drops proposed here. This future model will therefore provide a much more complete picture of the thermo-fluidic mechanisms of the AJ printing process where the fluid dynamics of deposition is coupled with the post-deposition dynamics of spreading and polymerization with the two stages (deposition and post-deposition) affecting each other through the interplay of the corresponding timescales τ_d, τ_s, and τ_p making it mandatory to capture the dynamics of multiple interacting polymer drops.

2.5 Conclusions

We have studied here an interesting thermo-solutal-fluidic drop dynamics problem where a polymer drop simultaneously spreads and photopolymerizes (in presence of *in situ* UV curing). The problem is dictated by the relative interplay of the spreading time scale (τ_s) and the photopolymerization time scale (τ_p), which in turn dictates the instantaneous drop properties under which the drop spreads. We study the problem for two cases with disparate relative values of τ_s and τ_p and demonstrate the significant differences in the velocity, temperature and concentration (of monomers) of the polymer drop between these two cases. In addition to being an extremely intriguing thermo-solutal-fluidic problem, this problem will be critical to understand the post-drop-deposition behaviour in AJ printing of polymers with *in-situ* curing. Such an understanding, while being important for pinpointing the overall time of printing and the dimensions of the printed traces, when combined with our previous study on modelling the size-based drop deposition and overspray formation in AJ printing,[26] will form the first comprehensive numerical model of the AJ printing process.

Chapter 3: Coalescence of Microscopic Polymeric Drops: Effect of Drop Impact Velocities*

Abstract

In this chapter, we employ the Direct Numerical Simulation (DNS) method for probing three-dimensional, axisymmetric coalescence of microscale, power-law-obeying, and shear thinning polymeric liquid drops of identical sizes impacting a solid, solvophilic substrate with a finite velocity. Unlike the cases of drop coalescence of Newtonian liquid drops, coalescence of non-Newtonian polymeric drops has received very little attention. Our study bridges this gap by providing (1) the time-dependent, three-dimensional (3D) velocity field and 3D velocity vectors inside two coalescing polymeric drops in the presence of a solid substrate and (2) the effect of the drop impact velocity (on the solid substrate), quantified by the Weber number (We), on the coalescence dynamics. Our simulations reveal that the drop coalescence is qualitatively similar for different We, although the velocity magnitudes involved, the time required to attain different stages of coalescence, and the time needed to attain equilibrium vary drastically for finitely large We. Finally, we provide detailed simulation-based, as well as physics-based, scaling laws describing the growth of the height and the width of the bridge (formed due to coalescence) dictating the 3D coalescence event. Our analyses reveal distinct scaling laws for the growth of bridge height and width for early and late stages of coalescence as a function of We. We also

* Contents of this chapter is published as: V. S. Sivasankar, S. A. Etha, D. R. Hines, and S. Das, "Coalescence of Microscopic Polymeric Drops: Effect of Drop Impact Velocities". *Langmuir*, 37(45), 13512-13526 (2021).

provide simulation-based coalescence results for the case of two unequal sized drops impacting on a substrate (non-axisymmetric coalescence) as well as results for axisymmetric coalescence for drops of different rheology. We anticipate that our findings will be critical in better understanding events such as inkjet or aerosol jet polymer printing, dynamics of polymer blends, and many more.

3.1 Introduction

Coalescence of liquid drops has been one of the most well-studied problems in the realm of capillarity driven fluid flows.[83-91] The fundamental fluid mechanics issues associated with such coalescence that have received significant attention include the identification of different flow regimes and their effects on coalescence[92-98] as well as the identification of the effect of substrate wettability,[99] axisymmetry,[100] surrounding fluid,[101-103] drop surface tension,[104-105] and drop viscosity[106] on the coalescence. Such fundamental knowledge on coalescence has implications in a large number of natural and engineering phenomena such as the formation of rain drops[107] and thunderstorms[108], droplet-based 3D printing (e.g., inkjet printing[109,110] and aerosol jet or AJ printing[111]), stability of foams[112] and emulsions[113], desalting of crude oil[114], and many more. The drop coalescence occurring with the drops either freely suspended inside another fluid medium or in a partially (dynamic) wetting state in contact with a solid has been equally explored. The drop coalescence in the presence of a solid substrate has been typically quantified in terms of the time evolution of the height (h_0)[83,92] and the width (W) of the bridge[92], which characterizes the onset of coalescence (see Fig. 3.1).

Of course, like most capillarity-driven fluid flow problems, for the case of the study of drop coalescence as well, the focus has been primarily on Newtonian drops. However, a large number of applications require probing the drop dynamics and coalescence for polymeric, non-Newtonian liquid drops. Some such examples include the possible in-flight coalescence of polymeric drops as they are transported in a background carrier gas flow inside the printer nozzle during the AJ printing (i.e., when the coalescence occurs with the drops being suspended entirely in another background fluid)[26,111], coalescence of

polymeric drops (with and without *in situ* curing) that have impacted the printing substrate (with a finite velocity) during inkjet printing and AJ printing (i.e., the coalescence event occurs with the drops being in a dynamic wetting state on a solid substrate),[109-111] the mechanisms dictating the dynamics of polymer blends,[115] etc. Very recently, Varma *et al.*[116] presented one of the first studies on the coalescence of polymeric drops. They combined experiments with theory to establish a universality in the dynamics of the neck radius (equivalent to bridge width) characterizing the coalescence between one static drop resting on a solid and another drop being deposited on top of this resting drop. Their claim to universality was based on studies of several types of polymeric drops. Other than this paper, there have been some attempts to probe the collision dynamics of polymeric drops with the drops being primarily suspended in a fluid medium;[117,118] however, there has been little effort to probe in detail the multidirectional dynamics of polymeric-drop coalescence particularly in the presence of a solid substrate and for the case when the polymeric drops have a finite impact velocity on the solid substrate.

In this paper, we develop a direct numerical simulation (DNS) model to probe the three-dimensional (3D) coalescence of two drops of a shear-thinning power-law-obeying polymeric liquid simultaneously impacting and wetting a solid substrate (see Fig. 3.1). Consideration of such impacting drops is motivated by our desire to closely mimic the scenario encountered during droplet-based 3D printing (e.g., inkjet printing or aerosol jet printing): during such printing polymeric droplets (for cases where polymeric materials are being printed) impact the printing surfaces at finitely large velocities and undergo coalescence (and in the process start building up the desired printed component). We study the cases of axisymmetric coalescence (*i.e.*, when the two drops are of identical sizes) and

non-axisymmetric coalescence (*i.e.*, when the two drops are of unequal sizes). For the case of axisymmetric coalescence, we consider separate cases to elucidate the effect of drop rheology (i.e., the effect of changing the exponent n in the power-law behavior dictating the drop rheology). Therefore, in comparison to the existing (very few) studies on polymeric drop coalescence, our paper investigates (1) 3D axisymmetric and non-axisymmetric coalescence dynamics of the polymeric drops in the presence of a solid substrate, (2) detailed DNS-based time-dependent 3D velocity fields and the velocity vectors inside the coalescing drops, (3) effect of the drop impact velocity on the spreading dynamics, and (4) scaling laws (obtained from simulations and physics-based calculations) describing the different stages of drop coalescence. The 3D velocity fields are provided as functions of the *Weber number* (*We*), quantifying the strength of the drop impact velocity. We find that qualitatively the drop coalescence proceeds along similar lines for all the *We* values, although the coalescence occurs faster and with larger velocity magnitudes for the cases of finite *Weber number.* Very interestingly, the total time of coalescence (that is measured from the time when the coalescence starts to the time when equilibrium is reached) varies non-trivially with *We.* For the case of We=1, the coalesce proceeds faster (as compared to the case with We=0.1) at the initial stages; however, since the velocity inside the drop is larger for We=1, it takes a longer time to attain equilibrium for We=1. Finally, we identify that the 3D drop coalescence is characterized by the simultaneous growth of the height (h_0) and width (W) of the bridge that is formed due to drop coalescence.[119] We demonstrate DNS-yielded distinct scaling laws describing the growth of h_0 and W at different stages of the coalescence process as functions of We. We find that the rate of growth of h_0 and W at early stages of coalescence increases significantly with

We; we justify this behavior by arguing the presence of a post-impact accelerating fluid disc[120] that contributes to the coalescence event. We also establish that at late stages of coalescence, such an effect of drop impact is lost and hence the (slow) rates of growth of h_0 and W are independent of *We*. Very importantly, we provide the physics-based derivation of these scaling behaviors for h_0 and W for various conditions and obtain excellent match with the DNS-based predictions.

3.2 Materials and methods

We consider a system as shown in Fig. 3.1, where two identical-sized (of radius R) polymeric drops, separated by an initial center-to-center distance d, simultaneously impact a philic substrate at a low-enough Weber number ($We= \rho_1 v^2 R/\sigma=0.1, 1$) so that there is no splashing [see Figs. 3.1(a,b)]. Here ρ_1, v, and σ represent the density of the drops, the initial velocity of the drops, and the surface tension of the drops (or the surface tension of the drop-air interface), respectively. Such Weber number values are witnessed in the AJ printing where polymeric drops of a few micron diameter impact the substrate with a speed of several m/s.[26] In Fig. 3.1, the distance between the point of impact of the two drops (d) is such that it is much smaller than the sum of the equilibrium spreading radii (r_{eq}) of the two drops (i.e., $d < 2r_{eq}$). Such a setting will ensure that the two drops will coalesce (being of identical sizes, we can denote this coalescence as axisymmetric coalescence). This coalescence event leads to the formation of a bridge, characterized by the height h_0 [see Fig. 3.1(c)] and width W [see Fig. 3.1(d)]. The coalescence event is quantified by noting the time evolution of h_0 and W.

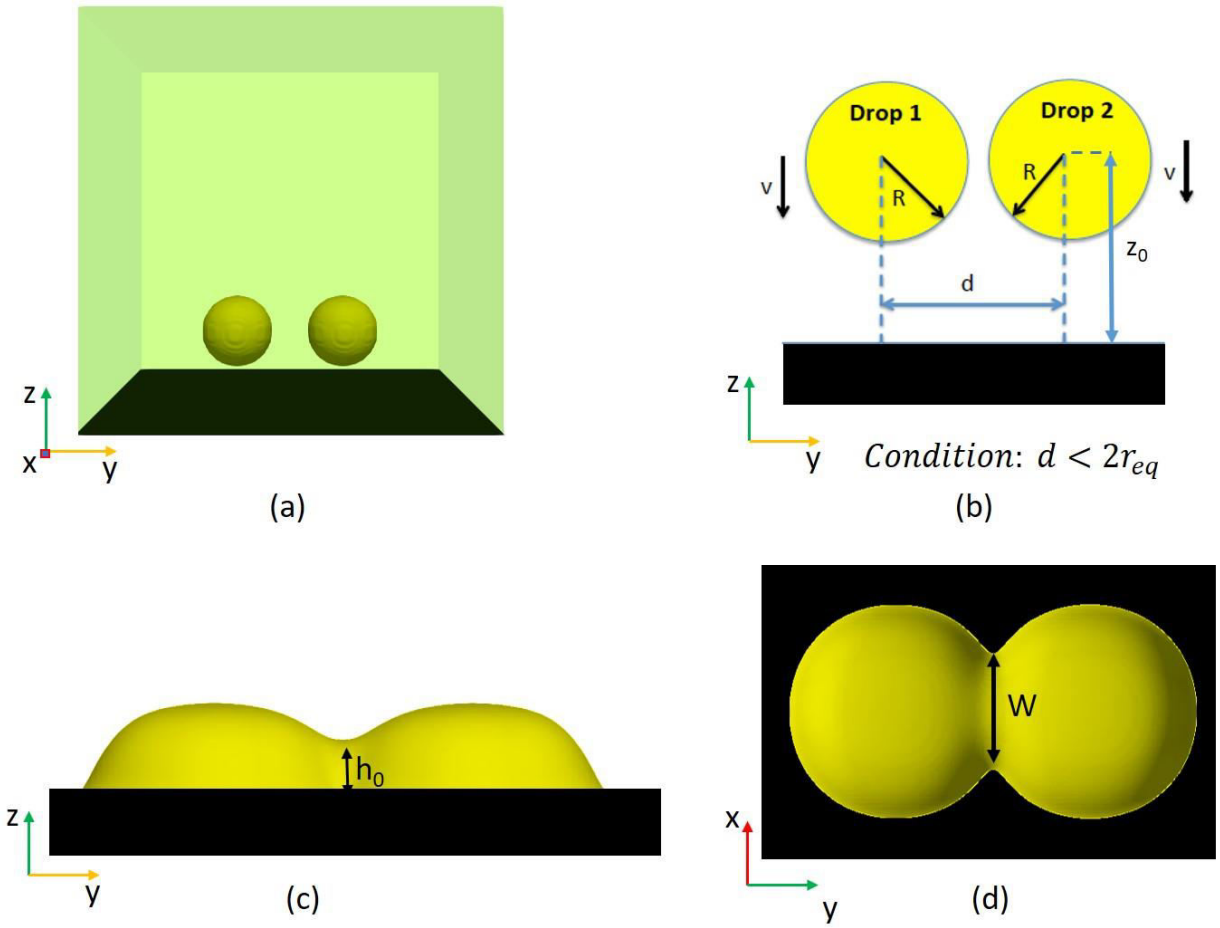

Figure 3.1: The schematics showing the initial simulation set-up [see (a,b)] and the instantaneous height h_0 [see (c)] and the width W [see (d)] of the bridge that is formed due to coalescence (and hence characterizes the coalescence). For our simulations, we consider the radius (R) of the both the drops [see (b)] as 10 μm, the distance (d) between the drop center as 30 μm, and the initial distance (z_0) of the drop center (for both the drops) from the bottom substrate as 20 μm. Finally, in (b) v represents the velocity of both the drops with which they impact the substrate.

3.2.1 Simulation set-up

We employ a DNS based model and capture the 3D dynamics of the coalescence of the two power-law obeying polymeric drops by using an incompressible two-phase laminar flow-based volume of fluid (VOF) method. We use a 3D model which includes the surface tension effects to capture the interface of the drop. The initial set-up of the drops is shown in Fig. 3.1. The simulation box is of size 100 μm x 100 μm x 100 μm. In this study, we use a structured hexahedral mesh with 5625000 cells (150 x 150 x 250) constructed using OpenFOAM (grid convergence is shown in Appendix B).[121] The two-phase incompressible laminar flow of a power-law obeying liquid with surface tension effects is solved using the OpenFOAM solver interFoam. The power-law model involves tracking the local and instantaneous gradients of velocity (and hence the shear rate) within the coalescing drops, which in turn is used to determine the local and instantaneous viscosity that is incorporated in the momentum equation through the viscous stress term. In Appendix B, we have provided a typical distribution of this velocity gradient within the coalescing drops (which in turn enables us to compute this local and instantaneous viscosity) during the coalescence of the drops.

3.2.2 Governing equations

3.2.2.1 Continuity and Navier-Stokes equations:

The simulation system consists of polymeric drops and the surrounding air. Therefore, one needs to capture the flow field inside the polymeric drops as well as the surrounding air as the drops impact the solid, spread, and coalesce. The flow field in the system is governed by the continuity and the Navier-Stokes equation as described below:

$$\nabla.(\boldsymbol{u}) = 0, \qquad (3.1)$$

$$\rho\frac{\partial \boldsymbol{u}}{\partial t} + \rho(\boldsymbol{u}.\boldsymbol{\nabla})(\boldsymbol{u}) = \nabla.[-pI + \mu(\nabla\boldsymbol{u} + (\nabla\boldsymbol{u})^T)] + \rho\boldsymbol{g} + \boldsymbol{F}_\sigma. \qquad (3.2)$$

Here, $\boldsymbol{u}$ is the velocity vector, p is the pressure field, ρ is the fluid density, μ is the dynamic viscosity of the fluid, I is the identity matrix of order three, and $\boldsymbol{g}$ is the acceleration due to gravity. Also, $\boldsymbol{F}_\sigma$ is the surface tension force, which is modeled using the continuum surface force (CSF) model,[122] and is expressed as:

$$\boldsymbol{F}_\sigma = \sigma\kappa\nabla\alpha, \qquad (3.3)$$

where σ is the liquid-air surface tension, κ is the local surface curvature (on the free surface or the liquid-air interface), and α is the volume fraction of the liquid whose value varies between 0 (the case of pure air) and 1 (the case of pure liquid). Also, the drops make an equilibrium constant contact angle of 25^0 with the solid surface. The density ρ and the dynamic viscosity μ at any location in the system is a function of the volume fraction and is described as follows:

$$\rho = \alpha\rho_1 + (1-\alpha)\rho_2\,, \qquad (3.4)$$

$$\mu = \alpha\mu_1 + (1-\alpha)\mu_2. \qquad (3.5)$$

Here, the subscripts 1 and 2 denote the properties of the polymeric liquid and the air, respectively. The various parameters used for the simulation have been provided in Table 3.1. It is to be noted that the liquid drop studied here is a power-law obeying shear thinning polymeric liquid whose viscosity can be expressed as a function of the shear rate ($\dot{\gamma}$) as:

$$\mu_1 = m\,\dot{\gamma}^{n-1}, \qquad (3.6)$$

where *m* is the consistency index and *n* is the power law index.

The liquid-air interface is tracked by solving the following governing equations:

$$\frac{\partial \alpha}{\partial t} + \nabla.(\alpha \mathbf{u}) + [\,\nabla.(\alpha(1-\alpha)\mathbf{u_r})] = 0 \quad (3.7)$$

The last term on the left-hand side of the equation provides an artificial compression so as to maintain a sharp interface, and this term is active only at the interface region. Here, the term $\mathbf{u_r}$ is the artificial compressive velocity.

Please note that in our formulation, we have modelled air as an incompressible fluid. Our results (discussed later) lead to a maximum pressure change of 0.19 bar for the highest Weber number (*We*=1) at any point in time. This is too small a pressure change to trigger any compressibility effect; therefore, we believe that our consideration of air as an incompressible fluid for the present case should be valid.

3.2.2.2 Initial conditions for the Simulations

Initially the two drops are placed at a height of z_0 from the bottom substrate. All the components of the velocity vector throughout the simulation set up are taken to be zero except for the z-component of the velocity of the drops, which is dictated by the chosen Weber number $\left(i.e., v = \sqrt{\frac{(We)\sigma}{\rho R}}\right)$. The pressure at all the nodes is taken to be the atmospheric pressure.

3.2.2.3 Velocity and pressure boundary conditions

Atmospheric pressure boundary condition is used on all the surfaces of the simulation box except for the bottom surface. A no-slip and a no-penetration boundary condition are used for velocity at the bottom surface. Even though a no-slip condition is used, a numerical slip is introduced to prevent the stress singularity that occurs at the moving contact line when no-slip condition is applied.[123] This numerical slip, which is inherent to our employed advection algorithm, causes the interface to move based on the face-normal value of the cell (which contains the interface). The effective slip length, governing this slip, is of the order of the size of the meshes.[124]

Parameter	**Definition**	**Value**	**Reference**
ρ_1	Density of the polymeric liquid	1250 [kg/m^3]	53
ρ_2	Density of air	1.205 [kg/m^3]	56
m	Consistency index	2	53
n	Power law index	0.6	
μ_2	Dynamic viscosity of air	1.82 x 10^{-5} [Pa.s]	56
σ	Liquid-air surface tension	24 [mN/m]	26
θ	Contact angle	25^0	
R	Radius of the drops	10 [μm]	

d	Distance between the drop center	30 μm	
z_0	Initial distance (z_0) of the drop center from the bottom substrate	20 μm	

Table 3.1: List of parameters used in the simulation.

3.3 Results and Discussions

In this study, we first investigate the effect of the Weber number (We) on the axisymmetric coalescence dynamics of the two power-law-obeying, shear-thinning, and identical sized polymeric drops. For that purpose, we first study the velocity distribution inside the coalescing drops as a function of We. Next, we compare and analyze the time variation of the height (h_0) and width (W) of the bridge formed by the coalescing drops. The results are provided for We = 0, 0.1, and 1.

3.3.1 Velocity distribution in and around the coalescing drops

In Figs. 3.2 and 3.3, we show the velocity distributions at various instances (from the time when the drops impact on the substrate) for the case of We = 0. At t=0 (the start of the simulation), the drops are at a distance of z_0 from the substrate. In Fig. 3.2, we show the distribution of the magnitude of the velocity inside the drop as well as in the air in the immediate vicinity of the drop across a cross-section (i.e., the y-z plane) that passes through the center of the drops (i.e., x=0). For improved clarity, the velocity vectors, indicating the local direction of the flow, have been shown only for the polymeric drops. The presence of the no-slip condition (at the drop-substrate interface) and viscous effects lead to a velocity gradient inside the drop at locations near the substrate at all times [clearly seen in Figs. 3.2(a)-(d)]. We also witness a continuous decrease in the velocity inside the drop as the drops eventually attain equilibrium. In Fig. 3.2(a), we clearly witness that the velocity is maximum at the three-phase contact line (TPCL) as the drops start to spread, with the velocity attaining a value as high as 0.66 m/s (or U* = 0.48) near the TPCL at t = 0.72 ms (or t* = 99.76) (i.e., the time instant when the drops hit the surface and start to spread).

Here U* and t* refer to the dimensionless velocity and the dimensionless time; please see the caption of Fig. 3.2 for their definitions. The velocity vectors inside the drop for the period before the drops start to coalesce (i.e., in the time interval of t=0.72 ms (t* = 99.76) to t=0.78 ms (t* = 108.08)) are primarily directed towards the three-phase contact line: this is a characteristic feature of the dynamics of drop spreading. Finally, as the drops come into contact with each other, a part of the TPCL disappears and it leads to the formation of a bridge connecting the two drops. Therefore, the onset of this bridge formation signals the onset of the drop coalescence. This bridge grows with time, which is clearly shown by the changes in the position of the interface with time [see Fig. 3.2(e)-(f)], until it attains an equilibrium height. At the location of the bridge, the drops are restricted from spreading freely along the substrate and from attaining equilibrium. As it can be clearly seen in Figs. 3.2(e)-(f), for either of the drops, the majority of the velocity vectors at the location where the drops are interacting, are directed towards the bridge causing more and more liquid to accumulate (at the region where the two drops are coalescing) enforcing the bridge to grow in height. Of course, the velocity vectors inside the drop near the location where the TPCL is still present (i.e., the location opposite to where the drops coalesce and the bridge develops) are still directed towards the TPCL, as the TPCL advances on the solid substrate. At finite *We* (*We*=0.1, 1), we find qualitatively very similar behavior, although there are significant differences in the quantities associated with the drop spreading and coalescence (please see Figs. 3.4 and 3.6). For example, the coalescence between the two drops begins around 44 μs (or t* = 6.1) and 20 μs (or t* = 2.77) for *We*=0.1 and 1, respectively. Similarly, as evident from the color bars, the velocity magnitude both inside and outside of both the drops are significantly larger for such finite *We* at any given time during their

coalescence. The overall time for the drop to come to equilibrium, however, shows interesting non-trivialities for the cases of *We*=0.1 and 1. For *We*=1, the coalescence is faster at the beginning; this is evident from the fact that nearly identical profiles of coalescing drops become apparent from the profiles at t=120 μs (or t* = 16.63) for *We*=0.1 and t=100 μs (t* = 13.86) for *We*=1. However, the time to reach equilibrium is larger for the case of *We*=1 (for example, the equilibrium profiles are obtained at t=600 μs (or t* = 83.14) and t=700 μs (t* = 96.99) for *We*=0.1 and *We*=1, respectively), stemming from the fact that the velocity at a particular time instant (after the drops have started to coalesce) inside the coalescing system of drops is always higher for the case of *We*=1 and hence it requires a larger time to ensure that the coalescing system reaches equilibrium and comes to a rest.

In Figure 3.3, we show the velocity distribution across the x-y plane at z = 1 μm (i.e., at a vertical height of 1 μm from the solid substrate) both inside the coalescing drop as well as in the surrounding air in the immediate vicinity of the drops. Also, for the sake of clarity, we only provide the velocity vectors inside the coalescing drops. After the drops impact, the velocity magnitude is larger near the liquid-air interface and is much smaller at the center (of the individual drops) at all times. This is because the contact line moves away from the point of impact (for hydrophilic surfaces) to attain equilibrium. It is clearly seen that the velocity vectors are directed radially outwards from the center (of the individual drops) and directed towards the air-liquid interface [please see Figs. 3.3(a)-3.3(h)]. As time progresses and the drops come into contact, the liquid-air interface vanishes as a bridge is formed between the drops at the point of contact. Therefore, at this point, some of the velocity vectors are directed towards the non-coalescing part of the air-liquid interface,

while the remainder of the vectors are directed towards the location where the bridge has been formed enforcing more liquid mass to accumulate at such locations. Therefore, the bridge grows in time and its lateral width W [see Fig. 3.1(d) for the schematic description] also increases with time until it attains an equilibrium width. It can also be clearly seen that a larger fraction of these velocity vectors is directed towards the bridge as time progresses [see Fig. 3.3(a)-(h)]. At finite We (We=0.1, 1), we find qualitatively very similar behavior, although there are quantitative differences (please see Figs. 3.5 and 3.7). For example, a larger We implies a larger magnitude of the velocity vectors at a given instant of time, a faster progression of the coalescence at early stages, and a slower attainment of equilibrium (as has been already identified for the same system visualized in a different direction; please compare Figs. 3.2, 3.4, and 3.6 and also see the previous paragraph).

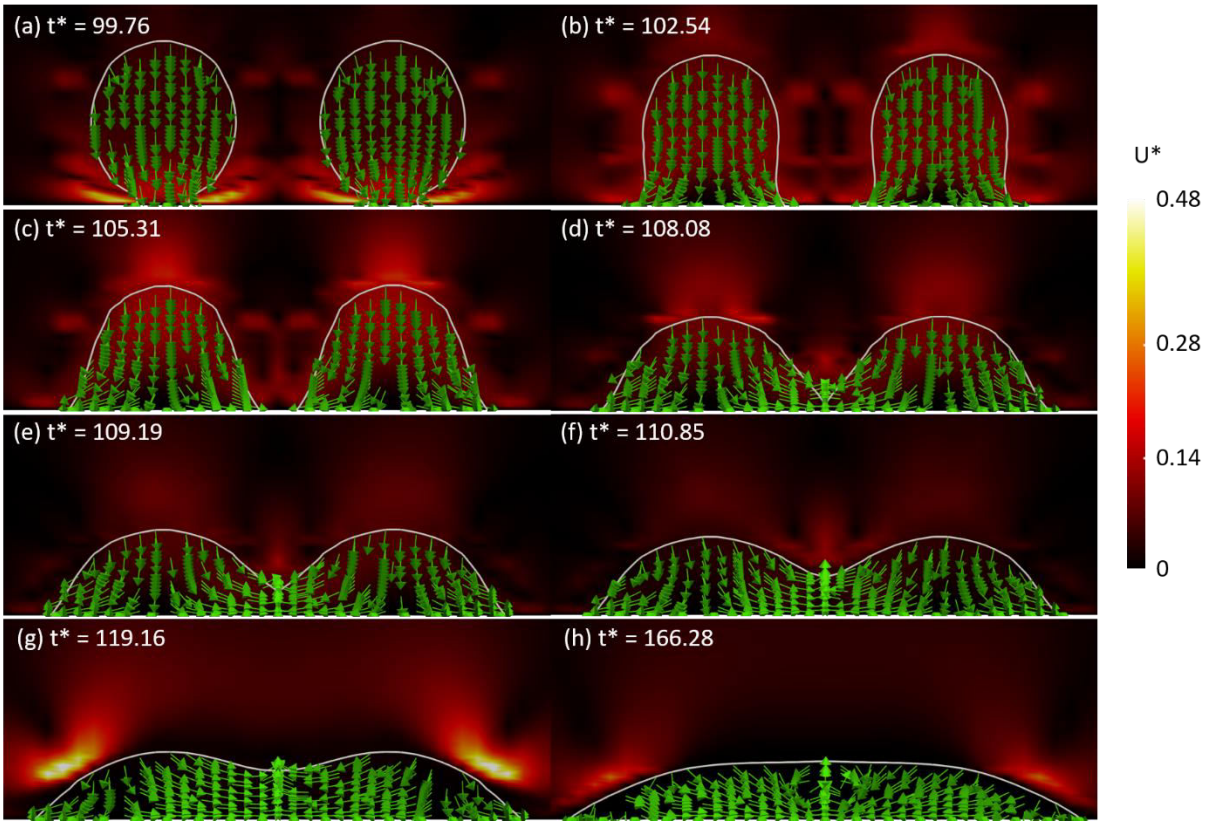

Figure 3.2: Variation of the dimensionless velocity field inside the drops as well as in the air in the immediate vicinity of the drops across a cross-section (i.e., the y-z plane) that passes through center of the drops (x=0) at different time instants (dimensionless) inside the coalescing drops for We=0. Velocity vectors, shown only for the drops, are not in scale with the magnitude of the local velocity. Here the dimensionless time is $t^* = t/t_c$, the dimensionless velocity is $U^* = U/U_0$ (where U_0=R/t_c is the characteristic velocity scale), and $t_c = \sqrt{\rho_1 R^3/\sigma}$ is the capillary time scale.

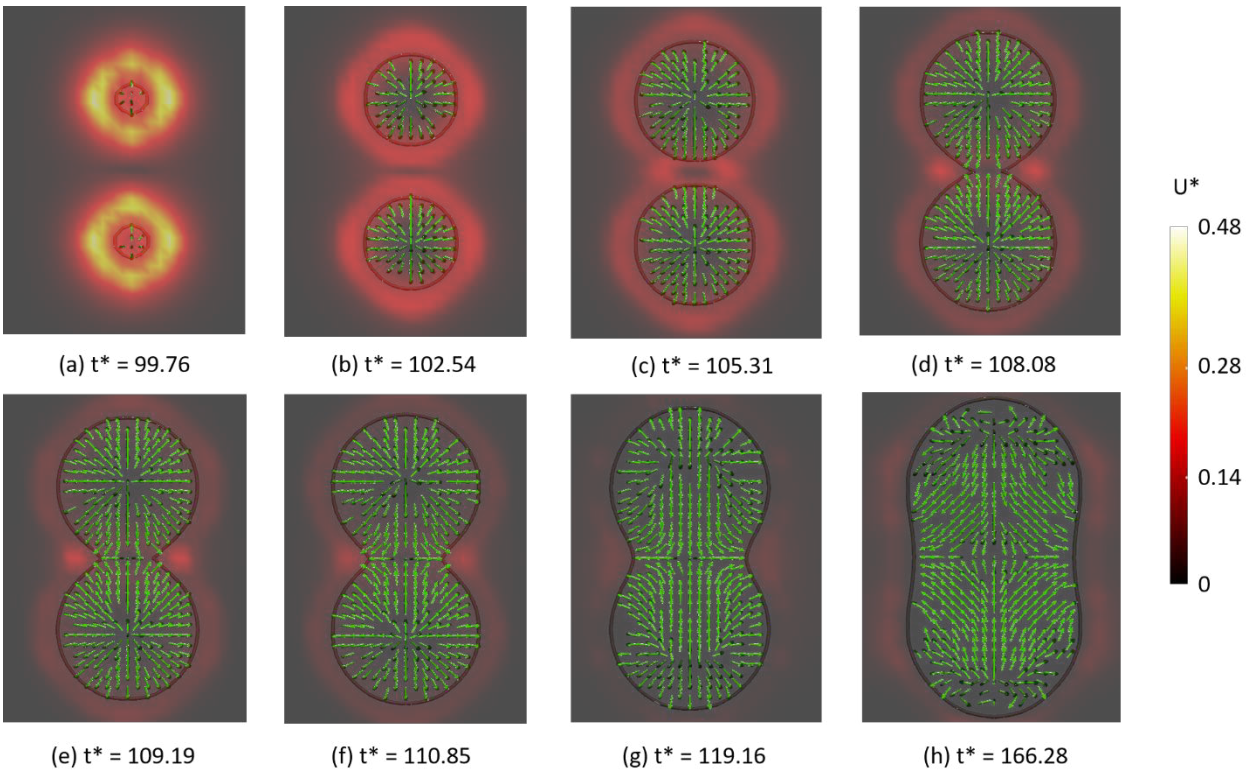

Figure 3.3: Variation of the dimensionless velocity field inside the drops as well as in the air in the immediate vicinity of the drops across the x-y plane at z = 1 μm at different time instants (dimensionless) inside the coalescing drops for We=0. Velocity vectors, shown only for the drops, are not in scale with the magnitude of the local velocity. Here the dimensionless time is $t^* = t/t_c$, the dimensionless velocity is $U^* = U/U_0$ (where U_0=R/t_c is the characteristic velocity scale), and $t_c = \sqrt{\rho_1 R^3/\sigma}$ is the capillary time scale.

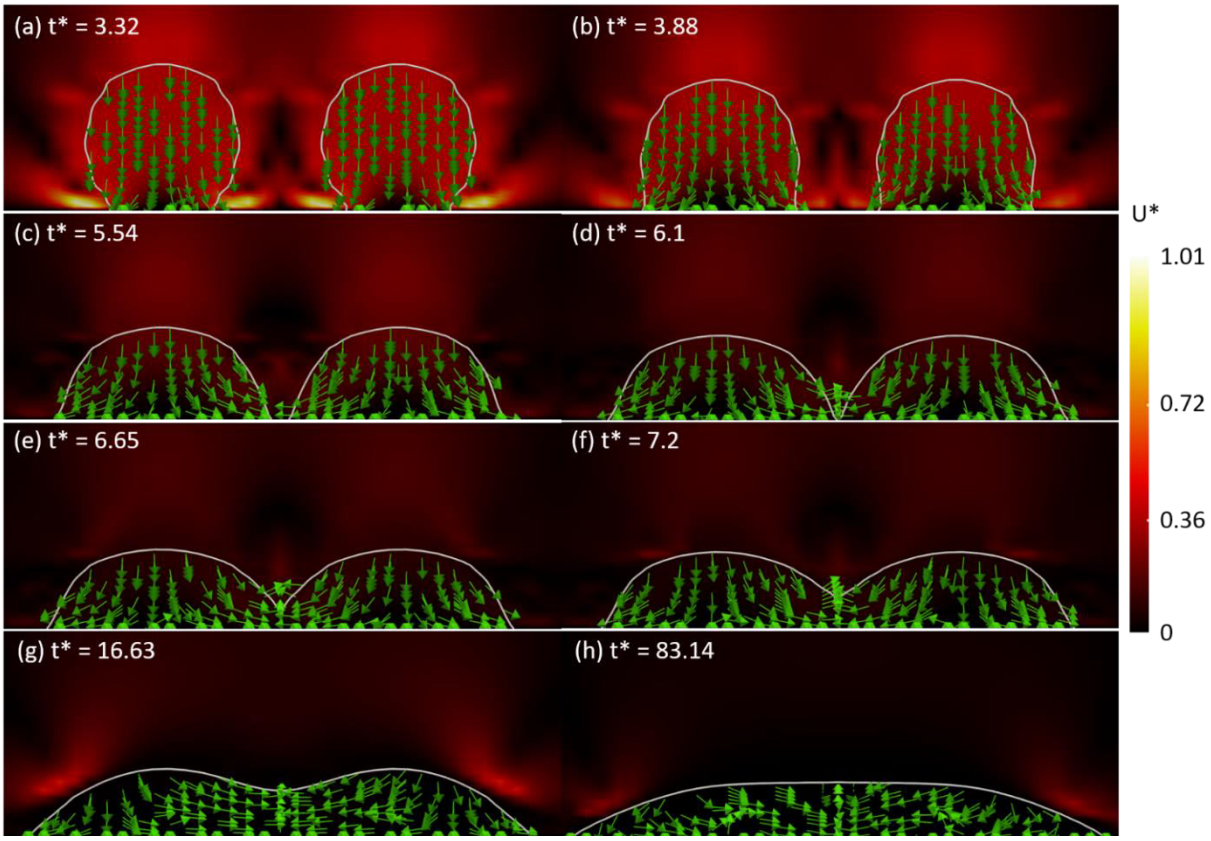

Figure 3.4: Variation of the dimensionless velocity field inside the drops as well as in the air in the immediate vicinity of the drops across a cross-section (i.e., the y-z plane) that passes through center of the drops (x=0) at different time instants (dimensionless) inside the coalescing drops for We=0.1. Velocity vectors, shown only for the drops, are not in scale with the magnitude of the local velocity. Here the dimensionless time is $t^* = t/t_c$, the dimensionless velocity is $U^* = U/U_0$ (where U_0=R/t_c is the characteristic velocity scale), and $t_c = \sqrt{\rho_1 R^3/\sigma}$ is the capillary time scale.

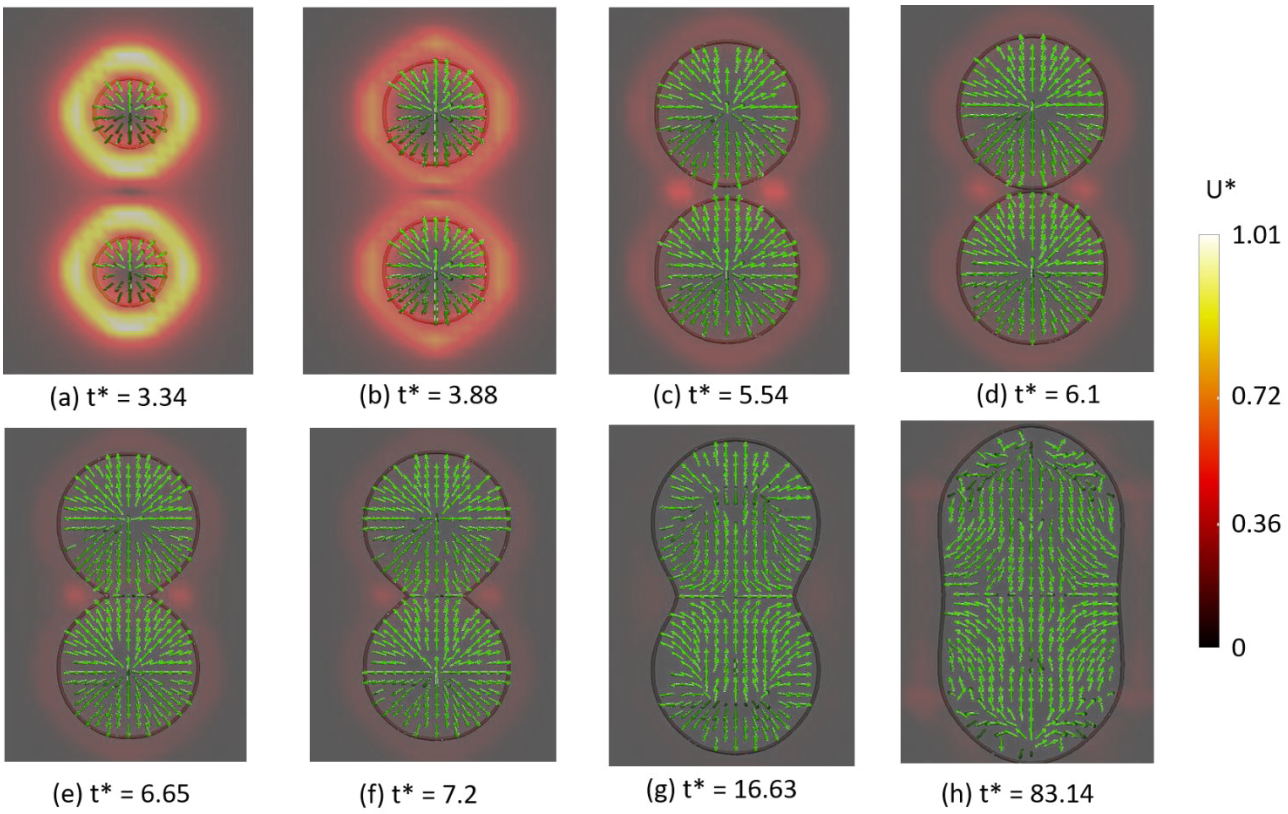

Figure 3.5: Variation of the dimensionless velocity field inside the drops as well as in the air in the immediate vicinity of the drops across the x-y plane at z = 1 μm at different time instants (dimensionless) inside the coalescing drops for We=0.1. Velocity vectors, shown only for the drops, are not in scale with the magnitude of the local velocity. Here the dimensionless time is $t^* = t/t_c$, the dimensionless velocity is $U^* = U/U_0$ (where U_0=R/t_c is the characteristic velocity scale), and $t_c = \sqrt{\rho_1 R^3/\sigma}$ is the capillary time scale.

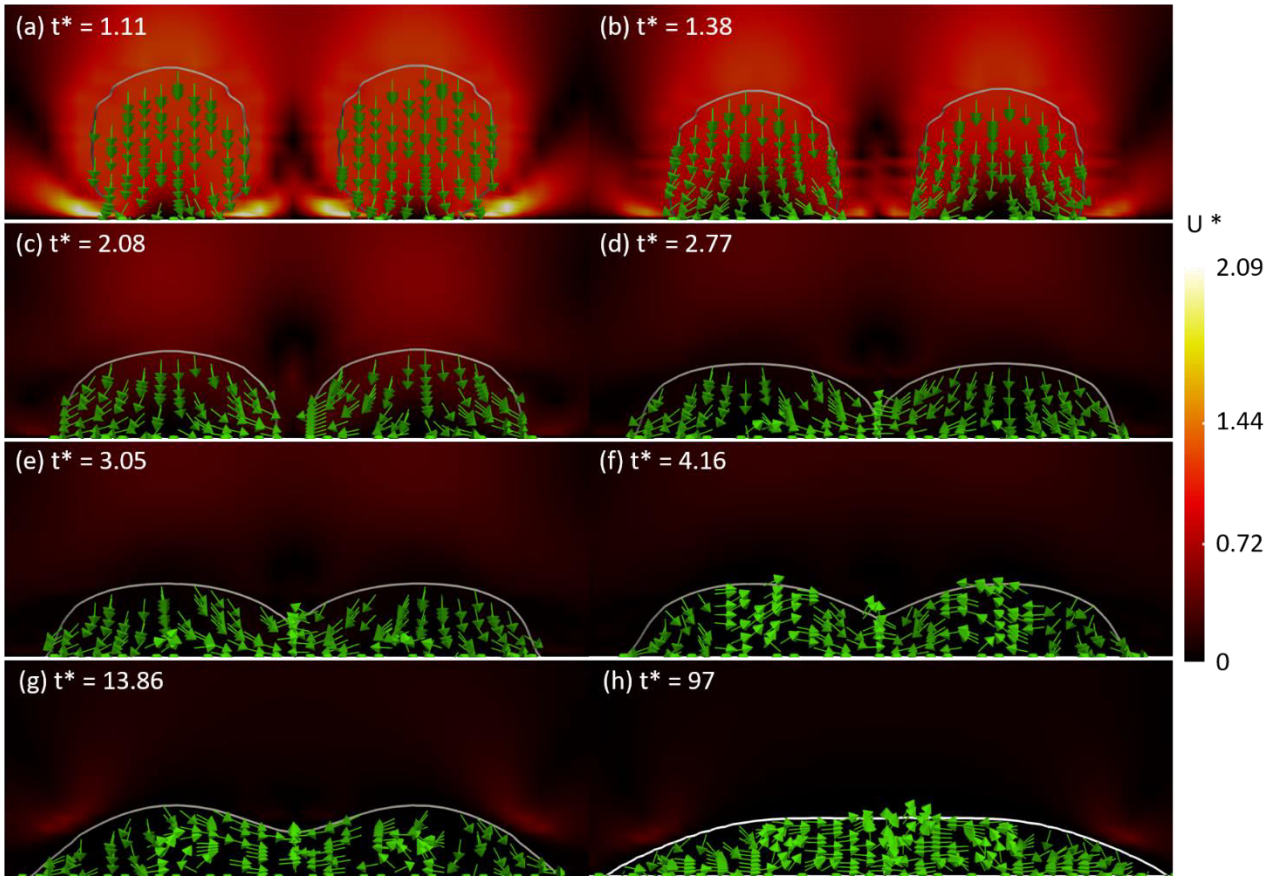

Figure 3.6: Variation of the dimensionless velocity field inside the drops as well as in the air in the immediate vicinity of the drops across a cross-section (i.e., the y-z plane) that passes through center of the drops (x=0) at different time instants (dimensionless) inside the coalescing drops for We=1. Velocity vectors, shown only for the drops, are not in scale with the magnitude of the local velocity. Here the dimensionless time is $t^* = t/t_c$, the dimensionless velocity is $U^* = U/U_0$ (where U_0=R/t_c is the characteristic velocity scale), and $t_c = \sqrt{\rho_1 R^3/\sigma}$ is the capillary time scale.

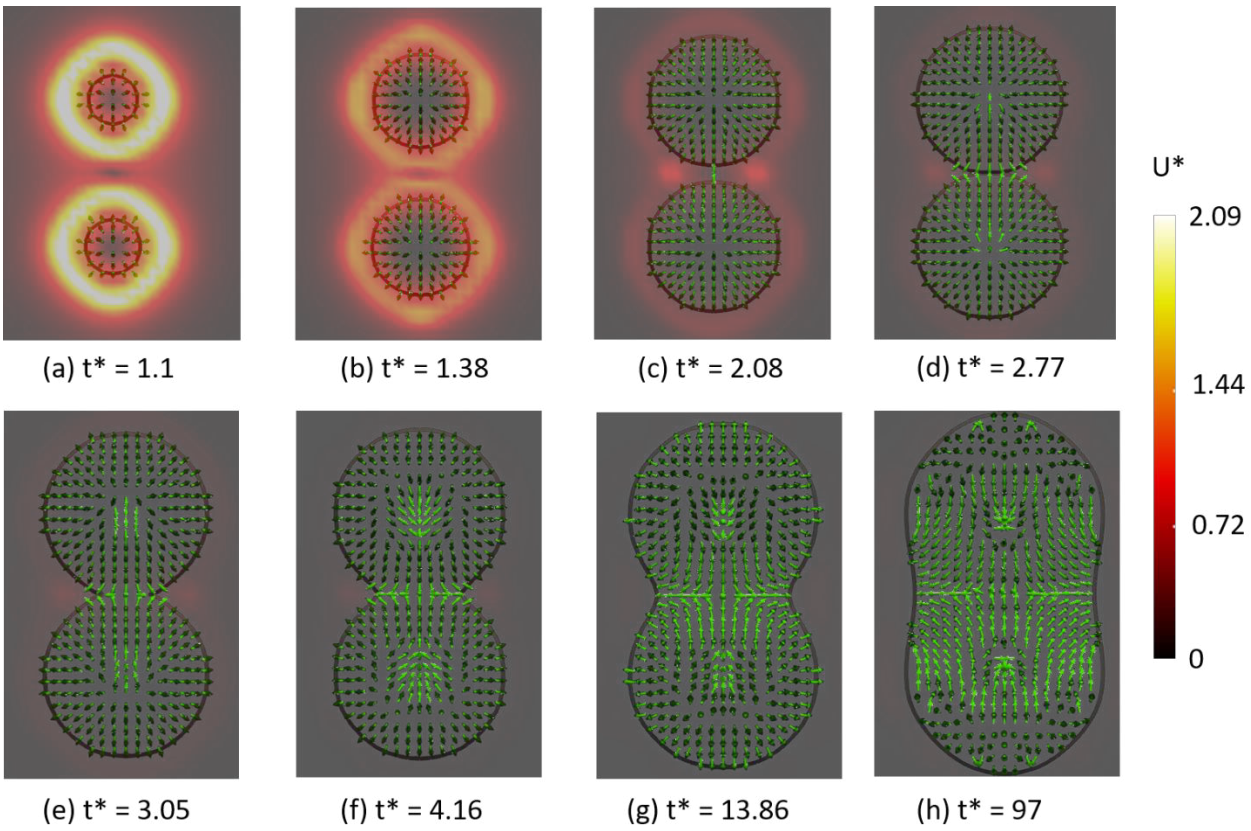

Figure 3.7: Variation of the dimensionless velocity field inside the drops as well as in the air in the immediate vicinity of the drops across the x-y plane at z = 1 μm at different time instants (dimensionless) inside the coalescing drops for We=1. Velocity vectors, shown only for the drops, are not in scale with the magnitude of the local velocity. Here the dimensionless time is $t^* = t/t_c$, the dimensionless velocity is $U^* = U/U_0$ (where U_0=R/t_c is the characteristic velocity scale), and $t_c = \sqrt{\rho_1 R^3/\sigma}$ is the capillary time scale.

3.3.2 Dynamics of the bridge height and width of the coalescing drops: Scaling Variations

Next, we study the dynamics of the drop coalescence by quantifying the rate of growth of the dimensionless height (h_0/R) and the dimensionless width (W/R) of the bridge and attempting to explain these behaviors through scaling calculations. We analyze the dynamics of drop coalescence for the different Weber numbers (We = 0, 0.1, 1) by considering two distinct regimes, namely the early-stage and the late-stage coalescences (for both h_0/R-*vs*-t^* and W/R-*vs*-t^* variations), demonstrating distinct scaling behaviors.

Fig. 3.8 provides the simulation results for the h_0/R-*vs*-t^* variation for different We. We clearly find that simulations predict $h_0/R \sim (t^*)^n$ for shorter times (i.e., early stages of drop coalescence) and $h_0/R \sim (t^*)^m$ for larger times (i.e., late stages of drop coalescence) ($t^*=t/t_c$). Interestingly, n increases monotonically with We (n=1/2, 2/3, and 3 for We=0, 0.1, and 1, respectively), while m=1/10 for all We.

Fig. 3.9 provides the simulation results for the W/R-*vs*-t^* for different We. Here too $W/R \sim (t^*)^p$ for shorter times (i.e., early stages of drop coalescence) and $W/R \sim (t^*)^q$ for larger times (i.e., late stages of drop coalescence), with p increasing with We (p=1/3, 1/2, and 1 for We=0, 0.1, and 1, respectively) but q=1/4 for all We. Below, we provide a physics-based argument explaining these different scaling regimes.

3.3.2.1 Dynamics of Drop Coalescence at We = 0: Variation of Bridge Height at Early Stages of Drop Coalescence

In the initial stages of the bridge growth, where the inertial forces dominate, we observe a

sharp increase in the bridge height. For the case of *We* = 0, our simulation results indicate $h_0/R \sim (t^*)^{1/2}$ for such initial stages [please see Fig. 3.8(a)], which is consistent with the scaling obtained in various other works for standard Newtonian drops.[84,88,125-127] As identified by Eggers *et al.*,[84] at these initial stages, the growth of the bridge height is dictated by the balance of the driving capillary forces and resisting inertial forces. In other words, at the instantaneous bridge height value of $h_0 = h_0(t)$, the bridge growth is driven by the interfacial capillary stresses which can be expressed as $\frac{\sigma R}{h_0^2}$ and is resisted by the dynamic pressure jump corresponding to the inertial force across the interface [which is given by $\rho v^2 \sim \rho v_z^2 \sim \rho \left(\frac{dh_0}{dt}\right)^2$][84,125] (where v_z is the velocity in z direction). Therefore, we can write (using $t_c = \sqrt{\rho R^3/\sigma}$):

$$\frac{\sigma R}{h_0^2} \sim \rho \left(\frac{dh_0}{dt}\right)^2 \Rightarrow \frac{\sigma R}{h_0^2} \sim \rho \left(\frac{h_0}{t}\right)^2 \Rightarrow \frac{h_0}{R} \sim \sqrt{\left(\frac{t}{\sqrt{\rho R^3/\sigma}}\right)} \sim \sqrt{\left(\frac{t}{t_c}\right)}, \quad (3.7)$$

i.e., we recover the $h_0/R \sim (t^*)^{1/2}$ regime.

3.3.2.2 Dynamics of Drop Coalescence at We = 0: Variation of Bridge Height at Late Stages of Drop Coalescence

Our simulation results indicate $h_0/R \sim (t^*)^{1/10}$ (i.e., $h_0/R \sim (t^*)^{0.1}$) at late stages of drop coalescence. At such late stages, we can assume that the rate of the growth of the bridge height (dh_0/dt) is similar to the rate of spreading (dr/dt) of the TPCL (i.e., the non-coalesced part of the drop). Here r refers to the instantaneous spreading radius. Please note that while R (representing the radius of the drops at the start of the simulation) is a constant, the spreading radius r varies with time. This assumption (of dh_0/dt being similar to dr/dt) stems from the fact that at the region of the coalescence, i.e., where the bridge has been formed,

the mass of liquid that contributes to the growth of the bridge is similar to the mass of the liquid that wets the solid as the non-coalescing part of the TPCL spreads. This is also evident from the velocity vectors shown in the simulation snapshots for late stages of coalescence: one can see similar sized velocity vectors contributing to the bridge growth as those contributing to the spreading of the TPCL [see Fig. 3.2(e-h)]. The dynamic contact angle made by the spreading TPCL is θ_d; accordingly, one can write (following Seevaratnam *et al.*[128] that probes the spreading dynamics of the shear-thinning liquid, with $\mu_1 \sim \dot{\gamma}^{n-1}$ and n<1):

$$\theta_d^{\frac{2+n}{n}} \sim Ca_{U_{TPCL}} \sim U_{TPCL} \sim \frac{dr}{dt}. \quad (3.8)$$

In the above equation, $Ca_{U_{TPCL}} = \frac{\mu_1^0 U_{TPCL}}{\sigma}$ is the capillary number based on the velocity of the TPCL ($U_{TPCL} \approx \frac{dr}{dt}$), μ_1^0 is the zero-shear viscosity of the polymeric liquid, and σ is the surface tension of the drop.

Also, the geometrical requirements will imply that

$$\theta_d \sim \frac{Volume}{r^3}. \quad (3.9)$$

Using eq.(3.9) in eq.(3.8) and integrating, we arrive at:

$$r \sim t^{\frac{n}{6+4n}} \sim t^{0.07} \ (with\ n = 0.6). \quad (3.10)$$

Therefore, the scaling prediction also indicates that at late stages of spreading (using the fact that both R and the capillary time scale t_c are constants),

$$h_0 \sim t^{0.07} \Rightarrow \frac{h_0}{R} \sim \left(\frac{t}{t_c}\right)^{0.07}, \quad (3.11)$$

which is very close to the simulation-based prediction of $h_0 \sim t^{0.1}$.

3.3.2.3 Dynamics of Drop Coalescence at We = 0: Variation of Bridge Width at Early Stages of Drop Coalescence

For such early stages, our simulation results indicate $W/R \sim (t^*)^{1/3}$, i.e., $W/R \sim (t^*)^{0.33}$. Simulation snapshots demonstrate that from the very beginning of the formation of the bridge, there is a distinct flow component that aids in the growth of bridge width. Therefore, we can argue that even at the initial stages, the viscous forces associated with the flow field is involved in the forces that govern the growth of the width W of the bridge. Therefore, the growth of the bridge width occurs due to the balance of the driving capillary stresses and the resisting viscous stresses and resisting inertial pressure. The balance of the capillary stresses with the inertial pressure will lead to $W \sim t^{0.5}$ (following the same derivation as that in eq. 3.7 with h_0 being replaced by W). On the other hand, here we explore what will be the scaling if the growth of the bridge width occurs by the balance of the capillary and the viscous forces. The capillary pressure scales as $\frac{\sigma R}{W^2}$, which will be balanced by the viscous stress that scales as $\mu_1 \nabla \boldsymbol{u} \sim m\dot{\gamma}^n$. Accordingly, we can write (with $v_r \sim$ dW/dt being the velocity in the radial direction that dictates the growth of the bridge width and using the fact that both R and the capillary time scale t_c are constants):

$$\frac{\sigma R}{W^2} \sim m\dot{\gamma}^n \Rightarrow \frac{\sigma R}{W^2} \sim m\left(\frac{v_r}{W}\right)^n \Rightarrow \frac{\sigma R}{W^2} \sim m\left(\frac{W/t}{W}\right)^n \Rightarrow W \sim t^{n/2} \Rightarrow W \sim t^{0.3} \Rightarrow \frac{W}{R} \sim \left(\frac{t}{t_c}\right)^{0.3} \quad \text{(with } n\text{=0.6).} \tag{3.12}$$

The simulation results predict $W/R \sim (t^*)^{0.33}$: therefore, this exponent (0.33) is in between the exponent predicted (0.5) with the inertial pressure being the dominant resisting force and that predicted (0.3) with the viscous stress being the dominant resisting force.

3.3.2.4 Dynamics of Drop Coalescence at We = 0: Variation of Bridge Width at Late Stages of Drop Coalescence

At the late stages of drop coalescence for *We*=0, we find that simulations predict $W/R \sim (t^*)^{1/4}$. Lee *et al.*[119] showed that for two drops coalescing on partially wettable substrates (this is also the case that we are studying), one can relate the dynamic contact angle θ'_d (note this θ'_d refers to the dynamic contact formed by the coalescing part of the drop) to the instantaneous width (W) and instantaneous height (h_0) of the bridge as:

$$tan\theta'_d = \frac{h_0}{W}. \quad (3.13)$$

Therefore, towards the late stage of coalescence (i.e., when θ'_d is small), we can write:

$$\theta'_d \approx \frac{h_0}{W}. \quad (3.14)$$

Following Ref. 45, for a shear thinning liquid, we can write the equivalent form of the Cox-Voinov law as:

$$(\theta'_d)^{\frac{2+n}{n}} \sim (Ca)_{v_r} \sim v_r \sim \frac{dW}{dt}, \quad (3.15)$$

where $Ca_{v_r} = \frac{\mu_1 v_r}{\sigma}$ is the capillary number based on the radial velocity v_r (i.e., the velocity that contributes to the growth of width W of the bridge).

Using eqs.(3.11,3.14) in eq.(3.15) and subsequent integration, we can obtain (using the fact that both R and the capillary time scale t_c are constants):

$$W \sim t^{0.24} \Rightarrow \frac{W}{R} \sim \left(\frac{t}{t_c}\right)^{0.24} \text{ (with } n\text{=0.6)}, \quad (3.16)$$

i.e., our scaling prediction matches excellently with the simulation-based prediction of $W/R \sim (t^*)^{0.25}$.

3.3.2.5 Dynamics of Drop Coalescence at We = 0.1, 1.0: Variation of Bridge Height at Early Stages of Drop Coalescence

At early stages of drop coalescence, for cases of finite *We* (i.e., when the drop impacts the surface with a finitely large velocity), we see a much steeper variation of the bridge height (h) with time. Therefore, the bridge height varies as $h_0/R \sim (t^*)^n$ (with n=1/2, 2/3, and 3 for We=0, 0.1, and 1). A finitely large drop impact velocity will imply that after the drop impacts the solid, it forms a disc that has a finite acceleration. The formation of such a disc is evident by comparing (for different *We*) the drop profiles in the period after it impacts the solid and before it coalesces with the other drop: for larger *We*, one can find a much shorter drop height and a much larger contact radius of the drop immediately before the coalescence starts to take place (for example, compare the drop profiles at t=0.78 ms (or t* = 108.08) and t=20μs (or t* = 2.77) for We=0 and 1, respectively in Figs. 3.2 and 3.6). The presence of such a post-impact acceleration disc is the most common characteristic of an impacting drop.[39] For the present case, the presence of such an accelerating disc will imply that a much larger amount of liquid mass contributes to the coalescence process in a given time interval (in particular, at the beginning of the coalescence process), and therefore, the height of the bridge (that characterizes the coalescence event) shows a rapid growth with time for larger *We*.

3.3.2.6 Dynamics of Drop Coalescence at We = 0.1, 1.0: Variation of Bridge Height at Late Stages of Drop Coalescence

At late stages of drop coalescence, we find that simulation always yields, $h_0/R \sim (t^*)^{0.1}$ for all *We* values. This stems from the fact that at such late stages of coalescence, the effect of

the finite impact velocity and the manner in which such impact led to the formation of an accelerating disc and a faster rate of growth of bridge height at initial stages (as discussed above), are completely lost. Therefore, the scaling calculations as proposed for the case of *We*=0 remains valid even for *We*=0.1, 1.0, leading to a scaling prediction of $h_0/R \sim (t^*)^{0.07}$.

3.3.2.7 Dynamics of Drop Coalescence at We = 0.1, 1.0: Variation of Bridge Width at Early Stages of Drop Coalescence

Very much like the bridge height, the bridge width, too, is impacted by the formation of the post-drop-impact accelerating disc, which in turn brings a much larger mass of liquid (in a given time interval) to trigger the coalescence event. Presence of this enhanced accelerating mass ensures that at such early stages of coalescence, the simulation-driven growth of the bridge width shows $W/R \sim (t^*)^p$ (with *p*=1/3, 1/2, and 1 for *We*=0, 0.1, and 1).

3.3.2.8 Dynamics of Drop Coalescence at We = 0.1, 1.0: Variation of Bridge Width at Late Stages of Drop Coalescence

Very much like the case of bridge height, here too, at late stages of drop coalescence, simulations predict no effect of *We* on the time-dependent variation of *W*. Hence for all *We*, simulations predict $W/R \sim (t^*)^{0.25}$. Of course, in presence of no effect of *We*, the same scaling calculations as employed for *We*=0 will remain valid for this case as well, yielding $W/R \sim (t^*)^{0.24}$ (i.e., there is an excellent match with the simulation predicted variation).

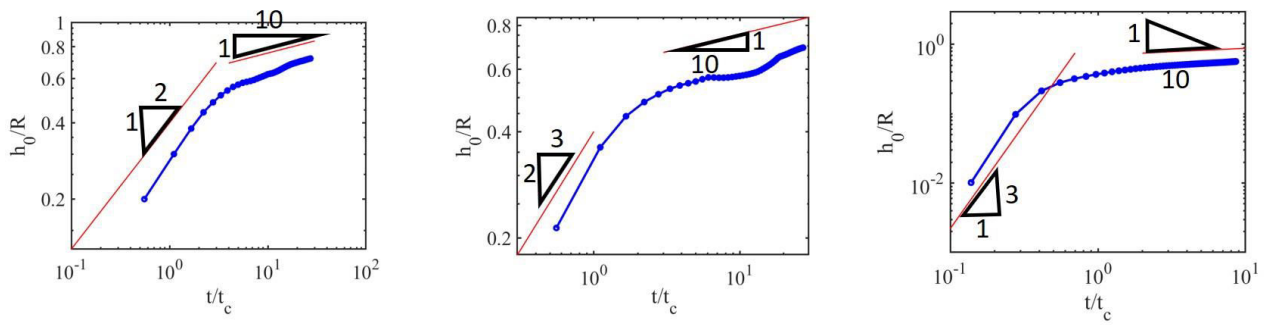

(a) We = 0 (b) We = 0.1 (c) We = 1

Figure 3.8: Variation of the dimensionless bridge height (h_0/R) as a function of the dimensionless time ($t/t_c = t^*$) for different Weber number. In the figures, we have identified the different scaling regimes and the exponents governing these regimes (i.e., n values for $h_0/R \sim (t^*)^n$ for early stages of drop coalescence and m values for $h_0/R \sim (t^*)^m$ variation for late stages of drop coalescence). Here t_c is the capillary time scale expressed as $t_c = \sqrt{\rho_1 R^3/\sigma}$.

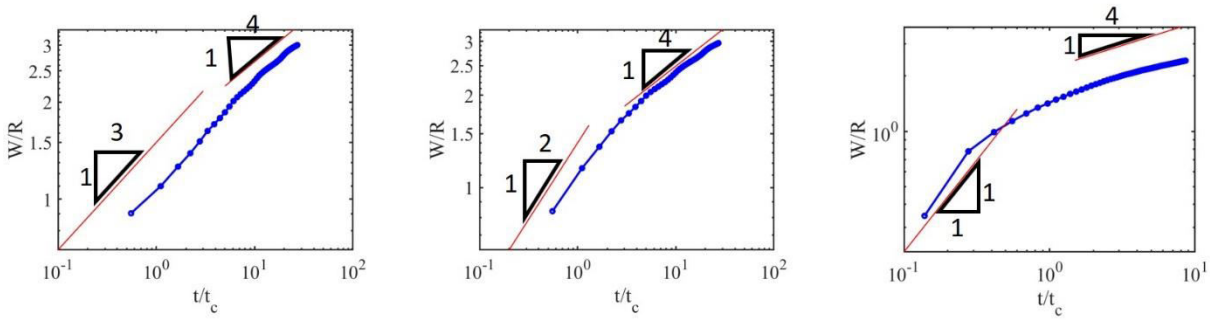

Figure 3.9: Variation of the dimensionless bridge width (W/R) as a function of the dimensionless time ($t/t_c = t^*$) for different Weber number. In the figures, we have identified the different scaling regimes and the exponents governing these regimes (i.e., p values for $W/R \sim (t^*)^p$ for early stages of drop coalescence and q values for $W/R \sim (t^*)^q$ variation for late stages of drop coalescence). Here t_c is the capillary time scale expressed as $t_c = \sqrt{\rho_1 R^3/\sigma}$.

3.3.3 Coalescence of Polymeric Drops of Unequal Sizes: Non-axisymmetric Polymeric Drop Coalescence

In this subsection, we study the coalescence of unequal-sized polymeric drops (of radii 10 μm and 7.5 μm) impacting on a substrate with identical *We* number. The drops being unequal in size, is an example of non-axisymmetric polymeric drop coalescence. In order to explicate the coalescence event, in Figs. 3.10-3.11, we plot the distribution of the magnitude of the velocity inside and around the drops at various stages of spreading corresponding to *We* = 1 (Weber number is defined based on the average of the radii of the two drops, please see the caption of Fig. 3.10). The velocity vectors are provided, in addition to the velocity magnitude, in order to give a sense of the direction of motion of the liquid at each location. Just as the case of the axisymmetric coalescence (see Figs. 3.2 and 3.3), here too, the centers of the of both the drops are at a distance of $z_0 = 20\ \mu m$ from the substrate at the start of the simulation (t* = 0, please see the caption of Fig. 10 for the definition of t*). This also implies that the smaller drop impacts the substrate at a slightly later instant as compared to the larger drop, and hence starts the spreading at a later time instant. This is corroborated by the fact that the droplets are at different stages of spreading at t* = 1.69 [see Fig. 3.10(a)]. Also, the velocity magnitude is larger near the contact line of the smaller droplets at t* = 1.69 since the smaller droplet is at the earlier stage of spreading as compared to the larger drop. Of course, for both the drops at a given time instant, the velocity magnitude is maximum near the three-phase contact line (TPCL), and it continuously decreases as the droplets continue to spread and attain equilibrium [see 3.10(a)-(f)]. It is also clear that the velocity vectors are directed towards the TPCL for both droplets before the drops start to coalesce and form a bridge see [3.10(a)-(d)]. It can also

be seen from Fig. 3.11, that the velocity vectors are directed away from the center of the drops (radially outwards) towards the air-liquid interface as they spread on the substrate. This increase in height (h_0) and width (W) of the bridge occur as the fluid mass gets directed towards the bridge, as shown by the velocity vectors near the bridge formed by these two drops. From Figs 3.10 and 3.11, it can also be seen that the growth of the bridge (height and width) is much slower, and it takes much longer to attain equilibrium (t* = 253) when compared to the case of axisymmetric coalescence with two droplets of 10 μm (t* = 97) for same Weber number. This is primarily attributable to the presence of a smaller droplet (7.5 μm) for this case.

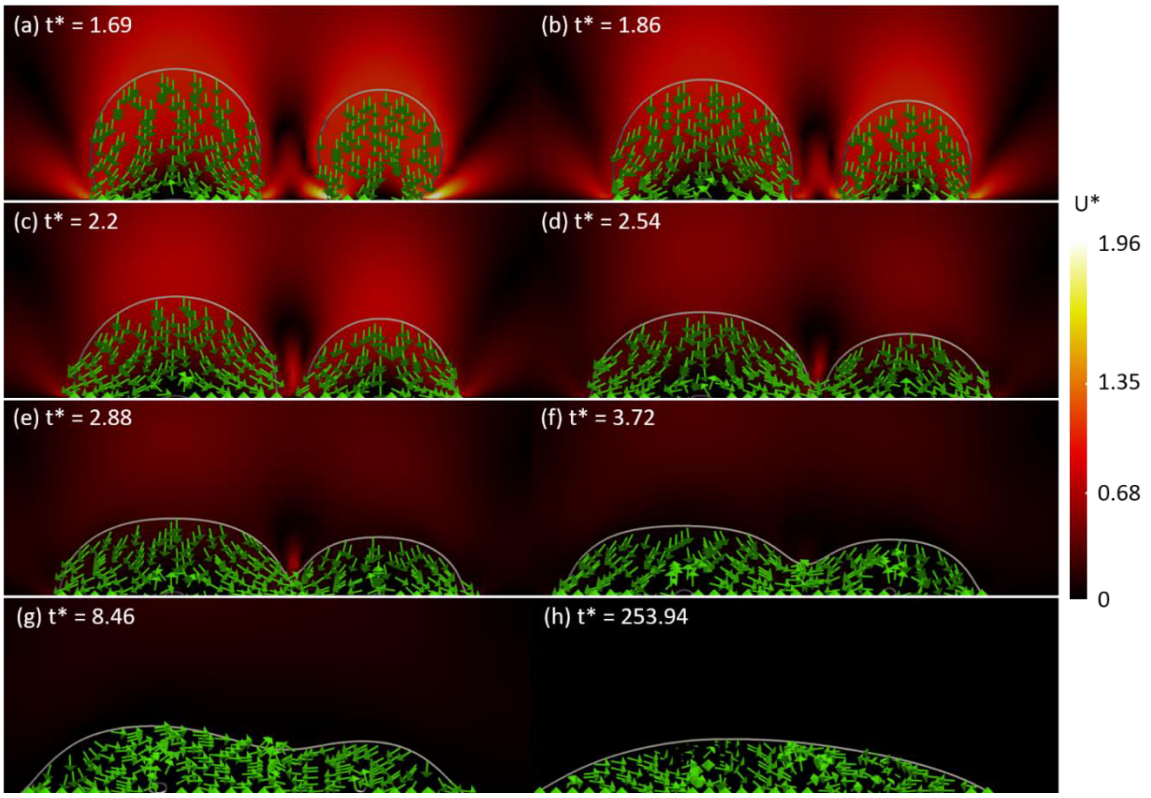

Figure 3.10: Variation of the dimensionless velocity field inside the two drops of radius 10 μm and 7.5 μm and the air in the immediate vicinity of the drops across a cross-section (i.e., the y-z plane) that passes through center of the drops (x=0) at different time instants (dimensionless) inside the coalescing drops for We=1. Velocity vectors, shown only for the drops, are not in scale with the magnitude of the local velocity. Here the dimensionless time is $t^* = t/t_c$, the dimensionless velocity is $U^* = U/U_0$ (where U_0=R_0/t_c is the characteristic velocity scale), $t_c = \sqrt{\rho_1 R_0^3/\sigma}$ is the capillary time scale, and $R_0 = \frac{R+R'}{2}$ (R and R' are the radii of the larger and smaller drops). Also, $We = \frac{\rho_1 v^2 R_0}{\sigma}$ is the Weber number and v is the velocity with which both the larger and the smaller drops impact the substrate.

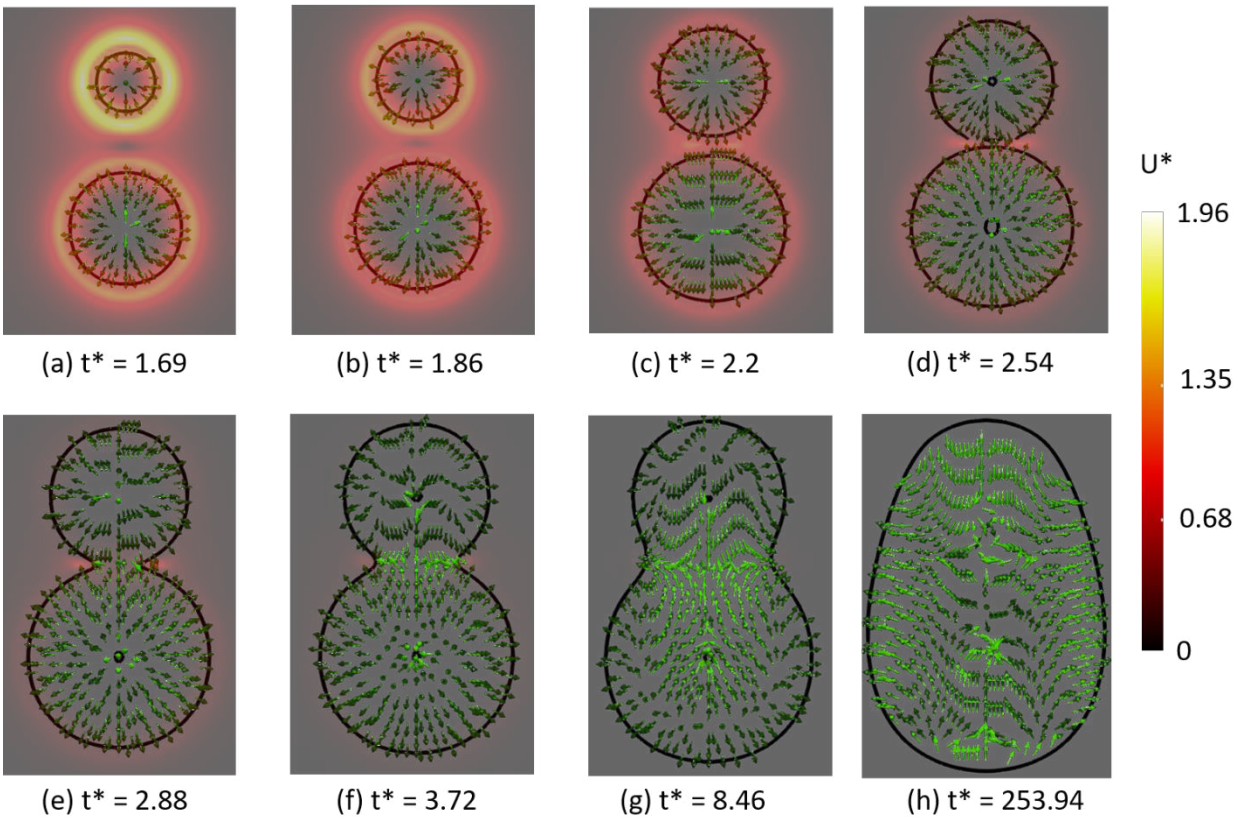

Figure 3.11: Variation of the dimensionless velocity field inside the two drops of radius 10 μm and 7.5 μm and the air in the immediate vicinity of the drops across the x-y plane at z = 1 μm at different time instants inside the coalescing drops for We=1. Velocity vectors, shown only for the drops, are not in scale with the magnitude of the local velocity. Here the dimensionless time is $t^* = t/t_c$, the dimensionless velocity is $U^* = U/U_0$ (where U_0=R_0/t_c is the characteristic velocity scale), $t_c = \sqrt{\rho_1 R_0^3/\sigma}$ is the capillary time scale, and $R_0 = \frac{R+R'}{2}$ (R and R' are the radii of the larger and smaller drops). Also, $We = \frac{\rho_1 v^2 R_0}{\sigma}$ is the Weber number and v is the velocity with which both the larger and the smaller drops impact the substrate.

3.3.4 Effect of Viscosity in Axisymmetric Coalescence of Polymeric Drops

In this section, we investigate the effect of rheology of the power-law obeying polymeric drops (following the same rheology equation as eq. 3.6, but with n=0.8) on axisymmetric coalescence and its effect on the growth of the height and the width of the bridge formed by two identical sized ($R = 10$ μm) coalescing drops. We provide the results for We = 0. Firstly, in Figs. 3.12 and 3.13, we show the distribution of the velocity magnitude (non-dimensional) inside and around the spreading droplets at various instances. The direction of the fluid flow inside the droplets is indicated by the velocity vectors. We find that the velocity vectors are directed towards the three-phase contact line (TPCL) as the drops start spreading [see Fig. 3.12 (a-d)]. This is consistent with the behavior seen for the case with power law exponent of n = 0.6. Similarly, we also observe that once the drops interact with each other and form a bridge, the fluid mass that was directed towards the contact lines (before the formation of the bridge) contributes to the growth of the bridge. This is clearly indicated by the velocity vectors that are directed upwards at the area near the bridge (see Fig. 3.12 (e-h)). Secondly, in Fig. 3.13, we observe that the velocity magnitude is maximum near the liquid-air interface and minimum near the center of the droplet, as the fluid at the contact line moves away from the point of impact to achieve equilibrium configuration, as is also pointed out by the velocity vectors directed away from the center towards the contact line. This is also consistent with the findings for the case with power law exponent of n = 0.6, showing that the qualitative coalescence behavior remains similar for fluids of different viscosity. Thirdly, we observe that the magnitude of the velocity of the droplets for this case (n = 0.8) is much smaller than the case of n = 0.6: this can be attributed to the larger viscosity of the drops for n=0.8 as compared to the drops with n=0.6.

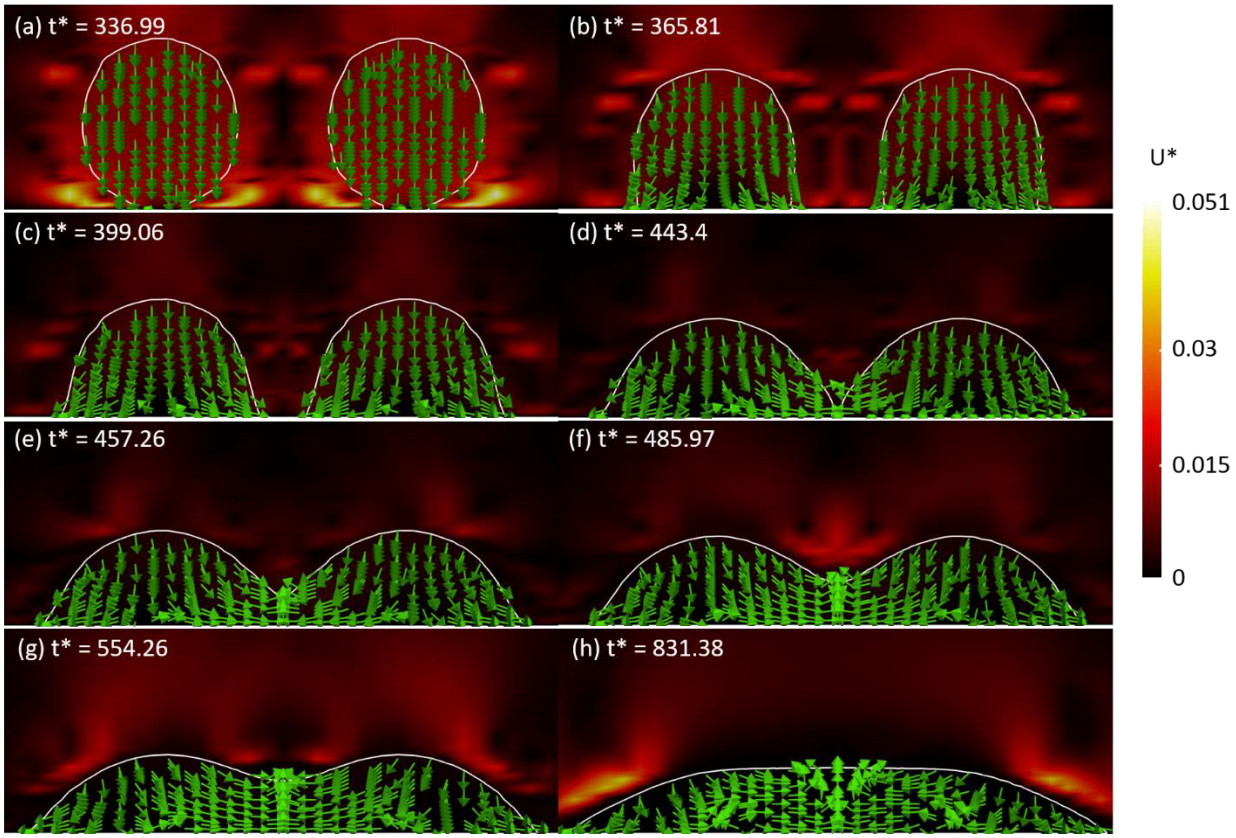

Figure 3.12: Variation of the dimensionless velocity field inside the drops as well as in the air in the immediate vicinity of the drops across a cross-section (i.e., the y-z plane) that passes through center of the drops (x=0) at different time instants (dimensionless) inside the coalescing drops for We=0. Velocity vectors, shown only for the drops, are not in scale with the magnitude of the local velocity. Here the dimensionless time is $t^* = t/t_c$, the dimensionless velocity is $U^* = U/U_0$ (where U_0=R/t_c is the characteristic velocity scale), and $t_c = \sqrt{\rho_1 R^3/\sigma}$ is the capillary time scale. Here, the power law exponent (n) for the viscosity model [see eq.(6)] of the liquid is taken as 0.8. The other parameters remain the same as that used in Fig. 3.2.

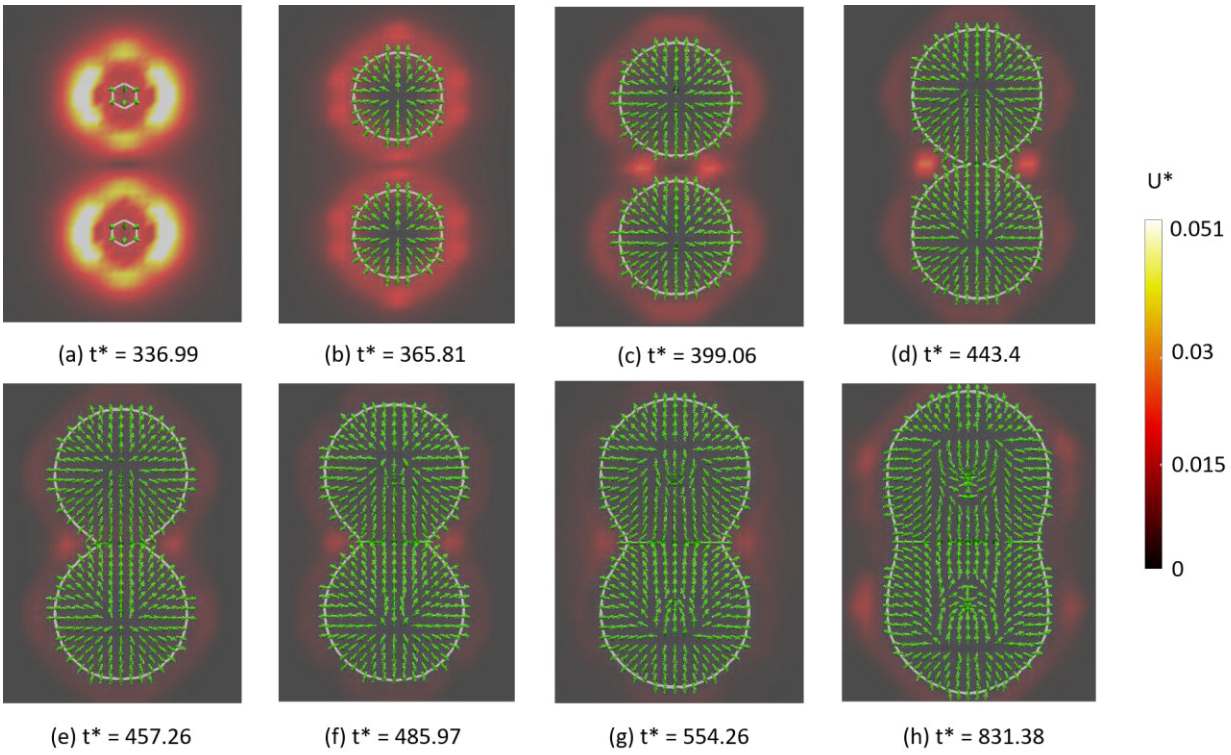

Figure 3.13: Variation of the dimensionless velocity field inside the drops as well as in the air in the immediate vicinity of the drops across the x-y plane at z = 1 μm at different time instants (dimensionless) inside the coalescing drops for We=0. Velocity vectors, shown only for the drops, are not in scale with the magnitude of the local velocity. Here the dimensionless time is $t^* = t/t_c$, the dimensionless velocity is $U^* = U/U_0$ (where U_0=R/t_c is the characteristic velocity scale), and $t_c = \sqrt{\rho_1 R^3/\sigma}$ is the capillary time scale. Here, the power law exponent (n) for the viscosity model [see eq.(6)] of the liquid is taken as 0.8. The other parameters remain the same as that used in Fig. 3.2.

3.3.5.1 Dynamics of Bridge Height at Early Stages of Coalescence for Power-Law Obeying Polymeric Drops (with n=0.8) for We = 0:

Numerical results [see Fig. 3.14(a)] confirm that the bridge height scales as $h_0/R \sim (t^*)^{1/2}$ ($t^*=t/t_c$) during the initial stages of the drop coalescence for a Weber number $We = 0$. This is consistent with the scaling exponent observed for various Newtonian liquids[2,6,45-47] as well for the case of the identical sized power-law obeying polymeric drops with power law exponent n = 0.6, stemming from the fact that at such early stages the growth of the bridge is dictated by the balance of the inertial force and the capillary stress with negligible effect of the viscous forces.

3.3.5.2 Dynamics of Bridge Height at Late Stages of Coalescence for Power-Law Obeying Polymeric Drops (with n=0.8) for We = 0:

In Fig. 3.14(a), numerical simulation predict that the bridge height grows as $h_0/R \sim (t^*)^{1/10}$ at later stages of drop coalescence. Previously, we have derived that for the late stages of coalescence, the bridge height varies as:

$h_0 \sim t^{\frac{n}{6+4n}}$, (3.17)

which yields (with n=0.8 and R and t_c as constants)

$\frac{h_0}{R} \sim \left(\frac{t}{t_c}\right)^{0.087}$, (3.18)

which is very close to the scaling prediction obtained from the simulation, i.e., $h_0/R \sim (t^*)^{0.1}$.

3.3.5.3 Dynamics of Bridge Width at Early Stages of Coalescence for Power-Law Obeying Polymeric Drops (with n=0.8) for We = 0:

Numerical simulations predict that the bridge width grows as $W/R \sim (t^*)^{0.38}$ during the early stages of coalescence [see Fig. 3.14(a)]. In the previous section, we had hypothesized that at the early stages of the drop coalescence, the capillary stresses drive the growth of the bridge width, while both the viscous stresses as well as the inertial pressure resist the growth of the bridge width. The balance between the capillary stress and the inertial pressure will yield (following the same calculations as provided for the growth of the bridge *height* at early stages of coalescence for *We = 0*)

$$\frac{W}{R} \sim \left(\frac{t}{t_c}\right)^{0.5}. \qquad (3.19)$$

On the other hand if the capillary stresses are balanced by the viscous stresses (which scales as $\mu_1 \nabla \boldsymbol{u} \sim m\dot{\gamma}^n$), we can write [using eq.(3.12), n=0.8, and R and t_c as constants]:

$$W \sim t^{n/2} \sim t^{0.4} \Rightarrow \frac{W}{R} \sim \left(\frac{t}{t_c}\right)^{0.4}. \qquad (3.20)$$

Given that there is not much variation in the scaling exponent in the *W/R*-vs-*t** variation for the two scenarios (balance between the capillary and inertial effect yields the exponent as 0.5, while the balance between the capillary and viscous effect yields the exponent as 0.4), we can easily justify the numerical result where this exponent is ~ 0.38.

3.3.5.4 Dynamics of Bridge Width at Late Stages of Coalescence for Power-Law Obeying Polymeric Drops (with n=0.8) for We = 0:

In Fig. 3.14(b), we report our simulation-based observations that the bridge width grows as $W/R \sim (t^*)^{3/10} \sim (t^*)^{0.3}$ at late stages of drop coalescence.

Using eq.(3.15), eq.(3.17) (to express the variation of h_0 with t), n=0.8, and considering R and t_c as constants, we can write the scaling equation governing the growth of the bridge width at late stages of coalescence as:

$$(\theta'_d)^{\frac{2+n}{n}} \sim \frac{dW}{dt} \Rightarrow \left(\frac{h_0}{W}\right)^{\frac{2+n}{n}} \sim \frac{dW}{dt} \Rightarrow \left(\frac{n}{t\frac{n}{6+4n}}{W}\right)^{\frac{2+n}{n}} \sim \frac{dW}{dt} \Rightarrow W \sim t^{\left(\frac{8+5n}{6+4n}\right)\left(\frac{n}{2+2n}\right)} \Rightarrow \frac{W}{R} \sim \left(\frac{t}{t_c}\right)^{0.29}, \quad (3.21)$$

i.e., our scaling prediction matches excellently with the simulation-based prediction of $W/R \sim (t^*)^{0.3}$.

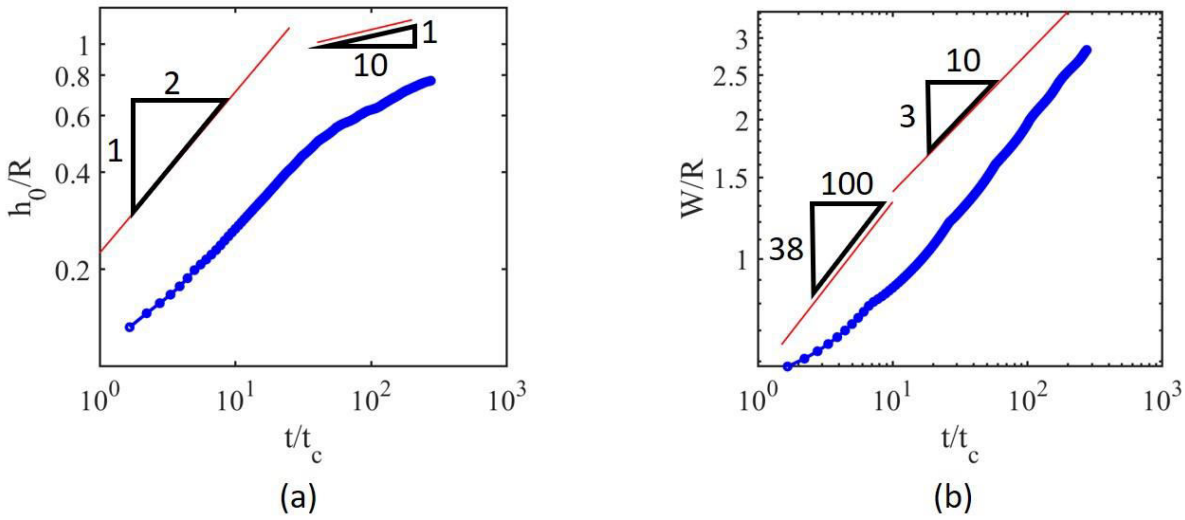

Figure 3.14: Variation of (a) dimensionless bridge height (h_0/R) and (b) dimensionless bridge width (W/R) as a function of dimensionless time (t/t_c) for coalescence of two power-law obeying polymeric equal-sized droplets of radius 10 μm for a Weber number We = 0. Here, the power law exponent (n) of the liquid is taken as 0.8. The other parameters remain the same. In the figures, we have identified the different scaling regimes and the exponents governing these regimes: In the figures, we have identified the different scaling regimes and the exponents governing these regimes (i.e., n values for $h_0/R \sim (t^*)^n$ for early stages of drop coalescence, m values for $h_0/R \sim (t^*)^m$ variation for late stages of drop coalescence, p values for $W/R \sim (t^*)^p$ for early stages of drop coalescence, and q values for $W/R \sim (t^*)^q$ for late stages of drop coalescence). Here t_c is the capillary time scale expressed as $t_c = \sqrt{\rho_1 R^3/\sigma}$.

3.4 Conclusions

In this paper, we have probed the axisymmetric (with two separate rheologies) and non-axisymmetric 3D coalescence of shear-thinning polymeric drops impacting on solid surfaces with a finite impact velocity (or finite *We*) by employing sophisticated direct numerical simulation technique. The results reveal unprecedented details of 3D coalescence by providing the 3D velocity field and 3D velocity vectors inside the coalescing drop. Such information enables us to identify that while the qualitative coalescence dynamics is independent of the choices of *We*, quantitatively the coalescence dynamics (i.e., in terms of the velocity fields involved, the time to attain different coalescing states, and the time to equilibrium) is a strong function of *We*. Furthermore, the simulations reveal distinct scaling laws dictating the growth rate of the height and the bridge (formation and evolution of the bridge is a manifestation of the coalescence event) at different stages of the coalescence event as functions of *We*. We also provide physics-based derivation of several of these scaling regimes and obtain excellent match with those predicted by the simulations.

Our combined simulation and scaling-law calculation results will be useful in a vast number of areas ranging from inkjet and aerosol jet printing to polymer blending, where the coalescence of such polymeric drops (with or without a substrate and in presence or in absence of a finite drop velocity) become critical. One example of where such an improved theoretical understanding of drop coalescence could dramatically impact improvements in manufacturing using AJ printing is in the area of printing smoothing layers.[51] Figure 3.15(a) shows a side view of an as-printed fillet which was fabricated using in-situ UV curing of a polymeric ink. Please notice the ‘stair step’ structure on the surface of such a

fillet resulting from locking-in the position of the ink stream as it is being printed. Locking-in the ink stream is a requirement for the fabrication of such a 3D printed structure. However, in order for the fillet to be useful, the final surface needs to be smooth. This can be accomplished by printing a final smoothing layer over the fillet surface. For such a smoothing layer, the volume of ink that needs to be printed is equal to the unfilled volume created by the stair step geometry. This volume of ink needs to be printed such that the ink stream is deposited on each 'stair' and is given enough time to re-lay and fill in the open volume. Once the polymer ink has relaxed sufficiently and filled in the open volume, it can then be UV cured to be locked in place. The result of printing such a smoothing layer is shown in Fig. 3.15(b). In order to properly print such a smoothing layer, the exact time needed for an ink to relax and fill-in the stair geometry must be determined and the UV curing must be performed at the exact time when the proper relaxation time has passed. Otherwise, the un-cured ink will continue to flow and pool up in unwanted regions of the fillet surface resulting in a less than optimized smoothing layer. To date, such relaxation times between printing and curing has only been able to be deduced experimentally. The current simulation study extends an understanding of the time-dependent variation of the shape of the uncured polymer mass formed by the interaction of two polymer drops: therefore, our study will form the basis of predicting the time-dependent variation of the shape of the uncured polymer mass when multiple drops are deposited (through AJ printing or inkjet printing) as the smoothing layer (as discussed above). Accordingly, our study will help to better control (and also predict the necessary time) for smoothing the surface roughness of a printed structure.

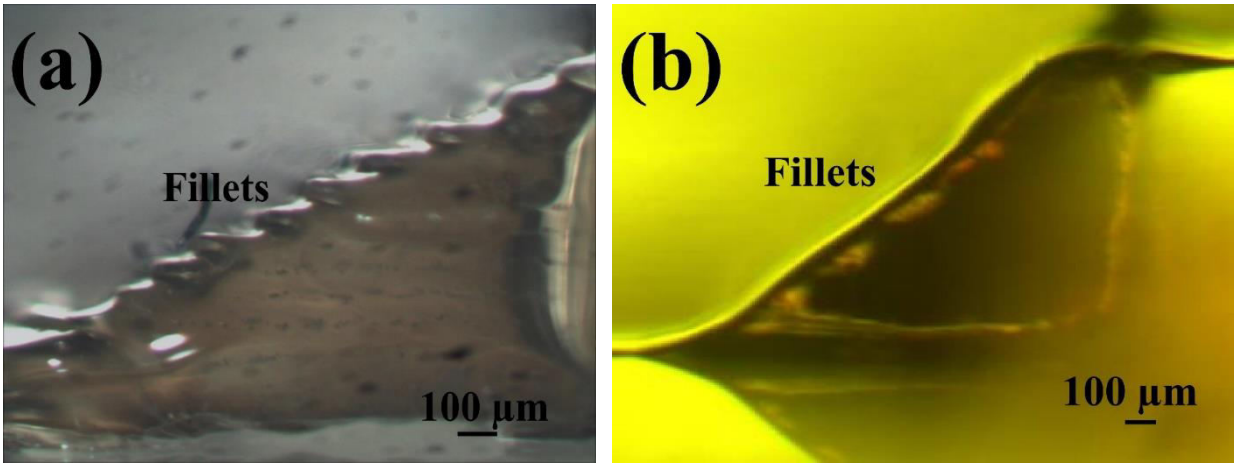

Figure 3.15: Edge-on optical images of an AJ printed fillet (a) without an added smoothing layer and (b) with an added smoothing layer. Both the parts (a) and (b) of the figure have been reproduced from Gu et al.,[51] Copyright 2017 by John Wiley and Sons.

Chapter 4: Study of the Coalescence and Mixing of Drops of Different Polymeric Materials*

Abstract

In this chapter, we employ Direct Numerical Simulation (DNS) to investigate the solutal-hydrodynamics dictating the three-dimensional coalescence of microscopic, identical sized sessile drops of different but miscible shear-thinning polymeric liquids (namely PVAc or polyvinyl acetate and PMMA or polymethylmethacrylate) with the drops being in partially wetted configuration. Despite the ubiquitousness of the interaction of different dissimilar droplets in a variety of engineering problems ranging from additive manufacturing to understanding the behavior of photonic crystals, coalescence of drops composed of different polymeric and non-Newtonian materials has not been significantly explored. Interaction of such dissimilar droplets often involves simultaneous drop spreading, coalescence, and mixing. The mixing dynamics of the dissimilar drops are governed by the interphase diffusion, residual kinetic energy of the drops stemming from the fact that coalescence starts before the spreading of the drops have been completed, and the solutal Marangoni convection. We provide the three-dimensional velocity fields and velocity vectors inside the completely miscible, dissimilar coalescing droplets. Our simulations explicate the relative influence of these different effects in determining the flow field at different locations and at different time instants and the consequent mixing behavior inside

* Contents of this chapter is published as: V. S. Sivasankar, D. R. Hines, and S. Das, "Numerical Study of the Coalescence and Mixing of Drops of Different Polymeric Materials". *Langmuir*, *38*(46), 14084-14096.

the interacting drops. We also show the non-monotonic (in terms of the direction of migration) propagation of the mixing front of the miscible coalescing drops over time. We also establish that the overall mixing (on either side of the mixing front) speeds up as the Marangoni effects dictate the mixing. We anticipate that our study will provide an important foundation for studying miscible multi-material liquid systems, which will be crucial for applications such as inkjet or aerosol jet printing, lab on a chip, polymer processing, etc.

4.1 Introduction

Coalescence of microscopic or macroscopic liquid drops has been one of the most widely researched multiphase problems owing to its significant role in a variety of phenomena like cloud formation and precipitation,[129] oil spills,[130] emulsions,[131] additive manufacturing processes[19,99,109-111] such as aerosol jet printing, inkjet printing, syringe/extrusion printing, electrohydrodynamic (EHD) jet printing, etc. The effect of viscosity, surface tension, and surface wettability on the coalescence dynamics of Newtonian droplets on both solid surfaces and liquid films have been well studied.[100-106] Recently, a number of researchers have studied the coalescence dynamics of non-Newtonian polymeric droplets,[116,132-133] including the effect of impact velocity. The coalescence dynamics of the drops are usually quantified by studying the growth of the bridge connecting the drops. The time evolution of the bridge height, and the bridge width during the coalescence process have been widely reported.[100-103,116,132]

Many of these studies probe the dynamics of coalescence of droplets of identical materials; however, there are many interesting phenomena involving multi-jet multi-material printing,[134] photonic crystals,[135] etc., that involve the coalescence of drops of different materials. There have been several studies that have probed the coalescence of drops of different materials,[136-141] although a majority of these studies have focused on the coalescence of drops that are identical in all respect except the surface tension values.[136-138] For example, Borcia and Bestehorn studied the effect of the Marangoni forces (on account of the different surface tension of the two coalescing drops) in driving the coalescence process, although they did not provide any detailed information on the fluid flow inside the two drops.[139,140] On the other hand, Hack *et al.* studied the coalescence

between two water drops (with different concentrations of ethanol) impacting (at a finite Weber number) and coalescing (in air): they studied the effect of induced capillary waves in dictating the coalescence in presence of a finite Weber number and surface tension difference (between the two drops).[141] Other related studies include the study by Blanchette,[142] where they model the mixing behavior of two droplets having different surface tension values and released mid-air far away from the substrate: the findings reveal the effect of the Reynolds (or droplet velocities) and the difference in the surface tension values between the two drops on the mixing behavior. Sellier *et al.* employed lubrication approximation for investigating the effect of the droplet size and the strength of Marangoni flow (caused by the surface tension difference) on the coalescence behavior of miscible droplets having different surface tension values.[143] In a different work, Sellier *et al.* provided experimental evidence of surface tension gradient induced droplet actuation on highly philic surfaces.[144] Further, the effect of the impact velocity and the separation between two Newtonian drops having different surface tension values was studied by Castrejon-Pita *et al.* using Lattice-Boltzmann model and validated using experiments.[145] In another study, Jehannin *et al.* studied the coalescence behavior of two chemically reacting drops (such chemical reaction effect induced diffusion and convection), with the coalescence showing stationary and oscillatory behaviors depending on the system parameters.[146] Sykes *et al.* experimentally studied drops composed of ethanol and deionized (DI) water and quantified the effect of the ethanol concentration (in DI water) (and hence varying surface tension of the drops), drop impact velocity (one drop impacting a stationary sessile drop), and lateral separation between the centers of the stationery and the impacting drops on the coalescing behavior of drops.[147] Depending on this lateral

separation distance, the authors observed well-defined surface jets that transported the liquid from the impacting drop towards the sessile drop.[147] Further experiments on collision of miscible droplets were conducted by Focke *et al.* and they reported the encapsulation of higher viscosity drops by the lower viscosity drops.[148] Karpitschka and Riegler conducted experiments and provided a phase space of coalescence and non-coalescence behavior of two miscible organic liquids (hexadecane and pentadecane) as a function of their surface tension differences.[149] Karpitschka and Riegler, in another paper studied the non-coalescence of different miscible liquids, highlighting the hydrodynamic mechanism of stable non-coalescence through self-stabilizing travelling wave.[150] Borcia *et al.* experimentally showed the delayed coalescence of miscible liquids with surface tension differences, especially for low contact angles (highly wetting) liquids.[151] Borcia *et al.*, in another study, numerically investigated the coalescence of miscible liquid drops in a confined box geometry demonstrating, based on the surface tension difference between the liquids, the presence of different regimes (namely "chasing droplet" or "droplet repulsion" regimes).[152] Also, there have been efforts to study the effect of Marangoni forces in dictating the coalescence between a drop and a liquid reservoir.[153-155] Of course, all these studies only consider Newtonian liquids.[139-152] A big gap in the existing literature stems from the fact that there is very little research and understanding on the coalescence between two *actual non-Newtonian* polymeric drops of different polymeric materials: such an endeavor is essential for different applications, especially, for multi-material and multi-jet droplet based printing.[156-160]

In this paper, we numerically probe the spreading and coalescence of two different non-Newtonian, shear-thinning, and miscible polymeric drops of two different materials.

One drop is of polyvinyl acetate (PVAc) drop (or drop-1), while the other drop is of poly-methylmethacrylate (PMMA) drop (or drop-2). We consider the drops to be in partially wetting configuration and consider their spreading and coalescence on a substrate that is philic to both the drops. However, PVAc spreads much faster than the PMMA drop on account of (1) the substrate being more philic to the PVAc drop and (2) PMMA having a larger viscosity than PVAc (particularly for larger shear rates). Our results report the spreading of both the drops, followed by the interaction and the coalescence of the drops. The coalescence leads to a host of different fluid flow events inside the two drops, which also determine the motion of the mixing front between the two liquid drops and the eventual mixing of the two liquids. We identify that once the drops start to interact, the fluid dynamics inside the drops get determined by the local diffusion at the coalescence zone as well as whether the residual kinetic energy of the drops at the time they start to coalesce (such residual kinetic energy is associated with the fact that the drops starts to coalesce with finite spreading velocity at their coalescing three-phase contact lines) or the Marangoni forces drive the advection of the liquids of the two drops at the coalescing zone. Subsequently, we quantify the mixing of the two drops post coalescence: we find that the mixing front develops around the interface. We also identify that at earlier stages of interaction where mixing is dictated by the diffusive transport, the mixing occurs very slowly; however, once Marangoni convection effects start to dominate the mixing dynamics, mixing occurs quicker ensuring a nearly homogenous composition across the entire *single* drop (resulting from the coalescence of the two drops).

4.2 Theory and Simulation methods

In this study, we consider the coalescence of two identical sized (radius = R= 10 μm) drops of different but miscible liquids, namely two different power-law obeying shear-thinning liquids (PVAc and PMMA) separated by an initial center-to-center distance of *d* as shown in Fig. 4.1. These droplets with different material properties are allowed to simultaneously come in contact with the solid (philic to both the drops) and spread. The center-to-center distance (*d*) between the drops is chosen to be smaller than the sum of the equilibrium spreading radius of the two drops, i.e., $d < a_1 + a_2$ (where a_1 and a_2 are the equilibrium spreading radii for drops 1 and 2), in order to ensure that the drops coalesce.

4.2.1 Simulation set-up

We probe the three-dimensional coalescence and mixing dynamics of the PVAc and the PMMA drops using Direct Numerical Simulation (DNS). We employ a multiphase, incompressible, laminar flow-based volume of fluid (VOF) method.[161,162] The OpenFOAM solver interMixingFoam, which works based on the finite volume technique is used to solve the soluto-hydrodynamics of the two drops.[121,163-169] Surface tension effects are incorporated in this solver. Such VOF-based framework to study the dynamics of miscible fluid (undergoing mixing) have been widely employed in several studies in the literature.[142,148,170] There are various studies that have provided the benchmark for the used standard VOF-based solver interMixingFoam.[163,166-169] The simulation domain used in this study is of size 125 μm x 125 μm x 100 μm. The domain is meshed with a structured hexahedral mesh with 5,120,000 cells using the OpenFOAM mesh generator.[121]

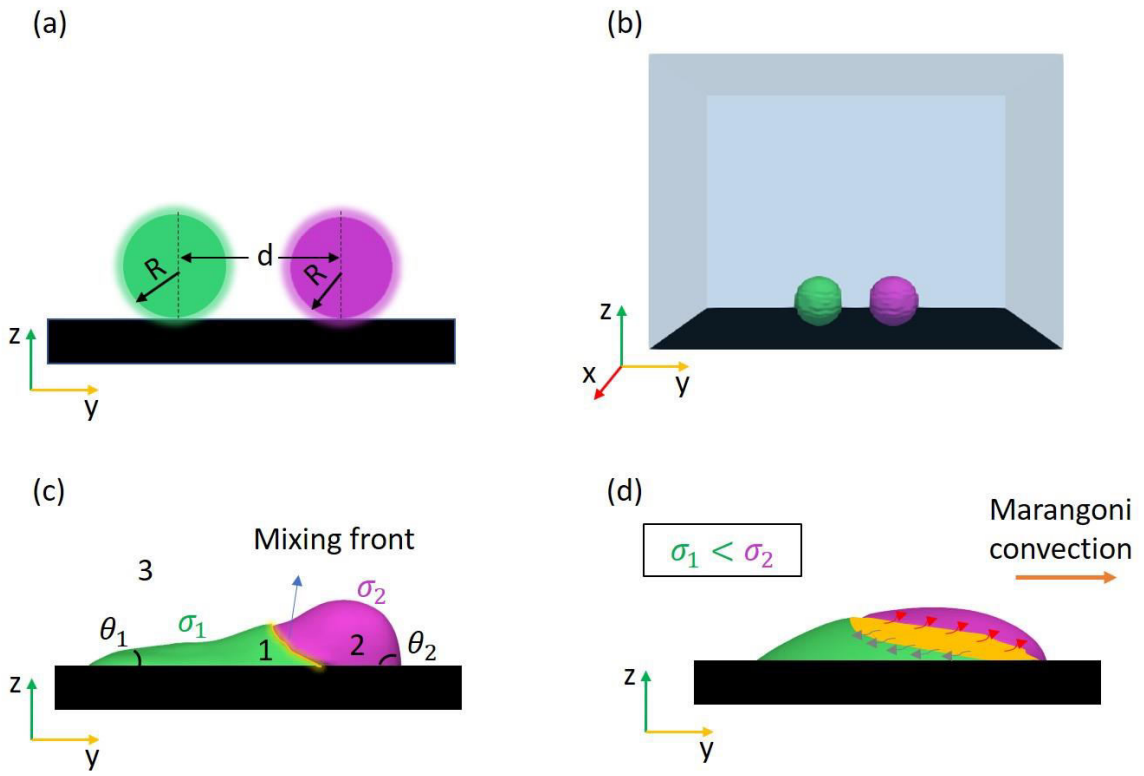

Figure 4.1: (a) Schematic showing the initial configuration of the two identical sized drops (radius R) of two different materials [(drop-1: PVAc drop (green); drop-2: PMMA drop (purple)]. (b) 3D schematic showing the simulation domain and the droplets. (c) Schematic showing the mixing front during the coalescence of these two droplets of dissimilar materials. The numbers denoted in (c) represent the different phases – 1: liquid material – 1 (PVAc drop), 2: liquid material – 2 (PMMA drop), 3: air. Please note that the contact angles the drops make with the substrate are different ($\theta_1 \neq \theta_2$). (d) Schematic showing the diffusion of phase 1 and phase 2 into each other as shown by the arrows near the mixing front. The surface tension gradients cause a Marangoni convection pushing the liquid drops

towards the droplet with higher surface tension. Schematic in Fig. 4.1(d) depicts the situation where the surface tension of phase 1 (σ_1) is lower than that of phase 2 (σ_2).

4.2.2 Governing equations

4.2.2.1 Continuity and Navier-Stokes equations:

The simulation setup consists of two miscible polymeric drops of different materials that are surrounded by air. The flow field inside and outside the drops have to be solved during the coalescing and the mixing process to fully capture the dynamics of coalescence of the miscible and dissimilar polymeric drops. The fluid flow in this system is governed by the coupled continuity and Navier-Stokes momentum equations, described as follow:

$$\nabla.(\boldsymbol{u}) = 0, \qquad (4.1)$$

$$\rho\frac{\partial \boldsymbol{u}}{\partial t} + \rho(\boldsymbol{u}.\nabla)(\boldsymbol{u}) = \nabla.[-p\bar{I} + \mu(\nabla\boldsymbol{u} + (\nabla\boldsymbol{u})^T)] + \rho\boldsymbol{g} + \boldsymbol{F}_\sigma. \qquad (4.2)$$

In eqs. (4.1-4.2), the term $\boldsymbol{u}$ represents the velocity vector, p represents the pressure, ρ represents the density of the fluid, μ is the fluid viscosity, $\bar{I}$ is the identity tensor, $\rho\boldsymbol{g}$ represents per unit volume gravitational body force, and $\boldsymbol{F}_\sigma$ is the per unit volume surface tension force. The surface tension effect is modeled using the continuum surface force (CSF) model (that includes the surface tension gradient effect) as:[171-173]

$$\boldsymbol{F}_\sigma = \sigma\kappa\nabla\alpha + \nabla_s\sigma\delta. \qquad (4.3)$$

Here, σ is the liquid-air surface tension, κ is the local, instantaneous curvature at the liquid-air interface, α is the scalar representing the volume fraction of the phases, ∇_s is the surface gradient operator, δ is the surface-delta function given by $\delta = |\nabla\alpha|$. The material properties at any location are determined by the scalar quantities $\alpha_1, \alpha_2, and\ \alpha_3$ representing the volume fractions of phase – 1 (liquid material-1 or PVAc drop), phase – 2 (liquid material-2 or PMMA drop), and phase – 3 (air), respectively. Therefore, the fluid density, viscosity, and surface tension at any location are expressed as:

$$\rho = \alpha_1\rho_1 + \alpha_2\rho_2 + \alpha_3\,\rho_3, \qquad (4.4)$$

$$\mu = \alpha_1\mu_1 + \alpha_2\mu_2 + \alpha_3\,\mu_3. \qquad (4.5)$$

$$\sigma = \frac{(\alpha_1\sigma_1+\alpha_2\sigma_2)}{\alpha_1+\alpha_2}. \qquad (4.6)$$

Eq.(4.6) considers that the surface tension of the polymer mixture, which will result from the mixing of the non-identical (but miscible) polymeric drops, varies linearly with the volume fraction of the non-identical liquid components. Such a consideration has been widely used in the literature.[151,174-175] Furthermore, several experimental measurements of some of the commonly found polymeric blends show such a linear variation of surface tension with both weight percentage and molecular weight of the individual polymers constituting the blend.[176-177] In the absence of measurement of the exact surface tension variation of PMMA/PVAc blend (or mixture) with the volume fraction of the individual polymeric material (PMMA or PVAc), such a linear variation assumption is incorporated. The miscibility of the two chosen polymers, namely PVAc and PMMA, has been established by the studies investigating the specific polymer blend consisting of PVAc and PMMA. The extent of miscibility of the two polymers can be quantified by means of the diffusion coefficient (D_{12}) of one species into another. This diffusion coefficient (D_{12}), which has been obtained from the literature (see Ref. 178) has been used in the transport equation that solves for the conservation of the scalar variable (α_2) in eq. (4.8).

In eqs. (4-6), ρ_i, μ_i, and σ_i are the density, dynamic viscosity, and surface tension of phase *i* (*i*=1, 2, or 3).

Here, the liquid phases (phases 1 and 2) are polymeric shear thinning liquid whose viscosities obey a power law model. For each liquid phase *i* (*i=1,2*), viscosity is described as:

$$\mu_i = m_i \dot{\gamma}^{n_i-1} \qquad (4.7)$$

In eq.(4.7), m_i and n_i are the consistency index and power law index of the liquid phase *i*.

The volume fractions of the different phases have to be tracked over time, in addition to the Navier-Stokes and continuity equations, in order to completely track the mixing and coalescence dynamics of the two dissimilar, miscible drops. This is done by solving the following governing equations:

$$\frac{\partial \alpha_2}{\partial t} + \nabla.(\alpha_2 \boldsymbol{u}) - \nabla^2(D_{12}\alpha_2) - [\nabla.(\alpha_2\alpha_3 \boldsymbol{u_r})] = 0, \qquad (4.8)$$

$$\frac{\partial \alpha_3}{\partial t} + \nabla.(\alpha_3 \boldsymbol{u}) + [\nabla.(\alpha_1\alpha_3 \mathbf{u_r}) + \nabla.(\alpha_2\alpha_3 \boldsymbol{u_r})] = 0. \quad (4.9)$$

In the above equations, the volume fractions (α_i) of various phases are related by the following equation:

$$\alpha_1 + \alpha_2 + \alpha_3 = 1. \qquad (4.10)$$

The terms within the square brackets on the left-hand side of eqs.(4.8-4.9) ensures an artificial compression so as to maintain a sharp interface, and these terms are active only at the interface region. Here, the term $\boldsymbol{u_r}$ is the artificial compressive velocity used by the MULES (Multidimensional Universal Limiter with Explicit Solution) limiter to limit the phase fluxes,[179-182] and D_{12} is the diffusion coefficient of liquid phase 1 in liquid phase 2. This artificial compression velocity is instantaneously calculated by the MULES based solver using the face flux values.

4.2.2.2 Initial conditions:

Two identically sized drops of dissimilar materials are initially placed a distance of *d* apart on the substrate as shown in Fig. 4.1(a). All the velocity components throughout the domain (inside and outside the droplets) are set to be zero. The initial pressure at all nodes is set to be atmospheric pressure.

4.2.2.3 Boundary conditions:

We use the atmospheric boundary condition on all the surfaces of the simulation domain except for the bottom surface where the drops where the spreading and coalescence occurs. We further use a no-slip and no-penetration condition for the velocity at the bottom surface. A numerical slip condition is incorporated near the moving contact line to avoid the stress singularity that occurs in the presence of no-slip condition. The mass flux of the dense phase in the cell adjacent to the wall is computed and it is averaged over the grid to yield an apparent interface velocity (which serves as the slip velocity and is used to calculate the corresponding slip length).[123,183,184] The magnitude of this numerical slip velocity (and the corresponding slip length) is inherent to the numerical algorithm used. The artificial slip length is of the same order of magnitude as the grid size (typically h/2 with h being the grid size).[124] The mesh size has an impact on the contact line motion as the numerical slip is inherently dependent on the grid size. The sensitivity to grid size becomes less significant with finer grids.[123,183] Hence, a technique of grid convergence (plot of grid convergence is shown in Fig. C1 in Appendix C) has been widely used in the VOF solvers to reduce grid dependence, and this technique is used in this study as well. The meshes are finer around the wall for this reason. In this study, no adaptive remeshing was employed.

Next, the equilibrium contact angle at the TPCL is set by means of a contact angle boundary condition. This condition is set as the boundary condition for the equations of the scalar quantity (α_i) at the bottom surface (the surface where the TPCL is present). Such boundary condition prevents the droplet from completely wetting thus ensuring that it attains the equilibrium contact angle. In this approach, the mean curvature of the liquid-air interface (free surface) changes over time until the assigned equilibrium contact angle (in α_i equation) is achieved.[123,185-186]

Below, we describe the equations that are used to ascribe this boundary condition (in terms of the contact angle) to the equation governing α_i.

At the substrate boundary, the boundary condition that relates α_i to the (instantaneous) contact angle [$\bar{\theta} = \bar{\theta}(t)$] can be expressed as:[123]

$$\frac{\nabla\alpha_i}{|\nabla\alpha_i|} = \hat{n} = \hat{n}_w cos\bar{\theta} + \hat{t}_w sin\bar{\theta}, \quad (4.11)$$

where, $\hat{n}$ is the normal vector to the interface, $\hat{n}_w$ and $\hat{t}_w$ are the unit normal and unit tangential vectors to the substrate, and $\bar{\theta}(t) = \alpha_1\theta_{1,eq} + \alpha_2\theta_{2,eq}$ is the (instantaneous) equilibrium contact angle of the drops at the substrate. Please note that $\bar{\theta}(t)$ has been expressed as a function of the volume fraction of the species and the equilibrium angles ($\theta_{1,eq} = \theta_{PVAc,eq}$ and $\theta_{2,eq} = \theta_{PMMA,eq}$) made by the drops of the pure (unmixed) liquids (PMMA and PVAc) on silicon (Si/SiO_2). The values of $\theta_{1,eq} = \theta_{PVAc,eq}$ and $\theta_{2,eq} = \theta_{PMMA,eq}$ have been obtained from the literature and have been provided in Table 4.1. A few studies have shown such linear variation of the contact angle with the volume fraction of the species.[187-189] In the absence of measurement of the exact variation of the contact

angle, which the PMMA/PVAc blend (or mixture) makes with the substrate, with the volume fraction of the individual polymeric material (PMMA or PVAc), such a linear variation assumption has been incorporated.

The different parameters used in this study have been listed in Table 4.1.

Parameter	Definition	Value	Reference
ρ_1	Density of the polymeric liquid-1	1191 [kg/m^3]	[190]
ρ_2	Density of the polymeric liquid-2	1180 [kg/m^3]	[191]
ρ_3	Density of air	1.205 [kg/m^3]	[184]
m_1	Consistency index of polymeric liquid – 1	14.58	[192]
n_1	Power law index of polymeric liquid – 1	0.365	
m_2	Consistency index of polymeric liquid – 2	1.629	[193]
n_2	Power law index of polymeric liquid – 2	0.6344	
μ_3	Dynamic viscosity of air	1.82 x 10^{-5} [Pa.s]	[184]
σ_1	Liquid-air surface tension of polymeric liquid – 1	40.72 [mN/m]	[194]
σ_2	Liquid-air surface tension of polymeric liquid – 2	44.5 [mN/m]	[195]

$\theta_{1,eq}$	Contact angle of polymeric liquid-1 with substrate	38°	[194]
$\theta_{2,eq}$	Contact angle of polymeric liquid-1 with substrate	60.8°	[196]
D_{12}	Diffusivity of the liquid species 1 in liquid species 2	6.1 $\times 10^{-8}[m^2/s]$	[178]
R	Radius of the drops	10 [μm]	
d	Distance between the drop center	25 [μm]	

Table 4.1: List of parameters used in the simulation.

4.2.2.4 Multiphase interface-capturing technique:

There are several interface-tracking methods including the VOF method (used in this study), level set method, moving mesh method, and phase-field method, with each having its own sets of limitations and advantages. For instance, the level set (LS) method of interface tracking is comparatively simple to handle and has the ability to handle large topological changes. It can also provide a reasonably sharp interface. However, the key limitation of the LS method is that it has serious issues in ensuring mass conservation,[194] and modifications, such as imposition of constraints[195] (re-distancing constraint), reduction of spatial discretization errors,[196] use of re-initialization,[197-198] and employment velocity extension techniques, have been employed to correct that.[199] On the other hand, moving mesh interface tracking has the ability to provide a very sharp interface as the interface is captured by means of a physical domain interface. However, in addition to being computationally expensive, this method also has the problem with handling large deformations as that would destroy the mesh quality. There are other techniques such as automatic remeshing and adaptive refinement that are used with moving mesh to help with this issue of large deformation. Hack *et al.*,[141] for instance, used moving mesh (or Lagrangian-Euler technique) method to capture the coalescence behavior of droplet in mid-air with mesh reconstruction (automatic remeshing). However, it becomes increasingly difficult to capturing the coalescence event for two highly wetting and spreading droplets coalescing with each other on a surface that is highly philic to both the drops. On the other hand, the VOF technique, which uses the implicit interface tracking technique, has no mass-conservation issue and can handle substantially large deformation with ease. Of course, with the VOF method, there are problems such as the generation of diffuse interface

and spurious currents. Numerical techniques using flux limiters like MULES and artificial compression velocity are typically used to obtain a sharp interface.[179-182] Furthermore, discretization techniques like Gauss interfaceCompression techniques and the use of limiting timesteps based on criteria like Brackbill condition (t_B), Galusinski and Vigneaux constraint, etc. help us avoid the issue of spurious currents in this technique.[180,200,201]

4.3 Results and Discussions

In this study, we numerically investigate the multi-material coalescence of two identical sized drops of different (but miscible), shear-thinning, power law-obeying polymeric materials. We consider one drop of PVAc and another drop of PMMA (the detailed properties of the two drops have been provided in Table 4.1). In order to fully understand such coalescence, we track (1) the time variation of the velocity distribution inside the coalescing drops, (2) the progression of the mixing front, and (3) the extent of solutal-Marangoni-convection-induced lateral motion of the drops. Before discussing the main results, we shall like to point out that we have validated our numerical model by comparing the findings from our model with that provided in the numerical study by Borcia and Bestehorn[140] (please see discussion above Fig. C2 in section C2 of the Appendix C for the details). Additionally, we have provided a validation of our model by numerically reproducing the time-dependent drop profiles (occurring during the coalescence of 45% 1,2-butanediol/water mixture and 28% 1,2-butanediol/water mixture) and comparing these numerically obtained drop profiles against the corresponding experimental results of Karpitschka and Riegler.[136] The comparison has been provided in Fig. C4 in Appendix C and these two liquids (namely, 45% 1,2-butanediol/water mixture and 28% 1,2-butanediol/water mixture) have a surface tension difference of 4 mN/m. The comparison reveals a reasonable match between the numerical and experimental results, which substantiates the validity of our numerical framework.

4.3.1 Velocity distribution inside coalescing and mixing droplets

First, we study the time variation of the velocity distribution inside the spreading, coalescing, and mixing droplets (of two different, but miscible liquids) from the time at which the individual droplets come in contact with the solid substrate (see Fig. 4.2). The substrate is "philic" to both the droplets, leading to an onset of spreading immediately after the drops come in contact with the substrate. The substrate is more philic to PVAc drop ($\theta_{PVAc,eq} = \theta_{1,eq} = 38^0$) than the PMMA drop ($\theta_{PMMA,eq} = \theta_{2,eq} = 60.8^0$): hence the PVAc drop spreads faster than the PMMA drop [see Figs. 4.2(a,b)]. Of course for both the drops, at a given time instant during the early stages of spreading (e.g., at a time $t = t_{-2} = 5\ \mu s$ or t^*_{-2} = 0.948; here and everywhere else $t_i{}^* = t_i/t_c$, where t_c is the capillary time scale as defined in the caption of Fig. 4.2), the velocity vectors (at the central part of the drop) are directed downwards towards the substrate, while all the velocity vectors in the vicinity of the three-phase contact line (TPCL) are directed towards the corresponding TPCL. This confirms the spreading event: the liquid from the central part of the drop moves towards the TPCL accomplishing the spreading. As time proceeds, the rate of spreading for a given drop slows down, as evident by the smaller magnitude of the average velocity of the liquid moving towards the TPCL.

As the two drops continue to spread (at different rates), the drops eventually come into contact with each other and start to coalesce and mix before they could attain equilibrium. This happens since $d < (a_1 + a_2)$, where d is the initial center to center distance between the drops, and a_1 and a_2 are the equilibrium spreading radii of the drops 1 and 2, respectively. This coalescence event, which effectively starts at $t = t_0 = 20\ \mu s$ ($t_0^* = 3.792$) [see Fig. 4.2(c)] lead to the disappearance of the TPCLs (one part of the TPCLs) of

the coalescing drops. Immediately after the drops have coalesced, at this coalesced zone, liquids 1 and 2 mix into one another (since the drops are miscible); on the other hand, at the non-coalesced TPCLs, the drops continue to spread and wet the unwetted solid. Like the case of the coalescence of two identical material drops (see Refs. 105,106,116,132-133), here too, the coalescence proceeds by the growth of a bridge: the only difference in the present case is that there is mixing between the two liquids occurring at the region where the bridge develops. Such mixing leads to the development of a mixing front, which gets displaced over time, as will be discussed in detail below.

Here, we describe the post-coalescence fluid flow inside each of the two drops and the resulting dynamics of the mixing front. As the two miscible drops start to interact and mix (by diffusing into one another), there develops this mixing front. This mixing front characterizes the mixing zone. In other words, if we define a parameter ϕ such that $\phi = \frac{\alpha_2-\alpha_1}{\alpha_1+\alpha_2}$ (where α_1 and α_2 are the volume fractions of liquids constituting drop-1 and drop-2, respectively), a region with $\phi \rightarrow 0$ (from either a negative value or a positive value) grows around the mixing front. Over time, the area of this zone around the interface that has $\phi \rightarrow 0$ increases, implying the attainment of near complete mixing (to be discussed later).

At a time $t=t_1$ (where $t_1>t_0$, but the difference between t_1 and t_0 is small, i.e., $t_1=25$ μs or $t_1^*=4.74$, while $t_0=20$ μs or $t_0^*=3.792$) [see Fig. 4.2(d)], very much like at $t=t_0=20$ μs, we find that for both the drops, wetting interactions dominate at the non-coalesced TPCL (making the drops spread and wet the unwetted solid at their non-coalesced ends), while at their coalesced ends they undergo mixing. In addition, we find distinct advection (as indicated by the velocity vectors in the mixing zone) of one liquid into the other, which

eventually leads to the advection of the mixing front (discussed later). We would like to explore here the forces/influences experienced by the different drops that lead to such advection [see the schematic in Fig. 4.3]. Obviously, at the non-coalesced ends of the two drops, spreading effects dominate ensuring that the corresponding velocity vectors are associated to spreading effects (and hence denoted as $v_{sp,1}$ or $v_{sp,2}$). On the other hand, at the coalesced ends, both the drops experience advection due to (1) the Marangoni force (caused by the surface tension gradient enforcing a tendency to move towards the liquid-2 that is of greater surface tension) and (2) the residual kinetic energy present in both the spreading drops stemming from the fact that their spreading haven't completed at the time when they start to coalesce. At the coalescing end, the residual kinetic energy and the capillarity fills up the "bridge" from both the sides of the mixing front and the Marangoni asymmetrically moves the liquid mass towards one direction, just as reported by the experimental works by Karpitschka et al. and Borcia et al.[150,151] A number of studies exploring the effects of reduced surface tension $\left(\Delta\bar{\sigma} = \frac{(\sigma_1-\sigma_2)}{(\sigma_1+\sigma_2)/2}\right)$ difference of miscible Newtonian drops has shown "rapid coalescence" rather than a delayed quasi-stationary coalescence at lower values of $\Delta\bar{\sigma}$.[136,149,202-205] This is consistent with the "rapid coalescence" observed in our study with $\Delta\bar{\sigma}$~0.088 (using the surface tension values of PMMA and PVAc, see Table 4.1). For the ease of representation, velocity components associated with the Marangoni force and the residual kinetic energy are denoted as $v_{Mar,1}$ and $v_{res,1}$ for drop-1 and $v_{Mar,2}$ and $v_{res,2}$ for drop-2. It is intuitive that $v_{res,1}$ ($v_{res,2}$) is from left to right (right to left), since the residual kinetic energy of drop 1 (drop 2) will advect liquid of drop-1 (drop-2) in the coalescing zone from left to right (right to left). On the other hand, both $v_{Mar,1}$ and $v_{Mar,2}$ is from left to right, given that liquid 2 (PMMA) has a

higher surface tension than liquid-1 (PVAc) and the Marangoni forces drive liquid from low to high surface tension regions. Under these circumstances, the liquid of drop-1 will be advected from left to right in the mixing zone (this advection is aided by both $v_{res,1}$ and $v_{Mar,1}$). On the other hand, the larger magnitude of $v_{res,2}$ (given the fact that the drop-2 is still at early stages of spreading when the coalescence starts, see above) implies that the liquid of drop-1 will be advected from right to left in the mixing zone (despite $v_{Mar,2}$ being from left to right). In fact, $v_{res,2}$ is so high that in the coalescence (or mixing) zone, the extent of right-to-left motion of the liquid of drop-2 overwhelms the left-to-right motion of the liquid of drop-1, thereby ensuring that the mixing front moves from right to left (discussed later).

At a later time, $t=t_2$ (t_2=35 μs or t_2^*=6.635) [see Fig. 4.2(e) and Fig. 4.3(c)], the spreading forces on the non-coalesced end of drop-1 have nearly vanished (since the drop is very close its equilibrium condition). Such vanishing of the spreading forces also signals the disappearance of the $v_{res,1}$ (associated with the residual kinetic energy due to the onset of coalescence before the spreading has ceased) experienced by the liquid of drop-1 at the coalescence zone. Therefore, at this instant of time, the Marangoni convection forces (resulting at the coalescing end of the drop-1), which drive the liquid in drop-1 from left to right at the coalescing end of the drop-1 (as discussed above), become the dominant driving force for the liquid of drop-1 and drives the flow inside the entire drop-1 [see Fig. 4.2(e) and Fig. 4.3(c)]. Hence, we find that throughout the entire drop-1, the velocity vectors are directed towards drop-2 (i.e., from left to right). On the other hand, for drop-2, even at $t=t_2$, the wetting interactions remain significant at the non-coalesced end of drop-2 (since drop-2 is still significantly away from reaching equilibrium contact angle at the non-coalesced

end). Therefore, at this non-coalesced end of drop-2, the velocity vectors are entirely associated with the spreading effects (and hence denoted as $v_{sp,2}$) [see Fig. 4.2(e) and Fig. 4.3(c)]. This also signals that $v_{res,2}$ (associated with residual kinetic energy associated with incomplete spreading), driving the liquid of drop-2 from right to left remains large at the zone of the coalescence. Therefore, similar to the case at $t=t_1$, at $t=t_2$ as well, the liquid of drop-2 moves from right to left (due to the dominant influence of $v_{res,2}$ as compared to $v_{Mar,2}$) and the extent of the motion (right to left) of liquid of drop-2 overwhelms the extent of motion (left to right) of liquid of drop-1, thereby enforcing the right-to-left movement of the mixing front [see Fig. 4.2(e), Fig. 4.3(c)]. Very similar fluid flows inside drop-1 and drop-2 are observed even at a further later time instant, i.e., at $t=t_3=50\ \mu s$ or $t_3^*=9.479$ [see Fig. 4.2(f) and Fig. 4.3(d)].

Finally, at very late stages of the coalescence/mixing process, namely at $t=t_4=625\ \mu s$ or $t_4^*=118.49$ [see Fig. 4.2(g)], the spreading interactions of drop-2 become insignificant (i.e., drop-2 reaches to near equilibrium conditions). This is confirmed by the fact that the instantaneous contact angle at the non-coalescing end (NCE) of both the drops [discussed later] at time $t = t_4$ is very close to the corresponding equilibrium contact angles of the two pure drops. The evolution of the instantaneous contact angle over time will be discussed in detail later. This also signals that the effect of $v_{res,2}$ in driving the liquid of drop-2 in the coalescence zone becomes negligible. Therefore, only Marangoni effects now dictate the fluid flow inside both the drops. Of course, for the entire system, the location of the highest surface tension is within drop-2 at farthest possible distance from the mixing (coalescence) zone: this stems from the fact that in the vicinity of the coalescence zone, the mixing between the two drops decreases the surface tension near this location, and

therefore the higher surface tension of the unmixed drop-2 should be deep inside drop-2 at significant distances away from the mixing zone. As a consequence, liquids from both the drops will be directed towards this location: hence all the velocity vectors inside liquid drop-1 and the majority of the velocity vectors inside liquid drop-2 are directed towards this location (i.e., directed from left to right) [see Fig.4.2(g) and Fig. 4.3(e)]. This also implies that the mixing front between the two drops now moves from left to right (discussed later). Very similar fluid flows inside drop-1 and drop-2 are observed even at a further later time instant, i.e., at $t=t_5$=2000 μs or t_5^*=379.17 [please see Fig. 4.2(h) and Fig. 4.3(f)].

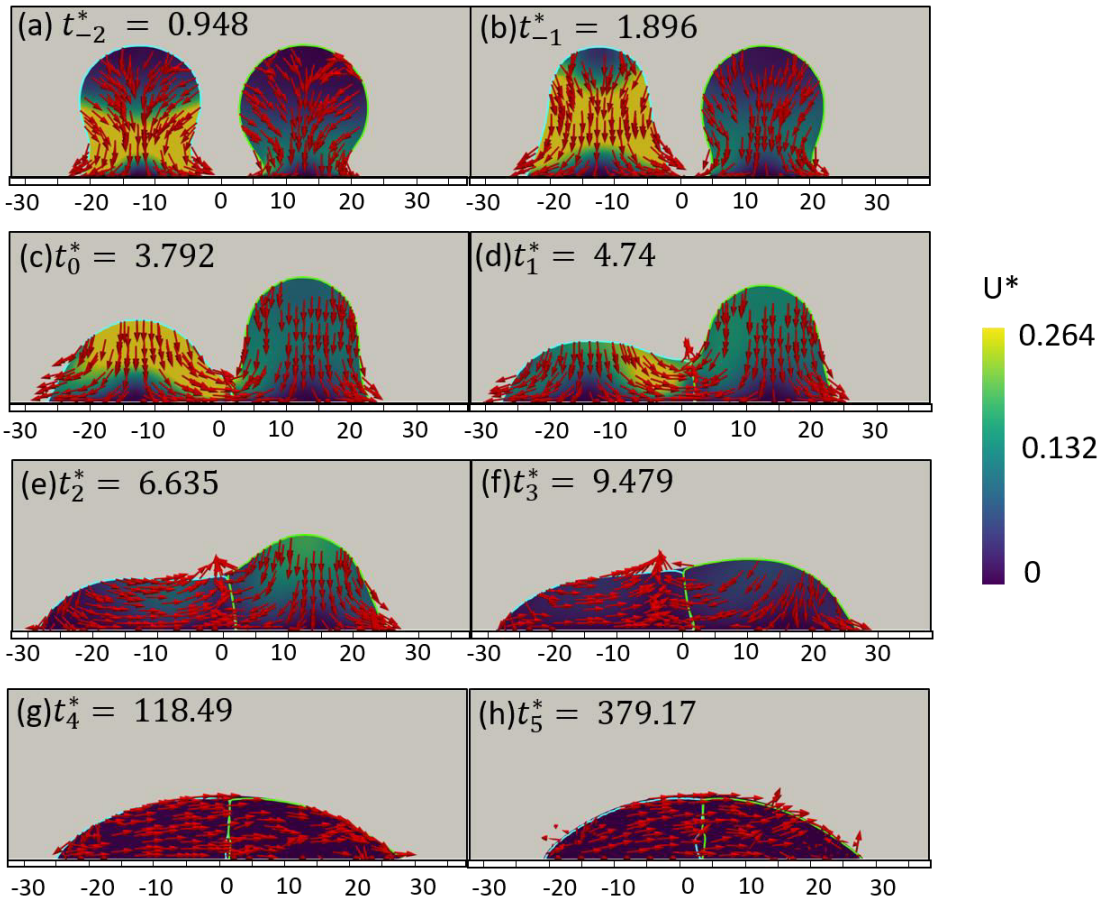

Figure 4.2*:* Dimensionless velocity distribution inside the coalescing dissimilar polymer droplets across the y-z plane that passes through x = 0 at different time instances (from the moment of impact), i.e., at (a) $t = t_{-2} = 5\ \mu s$ or $t^*_{-2} = 0.948$, (b) $t = t_{-1} = 10\ \mu s$ or $t^*_{-1} = 1.896$, (c) t = $t_0 = 20\ \mu s$ or t^*_0=3.792, (d) $t = t_1 = 25\ \mu s$ or $t^*_1 = 4.74$, (e) $t = t_2 = 35\ \mu s$ or $t^*_2 = 6.635$, (f) $t = t_3 = 50\ \mu s$ or $t^*_3 = 9.479$, (g) $t = t_4 = 625\ \mu s$ or $t^*_4 = 118.49$, and (h) $t = t_5 = 2\ ms$ or t^*_5=379.17. Please note that here "t" with a subscript "0" refers to the time when the coalescence starts: time instants before that time are denoted with "t" with a negative subscript (e.g., t_{-2} or t_{-1}), while time instant after that time are denoted with "t" with a positive subscript (e.g., t_1 or t_2 or t_3 or t_4 or t_5). Size of the velocity vectors shown inside the drops do not represent the velocity magnitude: these vectors

simply denote the direction of the flow. Velocity magnitude is represented by the color bar. U^* and ${t_i}^*$ represent the dimensionless velocity and time respectively. Here $U^* = U/U_c$, and ${t_i}^* = t_i/t_c$, where $U_c = R/t_c$ is the characteristic velocity scale and $t_c = \sqrt{\frac{\bar{\rho}R^3}{\bar{\sigma}}}$ is the capillary timescale. Here, $\bar{\rho} = (\rho_1 + \rho_2)/2$ and $\bar{\sigma} = (\sigma_1 + \sigma_2)/2$. Axes shown in the figure are in μm.

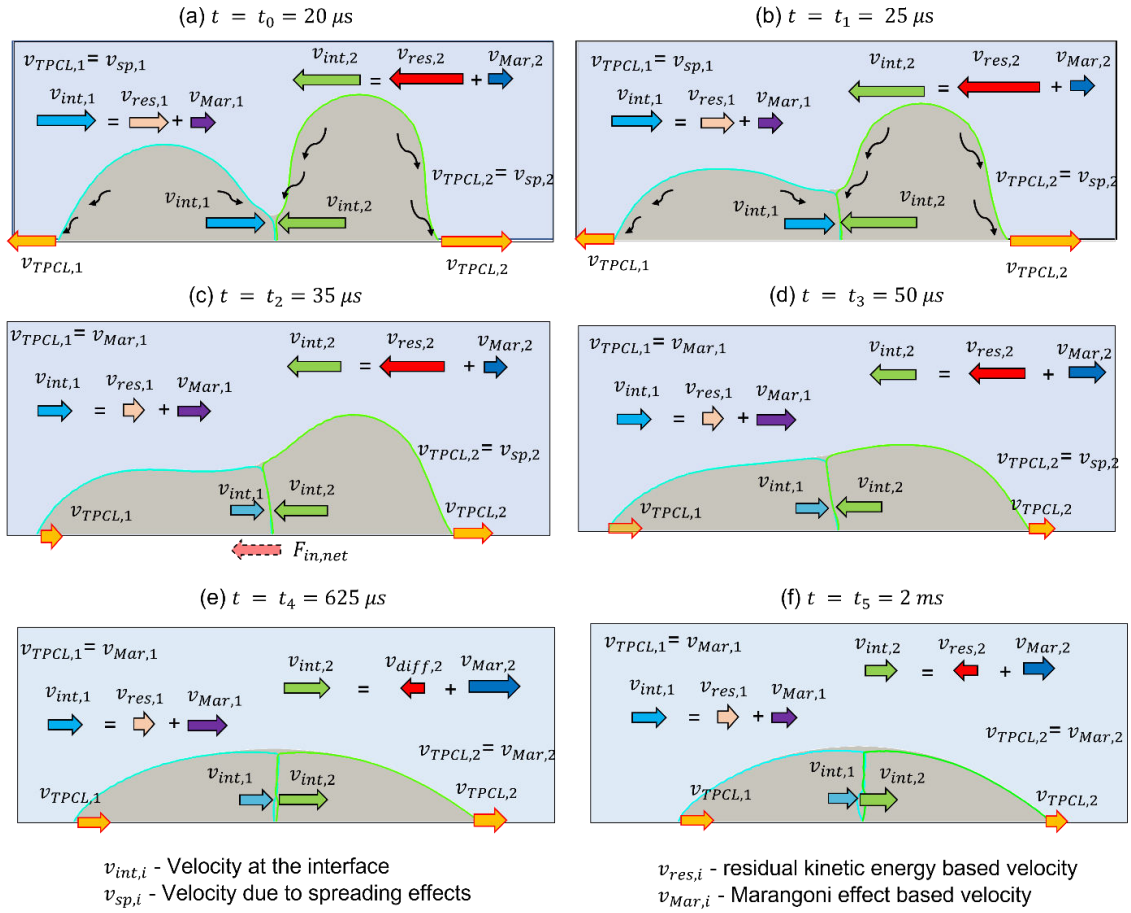

Figure 4.3*:* Schematic showing the velocity at different locations of the coalescing drops at different time instants. The length of the arrow qualitatively describes the magnitude of the velocity.

Next, in Fig. 4.4 we present the same velocity distribution and velocity vectors inside the drop, but now across the x-y plane at a height of $z = 1\ \mu m$ at various time instances. Figs. 4.4(a,b) depict the pre-coalescence stages during the drop motion. As expected, we find that for both the drops, the velocity magnitude is maximum near the liquid-air interface (i.e., at radial locations farthest from the centers of the drops). This is expected since the TPCL of the individual drops have the highest velocities after the drops impact the (hydrophilic) substrate: the motion of the air-water interface is indicative of this rapid spreading motion of the TPCL. At time $t = t_0 = 20\mu s$ ($t_0^* = 3.792$), the spreading droplets start to interact/coalesce/mix with each other [see Fig. 4.4(c)]. Subsequently, at different time instants, we find different factors dominating the liquid motion inside the two drops leading to different directions of the fluid flow at different sections of a given drop. As already explicated while discussing Fig. 4.2, at $t=t_1=25\ \mu s$ or $t_1^*=4.74$, we find that (i) dominating wetting interactions ensure velocity vectors near the non-coalescing TPCL being directed towards the TPCL for both the drops, (ii) a combination of Marangoni effect and the effect associated with residual kinetic energy (caused by the spreading being incomplete at the time of coalescence) ensures velocity vectors in the region of coalescence in drop-1 being directed towards drop-2, and (iii) a dominating residual kinetic energy driven velocity field ensures velocity vectors in the region of coalescence in drop-2 being directed towards drop-1 [see Fig. 4.4(d)]. Next at $t=t_2=35\ \mu s$ or $t_2^*=6.635$ as well as $t=t_3=50\ \mu s$ or $t_3^*=9.479$, we find that (i) the vanishing effect of the spreading forces and the dominating influence of the Marangoni forces ensure velocity vectors inside the entire drop-1 being directed towards drop-2 and (ii) a dominating residual kinetic energy driven velocity field ensures that the velocity vectors in the region of coalescence in drop-2 being

directed towards drop-1 [see Figs. 4.3(e,f)]. Finally, at $t=t_4=625\ \mu s$ or $t_4^*=118.49$ as well as $t=t_5=2000\ \mu s$ or $t_5^*=379.17$, we find that the dominating influence of the Marangoni forces ensure that for both the drops, the velocity vectors are directed from left to right (i.e., towards the location of the highest surface tension, which is deep within drop-2 at farthest possible distance from the interface) [see Figs. 4.4(g,h)].

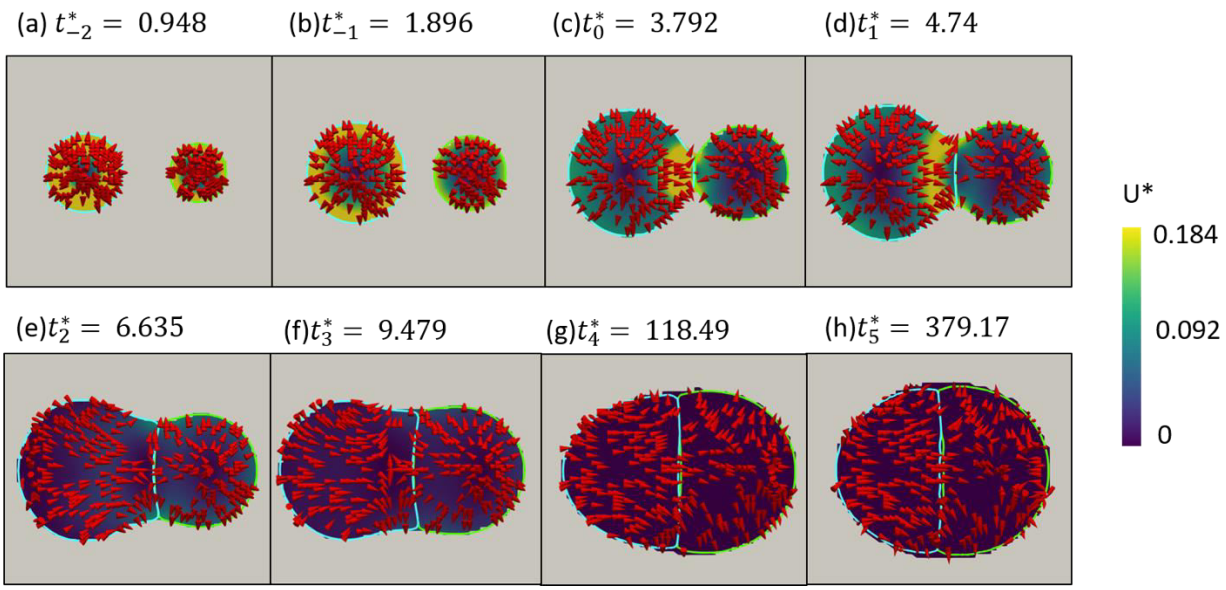

Figure 4.4*:* Dimensionless velocity distribution inside the coalescing dissimilar polymer droplets across x-y plane that passes through $z = 1\ \mu m$ at different time instances (from the moment of impact), i.e., at (a) $t = t_{-2} = 5\ \mu s$ or $t^*_{-2} = 0.948$, (b) $t = t_{-1} = 10\ \mu s$ or $t^*_{-1} = 1.896$, (c) $t = t_0 = 20\ \mu s$ or t^*_0=3.792, (d) $t = t_1 = 25\ \mu s$ or $t^*_1 = 4.74$, (e) $t = \mathrm{t}_2 = 35\ \mu s$ or $t^*_2 = 6.635$, (f) $t = \mathrm{t}_3 = 50\ \mu s$ or $t^*_3 = 9.479$, (g) $t = t_4 = 625\ \mu s$ or $t^*_4 = 118.49$, and (h) $t = t_5 = 2\ ms$ or t^*_5=379.17. Size of the velocity vectors shown inside the drops do not represent the velocity magnitude: these vectors simply denote the direction of the flow. Velocity magnitude is represented by the color bar. U^* and ${t_i}^*$ represents the dimensionless velocity and time respectively. Here $U^* = U/U_c$, and ${t_i}^* = t_i/t_c$, where $U_c = R/t_c$ is the characteristic velocity scale and $t_c = \sqrt{\frac{\bar{\rho}R^3}{\bar{\sigma}}}$ is the capillary timescale. Here, $\bar{\rho} = (\rho_1 + \rho_2)/2$ and $\bar{\sigma} = (\sigma_1 + \sigma_2)/2$.

So far, we have discussed the fluid flow inside the drops and have qualitatively described the evolution of the mixing front at the coalescing end (CE) of the drops and the three-phase-contact-line dynamics at the non-coalescing end (NCE) of the drops using the velocity vectors. In Fig. 4.5, we quantify the evolution of the mixing front by plotting the evolution of the instantaneous (a) contact angles at the non-coalescing end (NCE) of the two drops, (b) non-dimensional height (H/R) of the mixing front (formed at the coalescing end), (c) non-dimensional width (W/R) of the mixing front (formed at the coalescing end).

In Fig. 4.5(a), the contact angle of both drop-1 and drop-2 are found to first gradually decrease towards their respective equilibrium angle ($\theta_{1,eq} = 38°, \theta_{2,eq} = 60.8°$). Drop-2 attains its equilibrium angle a little later than drop-1 owing to its larger viscosity (especially at higher shear rates). The line corresponding to $t = t_4$ shown in Fig. 5(a) denotes the condition when the Marangoni effect starts to dictate the flow inside both the drops [see discussions of Fig. 4.2(g) and 4.3(e)]; interestingly, this time also denotes the attainment of near θ_{eq} at the NCE of both the drops. Beyond t=t_4, the mixing region grows and the liquid near the NCE of both the drops are no longer the pure liquids: as a result, the contact angles at the NCEs of the two drops start to go beyond their corresponding θ_{eq}. It is to be noted that the instantaneous contact angles of the drops would depend on the material concentration at locations near the NCE (non-coalesced end) of the drops. As the mixing induced change in the material concentration at the NCE occurs only at a much later time owing to the distance of the NCE from the mixing zone, the contact angle gets affected by the mixing process only after t = t_4. This implies that the contact angle at the NCE of drop 1 increase (becomes more than $\theta_{eq,1}$), while the contact angle at the NCE of drop 2 decreases (becomes smaller than $\theta_{eq,2}$). Eventually, we see that the near

complete mixing ensures that the contact angle at the NCEs for the both the drops saturate around a similar value (~49^0).

In Fig. 4.5(b), the growth of the non-dimensional height (H/R) of the mixing front at the CE is shown [(here *R* is the radius of the original drops, please see Fig. 4.1(a)]. We clearly observe two distinct regimes. The early regime (approximately till $t = t_4$) shows a rapid growth owing to the rapid mass influx from both sides of the mixing front. This regime shows a scaling of $\frac{H}{R} \sim \left(\frac{t}{t_c}\right)^2$. In the late regime, we do not observe any significant growth of the interfacial height (H).

Similarly, in Fig. 4.5(c), we observe two regimes of growth for the width (*W*/*R*) of the mixing front at the CE [(here *R* is the radius of the original drops, please see Fig. 4.1(a)]. The early regime shows a rapid growth of the non-dimensional width with a scaling of $\frac{W}{R} \sim \left(\frac{t}{t_c}\right)^{3/2}$. Such a growth is due to the rapid mass influx towards the mixing front. In the later stage, the growth is much slower with a scaling of $\frac{W}{R} \sim \left(\frac{t}{t_c}\right)^{1/13}$.

For the coalescence of identical Newtonian[99-103] or polymeric drops (non-Newtonian),[116132,133] where the coalescence is probed by studying the time evolution of the height and width of the "bridge" formed by the interacting drops (in the present study, the growths of the height and the width of the diffusion front are serving this purpose of quantifying the evolution of the coalescence process), such qualitatively fast (slow) growth of the height and width of the coalescing bridge at early (late) stages of coalescence is routinely noted.

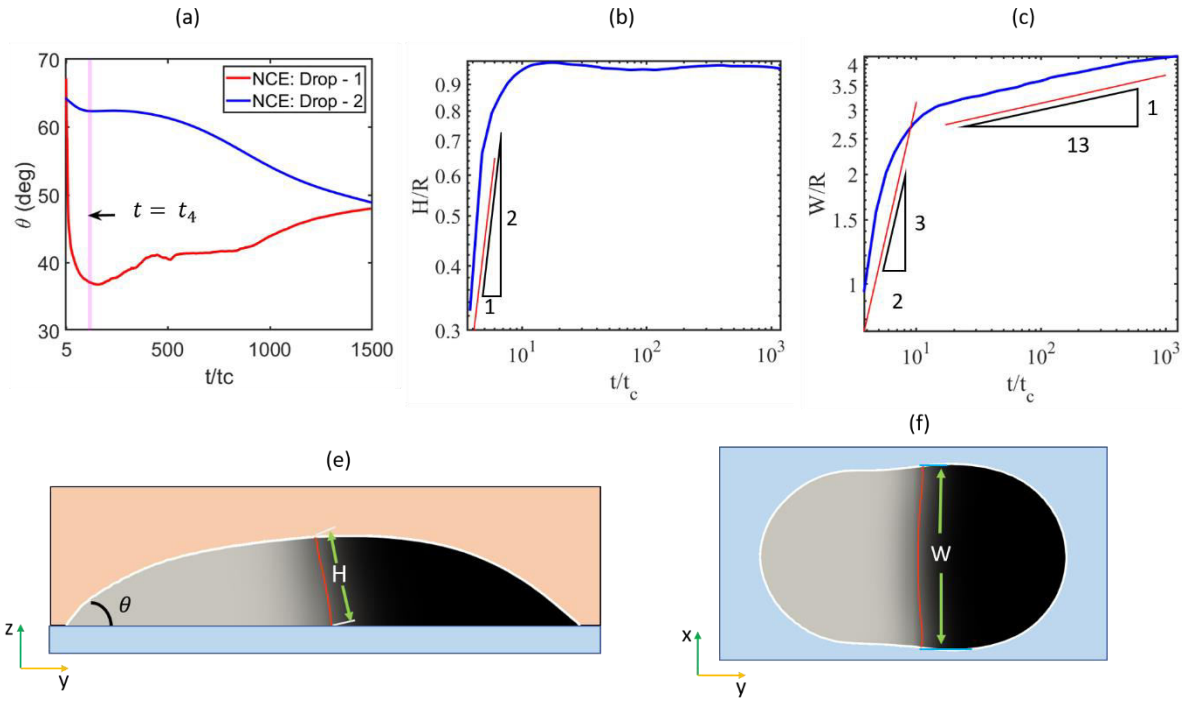

Figure 4.5: Time evolution of the instantaneous (a) contact angles at the NCE, (b) non-dimensional height (H/R) of the mixing front at the CE (c) non-dimensional width (W/R) of the mixing front at the CE. (e-f) Schematic representation of the front view (y-z plane at x=0), and top view (x-y plane at z = 0) of the coalescing drops showing the instantaneous contact angle (θ), height (H), and width (W) of the mixing front at the coalescing end (CE). The mixing front height and width reported are the end-to-end distance between the two ends as shown in Figs. 4.4(e-f). In all the figures, we consider dimensionless time t/t_c, where t_c has been defined in the caption of Fig. 4.2.

4.3.2 Mixing Inside Coalescing Droplets

After understanding the manner in which the drop-drop interactions trigger the changes in the liquid dynamics inside the two drops as well as the dynamics of the mixing front, we next aim to quantify the mixing triggered by such drop-drop interactions. Such mixing effect is explored in two stages. At first, we try to understand the manner in which the drop-drop interactions separately affect the time dependent spatial variation of the polymer concentrations (volume fraction) inside drop-1 and drop-2. The plots (see Fig. 4.6) provide the variation of this volume fraction (α_1 and α_2; $\alpha_1 = 1$ represents pure and unmixed drop-1, while $\alpha_2 = 1$ represents pure and unmixed drop-2) across the y-z plane at the drop center (x = 0) at various time instants. At time $t = t_0 = 20\ \mu s$ ($t_0^* = 3.792$), the interaction between the drop starts and mixing starts to happen leading to the formation of the drop-drop interface and an emergence of spatial locations (in the vicinity of the interface) where $\alpha_1 < 1$ and $\alpha_2 < 1$. As time progresses, mixing becomes more pronounced as evidenced by a continuously increasing darkened area in drop-2 and lightened area in drop -1 (areas corresponding to $\alpha_1 < 1$ and $\alpha_2 < 1$) around the mixing front [see Figs. 4.6(d-g)]. This growing region of mixing eventually fills the entire drop ensuring the polymer concentration becomes identical everywhere and the final *single* drop that has resulted from the coalescence becomes a homogeneous one.

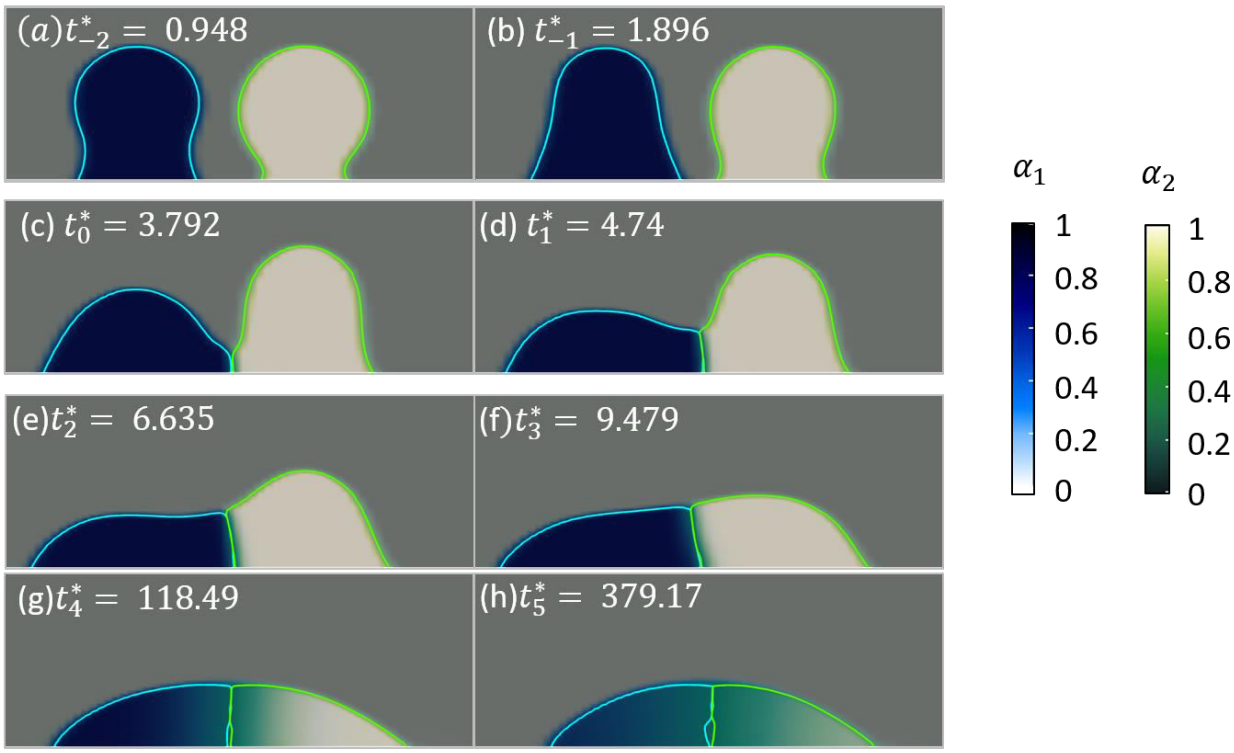

Figure 4.6: Distribution of the volume fraction of the two liquid phases across the y-z plane that passes through x = 0 at different time instants (from the moment of impact), i.e., at (a) $t = t_{-2} = 5\ \mu s$ or $t^*_{-2} = 0.948$, (b) $t = t_{-1} = 10\ \mu s$ or $t^*_{-1} = 1.896$, (c) $t = t_0 = 20\ \mu s$ or t^*_0=3.792, (d) $t = t_1 = 25\ \mu s$ or $t^*_1 = 4.74$, (e) $t = \mathrm{t}_2 = 35\ \mu s$ or $t^*_2 = 6.635$, (f) $t = \mathrm{t}_3 = 50\ \mu s$ or $t^*_3 = 9.479$, (g) $t = t_4 = 625\ \mu s$ or $t^*_4 = 118.49$, and (h) $t = t_5 = 2\ ms$ or t^*_5=379.17. Here, α_1 and α_2 represents the volume fraction of the phase-1 and phase-2 respectively. Here $t^*_i = t_i/t_c$, where $t_c = \sqrt{\frac{\bar{\rho}R^3}{\bar{\sigma}}}$ is the capillary timescale. Here, $\bar{\rho} = (\rho_1 + \rho_2)/2$ and $\bar{\sigma} = (\sigma_1 + \sigma_2)/2$.

While Fig. 4.6 provides a qualitative sense of the onset and progression of mixing inside the coalescing drops, in order to present a more quantitative understanding of mixing (and the progression of the mixing front), we study the spatio-temporal variation (inside coalescing drops) of the parameter $\phi = \frac{\alpha_2 - \alpha_1}{\alpha_1 + \alpha_2}$ (see Fig. 4.7). Obviously, $\phi = -1$ represents locations purely consisting of drop – 1 material (PVAc), $\phi = 1$ represents locations purely consisting of drop-2 material (PMMA), and $\phi = 0$ represents the mixing front formed between the two drops. One can clearly see the manner in which over time the region for which $\phi \to 0$ increases around the interface, confirming the progressive enhancement of mixing. The motion of the mixing front ($\phi = 0$) is highly interesting (see Fig. 4.7, center). At first, the mixing front moves in the negative y-direction (i.e., right to left) from time instances $t = 25\ \mu s$ to $t = 125\ \mu s$ (as also outlined while describing Fig. 4.2). This is consistent with the iso-contours shown in the surrounding images. The same mixing front at the later stages of coalescence is found to move from left-to-right, since at such time instants Marangoni convection effects dominate the liquid motion inside both the drops directing the liquid flow towards a location deep inside drop-2 (farthest away from the mixing front) where the surface tension is highest [please see the discussions for Figs. 4.2(g,h)].

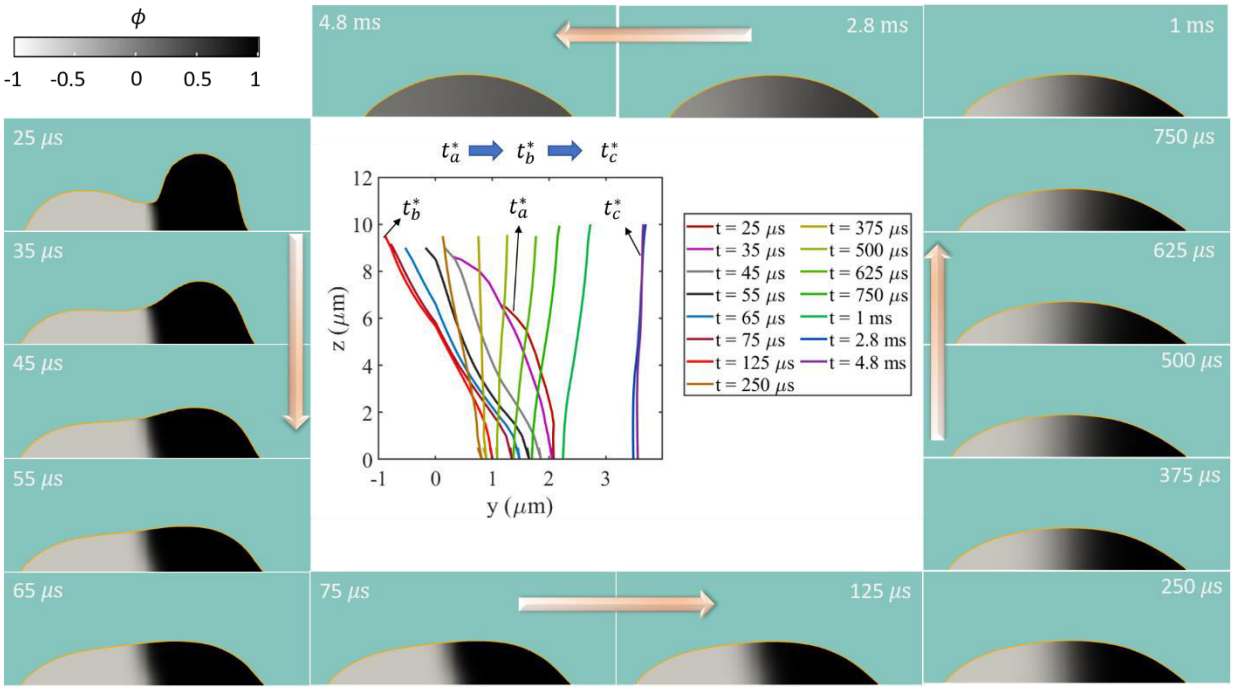

Figure 4.7: (Center) Time evolution of the mixing front ($\phi = 0$) in the y-z plane at the plane of drop center (x = 0). The subfigures surrounding this central figure provide the snapshots depicting the spatio-temporal variation of ϕ.

Finally, in Fig. 4.8, we show the time evolution of the growth of the mixing region which we define as a region bounded by $(-0.05 < \phi < 0.05)$. Of course, this upper and lower bounds can vary: we intentionally considered very small magnitude of these bounds to ensure that we are accounting for the regions with highest possible mixing. Technically, all the locations where $|\phi| \neq 1$, the phases are no longer pure, and can be considered as the mixing region. We specifically use the above threshold to quantify the region where the mixing process is more or less complete. The snapshots show a clear growth in the mixing region with time, owing to the interphase diffusion between the miscible phases. Although, we witness a gradual growth in the mixing region, the growth is significantly slower in the time range shown in Figs. 4.8(a) to 4.8(h) (until t = 250 μs) (i.e., when the influence of the Marangoni effects is relatively weak). Once the Marangoni convection becomes dominant in both the drops, the mixing region appears to grow much faster [see Figs. 4.8(i-p)]. At nearly 8 ms [see Fig. 4.8(p)], we clearly see that the entire drop seems to be completely mixed.

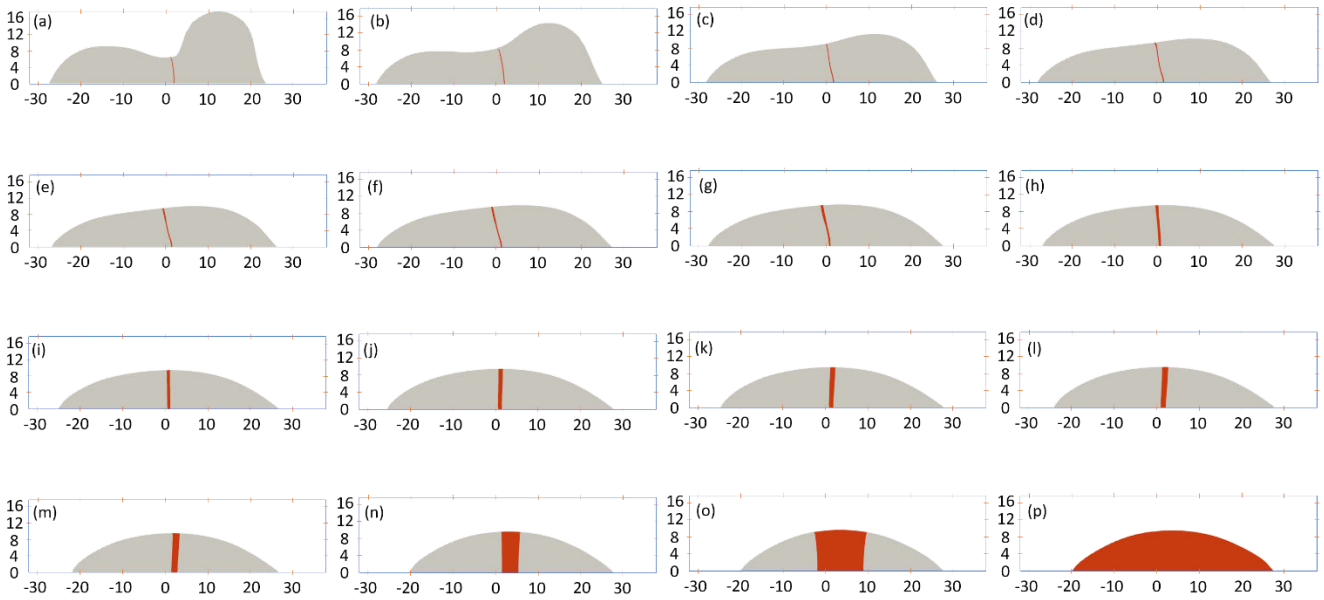

Figure 4.8: Time evolution of the mixing region defined as the area enclosed by ($-0.05 < \phi < 0.05$) in the y-z plane at the plane of drop center (x = 0) at various time instances: (a) 25 μs, (b) 35 μs (c) 45 μs (d) 55 μs (e) 65 μs (f) 75 μs (g) 125 μs (h) 250 μs (i) 375 μs (j) 500 μs (k) 625 μs (l) 750 μs (m) 1 ms (n) 2.8 ms (o) 4.8 ms (p) 8 ms. Axes shown in the figure are in µm.

4.4 Conclusions

In this work, we have analyzed the solutal-hydrodynamics of asymmetric three-dimensional coalescence of two polymeric shear-thinning liquid drops of different miscible materials with the drops originally being at a partially wetting configuration on a solvophilic (philic to both liquids) substrate. The results shed light on the dynamics of the coalescence process and identifies the factors driving the coalescence, the details of flow physics inside the coalescing drops, the evolution of the contact angles at the non-coalescing ends (NCEs) of the two drops, and the time variation of the height and the width of the interface formed by the two drops at their coalescing ends (CEs). We further track the evolution of the mixing front and the mixing region that provides us a clear understanding of the relative effects of the different factors in driving the mixing process. Our simulations provide key information that would significantly help in studying and designing miscible multi-material liquid systems, which will be crucial for applications such as inkjet or aerosol jet printing, lab on a chip, polymer processing, etc.

Multi-materials printing is expected to provide a pathway to next generation engineering of functionally graded materials (FGMs).[206-207] Additive manufacturing methods are already being applied to the fabrication of such FGMs but the understanding at the microscopic level, in terms of materials mixing and properties, is lacking. For example, materials mixing at the voxel level rather than simply changing materials voxel-to-voxel could ensure a very powerful ability of micro-manipulation at a small length scale (critical for the additive manufacturing of FGMs). Furthermore, this could help reduce or alleviate voxel level interfaces of dissimilar materials thus avoiding cracking and interface delamination phenomena. Currently FGM fabrication, as related to additive manufacturing,

has focused on standard 3D printers and materials mixing using syringe printing. To the authors knowledge, this current paper serves as one of the first studies on theoretical understanding essential for expanding the printing of FGMs into the realm of direct write printing employing inkjet and aerosol-jet printing methods.

Chapter 5: Coalescence of 3D polymeric drops in the presence of in-situ photopolymerization*

Abstract

In this chapter, we develop a combined numerical (using direct numerical simulation) and scaling model to study the dynamics of two identical photo-curable, shear-thinning polymeric drops undergoing spreading and coalescence (on a substrate) in presence of in-situ curing. Two separate cases are studied: (1) $\tau_s \ll \tau_p$ *(Case 1) and (2)* $\tau_s \sim \tau_p$ *(Case 2) (*τ_s *and* τ_p *represent the spreading and photo-curing timescales). Photo-polymerization-driven increase in the drop viscosity significantly delays the spreading and the coalescence events for case 2. Furthermore, for case 2, at any given time during the coalescence process, both the height and the width of the "bridge" that forms due to coalescence is always smaller than that for case 1. Our scaling analysis establishes three distinct regimes characterizing the bridge growth for both cases 1 and 2: the initial regime (viscous and capillary forces balance each other and the bridge growth rate is weak); the intermediate regime (inertia and capillary forces balance each other and the bridge growth rate is enhanced); and the late regime (viscous and capillary forces balance each other and the bridge growth rate is weak). Also, in regimes where viscous forces play a role (initial and late regimes), the bridge growth is weaker for case 2, while in the intermediate regime the rate of bridge growth is similar between cases 1 and 2. We also provide the temperature*

* Contents of this chapter is submitted as: V. S. Sivasankar, D. R. Hines, and S. Das, "Coalescence of 3D Polymeric Drops in the Presence of In-situ Photopolymerization". (Submitted to *Macromolecules*)

variation and the evolution of the curing front inside the coalescing drops for cases 1 and 2: the significantly rapid rate of polymerization for case 2 manifests in noticeable temperature drop, fast propagation of the curing front, and the fluid flow (associated with coalescence) affecting the migration of the curing front inside the coalescing drops. We anticipate that our study will be crucial in designing polymeric droplet based additive manufacturing systems and understanding the behavior of polymeric blends and polymeric emulsions.

5.1 Introduction

Coalescence of liquid drops in another fluid or while spreading on a solid substrate drives a large number of natural and technologically critical events such as cloud formation,[129] expansion of oil spills,[208] disruption of emulsions,[209,210] fabricating structures using droplet-based 3D printing (such as aerosol jet printing or inkjet printing),[211,212] etc. The fluid mechanics of drop coalescence has been extensively explored:[83,91,97,103,119,212-216] but most of these studies have focused on the coalescence of simple Newtonian drops. On the contrary, several of the applications identified above involve the coalescence of non-Newtonian polymeric drops. The physics of the coalescence of polymeric drops have only recently been started to be explored. For example, Kumar and co-workers, in multiple papers,[116,217] explored the coalescence dynamics of polymeric drops experimentally and provided the associated scaling calculations to explain the coalescence physics. In a separate set of studies, the present research group studied two variants of the polymeric drop coalescence problem numerically. In the first study,[132] the effect of finite impact speed on the post-impact coalescence of two polymeric drops of identical material (of same or different sizes) was investigated. In the second study,[218] the coalescence of two polymeric drops of different materials was probed. Other notable related works include the papers by Finotello *et al.*[117] and Verdier[118] (both these studies probe the polymeric drop coalescence in absence of a solid substrate), Dekker *et al.*,[219] Yue *et al.*,[220] and Pawar *et al.*[221] (these three papers consider the coalescence of *viscoelastic* drops), etc.

One important aspect of polymeric drop dynamics that has received very little attention is the effect of possible photo-curing (and the associated chemical reaction driven changes in the drop properties) during the drop dynamics. To the best of our knowledge,

the only study till date that has captured the detailed physics associated with the dynamics of polymeric drops with photo-curing (thereby changing the drop properties) has been our numerical study[222] probing the dynamics of the spreading of a photocurable, shear-thinning polymeric drop in presence *in-situ* curing (driven by ultra-violet or UV radiation). Our model captured UV-radiation-driven photo-curing and the associated chemical reactions, incorporated the effect of these reactions into the unsteady and flow-driven concentration distribution of the monomers and initiators (present inside the drop), and accounted for the change in drop viscosity and change in temperature on account of such photo-curing while modeling the spreading dynamics of the drop. Such fully coupled numerical model was the first of its kind and revealed the effect of photo-curing in drastically altering the spreading dynamics of the polymeric drop. Sung *et al.*[223] did report experimental results of the spreading of fast thermal curing single polymeric drops; of course, the study did not consider photo-curing, nor any theory was provided. Also, there have been studies that have probed the dynamics of polymeric drops with dynamically changing properties (e.g., spreading thermo-responsive polymeric drops probed by de Ruiter *et al.*[17]); however, the problem of the dynamics of polymeric drops undergoing photo-curing-driven chemical reactions have remained mostly unaddressed.

In this paper, we take our endeavor to study the dynamics of polymeric drops in presence of photo-curing driven chemical reactions one step forward: we study the *coalescence dynamics* of polymeric drops in presence of *in-situ* curing driven by UV radiation. Here the same set of equations as considered in our previous paper[222] have been used: however, instead of a single drop,[222] in this paper, we consider *the spreading and subsequent coalescence of two drops* in presence of *in-situ* curing. Like our previous

paper,[222] here too, we consider two separate cases. In Case 1, we consider $\tau_s \ll \tau_p$, while in Case 2, $\tau_s \sim \tau_p$. Here τ_s and τ_p refer to the drop spreading and drop curing (or drop polymerization) timescales. Hence for the case of $\tau_s \ll \tau_p$, given that the significant extent drop spreading and coalescence have occurred prior to any influence of photo-polymerization, the effect of *in-situ* curing on the drop coalescence dynamics will be relatively small. On the other hand, for the case of $\tau_s \sim \tau_p$, the photocuring effect is significant for the entire spreading and coalescence events ensuring that both the drop spreading and coalescence get significantly retarded (associated with the enhancement of viscosity caused by the polymerization). The most important result of this paper is the dynamics of the growth of the "bridge" characterizing the coalescence. For case 2, the significant increase in viscosity during coalescence ensures, at any given time, a reduced value of bridge height and width as compared to case 1. On the other hand, for both cases 1 and 2, we identify *initial* (viscous forces balance capillary forces), *intermediate* (inertial forces balance capillary forces), and *late* (viscous forces balance capillary forces) regimes dictating the bridge growth. The initial and late regimes are characterized by weak rates of bridge growth, while the intermediate regime sees a much-enhanced rate of bridge growth. However, for the initial and late regimes, given the dominant role of the viscous forces, the bridge growth rates are weakened for case 2, but for the intermediate regime, the bridge growth rate remains similar for both the cases. Interestingly, such *initial regime* (where viscous forces balance capillary forces) in bridge growth hasn't been explicitly mentioned in previous studies, although several experimental studies (particularly for high-viscosity liquids) have pointed out the presence of a regime (prior to the regime where inertial forces balance the capillary forces) where the bridge growth is significantly retarded (Ref. 133,

224). Also, the "early" regime considered by previous studies[83] on drop coalescence is the regime where the inertial forces balance the capillary forces and that is the "intermediate regime" for our case. We also study the corresponding time evolution of the temperature and curing profiles inside the drop. The exothermic nature of the curing reactions ensures that for case 2 (characterized by rapid polymerization), there is a substantial reduction of temperature at the beginning of the coalescence, while for case 1, the temperature reduction is insignificant. Finally, this fast curing for case 2 ensures that the curing front propagates very quickly inside the coalescing drops and gets influenced by the fluid flow inside the coalescing drops. Drop coalescence in the presence of *in-situ* is routinely encountered in applications where droplet-based 3D printing (e.g., AJ printing or inkjet printing) methods are employed to fabricate photo-curable polymer-based structures and components:[51,52,79,225-228] in such settings, the drops are deposited on the printing substrate in presence of *in-situ* curing and such curing-based solidification ensures a quick attainment of the desired shape of the polymer structure. Therefore, the present study, not only probes a novel type of drop dynamics event (coalescence of reactive polymeric drops), but also develops a framework better understand the droplet-based 3D printing of polymeric materials.

5.2 Theory and Simulation methods

In this study, we consider the coalescence of two identical shear-thinning, power law obeying, photo-curable polymeric liquid drops on a substrate to that is philic to the drops (the drops make an equilibrium contact angle is θ_{eq} on the substrate). The coalescence is considered to occur in presence of *in-situ* curing (or *in-situ* polymerization) driven by the application of ultra-violet (UV) radiation. The drops are each of radius R_0 and they are spaced apart by a center-to-center separation distance 'd' on the substrate (see Fig. 1). After coming in contact with the philic substrate, both the drops will start to spread and undergo coalescence. We choose the separation distance d such that $d < 2r_{eq}$, where r_{eq} is the equilibrium spreading radius of the drop on the chosen substrate (in the absence of *in-situ* curing): such a condition ($d < 2r_{eq}$) ensures that the spreading drops will coalesce regardless of whether there is an *in-situ* curing or not. The interaction between the two coalescing drops leads to the growth of bridge height (H_0) and the bridge width (W) [as shown in Fig. 5.1(a)] over time: the growth dynamics of the bridge (or the time variation of H_0 and W) get affected due to the presence of *in-situ* curing. In this paper, as discussed above, we shall consider two distinct cases – Case 1: $\tau_s \ll \tau_p$ and Case 2: $\tau_s \sim \tau_p$. For the case of $\tau_s \ll \tau_p$, given that the significant extent drop spreading and coalescence have occurred prior to any influence of photo-polymerization, the effect of *in-situ* curing on the drop coalescence dynamics will be relatively small. On the other hand, for the case of $\tau_s \sim \tau_p$, the photocuring effect is significant for the entire spreading and coalescence events ensuring that both the drop spreading and coalescence get significantly influence by *in-situ* curing.

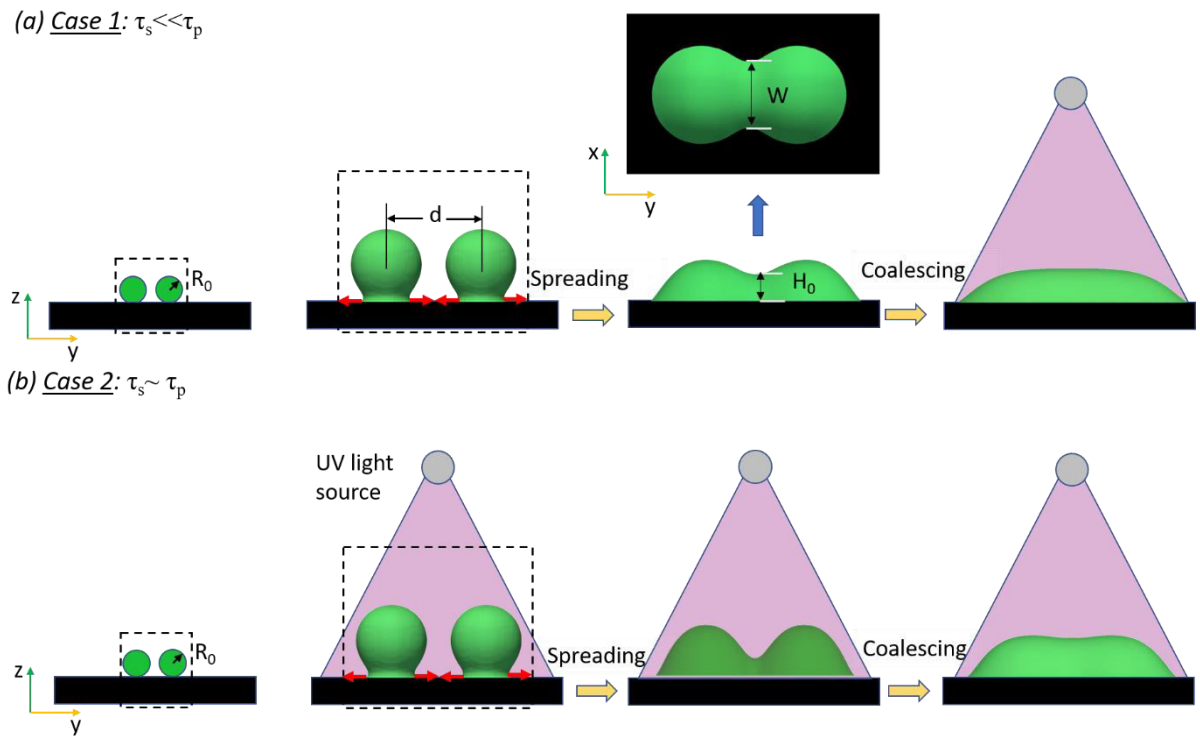

Figure 5.1: Schematic representing the droplet deposition in a typical droplet-based 3D printing process (of photopolymers) for two cases: (a) Spreading timescale (τ_s) is much smaller than the polymerization timescale (τ_p), and (b) Spreading timescale (τ_s) is comparable to the polymerization timescale (τ_p). Fig. 5.1(a) shows that the case - 1 is equivalent to turning on the UV-light source after near completion of spreading and coalescence of the drops. In Fig. 5.1(b), we can observe that the drop coalescence dynamics for case - 2 is significantly altered by the photopolymerization reaction. Here, d is the initial center-to-center distance between the drops of radius R_0. Also, in Fig. 5.1(a), H_0 represents the instantaneous bridge height, and W represents the instantaneous bridge width.

5.2.1 Simulation method

Direct Numerical Simulation (DNS) is employed to capture the 3D coalescence of the photocurable, polymeric drops in the presence of *in-situ* photopolymerization. We utilize the OpenFOAM-based volume of fluid (VOF) technique[161,162] to track the interface of the liquid-air interface and the surface tension effects. We developed our custom solver interCuringFoam based on the interFoam solver in the OpenFOAM framework to capture the solutal-thermo-hydrodynamics of the photocuring, coalescing drops.[229,230] OpenFOAM mesh generator is used to mesh the domain with 5625000 (150 x 150 x 250) hexahedral mesh cells.[121] The simulation domain is a rectangular box of size 100 μm x 100 μm x 100 μm.

5.2.2 Governing equations

5.2.2.1 Fluid flow: Continuity and Navier-Stokes equations:

In this study, we investigate the coalescence behavior of two shear-thinning, power-law-obeying, polymeric liquids of the same material in the presence of in-situ curing (elucidated in Fig. 5.1). In order to capture the interface of the spreading drop, we need to consider the multiphase fluid flow, which appropriately captures the flow inside the drop and the surrounding air. The velocity field (**u**) and pressure field (p) describing the fluid flow are obtained by solving the following governing equations:[161-162]

$$\frac{\partial \rho}{\partial t} + \boldsymbol{\nabla}.(\rho \boldsymbol{u}) = 0, \qquad (5.1)$$

$$\frac{\partial (\rho \boldsymbol{u})}{\partial t} + \boldsymbol{\nabla}.(\rho \boldsymbol{u}\boldsymbol{u}) = \nabla.[-p\bar{I} + \mu(\nabla \boldsymbol{u} + (\nabla \boldsymbol{u})^T)] + \rho \boldsymbol{g} + \boldsymbol{F}_\sigma. \qquad (5.2)$$

Here, a single set of equations is solved for the different phases, and the fluid properties [namely, density (ρ) and viscosity (μ) of the fluid] at each location are calculated based on a scalar function α which describes the volume fraction of the liquid phase:[229]

$$\rho = \alpha\rho_1 + (1-\alpha)\rho_2, \qquad (5.3)$$

$$\mu = \alpha\mu_1 + (1-\alpha)\mu_2. \qquad (5.4)$$

In eqs. (5.3-5.4), the subscripts 1 and 2 denote the liquid phase and the air phase respectively. The volume fraction of the liquid phase varies from 0 (representing pure air phase or phase - 2) to 1 (representing pure liquid phase or phase - 1). Also, in eqs.(5.1-5.2), $\bar{I}$ is the identity tensor, $\boldsymbol{g}$ is acceleration due to gravity, and $\boldsymbol{F}_\sigma$ is the surface tension force that is modeled implicitly using continuum surface force (CSF) model described by Brackbill *et al*.:[122]

$$\boldsymbol{F}_\sigma = \sigma\kappa\boldsymbol{\nabla}\alpha. \qquad (5.5)$$

In eq.(5.5), σ is the liquid-air surface tension which remains constant throughout the polymerization process and κ is the local curvature of the drop at the liquid-air interface, which is defined in terms of the normal vectors ($\hat{\boldsymbol{n}}$) at the liquid-air interface as:

$$\kappa = -\boldsymbol{\nabla}.\hat{\boldsymbol{n}} = -\boldsymbol{\nabla}.\left(\frac{\boldsymbol{\nabla}\alpha}{|\boldsymbol{\nabla}\alpha|}\right). \qquad (5.6)$$

Eq.(5.5) also depend on α, which is the volume fraction of the liquid drop. The spatio-temporal variation of α is governed by the following equation:[229-230]

$$\frac{\partial\alpha}{\partial t} + \boldsymbol{\nabla}.(\alpha\boldsymbol{u}) + [\boldsymbol{\nabla}.(\alpha(1-\alpha)\boldsymbol{u_r})] = -\frac{\alpha}{\rho_1}\frac{D\rho_1}{Dt}. \qquad (5.7)$$

In eq.(5.7), the first two terms on the left-hand side are used to respectively track the unsteady and advective motion of the volume fraction. The term within the square bracket on the left-hand side of eq.(5.7) is used to ensure that the interface remains sharp by using an artificial compression technique. MULES algorithm uses an artificial compression velocity ($\boldsymbol{u_r}$), which is calculated based on the face flux values, in order to limit the phase fluxes and maintain a sharp interface.[169-172] The term on the right-hand side of eq.(5.7) is a source term that arises due to the density variation of the liquid phase (kindly note that we consider the "material derivative", i.e., $\frac{D\rho_1}{Dt}$, while describing the density variation of the liquid phase).

The properties of the liquid phase change over time as the unpolymerized liquid drop undergoes photo-induced polymerization. Under such circumstances, the density of the polymeric liquid is expressed in terms of degree of cure (ξ) (or degree of polymerization, which will be defined later) as follows:

$$\rho_1 = (1 - \xi)\rho_m + \xi\,\rho_p. \qquad (5.8)$$

Here, ρ_m and ρ_p represent the density of the unpolymerized and the polymerized drops, respectively. Such a linear variation of density during polymerization has been commonly adopted in the literature for a polymerizing resin. [222,57,59] The viscosity of the polymer drop (μ_1), which also depends on the degree of cure (namely, the polymer viscosity is assumed to increase exponentially with the degree of cure), is expressed as:[55]

$$\mu_1 = \mu_0 \exp(\lambda\xi) \exp\left(\frac{U}{RT}\right). \qquad (5.9)$$

Here, λ is the viscosity coefficient dictating the extent of exponential viscosity increase with an increase in degree of cure (ξ) and the term U is the energy of activation of viscous flow that is associated with the drop spreading (the purpose of the term "U" is to determine the sensitivity of viscosity to temperature). The terms λ and U are assumed to be independent of the polymerization process and are considered as constants. Further, in eq. (5.9), R is the universal gas constant and T is the local temperature which is obtained by solving the energy equation as shown in the following subsection. μ_0 is the apparent viscosity of the unpolymerized (shear-thinning) liquid drop, and can be expressed as:[56]

$$\mu_0 = m\,\dot{\gamma}^{n-1}, \qquad (5.10)$$

where, $\dot{\gamma}$ is the shear rate, *m* is the power law consistency coefficient, and *n* is the power law index.

5.2.2.2 Temperature Distribution: Energy equation:

During the photo-polymerization reaction, the polymeric drops are be subjected to temperature changes due to (1) the exothermal reaction (photo-polymerization is an exothermic reaction) and (2) the absorption of the incident UV radiation. The changes in the temperatures inside and outside the drops during this process are captured by the following energy equation:[59]

$$\left(\frac{\partial(\rho C_p T)}{\partial t} + \nabla.(\rho C_p \boldsymbol{u} T)\right) = \nabla.(k\nabla T) + Q - \Delta H_r \frac{\partial c_m}{\partial t}. \qquad (5.11)$$

In eq.(5.11), C_p is the specific heat capacity at constant pressure for the fluid, *k* is the thermal conductivity of the fluid, Q is the heat source term (due to the absorption of UV-radiation by the initiator species inside the polymer drop), ΔH_r is the heat of polymerization

reaction, and c_m is the concentration of monomer inside the drop. The term Q as well as the term $\Delta H_r \frac{\partial c_m}{\partial t}$ (which represents the heat released during the polymerization reaction) are applied only inside the droplet. The values of specific heat capacity C_p and thermal conductivity k are determined based on the volume fraction of the liquid (α), i.e.,

$$C_p = \alpha C_{p1} + (1 - \alpha) C_{p2}, \qquad (5.12)$$

$$k = \alpha k_1 + (1 - \alpha) k_2. \qquad (5.13)$$

where C_{pi}, k_i are the specific heat capacity at constant pressure and the thermal conductivity of the fluid i (i = 1,2) respectively. Finally, in eq. (5.11), the heat source term Q is expressed as:

$$Q = I_r \epsilon c_i. \qquad (5.14)$$

Here ϵ is the absorption coefficient of the photo-initiator species in the drop, c_i is the concentration of the photo-initiator species in the drop and I_r is the local intensity of the radiation (in W/m^2). I_r can be calculated using Beer-Lambert's law as

$$I_r = I_0 e^{-\int \epsilon c_i(z_p) dz_p}, \qquad (5.15)$$

where I_0 is the incident radiation on the sample (polymer drop) and z_p is the length of the path the beam traverses through the material sample.

5.2.2.3 Free radical photo-polymerization reaction: Species conservation equation:

Using the species conservation equation (described below), we can capture the evolution of the extent of photopolymerization (or degree of cure, ξ) inside the polymeric drop. The degree of cure ξ is related to the instantaneous monomer concentration c_m by

$$\xi = \frac{(c_{m0} - c_m)}{c_{m0}}, \qquad (5.16)$$

where, c_{m0} is the initial monomer concentration, and c_m is the local, instantaneous value of the monomer concentration.

Before solving the species conservation to obtain the distribution of the monomer concentration, it is essential to understand the kinetics of the photopolymerization reaction. Here, the free-radical polymerization reaction takes place in three steps: initiation, propagation, and termination.[58]

Initiation: The monomeric species undergoes free radical polymerization which is initiated by the incident UV radiation. A photon from the incident UV-radiation interacts with the photo-initiating species *P* and activates it to create two free radicals.

$$P \xrightarrow{h\upsilon} 2R^{\circ} \qquad (5.17a)$$

Propagation: The second stage, also known as chain propagation, is responsible for the growth of the polymer chains and results in a bulkier, longer chain polymer. Free radical pair produced by photo-initiation reacts with monomeric units (M_1) to form a chain-initiating species $M_1{}^{\circ}$. On further reaction, the chain-initiating species ($M_{i-1}{}^{\circ}$) produced in the i^{th} propagation step reacts with other unreacted monomeric units to form a longer polymeric chain ($M^{\circ}{}_i$), where i denotes the current propagation step.

$$R^{\circ} + M_1 \xrightarrow{k_{p1}} M_1^{\circ}, \quad (5.17b)$$

$$M_{i-1}^{\circ} + M_1 \xrightarrow{k_{pi}} M^{\circ}_i \, . \quad (5.17c)$$

Here, k_{pi} is the rate constant dictating the kinetics of the chain-propagation reaction. In free radical polymerization reactions, it is commonly assumed that the rate constants of all the propagation steps are equal, i.e., it remains independent of the polymer chain length. Therefore, we consider $k_{p1} = k_{p2} = \cdots = k_{pi} = k_p$.

Termination: In this final stage, the long chains are terminated by means of coupling or disproportionation reaction. Either of these processes leads to the termination of activated polymer chain molecules by turning them into a dead polymer.

$$M_j^{\circ} + M_k^{\circ} \xrightarrow{k_t} dead\ polymer. \quad (5.17d)$$

Here, k_t is the rate constant determining the termination step of the free-radical polymerization reaction. Rate constants for both the propagation (k_p) and termination (k_t) stages are described by Arrhenius equation:

$$k_j = A_j e^{-\frac{E_j}{RT}}. \quad (5.18)$$

In eq. (18), A_j and E_j represent the frequency factor and activation energy of each stage *j* *(j = p, t*; "p" denotes the propagation step and "t" denotes the termination step*)*. Using these rate constants,[45,49] we can capture the evolution of the monomer concentration within the drop by using the following species transport equation (which takes the simplistic form since we consider $k_{p1} = k_{p2} = \cdots = k_{pi} = k_p$):[58]

$$\frac{\partial c_m}{\partial t} + \nabla.(-D_m.\nabla \mathrm{c}_m) + \nabla.(\boldsymbol{u}\mathrm{c}_m) \;=\; -k_p\, c_m \left(\frac{\phi I_{abs}}{k_t}\right)^{\frac{1}{2}}. \quad (5.19)$$

In eq.(19), D_m represents the diffusion coefficient of monomeric species inside the drop which is assumed to remain constant throughout the curing process, ϕ represents the quantum yield, which is a measure of efficiency of photoinitiation, and I_{abs} is the rate of photon absorption [in mol/(L.s)] that can be expressed as:[60,61]

$$I_{abs} = 4.57 \times 10^{-6} I_r \epsilon c_i, \quad (5.20)$$

where the term $4.57 \times 10^{-6} I_r (= I_{moles})$ is the intensity of light in units $mol/(m^2.s)$ which is related to the radiation intensity (I_r) which is in units W/m^2 through a conversion factor $4.57 \times 10^{-6}\ [mol/J]$.[61]

Finally, in eq.(5.19), the term $-k_p\, c_m \left(\frac{\phi I_{abs}}{k_t}\right)^{\frac{1}{2}} (=\; R_m)$ is the sink term which accounts for the rate at which the monomer is converted into polymer. This rate of reaction depends on parameters from the three stages of free-radical photopolymerization: quantum yield for initiation, propagation rate constant (for propagation), and termination rate constant (for termination).[51] Furthermore, we need to capture the distribution of the initiator concentration inside the drop to complete the setup. This is captured by using the following species transport equation for the initiator concentration (c_i):[47,51]

$$\frac{\partial c_i}{\partial t} + \nabla.(-\mathrm{D}_i \nabla c_i) + \nabla.(\boldsymbol{u} c_i) \;=\; -\mathrm{I}_{abs}, \quad (5.21)$$

Here D_i represents the diffusion coefficient of photo-initiator species inside the drop which is assumed to remain constant throughout the curing process. Please note that here the term "I_{abs}" serves the purpose of a "sink" term, since it is well accepted that the rate of

consumption of the initiator species is directly related to the rate of photon absorption by the photo initiator species.

5.2.2.4 Initial conditions:

Initially, the two drops with zero initial velocity are placed on the substrate separated by a center-to-center distance of d = 30 μm. All the velocity components are set to be zero, the pressure is set to be atmospheric, and the temperature is set to be 300 K. Monomer and the photo-initiator concentrations are set to be 2 M and 0.1 M, respectively within the droplet. The intensity of the radiation is set to be zero throughout the domain. Note that the species conservation equations are solved only inside the droplet.

5.2.2.5 Boundary conditions:

Fluid flow

In the 3D domain that we consider, the pressure is set to be atmospheric at all the boundary faces except for the bottom face (substrate) where the drops spread and coalesce. On the bottom face, no-penetration and no-slip conditions are incorporated. However, to deal with the stress singularity at the moving contact line, numerical slip is incorporated near the moving contact line. Magnitude of the numerical slip is inherent to the algorithm, as the algorithm uses the mass flux in the cells adjacent to the moving contact line and average it over the face to obtain the interface slip velocity.[123,183,184] The numerical slip length is typically of the order of the mesh grid size (typically h/2, where h is the grid length).[124]

The effect of contact angle is incorporated into the governing equations by setting a boundary condition for the equation governing the evolution of the scalar quantity (α) [see eq.(5.7)]. At the bottom surface, the boundary condition for α is set so as to ensure that the

drop continues to spread until the mean curvature of the drop makes an angle equal to the equilibrium contact angle (θ_{eq}). The boundary condition that connects the volume fraction and the equilibrium contact angle is given as:[123]

$$\frac{\nabla\alpha}{|\nabla\alpha|} = \hat{n}_w \cos(\theta_{eq}) + \hat{t}_w \sin(\theta_{eq}). \qquad (22)$$

Here, $\hat{n}_w$ and $\hat{t}_w$ are the unit normal and tangential vectors to the substrate, and θ_{eq} is the equilibrium contact angle. Here, for the case of $\tau_p \sim \tau_s$, with the quick conversion of monomer, the droplets could essentially be fully polymerized but still not be able to reach the equilibrium contact angle. The model considers the fully cured state to be a very highly viscous liquid which closely represents the solid polymer. However, it is useful to note that if the system were to be simulated for infinite time, the highly viscous cured polymer very slowly tends to its prescribed equilibrium contact angle.

Heat transfer

Temperature at the all the boundary faces is set to be isothermal condition at $T = 300\ K$.

Free radical photo-polymerization reaction

For both the monomer and initiator concentrations, the boundary condition at the bottom substrate is set to be no flux. Also, to ensure that the species remain confined inside the moving droplet, we must enforce no-flux condition at the drop-air interface. This is implemented by utilizing the OpenFoam function utility phaseScalarTransport which confines the species to the drop phase (phase -1).

Parameters used in this study and their definitions are provided in Table 5.1. The validation of the numerical model has been provided in Appendix D.

Parameter	**Definition**	**Value [Units]**	**Reference**
ρ_m	Density of the uncured solution	1250 [kg/m^3]	[53]
ρ_p	Density of the cured material	1375 [kg/m^3]	[57,59]
ρ_2	Density of phase - 2	1.205 [kg/m3]	[61]
m	Consistency index	2	[56]
n	Power law index	0.6	
μ_2	Viscosity of phase - 2	1.82×10^{-5} [Pa.s]	[123]
σ	Liquid-air surface tension	0.024 [N/m]	[26]
θ_{eq}	Equilibrium contact angle	25°	
k_1	Thermal conductivity of phase - 1	0.3 [W/(m.K)]	
k_2	Thermal conductivity of phase - 2	0.03 [W/(m.K)]	[123]
C_{p1}	Specific heat capacity of phase - 1	4185 [J/(kg.K)]	[26]
C_{p2}	Specific heat capacity of phase - 2	1007 [J/(kg.K)]	[123]

ϵ	Absorption coefficient of photoinitiator	150 [m^2/mol]	[59]
I_0	Intensity of incident UV-radiation	100 [mW/cm^2]	[67]
ΔH_r	Heat of polymerization reaction	-50 [kJ/mol]	[58]
E_p	Activation energy of propagation reaction	29.7 [kJ/mol]	
E_p	Activation energy of termination reaction	22.2 [kJ/mol]	
A_{p1}	Frequency factor of propagation reaction (case 1)	5×10^{10} [L/(mol.s)]	
A_{p2}	Frequency factor of propagation reaction (case 2)	1.2×10^{12} [L/(mol.s)]	
A_t	Frequency factor of termination reaction (identical for both cases)	1×10^{11} [L/(mol.s)]	
c_{i0}	Initial concentration of photoinitiator	0.1 [M]	[58]
c_{m0}	Initial concentration of monomer	2 [M]	[69]
D_m	Diffusion coefficient of monomer	1×10^{-9} [m^2/s]	[68]

D_i	Diffusion coefficient of photoinitiator	1×10^{-9} [m^2/s]	
ϕ	Quantum yield for photoinitiation	0.6	[60]
R_0	Radius of the drop	10 [μm]	
d	Initial center-to-center distance between the droplets	30 [μm]	

Table 5.1: List of parameters used in this study

5.3 Results and Discussions

In this study, we investigate the coalescence behavior of two power-law obeying, non-Newtonian polymer drops spreading on a solid substrate in the presence of UV-radiation induced photopolymerization. To understand the effect of the photopolymerization reaction on the spreading and coalescence dynamics, we study two cases: (i) Case (denoted henceforth as *Case 1*) where the spreading timescale is much smaller than the polymerization timescale (i.e., $\tau_s \ll \tau_p$), (ii) Case (denoted henceforth as *Case 2*) where the spreading timescale is comparable to that of polymerization timescale (i.e., $\tau_s \sim \tau_p$). Here, τ_s is the spreading timescale and is a combination of the capillary (t_c) and viscous (t_v) timescales, i.e., $\tau_s = t_c + t_v = \sqrt{\frac{\bar{\rho} R_0^3}{\sigma}} + \frac{\mu_0 R_0}{\sigma}$ (Here, $\bar{\rho}_1 = (\rho_m + \rho_p)/2$; please see Table 1 for definition of the terms). On the other hand, τ_s is the polymerization timescale that can be expressed as $\tau_p = \frac{1}{k_p \left(\frac{\phi I_{abs}}{k_t}\right)^{\frac{1}{2}}}$ [please refer to eqs.(5.18,5.20) for the definitions of the terms]. For these two cases we compare and analyze (1) the velocity distribution inside the coalescing drops, (2) dynamics of growth of bridge, (3) evolution of the temperature profile, and (4) evolution of the curing profile.

5.3.1 Velocity distribution inside the coalescing droplets

In Figs. 5.2 and 5.3, we show the velocity distribution inside the spreading and coalescing drop in the presence of *in-situ* photocuring for case 1 ($\tau_s \ll \tau_p$) and case 2 ($\tau_s \sim \tau_p$), respectively. The droplets are initially spaced apart by a *center-to-center* separation distance 'd' and are placed on the substrate which is philic to these droplets. In the early stages of spreading (see Fig. 5.2), we can observe that (i) most of the velocity vectors in

the interior part the drops (i.e., far away from the three-phase contact line or TPCL) are directed downwards towards the substrate and (ii) the velocity vectors near the three-phase contact line (TPCL) are directed toward the TPCL. Such a fluid flow directed from the central part of the drop towards the TPCL [as shown by the velocity vectors in Figs. 5.2(a-b)] is an indication of the onset of the spreading of the drops. In Fig. 5.2(a), we can observe a large velocity gradient inside the drop at near-wall locations, i.e., there is a rapid increase in the velocity magnitude as one moves away from the substrate. This can be obviously attributed to the no-slip condition at the wall and a strong fluid flow being directed from the drop interior towards the TPCL. Next, in Fig. 5.2(b)-5.2(c), we observe that the velocity magnitude inside the drop decreases gradually as the drop continues to spread. As the drops proceed to spread, they finally come into contact with each other and start to coalesce [see Fig. 5.2(d)]. The onset of the coalescence, which occurs for the present case (Case 1) at t = 0.12 ms, is marked by the disappearance of the TPCLs of the drops at their coalescing ends and the formation of a liquid bridge [see Fig. 5.2(d)]. Post coalescence, the fluid mass continues to flow towards the coalescing zone as indicated by the direction of the velocity vectors: it is this influx of the fluid mass that results in the growth of the liquid bridge [see Figs. 5.2(e)-5.2(h)]. The coalescence event, therefore, can be described by studying the temporal growth of the height and the width of this bridge.

In Fig. 5.3, which describes the coalescence event for case 2 (i.e., the case where photocuring significantly affects the coalescence event), we observe a spreading and coalescence behavior (for case 2) that is qualitatively similar to case 1. Here too, in Fig. 3(a), we observe a large velocity gradient within the drop at near-wall locations with the magnitude of velocity increasing quickly away from the substrate. Also, in Fig. 5.3(b-c),

we observe that the velocity vectors are directed away from center of the droplet towards the TPCL, which is characteristic of a spreading drop. However, it can be noted that the velocity magnitude inside the spreading drops (for case 2) are much smaller than that observed inside the drops for case 1 (see Fig. 5.2), and as a result the spreading is also slowed down for case 2. This is caused by the fact that the fluid viscosity massively increases during the spreading event for case 2: this can be attributed to the condition $\tau_s \sim \tau_p$, i.e., the photocuring (and hence an increase in the viscosity) occurring during the spreading. Such weekended spreading also ensures that the onset of the coalescence (and hence the bridge formation) is significantly delayed for case 2: this coalescence (bridge formation) onsets at t = 0.3 ms for case 2 [see Fig. 5.3(d)], while that for case 1 onset at t = 0.12 ms [see Fig. 5.2(d)]. Of course, once the bridge has started to form, very much like *Case 1*, here too, a continuous influx of the liquid mass from the coalescing drops causes a growth of the bridge [see Figs. 5.3(e-h)].

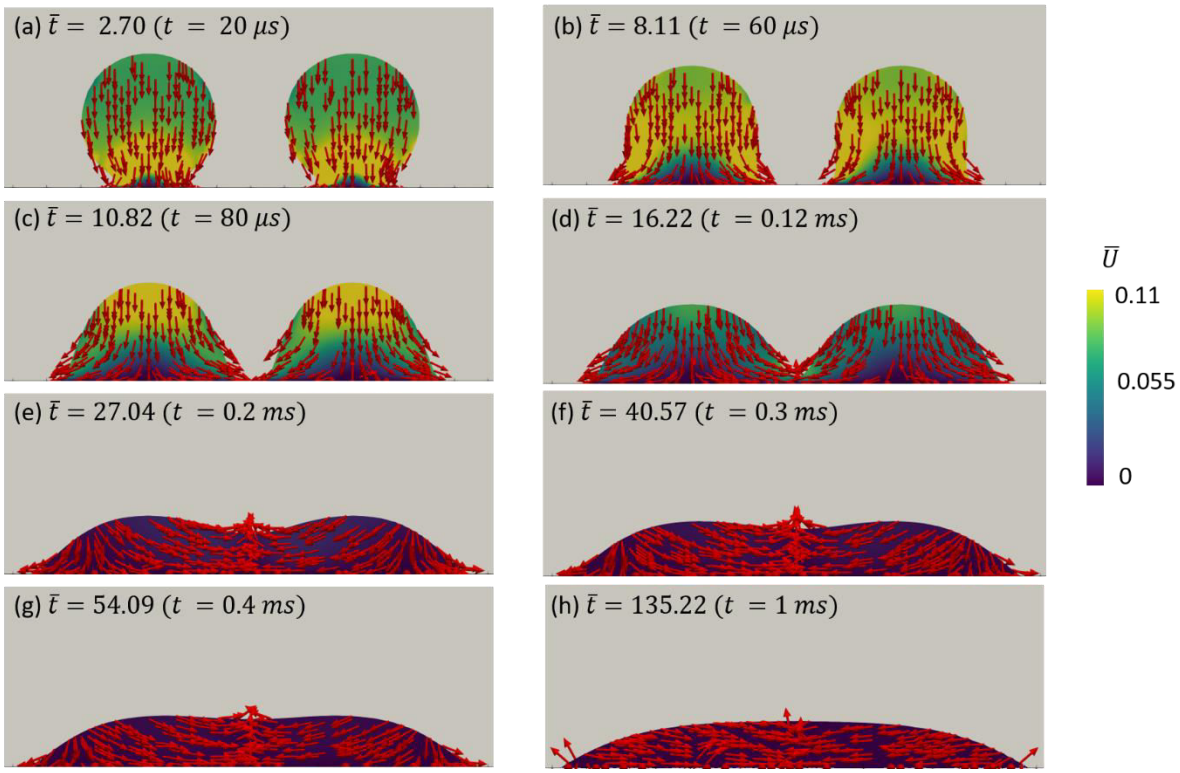

Figure 5.2: Non-dimensional velocity ($\bar{U}$) distribution inside the coalescing drops for case 1 $\left(\tau_s \ll \tau_p\right)$ at different time instances, i.e., at: (a) t $= 20\,\mu s$, (b) t $= 60\,\mu s$, (c) t $= 80\,\mu s$, (d) t $= 0.12\,ms$, (e) t $= 0.2\,ms$, (f) t $= 0.3\,ms$, (g) t $= 0.4\,ms$, (h) t $= 1\,ms$. For each time instant t, the corresponding dimensionless time $\bar{t}$ ($\bar{t} = t/t_c$) has been provided. In the figure, the arrows only represent the direction of the flow at the location (velocity vectors are not scaled to represent the corresponding velocity magnitude). Here, $\bar{U} = U/U_c$, U is the magnitude of the velocity and U_c $(= R_0/t_c)$ is the characteristic velocity, where $t_c = \sqrt{\frac{\bar{\rho}R_0^3}{\sigma}}$ is the capillary timescale, $\bar{\rho} = \frac{\rho_m+\rho_p}{2}$ is the average density of the drop, and R_0 is the drop radius.

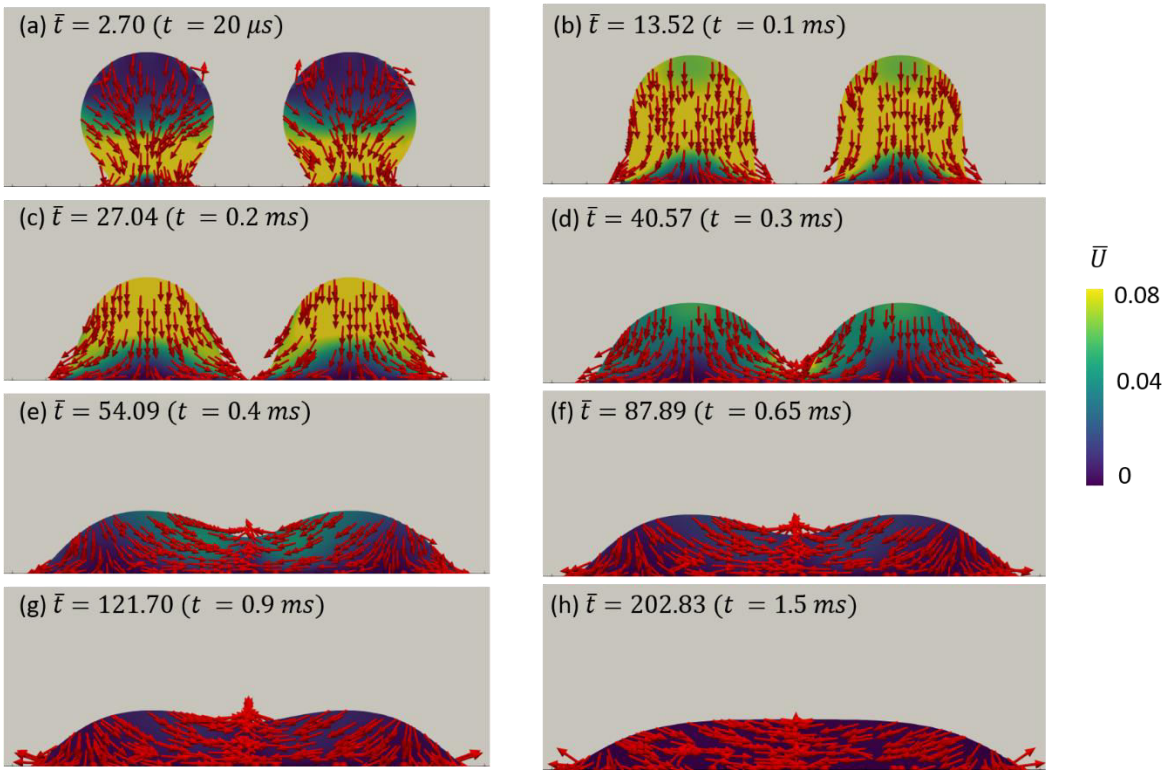

Figure 5.3: Non-dimensional velocity ($\bar{U}$) distribution inside the coalescing drops for case 2 ($\tau_s \sim \tau_p$) at different time instances, i.e., (a) t $= 20\ \mu s$, (b) t $= 0.1\ ms$, (c) t $= 0.2\ ms$, (d) t $= 0.3\ ms$, (e) t $= 0.4\ ms$, (f) t $= 0.65\ ms$, (g) t $= 0.9\ ms$, (h) t $= 1.5\ ms$. For each time instant *t*, the corresponding dimensionless time $\bar{t}$ ($\bar{t} = t/t_c$) has been provided. In the figure, the arrows only represent the direction of the flow at the location (velocity vectors are not scaled to represent the corresponding velocity magnitude). Here, $\bar{U} = U/U_c$, U is the magnitude of the velocity and U_c ($= R_0/t_c$) is the characteristic velocity, where $t_c = \sqrt{\frac{\bar{\rho} R_0^3}{\sigma}}$ is the capillary timescale, $\bar{\rho} = \frac{\rho_m + \rho_p}{2}$ is the average density of the drop, and R_0 is the drop radius.

5.3.2 Dynamics of coalescence: Growth of bridge height and width

Next, we compare the dynamics of the bridge growth for the two cases (case 1 and case 2) by studying the corresponding time evolution of the non-dimensional height (H_0/R_0) and the non-dimensional width (W/R_0) of the bridge [see Figs. 5.4(a,b)]. Before providing a detailed scaling argument to explain the different stages of the bridge growth for either of the cases, we make certain crucial observations. First, it is incorrect to compare the bridge growth for the two cases using the same time axis. This stems from the fact that the time of the onset of coalescence (t_{con}) is different for the two cases: t_{con} = 0.12 ms for case 1 and t_{con}=0.3 ms for case 2. Therefore, in Figs. 5.4(a,b), we use t*/t_c as the time axis, where $t^* = (t - t_{con})$ and hence different for cases 1 and 2. Second, regardless of the nature of the scaling dictating the variation of $\frac{H_0}{R_0} - vs - t^*/t_c$ and $\frac{W}{R_0} - vs - t^*/t_c$, one can clearly see that for a given t^*/t_c value, the magnitudes of $\frac{H_0}{R_0}$ and $\frac{W}{R_0}$ for case 1 are always greater than the magnitudes of $\frac{H_0}{R_0}$ and $\frac{W}{R_0}$ for case 2. This stems from the weaker coalescence dynamics for case 2, given the fact that for case 2, $\tau_s \sim \tau_p$, and hence photopolymerization and the resulting increase in the viscosity significantly affects the spreading and coalescence events.

Below, we attempt to provide detailed scaling analysis to explain the nature of the $\frac{H_0}{R_0} - vs - t^*/t_c$ and $\frac{W}{R_0} - vs - t^*/t_c$ variation governing the coalescence behavior for cases 1 and 2.

5.3.2.1 Coalescence dynamics

For both cases 1 and 2, one can identify three distinct regimes in the time variation of either $\frac{H_0}{R_0}$ or $\frac{W}{R_0}$. For each case, we find that either of these quantities ($\frac{H_0}{R_0}$ or $\frac{W}{R_0}$) first increases slowly with time (the corresponding regime is denoted as the *early regime*), then their rate of increase with time significantly enhances (the corresponding regime is denoted as the *intermediate regime*), and finally their rate of increase becomes significantly reduced (towards the end of the coalescence process) the corresponding regime is denoted as the *late regime*). Depending on whether we are considering case 1 or 2, or considering the variation of $\frac{H_0}{R_0}$ or $\frac{W}{R_0}$, the exact time dependence (of $\frac{H_0}{R_0}$ or $\frac{W}{R_0}$) change in these different regimes, although the qualitative nature of the variation in the different regimes (as identified above) does not change.

It is also worthwhile to point out that we would explain that these three regimes are characterized by balance of capillary forces with different resisting forces, as summarized below:

1. Early regime: Balance of Capillary forces with the Viscous forces
2. Intermediate regime: Balance of Capillary forces with the Inertial forces
3. Late regime: Balance of Capillary forces with the Viscous forces

5.3.2.1.1 Scaling analysis of the growth of bridge height

5.3.2.1.1.1 Early regime

In the early regime, as the droplets just start to coalesce, the mass inside the liquid bridge is significantly small. Therefore, the inertial effects are relatively small. On the other hand, in this early regime of coalescence, the velocity with which the liquid mass enters the coalescing zone is finite (given that coalescence is occurring between two spreading drops). Therefore, one can argue that growth of the bridge at this early regime of coalescence is governed by the balance of the capillary and viscous forces. Interestingly, such a viscous regime, while hasn't been pointed out for early stages of drop coalescence, it can be noted in various experiments.[133,224] For the drop coalescence of inviscid and low-viscosity liquids, this viscous regime at very early stages of coalescence persists for only tens of nanoseconds for very low-viscosity liquids).[86,88,231] However, for high-viscosity liquids, several experimental studies have identified a regime (at early stages of coalescence) where the growth of the bridge height or width is significantly retarded and this is this viscous regime (at early stages of coalescence).[92,97,214]

Case 1: Growth of the bridge height in the early regime

As explained above, the growth of the bridge height in the early regime of coalescence can be determined by balancing the driving capillary forces (or capillary stresses) and the resisting viscous forces (or shear stresses). Therefore, one can write [using eq.(5.9) to express the viscosity and noting that the term "$\exp\left(\frac{U}{RT}\right)$" is a constant]:

$$\frac{\sigma R_0}{{H_0}^2} \sim m\dot{\gamma}^n \exp(\lambda\xi), \qquad (5.23a)$$

$$\Rightarrow \frac{\sigma R_0}{{H_0}^2} \sim m\left(\frac{1}{H_0}\frac{dH_0}{dt}\right)^n \exp(\lambda\xi). \quad (5.23b)$$

In the above equations, we express the shear rate as $\dot{\gamma} \sim \frac{1}{H_0}\frac{dH_0}{dt}$.

For case 1, in the early regime of coalescence, the effect of photocuring is negligible, and hence the average degree of cure is negligible [i.e., $\exp(\lambda\xi) \approx 1$]. Accordingly, eq.(5.23b) yields:

$$\frac{\sigma R_0}{{H_0}^2} \sim m\left(\frac{1}{H_0}\frac{dH_0}{dt}\right)^n. \quad (5.23c)$$

Changing the integration variable from t to $\bar{t^*}$ (where $\bar{t^*} = \frac{t^*}{t_c} = \frac{t - t_{con}}{t_c}$) and integrating eq.(5.23c), we get:

$$H_0 \sim (\bar{t^*})^{n/2} \Rightarrow H_0 \sim (\bar{t^*})^{0.3} \text{ (for n= 0.6).} \quad (5.23d)$$

This is close to the simulation-based prediction of $H_0/R_0 \sim (t^*/t_c)^{1/3}$.

Both these theoretical scaling relationship as well as the simulation-based prediction have been provided in Fig. 5.4(c).

Case 2: Growth of the bridge height in the early regime

As for case 2, the extent of polymerization is significantly enough to considerably affect the viscosity of the drop even at early stages of coalescence. Such a photocuring-induced increase in the fluid viscosity results in a steep increase in the resisting viscous stresses. Such an increase in the resisting viscous stress explains the observed decreased rate of growth of the bridge height in the early viscous regime. This is confirmed in Fig. 5.4(d),

where the bridge height scales as $H_0 \sim (\overline{t^*})^{1/6}$ (for case 2) as compared to $H_0 \sim (\overline{t^*})^{1/3}$ for case 1 [see Fig. 5.4(c)]. Furthermore, we find that the transition from this early regime to the intermediate regime (or viscous to inertial regime, in terms of the forces that balance the driving capillary forces), occurs at a much later time for case 2 in comparison to case 1 [see Figs. 5.4(c,d)]. This is consistent with the findings of the experimental studies,[66,67] which demonstrate that the increase in the fluid viscosity increases the crossover time from viscous (i.e., the initial regime where the viscous forces balance the capillary forces) to an inertial regime (i.e., the intermediate regime where the inertial forces balance the capillary forces).

5.3.2.1.1.2 Intermediate regime

In the intermediate coalescence regime, a substantial amount of liquid mass has accumulated in the "bridge" region: accordingly, at this time, the variation of the bridge height and width will be dictated by the balance of the inertial and capillary forces (and the result is a significant enhancement in the rate of increase of the bridge height). As previously reported, in this regime, the balance between the driving capillary forces and the opposing inertial forces determines the growth of the bridge. So, we balance the interfacial capillary stress ($\sigma R_0/H_0^2$) and the opposing dynamic pressure jump that corresponds to the inertial force that spans across the interface ($\rho_1 v_z^2$). Here, v_z is the velocity with which the bridge grows ($v_z \sim dH_0/dt$). We show the scaling analysis for the two-cases studied here below:

Case 1: Growth of the bridge height in the intermediate regime

Given that in this regime, the growth of the bridge is dictated by the balance of the capillary and the inertial forces, one can balance the capillary pressure ($\sigma R_0/H_0^2$) with the dynamic pressure jump that corresponds to the inertial force that spans across the interface ($\rho_1 v_z^2$). Using $v_z \sim \frac{dH_0}{dt}$ and $\rho_1 = \rho_m + \xi(\rho_p - \rho_m) \approx \rho_m$ (stemming from the fact at this intermediate regime, the fluid properties remain significantly unaffected by the polymerization for case 1, where $\tau_s \ll \tau_p$), this balance yields:

$$\frac{\sigma R_0}{H_0^2} \sim \rho_m \left(\frac{dH_0}{dt}\right)^2. \qquad (5.24a)$$

Changing the integration variable from *t* to $\bar{t}^*$ ($\bar{t}^* = \frac{t - t_{con}}{t_c}$) and integrating eq.(5.24a), we get:

$$\frac{H_0}{R_0} \sim (\bar{t}^*)^{1/2}. \qquad (5.24b)$$

The fitting of the numerical results also produces $\frac{H_0}{R_0} \sim (\bar{t}^*)^{1/2}$ [see Fig. 5.4(c)].

Interestingly, this balance of the capillary and inertial effects, yielding $H_0 \sim (\bar{t}^*)^{1/2}$ has been identified as the "early" coalescence regime in several previous studies. *Here we modify that notion: we claim that while such* $H_0 \sim (\bar{t}^*)^{1/2}$ *scaling is indeed witnessed for coalescing drops, it occurs not in the early time regime, but in an intermediate time regime after the initial regime that is governed by the balance of the capillary and viscous forces.*

Case 2: Growth of the bridge height in the intermediate regime

In this case, the effect of the polymerization process is significant and hence the density of drop is given by

$$\rho_1 = \rho_m + \xi(\rho_p - \rho_m). \qquad (5.25a)$$

Here, the average degree of cure can be represented as the function of time as $\xi(t) = (1 - \exp(-t/\tau_p))$ [confirmed by the nature of the variation of $\xi(t)$, see Fig. 5.6]. At early/intermediate stage of coalescence, the time is small, and hence the degree of cure can be linearly approximated as

$$\xi(t) = \left(1 - \exp(-t/\tau_p)\right) \approx 1 - \left(1 - \frac{t}{\tau_p}\right). \quad (5.25b)$$

Accordingly, eq.(25.a) reduces to

$$\rho_1 \approx \rho_m + (\rho_p - \rho_m)t/\tau_p. \qquad (5.25c)$$

Using eq.(5.25c), the balance of the capillary stress and dynamic pressure jump across the interface due to inertial force can be expressed as:

$$\frac{\sigma R_0}{H_0^2} \sim \left[\rho_m + (\rho_p - \rho_m)t/\tau_p\right]\left(\frac{dH_0}{dt}\right)^2 \Rightarrow H_0 dH_0 \sim \left(1 + \frac{t}{t_0}\right)^{-1/2} dt, \qquad (5.25d)$$

where $t_0 = \frac{\rho_m}{(\rho_p - \rho_m)}\tau_p$.

Using binomial expansion (taking only first two terms as $\frac{t}{t_0} \ll 1$) and integrating (using $t \gg \frac{t^2}{4t_0}$, and the fact that R_0, t_c are constants),

$$\Rightarrow (H_0)^2 \sim t - \frac{t^2}{4t_0} \Rightarrow (H_0)^2 \approx t \Rightarrow H_0 \sim t^{\frac{1}{2}} \Rightarrow \frac{H_0}{R_0} \sim (\bar{t^*})^{1/2}. \quad (5.25e)$$

The fitting of the numerical results also produces $\frac{H_0}{R_0} \sim (\bar{t^*})^{1/2}$ [see Fig. 5.4(d)].

This is a most remarkable result that shows that in the intermediate coalescence regime, even after the effect of photopolymerization effect was taken into account (as we are considering case 2 or $\tau_s \sim \tau_p$), the bridge height growth, similar to that of case 1 (where $\tau_s \ll \tau_p$), scales as $\frac{H_0}{R_0} \sim (\bar{t^*})^{1/2}$.

5.3.2.1.1.3 Late regime

In the late regime, the growth of the bridge height tends to slow down significantly, as observed in Fig. 5.4(a) and 5.4(c). In this regime, the bridge height growth (dH_0/dt) can be assumed to be similar to the rate of growth of the spreading radius of the droplet (dr/dt). This is because of the fact that at this stage of coalescence, one can consider that the mass of liquid inside the drop that is directed toward the growth of the bridge is similar to that directed toward the non-coalescing part of the drop, i.e., TPCL. Based on the work by Seevaratnam et al.[128], spreading rate of the shear-thinning drop with a power law index of n is given as

$$\theta_d^{\frac{2+n}{n}} \sim Ca \sim \mu_1 U_{TPCL}. \quad (5.26a)$$

Here, θ_d is the dynamic contact angle, Ca = $\frac{\mu_0 U_{TPCL}}{\sigma}$ is the capillary number which is calculated based on the drop velocity at the TPCL ($U_{TPCL} \approx \frac{dr}{dt}$), and $\mu_1 \left(= \mu_0 \exp(\lambda\xi + \frac{U}{RT})\right)$ is the viscosity of the polymeric liquid. Also, from a geometric requirement of the drop,

$$\theta_d = \frac{V}{r^3}, \qquad (5.26b)$$

where V is the drop volume and r is the instantaneous spreading radius. From the eqs.(5.26a) and (5.26b), we can write:

$$\left(\frac{V}{r^3}\right)^{\frac{2+n}{n}} \sim \mu_1 \frac{dr}{dt}. \qquad (5.26c)$$

Case 1: Growth of the bridge height in the late regime

For case 1 (i.e., where $\tau_s \ll \tau_p$), one can express

$$\mu_1 = \mu_0 \exp(\lambda\xi) \exp\left(\frac{U}{RT}\right) = C_1 \exp(\lambda\xi) \approx C_1. \qquad (5.27a)$$

This stems from the fact that since $\tau_s \ll \tau_p$, even at late stages of coalescence, ξ remains significantly small and so $\exp(\lambda\xi) \approx 1$.

Using eq.(5.27a) in eq.(5.26c), we can write:

$$\left(\frac{V}{r^3}\right)^{\frac{2+n}{n}} \sim C_1 \frac{dr}{dt}. \qquad (5.27b)$$

Integrating eq.(27b), we finally obtain:

$$r \sim t^{\frac{n}{6+4n}} \Rightarrow r \sim t^{0.07} \text{ (for n = 0.6).} \qquad (5.27c)$$

We have already argued that for such late stages of coalescence, $\frac{dH_0}{dt} \sim \frac{dr}{dt}$, and hence from eq.(5.27c), we can write (using the fact that R_0, t_c are constants):

$$\frac{H_0}{R_0} \sim (\bar{t}^*)^{0.07}. \qquad (5.27d)$$

This is consistent with the scaling obtained from the fitting of our numerical simulation result, i.e., $\frac{H_0}{R_0} \sim (\bar{t}^*)^{0.095}$ [see Fig. 5.4(c)].

Case 2: Growth of the bridge height in the late regime

For case 2, in the late regime of drop coalescence, the fluid properties get significantly affected by the in-situ curing. Here, the evolution of viscosity (of the drop) with the degree of cure is given by

$$\mu_1 = \mu_0 \exp(\lambda\xi) \exp\left(\frac{U}{RT}\right) = C_1 \exp(\lambda\xi) \quad (5.28a)$$

During this time period, for case 2, the degree of cure attains a value of 0.39 (at time t = 1.5 ms) (see Fig. 5.6 later). This would imply that $\lambda\xi$ is finite, but less than unity. Accordingly, with some approximation, we can reduce eq.(28a) as:

$$\mu_1 \approx C_1(1+\lambda\xi) = C_1\left[1+\lambda\left\{1-exp\left(-\frac{t}{\tau_p}\right)\right\}\right] = C_2 - C_3 exp\left(-\frac{t}{\tau_p}\right), \quad (5.28b)$$

where $C_1 = \mu_0 \exp\left(\frac{U}{RT}\right)$, $C_2 = C_1(1+\lambda)$, and $C_3 = C_1\lambda$.

Using eq. (5.26c) and eq. (5.28b), we can write the scaling relation as

$$\left(\frac{V}{r^3}\right)^{\frac{2+n}{n}} \sim \left[C_2 - C_3\, exp\left(-t/\tau_p\right)\right]\frac{dr}{dt}. \quad (5.28c)$$

Changing the variables t to $\bar{t}^* = \frac{t-t_{con}}{t_c}$ and integrating, we get

$$r \sim (ln|C_4 \exp(C_5\bar{t}^*) - \bar{t}_1|)^{\frac{n}{6+4n}}, \quad (5.28d)$$

where, $C_4 = \frac{C_2}{t_c}, C_5 = \frac{t_c}{\tau_p}$, and $\bar{t}_1 = (C_3/t_c)exp(-t_{con}/\tau_p)$.

Using the same notion that at late stages of coalescence, $\frac{dH_0}{dt} \sim \frac{dr}{dt}$, we can use eq.(5.28d) to write:

$\frac{H_0}{R_0} \sim (ln|C_4 \exp(C_5 \bar{t^*}) - \bar{t}_1|)^{0.07}$ (for n = 0.6). (5.28e)

We plot this functional form of $\frac{H_0}{R_0} - vs - \bar{t^*}$ [provided in eq.(5.28e)] and the result matches very well with the numerical results [see Fig. 5.4(d)].

Also, a comparison of eqs.(5.27d) and (5.28e) confirms that the rate of growth of the bridge height is smaller for case 2.

5.3.2.1.2 Scaling analysis of the growth of bridge width

5.3.2.1.2.1 Early regime

Case 1: Growth of the bridge width in the early regime

In the early regime, as the mass in the liquid bridge formed is less, viscous forces associated with the fluid flow significantly affect the growth of the bridge width (as explained above). We can, therefore, obtain the growth rate of the width of the bridge in the early regime (if the viscous forces were dominant) by balancing the capillary stress and the resisting viscous stresses:

$\frac{\sigma R_0}{W^2} \sim m\dot{\gamma}^n \exp(\lambda\xi)$. (5.29a)

Using $\dot{\gamma} \sim \frac{1}{W}\frac{dW}{dt}$, $\exp(\lambda\xi) \approx 1$ (since for case 1, at early stages of coalescence, cure is negligible, i.e., $\xi \to 0$)] and integrating eq.(5.29a) (by changing the integration variable from t to $\bar{t}^*$), we can write:

$$\frac{W}{R_0} \sim (\bar{t}^*)^{n/2} \Rightarrow \frac{W}{R_0} \sim (\bar{t}^*)^{0.3} \text{ (for n= 0.6).} \qquad (29.b)$$

The scaling obtained by fitting the numerical simulation result is i.e., $\frac{W}{R_0} \sim (\bar{t}^*)^{1/3}$, which is very close to the prediction derived in eq.(5.29b). This comparison has been provided in Fig. 5.4(e).

Case 2: Growth of the bridge width in the early regime

As for case 2, the photopolymerization process significantly affects the viscosity of the drop. As discussed earlier, such photocuring-induced increase in the fluid viscosity results in a steep increase in the resisting viscous stresses and this caused the observed decreased rate of growth of the bridge width in the early viscous regime. This can be seen from Fig. 5.4(f), where the bridge width scales as $\frac{W}{R_0} \sim (\bar{t}^*)^{1/11}$ (for case 2) as compared to the width scaling of $\frac{W}{R_0} \sim (\bar{t}^*)^{1/3}$ as observed for case 1 [see Fig. 5.4(f)]. Further, here too, the transition from viscous to inertial regime happens at a much later time in comparison to the case 1.

5.3.2.1.2.2 Intermediate regime

Case 1: Growth of the bridge width in the intermediate regime

The growth of the bridge width is governed by the balance between driving capillary forces and the resisting inertial and viscous forces. Following the derivation of eq.(5.24b), where the capillary forces balance the inertial forces, one can obtain the scaling as $\frac{W}{R_0} \sim (\bar{t^*})^{0.5}$. Next, we can obtain the growth rate of the width of the bridge in the intermediate regime (if the viscous forces were dominant) by balancing the capillary stress and the resisting viscous stresses. Using the formulation in eq.(5.29b), we can get a scaling of $\frac{W}{R_0} \sim (\bar{t^*})^{0.3}$. From fitting the result from numerical simulation, we can obtain $\frac{W}{R_0} \sim (\bar{t^*})^{0.33}$: therefore, the scaling exponent is in between that obtained theoretically by considering the inertial force [for this case, we have inertial forces balancing capillary forces, i.e., $\frac{W}{R_0} \sim (\bar{t^*})^{0.5}$] and the viscous force [for this case, we have viscous forces balancing capillary forces, i.e.,$\frac{W}{R_0} \sim (\bar{t^*})^{0.3}$] as the dominant resisting force [see Fig. 5.4(e)].

Case 2: Growth of the bridge width in the intermediate regime

Similar to case 1, for case 2 we observe a numerical prediction of $\frac{W}{R_0} \sim (\bar{t^*})^{0.33}$: therefore, the scaling exponent is in between that obtained theoretically by considering the inertial force [for this case, we have inertial forces balancing capillary forces, i.e., $\frac{W}{R_0} \sim (\bar{t^*})^{0.5}$] and the viscous force [for this case, we have viscous forces balancing capillary forces, i.e.,$\frac{W}{R_0} \sim (\bar{t^*})^{1/11}$] as the dominant resisting force [see Fig. 5.4(f)].

5.3.2.1.2.3 Late regime

In the late regime of coalescence, as shown by Lee *et al.*,[119] the bridge width (W) can be related to the dynamic contact angle $\theta_d{}'$ that is formed by the coalescing part of the drop. This dynamic contact angle is related to the bridge height and width as

$$\tan\theta_d' = \frac{H_0}{W}. \qquad (5.30a)$$

At the later stages of the coalescence, this dynamic contact angle is small and hence we can write

$$\theta_d' \approx \frac{H_0}{W}. \qquad (5.30b)$$

Moreover, for a shear-thinning liquid, equivalent Cox-Voinov law can be written as

$$\theta_d'^{\left(\frac{2+n}{n}\right)} \sim Ca \sim \mu_1 v_r \sim \exp(\lambda\xi)\frac{dW}{dt} \;\Rightarrow \left(\frac{H_0}{W}\right)^{\frac{2+n}{n}} \sim \exp(\lambda\xi)\frac{dW}{dt}. \qquad (5.30c)$$

Here, v_r is the velocity with which the width of the bridge grows $\left(v_r \sim \frac{dW}{dt}\right)$.

Case 1: Growth of the bridge width in the late regime

For case 1, the effect of curing on the viscosity can be neglected ($\exp(\lambda\xi) \approx 1$) and hence the scaling for the growth of width of the bridge can be obtained by integrating eq.(5.30c) and by using $H_0 \sim t^{\frac{n}{6+4n}}$ [stemming from the fact that $r \sim t^{\frac{n}{6+4n}}$, see eq.(5.27c), and at late stages of coalescence, $\frac{dH_0}{dt} \sim \frac{dr}{dt}$]:

$$\frac{W}{R_0} \sim (\bar{t^*})^{\left(\frac{5n+8}{4n+6}\right).\left(\frac{n}{2+2n}\right)} \Rightarrow \frac{W}{R_0} \sim (\bar{t^*})^{0.24} \text{ (for n = 0.6).} \qquad (5.31a)$$

This is consistent with the fit to the numerical simulation, i.e., $\frac{W}{R_0} \sim \left(\frac{t^*}{t_c}\right)^{1/4}$ [see Fig. 5.4(e)].

Case 2: Growth of the bridge width in the late regime

For case 2, the effect of curing on the viscosity cannot be neglected. Using eq.(5.28b) and eq. (5.30c) the scaling for the growth of width of the bridge can be written as:

$$\left(\frac{H_0}{W}\right)^{\frac{2+n}{n}} \sim \left[C_2 - \mathrm{C_3}\exp(-t/\tau_p)\right]\frac{dW}{dt}. \qquad (5.32a)$$

Using eq.(5.28e) to express H_0 and changing the integration variable from t to $\bar{t}^* = \frac{t-t_{con}}{t_c}$, we can write

$$\frac{\left[\left(ln|C_4\exp(C_5\bar{t}^*)-\bar{t}_1|\right)^{0.07}\right]^{\frac{2+n}{n}}}{C_4-\bar{t}_1 exp(-C_5\bar{t}^*)} d\bar{t}^* \sim W^{\frac{2+n}{n}} dW, \qquad (5.32b)$$

$$\Rightarrow \frac{W}{R_0} \sim (ln|C_4\exp(C_5\bar{t}^*) - \bar{t}_1|)^{\frac{0.07(2+n)+n}{2+2n}} \qquad (5.32c)$$

$$\Rightarrow \frac{W}{R_0} \sim (ln|C_4\exp(C_5\bar{t}^*) - \bar{t}_1|)^{0.244} \text{ (using n=0.6)} \qquad (5.32d)$$

In the above equations, $C_4 = C_2/t_c$, $C_5 = \frac{t_c}{\tau_p}$, and $\bar{t}_1 = (C_3/t_c)exp\left(-t_{con}/\tau_p\right)$.

We plot this functional form of $\frac{W}{R_0} - vs - \bar{t}^*$ [provided in eq.(5.32d)] and the result matches very well with the numerical results [see Fig. 5.4(f)]; also this $\frac{W}{R_0} - vs - \bar{t}^*$ variation implies a weaker growth rate of the bridge width as compared to the bridge width growth rate for case 1 [see eq.(5.31a)] for the late regime.

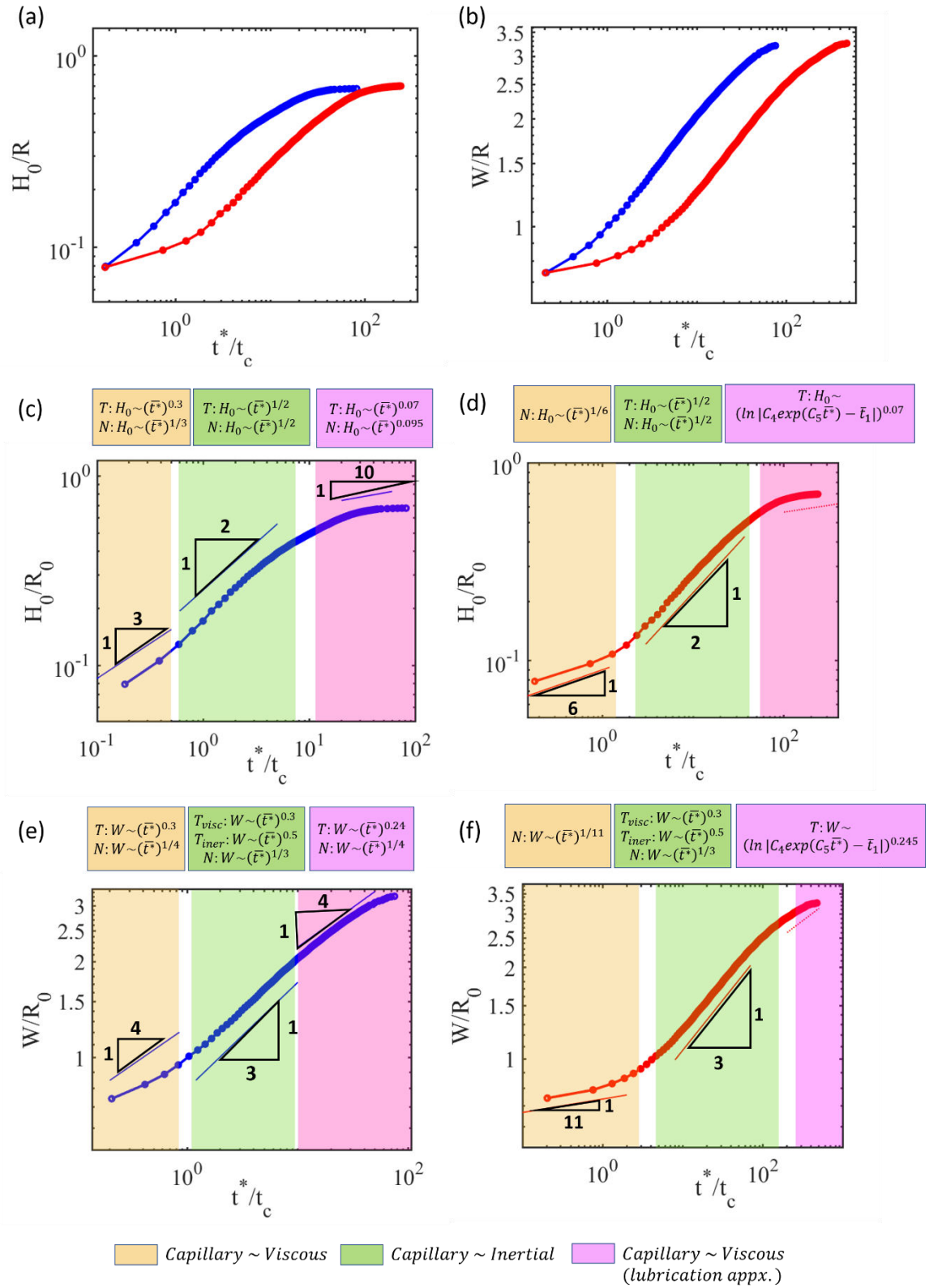
(a)
(b)
(c)
(d)
(e)
(f)
H_0/R
W/R
H_0/R_0
W/R_0
t^*/t_c
$T: H_0 \sim (\bar{t}^*)^{0.3}$ $N: H_0 \sim (\bar{t}^*)^{1/3}$
$T: H_0 \sim (\bar{t}^*)^{1/2}$ $N: H_0 \sim (\bar{t}^*)^{1/2}$
$T: H_0 \sim (\bar{t}^*)^{0.07}$ $N: H_0 \sim (\bar{t}^*)^{0.095}$
$N: H_0 \sim (\bar{t}^*)^{1/6}$
$T: H_0 \sim (\bar{t}^*)^{1/2}$ $N: H_0 \sim (\bar{t}^*)^{1/2}$
$T: H_0 \sim (ln\,|C_4 exp(C_5 \bar{t}^*) - \bar{t}_1|)^{0.07}$
$T: W \sim (\bar{t}^*)^{0.3}$ $N: W \sim (\bar{t}^*)^{1/4}$
$T_{visc}: W \sim (\bar{t}^*)^{0.3}$ $T_{iner}: W \sim (\bar{t}^*)^{0.5}$ $N: W \sim (\bar{t}^*)^{1/3}$
$T: W \sim (\bar{t}^*)^{0.24}$ $N: W \sim (\bar{t}^*)^{1/4}$
$N: W \sim (\bar{t}^*)^{1/11}$
$T_{visc}: W \sim (\bar{t}^*)^{0.3}$ $T_{iner}: W \sim (\bar{t}^*)^{0.5}$ $N: W \sim (\bar{t}^*)^{1/3}$
$T: W \sim (ln\,|C_4 exp(C_5 \bar{t}^*) - \bar{t}_1|)^{0.245}$
Capillary ~ Viscous
Capillary ~ Inertial
Capillary ~ Viscous (lubrication appx.)

Figure 5.4: Time evolution of (a) non-dimensional bridge height $\left(\frac{H_0}{R_0}\right)$ and (b) non-dimensional bridge width $\left(\frac{W}{R_0}\right)$ for the coalescing drops for cases 1 and 2. In (c-f), these same variable are re-plotted to explicitly provide the scaling variations: (c) variation of $\frac{H_0}{R_0}$ for Case 1; (d) variation of $\frac{H_0}{R_0}$ for Case 2; (e) variation of $\frac{W}{R_0}$ for Case 1; (f) variation of $\frac{W}{R_0}$ for Case 2. Here, $t^* = t - t_{con}$ is the time relative to the instant (t_{con}) drops come into contact with each other (the value of t_{con} is different for different cases 1 and 2), $t_c = \sqrt{\frac{\bar{\rho}R_0^3}{\sigma}}$ is the capillary timescale, $\bar{\rho} = \frac{\rho_m + \rho_p}{2}$ is the average density of the drop, and R_0 is the drop radius. Also, in (c-f), the three different regimes characterizing the bridge growth (namely early, intermediate, and late regimes) are identified with different color coding. Furthermore, in (c-f), we explicitly identify the theoretical scaling (denoted with "*T*") and numerical scaling (denoted with "*N*") determining the bridge growth in these three different regimes. Also, in (e,f), T_{iner} represents the inertia-force-based *theoretical* scaling and T_{visc} represents the viscous force-based *theoretical* scaling. Finally, please note, that in (d) and (f) the red dotted lines in the zone depicting the late regime of bridge growth represent the approximate theoretical forms [expressions are already provided; please see eqs.(5.28e) and 5.32(d)].

5.3.3 Evolution of temperature inside the coalescing drops

In Fig. 5.5, we show the evolution of the average temperature inside the coalescing droplets in the presence of *in-situ* photocuring for case 1 ($\tau_s \ll \tau_p$) and case 2 ($\tau_s \sim \tau_p$). The temperature evolution inside the coalescing droplets is dictated by the interplay of the following two effects: the volumetric heat addition (source) due to the incident UV radiation and the heat release (sink) due to the polymerization reaction (which is exothermal in nature).

Initially, the average temperature of the polymeric drops is 300 K and as the polymerization reaction proceeds, we observe that there is a temperature drop. This is because the heat released due to the polymerization reaction is much larger than the heat added through the absorption of UV radiation. The heat released during the polymerization reaction (Q_p) depends on the kinetics of the reaction. As $Q_p \propto \frac{\partial c_m}{\partial t}$, the heat removed from the droplet is directly proportional to the rate at which the monomer is depleted. This clearly explains the presence of two different peaks of temperature drop for the two cases.

For case 1, as the polymerization timescale is large ($\tau_p \gg \tau_s$), the reaction proceeds slowly very (which is clearly depicted in Fig. 5.6) and the maximum average temperature drop within the coalescing drops is only about 0.2 K, and given that the substrate is maintained at the room temperature of 300 K, the temperature gradually increases back to 300 K. However, for case 2, where the polymerization timescale is small ($\tau_p \sim \tau_s$), the reaction proceeds much quicker. As a result, the rate of heat release (associated with the exothermic polymerization reaction) can be significantly high initially, although it quickly subsides at later stages. Accordingly, we observe a large valley initially (a drop of ~3.2 K in the

average temperature of the coalescing drops) followed by a steep increase of the average temperature back to 300 K.

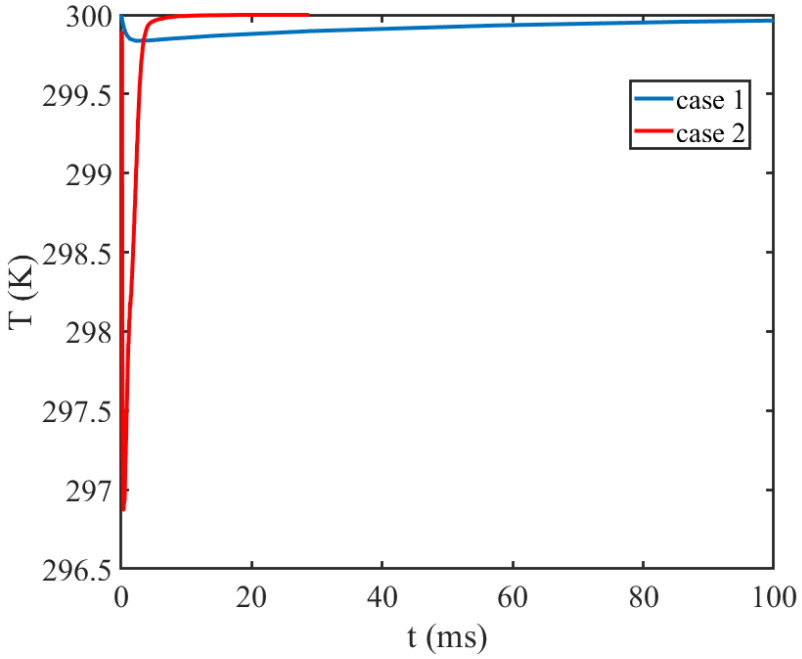

Figure 5.5: Evolution of the average temperature inside the coalescing drop in the presence of *in-situ* polymerization case 1 ($\tau_s \ll \tau_p$) and case 2 ($\tau_s \sim \tau_p$).

5.3.4 Evolution of the degree of cure inside the curing droplets

In Fig. 5.6, we show the evolution of average value of the degree of cure (or degree of polymerization, ξ) inside the coalescing droplets in presence of *in-situ* curing for case 1 ($\tau_s \ll \tau_p$) and case 2 ($\tau_s \sim \tau_p$). Degree of cure is directly related to the monomer concentration (c_m) as can be seen from eq. (5.16). $\xi = 1$ represents the fully cured state of the droplet. As it can be seen from Fig 5.6, for both the cases, the average degree of cure (ξ) starts at zero (i.e., when the drops are in an uncured state), ξ subsequently increases exponentially, and finally asymptotically reaches $\xi = 1$ (fully cured state). Degree of cure depends on the rate of polymerization reaction, which in turn depends on the instantaneous monomer concentration (c_m) [see eq.(5.19)]. Hence, the rate of polymerization reaction is much faster in the initial stages (at such stages, the monomer concentration inside the drop is very high) and becomes very slow in the later stages of the reaction (at such stages, the monomers have mostly reacted and hence the monomer concentration inside the drop is very low): this explains this particular variation of the degree of cure with time.

Further, in case 1, for which the polymerization timescale is $\tau_p \sim 66\, ms$, the rate of conversion of monomer is much slower in comparison to that of case 2 for which the polymerization timescale $\tau_p \sim 3.3\, ms$. Hence, one can clearly see that the monomer conversion (represented by the degree of cure) is around 67% at 3.3 ms for case 2, whereas for case 1 we see the same at around 80 ms.

Evolution of the curing front

Finally, in Fig. 5.7, we show the evolution of the curing front inside the coalescing droplets undergoing *in-situ* curing. Curing front is essentially the iso-surface of the parameter $\xi \left(= 1 - \frac{c_m}{c_{m0}}\right)$, which evolves with time as the incident radiation converts the monomers. This curing front progresses much more slowly for case 1, since for case 1 the rate of polymerization is very slow. Also, for both cases 1 and 2, the curing front starts from the region near the TPCL (see Fig. 5.7). This is because of the following reasons: the incident UV-radiation is only considered to be absorbed by the polymeric drop (the radiation absorption by surrounding air is considered negligible) and hence the absorbed radiation intensity is maximum at the drop-air interface. Moreover, the substrate is maintained at the room temperature of 300 K and the heat released due to the polymerization reaction is much larger than the heat added through the absorption of UV radiation: this will mean that the temperature will be maximum near the substrate. Hence the curing front starts from the TPCL where both the incident radiation and the local temperature are maximum.

There is another subtle difference between the curing fronts for cases 1 and 2. In case 1, where the spreading and coalescence events are more or less completed before the drops cure, the fluid flow does not significantly affect the progression of the curing front. Hence, we observe a systematic radially inwards progression of the curing front from the TPCL towards the innermost point near the substrate [see Fig. 5.7(a)]. However, the influence of fluid flow is significant enough to influence the curing front progression for case 2. This is particularly true when the curing front is at the last zone (i.e., at the top of the drop) [see Fig. 5.7(b)] and one can observe that due to this dominant influence of the fluid flow, the

radially inwards progression of the curing front gets disrupted and there occurs two "hump-like" structures around r=0.

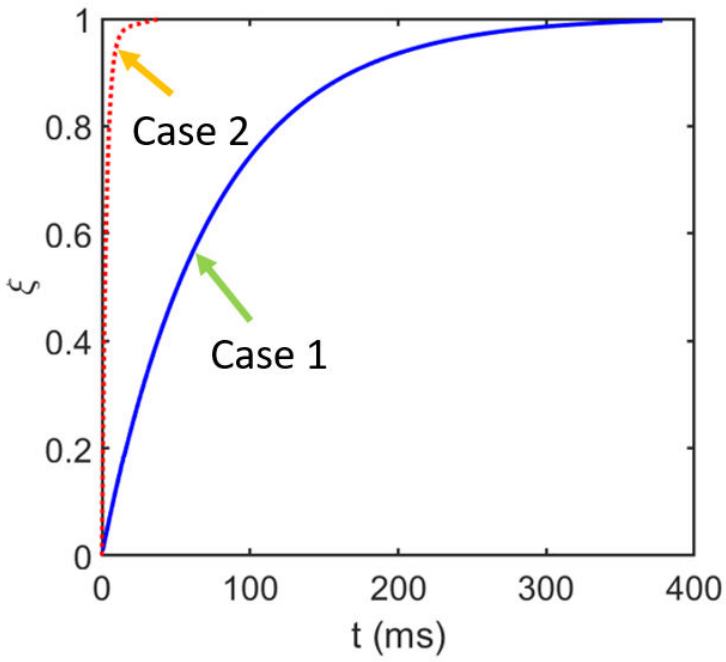

Figure 5.6: Evolution of the average degree of conversion (ξ) inside the coalescing drop in the presence of in-situ photo-polymerization for case 1 ($\tau_s \ll \tau_p$) and case 2 ($\tau_s \sim \tau_p$).

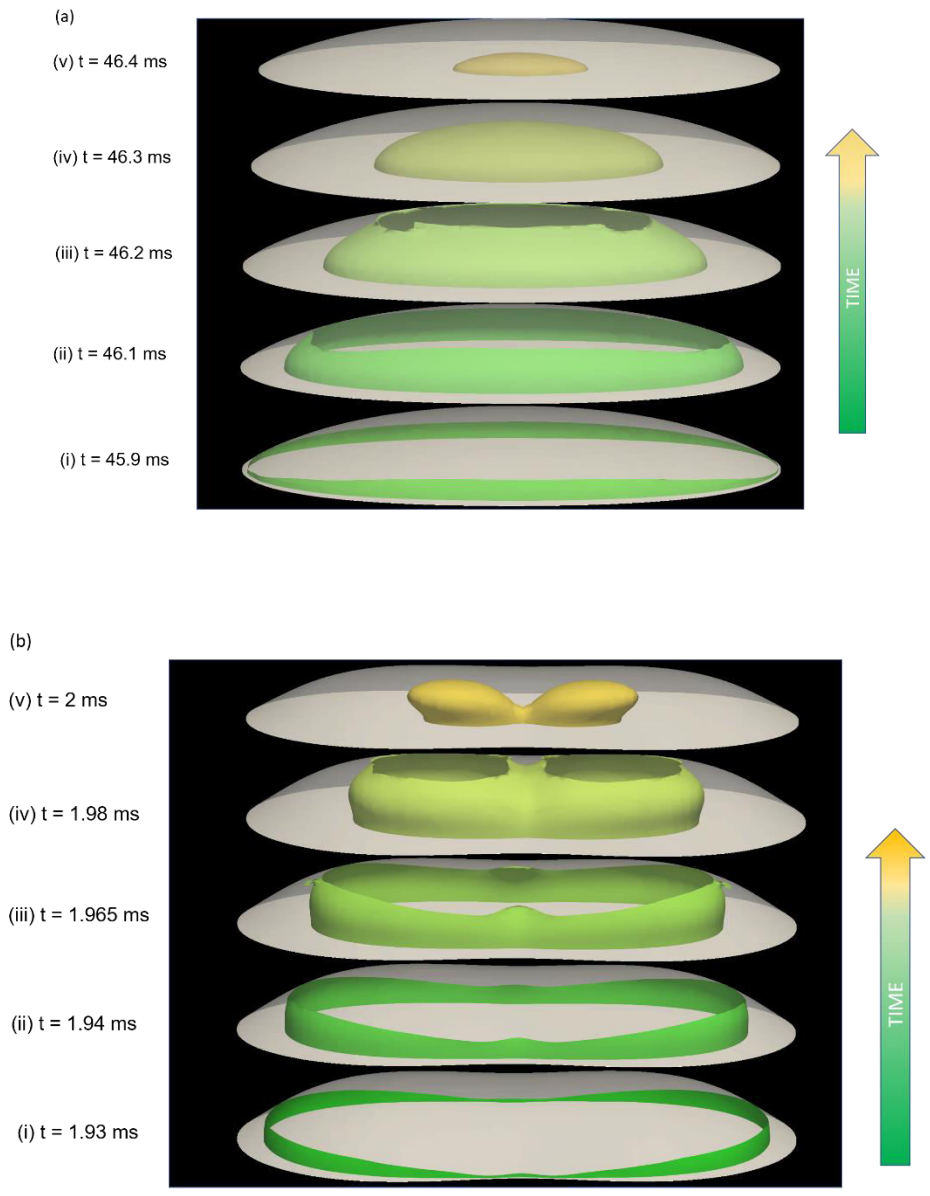

Figure 5.7: (a) Evolution of the curing surface (corresponding to $\xi = 0.5$) in a spreading and coalescing drop for case 1 ($\tau_s \ll \tau_p$), (b) Evolution of the curing surface (corresponding to $\xi = 0.5$) in a spreading and coalescing drop for case 2 ($\tau_s \sim \tau_p$).

5.4 Conclusions

This paper employs direct numerical simulations and detailed scaling calculations for studying the dynamics of two identical sized polymeric drop that are spreading and coalescing in presence of *in-situ* photocuring. *In-situ* photo-curing induced chemical reactions can significantly affect the spreading dynamics of liquid drops, as elucidated by our previous paper.[25] Here we extend that study to probe the coalescence dynamics of polymeric drops in presence of *in-situ* curing and associated chemical reactions. The key findings can be outlined as follow: (1) Case 2 ($\tau_s \sim \tau_p$), on account of the significant enhancement of the drop viscosity during spreading and coalescence events, shows a significantly slower spreading and coalescence (characterized by smaller values of height and width of the "bridge" formed by coalescence) as compared to Case 1 ($\tau_s \ll \tau_p$); (2) the bridge growth for both cases 1 and 2 are characterized by three separate regimes; (3) the bridge growth rates for case 1 is greater than that for case 2 in regimes influenced by the viscous forces; (4) the bridge growth rate is similar for the two cases for the regime where viscous effects are not important; (5) the significantly fast rate of photo-polymerization in case 2 considerably affects the temperature distribution within the coalescing drops and ensures that the fluid flow inside the coalescing drops affects the propagation of the curing front within the coalescing drops.

Chapter 6: Summary of Contribution and Future Scope

6.1 Summary of Contributions

In this dissertation, we have provided the computational fluid dynamics (CFD) framework for (1) studying the effect of photopolymerization on the spreading dynamics of a single polymeric microdroplet, (2) investigating the effect of the drop impact velocity on the coalescence dynamics of polymeric microdroplets of same material, (3) analyzing the simultaneous mixing and coalescence of polymeric microdroplets of different materials, and (4) investigating the effect of *in-situ* photopolymerization on the coalescence dynamics of polymeric microdroplets of the same material.

In this section, we summarize the major contributions of this dissertation to the existing body of knowledge:

- Study the spreading behavior of polymeric microdroplets subjected to *in-situ* photocuring
    - Our study elucidated the effect of photopolymerization on the spreading dynamics of a single non-Newtonian polymeric drop. We investigated the distribution of monomer concentration and temperature inside the curing droplets. We further probed the evolution of the curing front and investigate the role of photocuring on the premature contact line arrest. We showed that the ratio of the spreading timescale to the polymerization timescale was crucial in determining the propagation of the curing front and eventually the final drop shape.

- Study the effect of Weber numbers (or the drop impact) on the coalescence dynamics of polymeric drops.
    - Our study revealed the presence of two regimes of coalescence, and we further provided 1st principle-based scaling laws to explain the forces dictating the bridge growth. In addition, we provided evidences to show that even though the early stages of coalescence are faster for higher Weber numbers, it takes longer time for these drops to attain equilibrium configuration.

- Study the mechanism dictating the coalescence dynamics of dissimilar, miscible polymeric drops
    - Our study revealed the dynamics of the coalescence process and identified the factors driving the coalescence, the details of flow physics inside the coalescing drops, the evolution of the contact angles at the non-coalescing ends (NCEs) of the two drops, and the time variation of the height and width of the interface formed by the two drops at their coalescing ends (CEs). We were able to pinpoint the mechanisms (e.g., strong Marangoni effects) that dictated the mixing process at different locations and at different stages of coalescence.

- Study the coalescence of identical polymeric drops subjected to *in-situ* photopolymerization
    - Our study elucidated the effect of *in-situ* photocuring and the ratio of the spreading timescale and the polymerization timescale on the growth of the liquid bridge. Our simulations revealed that the bridge growth is characterized

by three distinct regimes in the presence of *in-situ* photopolymerization: this finding was corroborated by 1st principle-based scaling calculations. Our findings further revealed that the bridge growth rate is similar (for cases with different ratios of the spreading timescale and the polymerization timescale) for the regime where viscous effects are not important.

6.2 Future Scope

This dissertation sheds light on capillarity-driven dynamics (e.g., spreading and coalescence) of microscopic polymeric drops undergoing complex interactions initiated by means of chemical reaction, chemical potential gradient (mixing), or external force (like impact on substrate). Even though this dissertation mainly focuses on the dynamics and interactions between drops made of polymeric materials, the framework described in this dissertation can be useful for investigating generic reaction-controlled dynamics of drops. For instance, one can extend this framework to investigate and design active droplet motion achieved by activating photoreactive micro-swimmers like hematite, titania, $BiVO_4$ (with the droplet being laden with these micro-swimmers).[232-234] Further, complex microfluidic interactions in the reactive spreading of drops can be understood by extending this approach. Moreover, this can be used to investigate and design droplet based microreactors which is crucial for applications like gene-expression analysis, drug discovery, etc.[235]

Within the scope of understanding the droplet-based AM processes, especially post-deposition, which has been the motivation of this dissertation, there are several problems

that needs to be addressed. First, attempts should be made to develop experiments for studying the influence of photochemical reaction on the spreading of the polymeric drops. Understanding the reaction kinetics and its influence on the spreading and coalescence of drops made of similar and different material would be helpful in modeling efforts. Second, efforts should be made to probe the effect of drop focusing techniques (like acoustic focusing, sheath gas focusing, etc.) on the interactions between the drops in the stream and the subsequent spreading kinetics. For instance, the effect of focusing could lead to lateral movement of the drops (in a direction parallel to the substrate) as well as coalescence in mid-air (i.e., during flight) which can severely influence the deposition kinetics. Third, there has to be a thorough investigation of the evaporation of the particle laden drops to understand the sintering process of nano-particle based ink and the eventual deposition pattern. Explicit particle motion along with the inter-particle interactions would be one of the key factors deciding the particle deposition kinetics. Finally, efforts should be made to develop a Machine-learning based model to predict the post-deposition kinetics based on the models/experimental data. This requires the generation of an extensive set of training data which covers a wide range of different parameters that governs the dynamics such as Weber number, surface energies, chemical reaction rates, etc. Such a comprehensive model would be crucial for designing better additive manufacturing systems that ensure (1) a greater control over the geometry of the printed structures and (2) fabrication of structures with lesser defects and better (or desirable) and other mechanical properties.

Appendix A

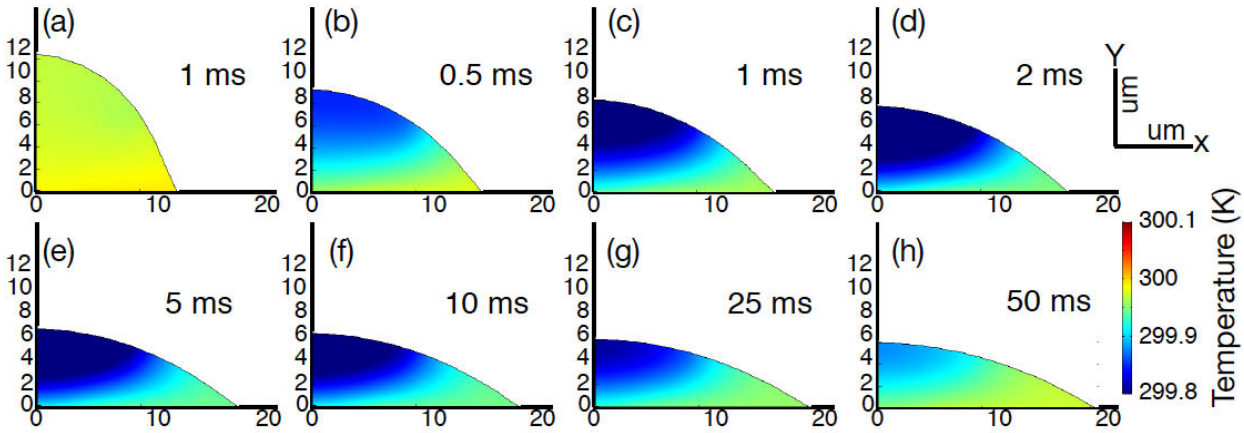

Figure A1 (a-h): Temperature distribution within the spreading polymer drop (radius 0.01 mm) at different time instants for case 1 ($\tau_s << \tau_p$). Here we have $\tau_s \approx 1.1$ ms and $\tau_p \approx 66$ ms.

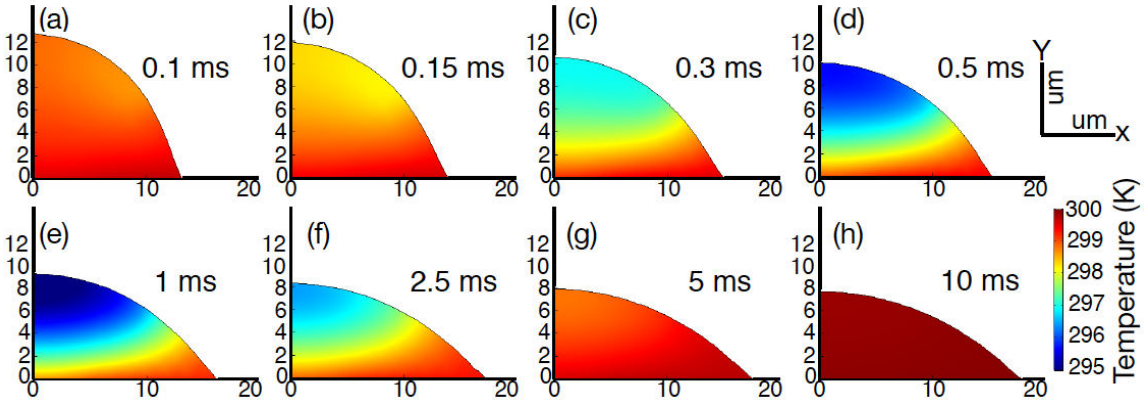

Figure A2 (a-h): Temperature distribution within the spreading polymer drop (radius 0.01 mm) at different time instants for case 2 ($\tau_s \sim \tau_p$). Here we have $\tau_s \approx 1.1$ ms and $\tau_p \approx 3.3$ ms.

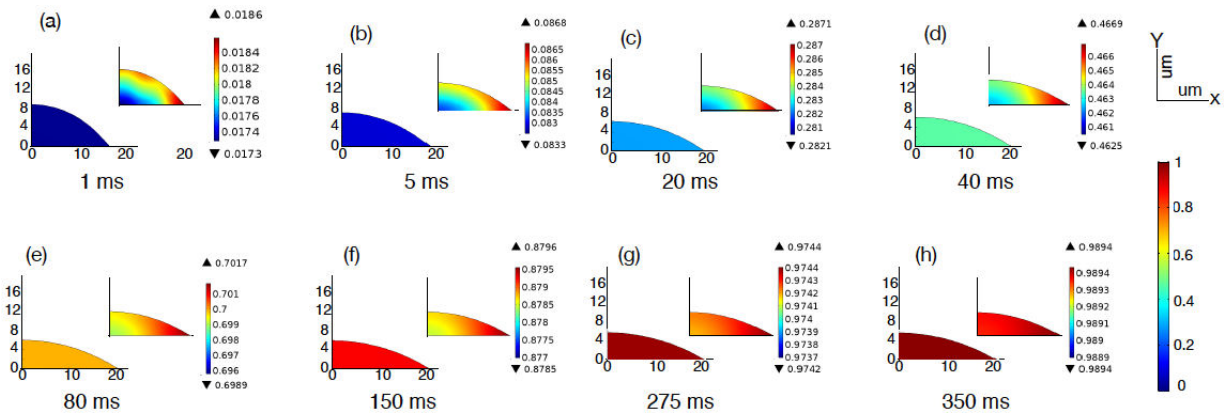

Figure A3 (a-h): Curing profiles within the spreading polymer drop (radius 0.01 mm) at different time instants for case 1 ($\tau_s << \tau_p$). Here we have $\tau_s \approx 1.1$ ms and $\tau_p \approx 66$ ms. In the inset of each subfigure, we plot the variation of the curing profile with a much smaller range of the color bar for highlighting the curing profiles (or equivalently, a distribution of the monomer concentration) within the drop itself at a given time instant.

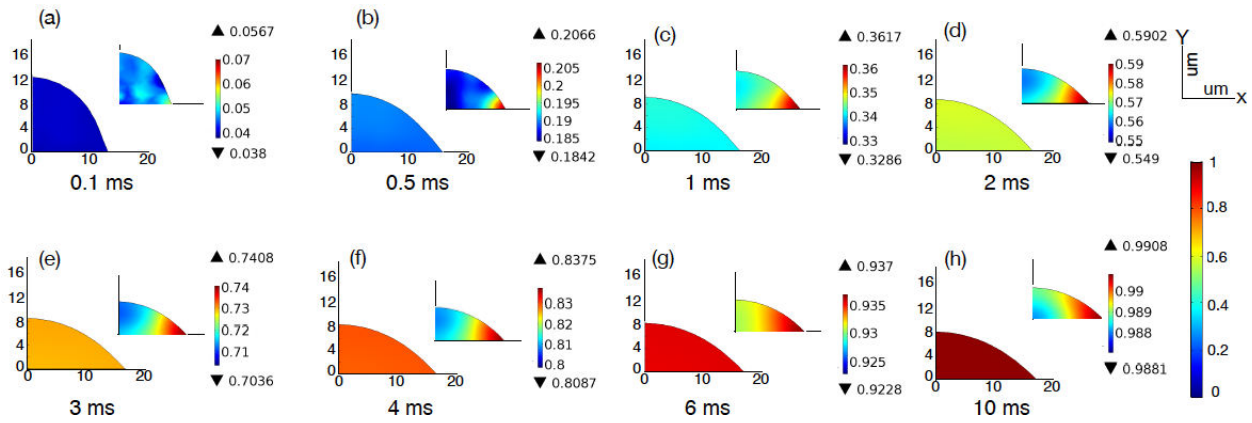

Figure A4 (a-h): Curing profiles within the spreading polymer drop (radius 0.01 mm) at different time instants for case 2 ($\tau_s \sim \tau_p$). Here we have $\tau_s \approx 1.1$ ms and $\tau_p \approx 3.3$ ms. In the inset of each subfigure, we plot the variation of the curing profile with a much smaller range of the color bar for highlighting the curing profiles (or equivalently, a distribution of the monomer concentration) within the drop itself at a given time instant.

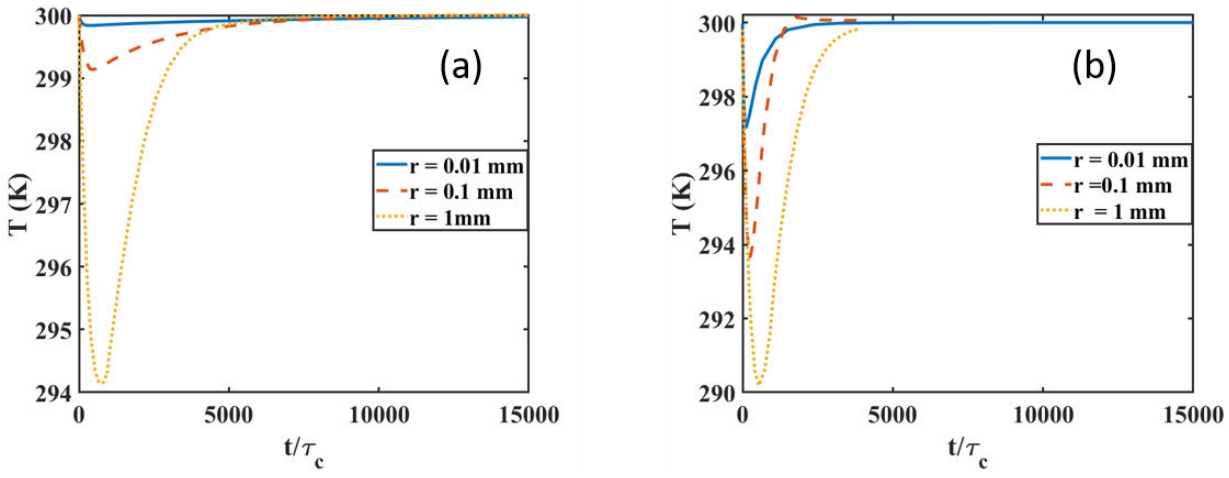

Figure A5: Variation of the average temperature of the drop with t/τ_c for (a) Case 1 and (b) Case 2 for the drops of three different sizes. The different parameters have been summarized in the caption of Fig. 8 of the Chapter 2.

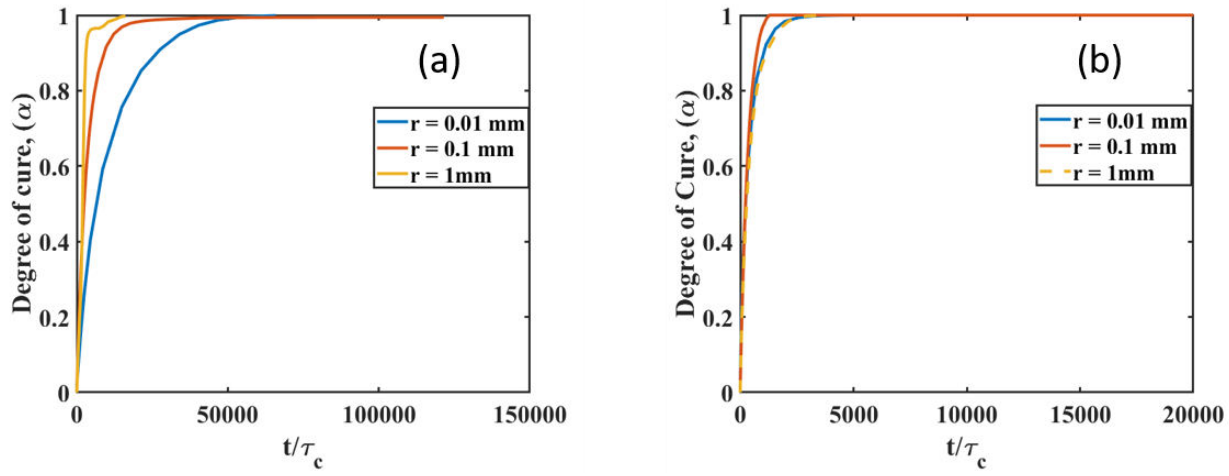

Figure A6: Variation of the average degree of cure for the drop with t/τ_c for (a) Case 1 and (b) Case 2 for the drops of three different sizes. The different parameters have been summarized in the caption of Fig. 8 of the Chapter 2.

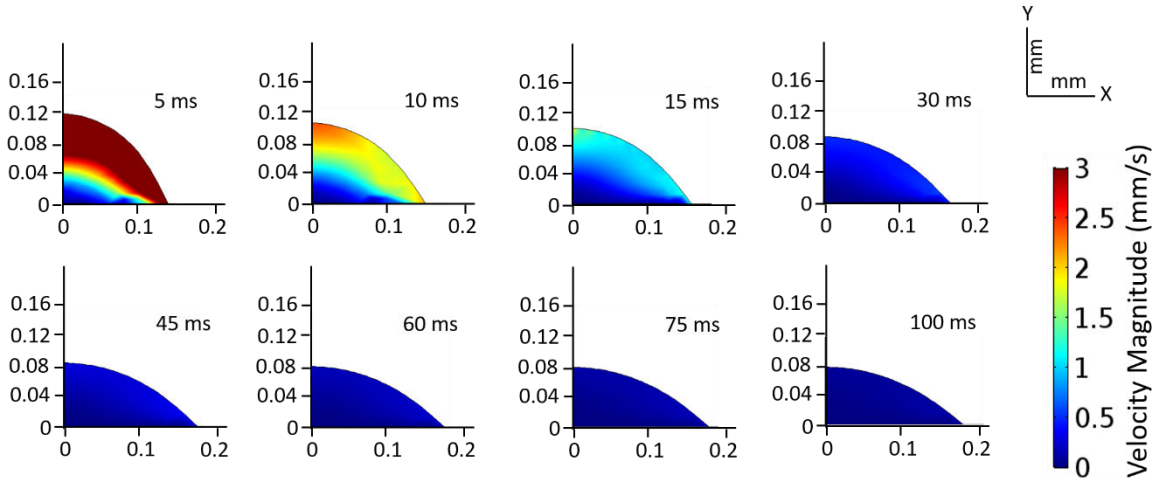

Figure A7: Velocity distribution within the spreading polymer drop at different time instants for case 1 ($\tau_s << \tau_p$) for a drop of radius 0.1 mm. Here we have $\tau_s \approx 10.2$ ms and $\tau_p \approx 660$ ms. Velocity profiles within the air have not been shown for the sake of clarity.

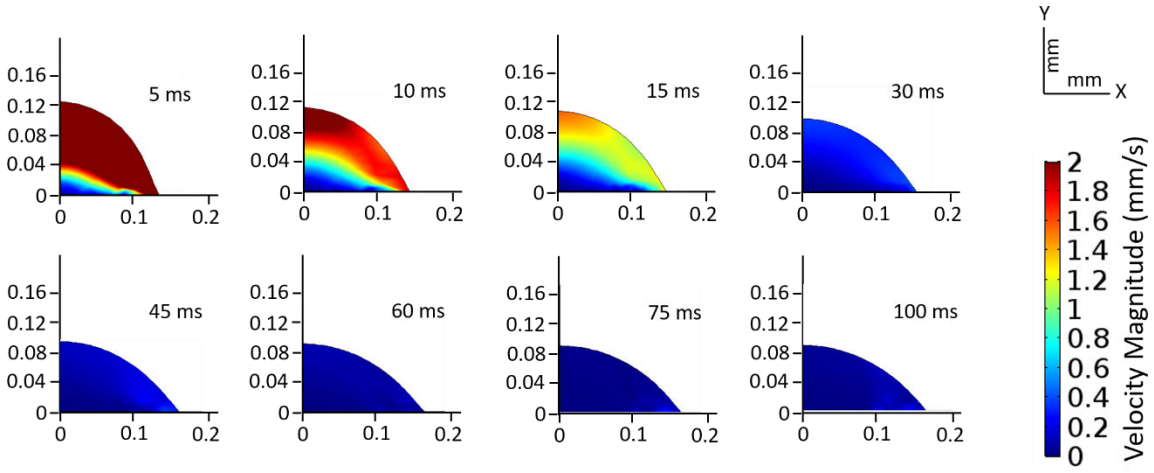

Figure A8: Velocity distribution within the spreading polymer drop at different time instants for case 2 ($\tau_s \sim \tau_p$) for a drop of radius 0.1 mm. Here we have $\tau_s \approx 10.2$ ms and $\tau_p \approx 66$ ms. Velocity profiles within the air have not been shown for the sake of clarity.

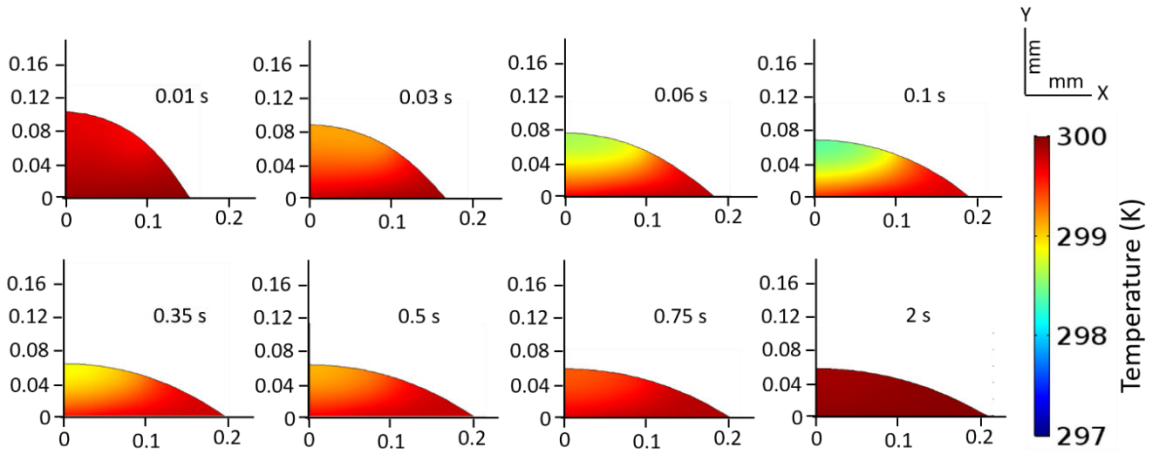

Figure A9: Temperature distribution within the spreading polymer drop at different time instants at different time instants for case 1 ($\tau_s \ll \tau_p$) for a drop of radius 0.1 mm. Here we have $\tau_s \approx 10.2$ ms and $\tau_p \approx 660$ ms.

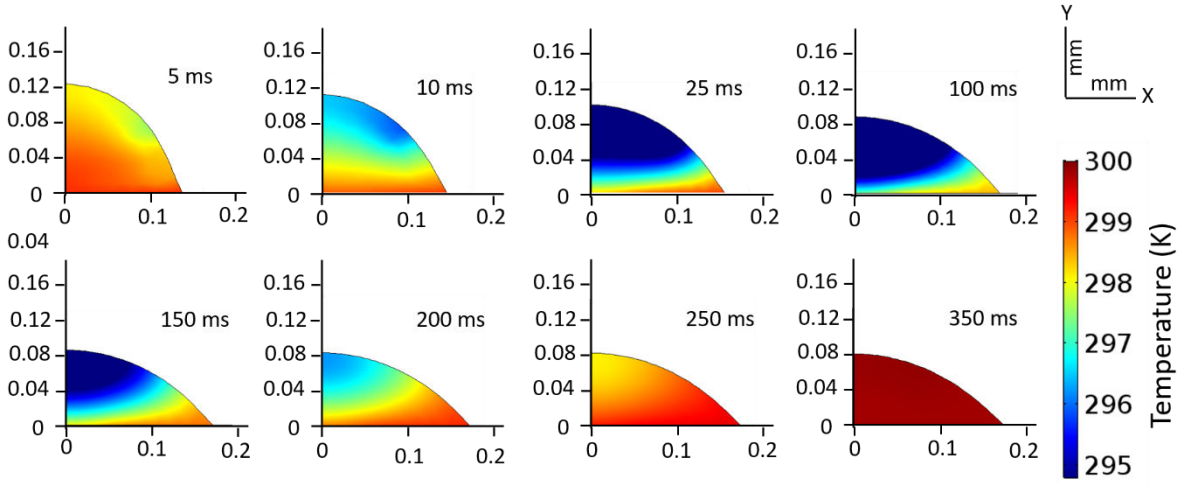

Figure A10: Temperature distribution within the spreading polymer drop at different time instants at different time instants for case 2 ($\tau_s \sim \tau_p$) for a drop of radius 0.1 mm. Here we have $\tau_s \approx 10.2$ ms and $\tau_p \approx 66$ ms.

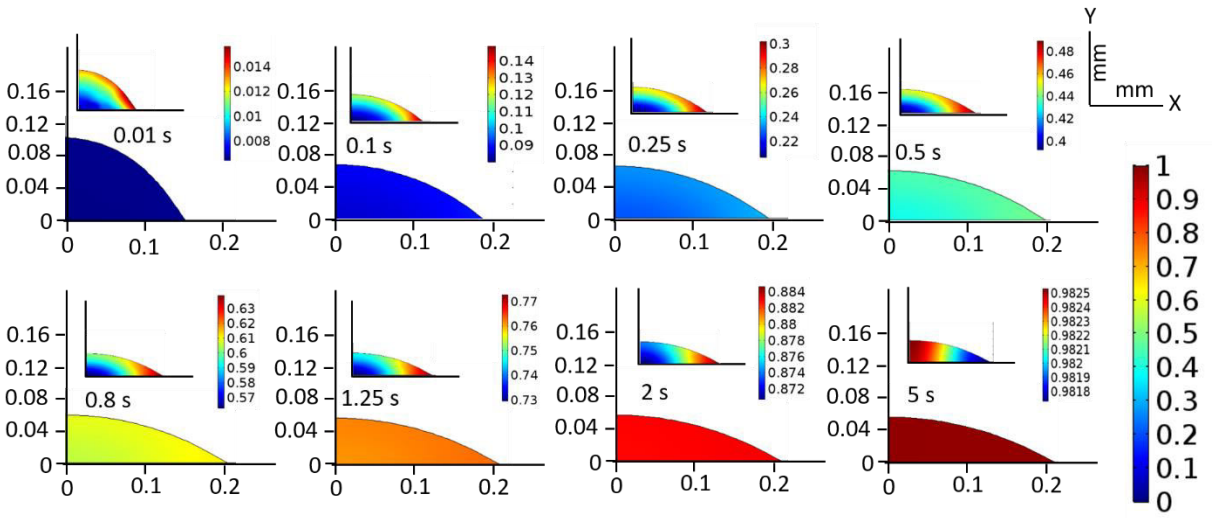

Figure A11: Curing profiles within the spreading polymer drop at different time instants for case 1 ($\tau_s << \tau_p$) for a drop of radius 0.1 mm. Here we have $\tau_s \approx 10.2$ ms and $\tau_p \approx 660$ ms.

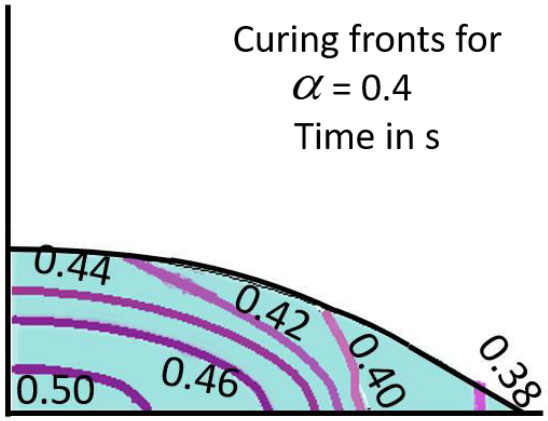

Figure A12: Progression of the curing front (corresponding to α=0.4) within the spreading polymer drop at different time instants for case 1 ($\tau_s << \tau_p$) for a drop of radius 0.1 mm. Here we have $\tau_s \approx 10.2$ ms and $\tau_p \approx 660$ ms.

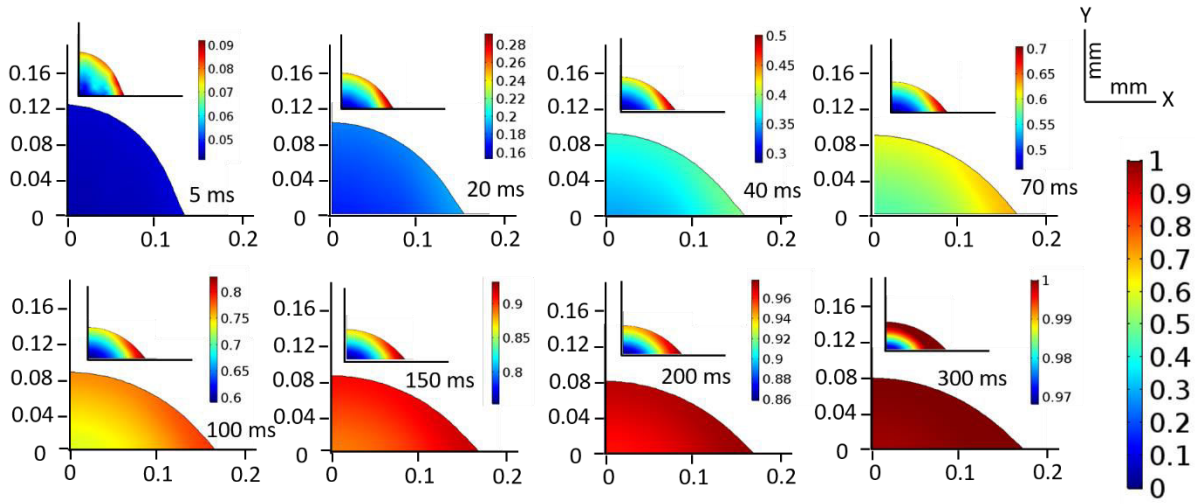

Figure A13: Curing profiles within the spreading polymer drop at different time instants for case 2 ($\tau_s \sim \tau_p$) for a drop of radius 0.1 mm. Here we have $\tau_s \approx 10.2$ ms and $\tau_p \approx 66$ ms. Here we have $\tau_s \approx 10.2$ ms and $\tau_p \approx 66$ ms.

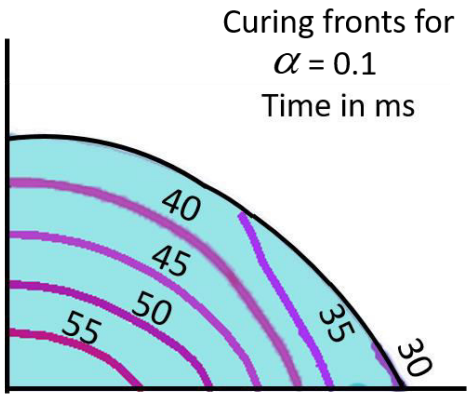

Figure A14: Progression of the curing front (corresponding to α=0.1) within the spreading polymer drop at different time instants for case 2 ($\tau_s \sim \tau_p$) for a drop of radius 0.1 mm. Here we have $\tau_s \approx 10.2$ ms and $\tau_p \approx 66$ ms.

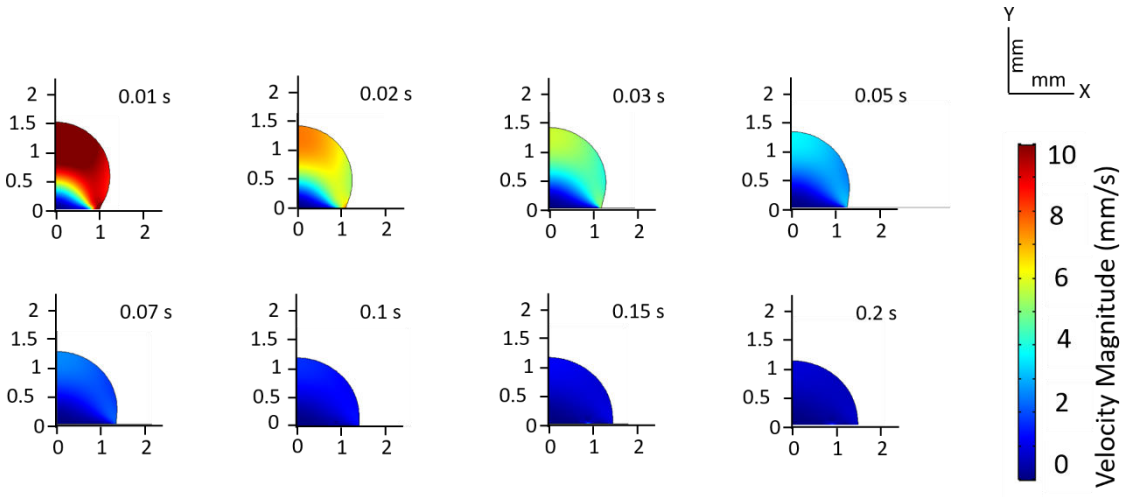

Figure A15: Velocity distribution within the spreading polymer drop at different time instants for case 1 ($\tau_s \ll \tau_p$) for a drop of radius 1 mm. Here we have $\tau_s \approx 107$ ms and $\tau_p \approx 1200$ ms. Velocity profiles within the air have not been shown for the sake of clarity.

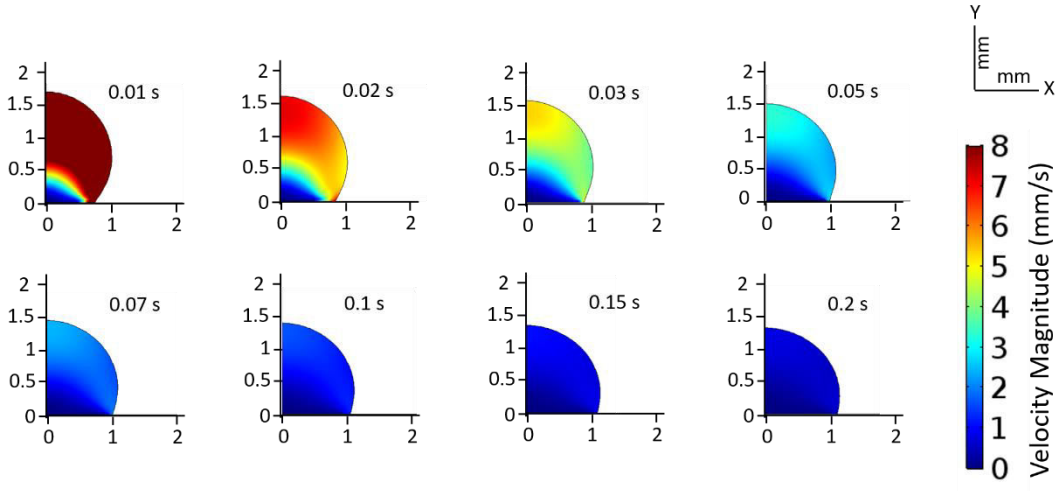

Figure A16: Velocity distribution within the spreading polymer drop at different time instants for case 1 ($\tau_s \sim \tau_p$) for a drop of radius 1 mm. Here we have $\tau_s \approx 107$ ms and $\tau_p \approx 660$ ms. Velocity profiles within the air have not been shown for the sake of clarity.

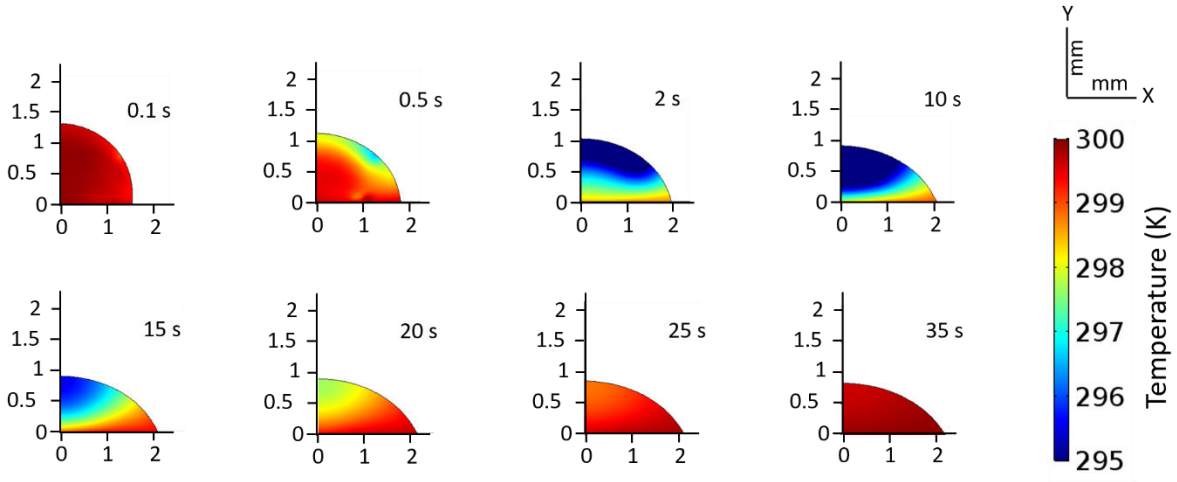

Figure A17: Temperature distribution within the spreading polymer drop at different time instants at different time instants for case 1 ($\tau_s << \tau_p$) for a drop of radius 1 mm. Here we have $\tau_s \approx 107$ ms and $\tau_p \approx 1200$ ms.

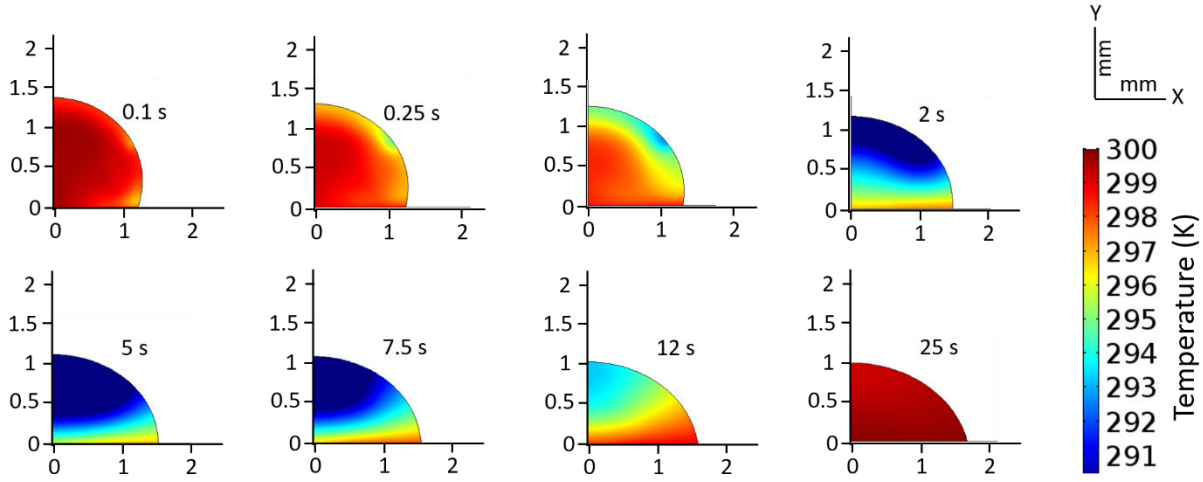

Figure A18: Temperature distribution within the spreading polymer drop at different time instants at different time instants for case 1 ($\tau_s \sim \tau_p$) for a drop of radius 1 mm. Here we have $\tau_s \approx 107$ ms and $\tau_p \approx 660$ ms.

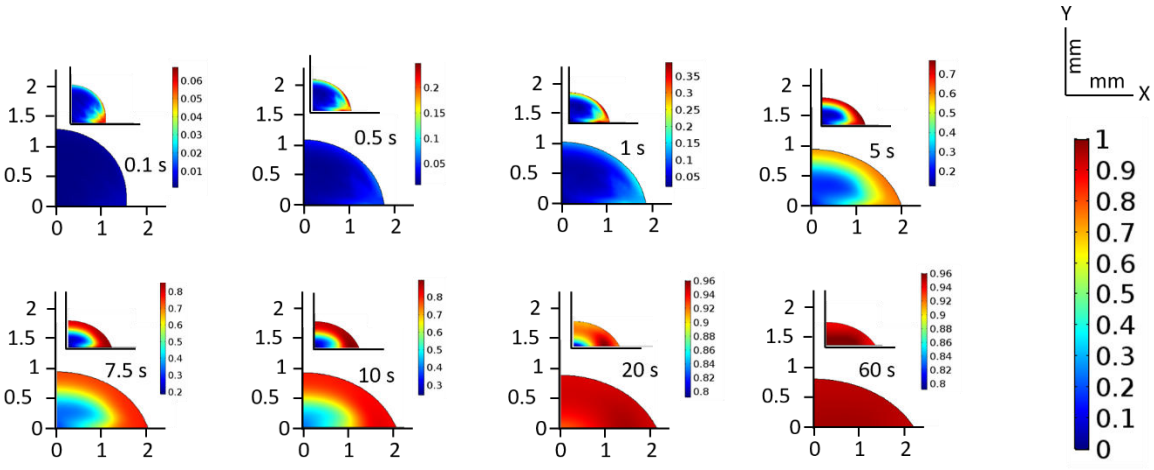

Figure A19: Curing profiles within the spreading polymer drop at different time instants for case 1 ($\tau_s << \tau_p$) for a drop of radius 1 mm. Here we have $\tau_s \approx 107$ ms and $\tau_p \approx 1200$ ms.

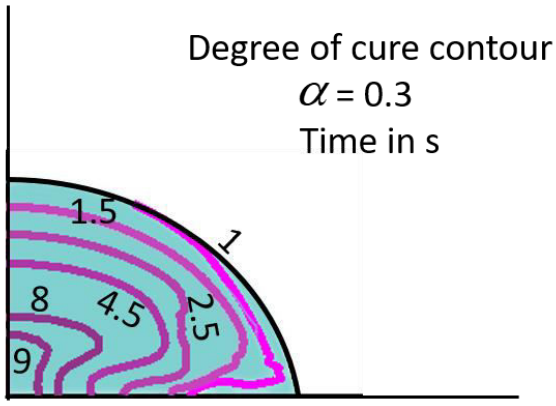

Figure A20: Progression of the curing front (corresponding to α=0.3) within the spreading polymer drop at different time instants for case 1 ($\tau_s << \tau_p$) for a drop of radius 1 mm. Here we have $\tau_s \approx 107$ ms and $\tau_p \approx 1200$ ms.

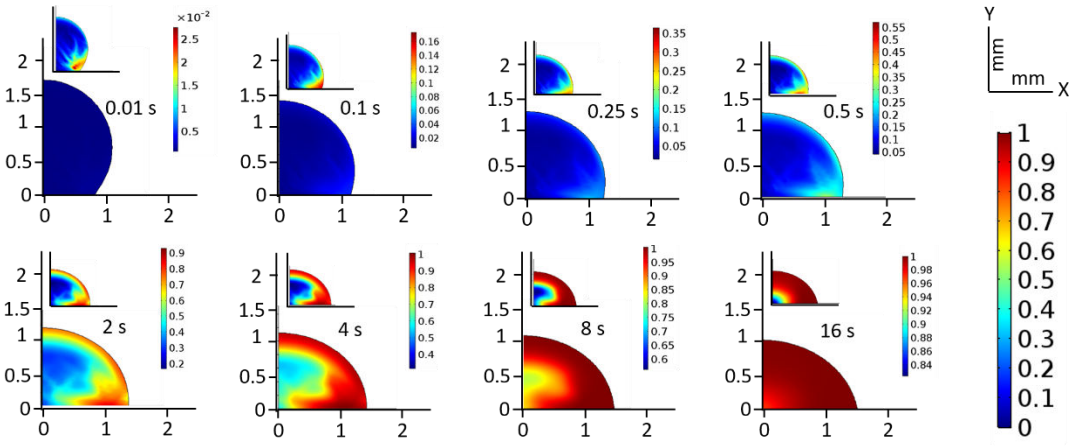

Figure A21: Curing profiles within the spreading polymer drop at different time instants for case 2 ($\tau_s \sim \tau_p$) for a drop of radius 1 mm. Here we have $\tau_s \approx 107$ ms and $\tau_p \approx 660$ ms.

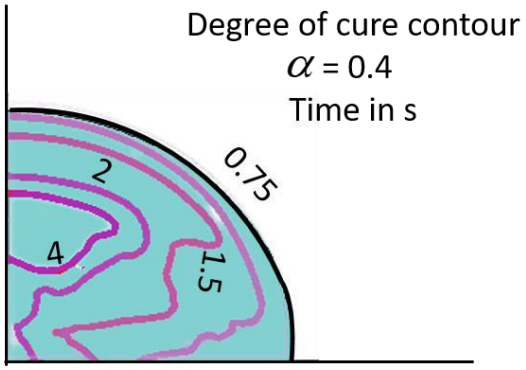

Figure A22: Progression of the curing front (corresponding to α=0.4) within the spreading polymer drop at different time instants for case 2 ($\tau_s \sim \tau_p$) for a drop of radius 1 mm. Here we have $\tau_s \approx 107$ ms and $\tau_p \approx 660$ ms.

Drop radius (mm)	**τ_c (miliseconds)**	**τ_s (miliseconds)**	**τ_p (miliseconds) for Case 1**	**τ_p (miliseconds) for Case 2**
1	7.21	107	660	1200
0.1	0.228	10.2	66	660
0.01	7.21×10^{-3}	1.1	66	3.3

Table A1: Different Timescales for Drops of Different Sizes

Table A2: Definition and values of the different parameters used for simulating the the 1-mm drop of 1 wt % of carboxymethylcellulose (CMC) solution (those that are not reported are identical to those reported in Table 2.1) (Here we don't have the literature for the values that dictate the polymerization process of the CMC drop; therefore, we have chosen these values to be such that ensures that $\tau_s << \tau_p$. Under such conditions, the exact values of these parameters don't matter as long as they ensure $\tau_s << \tau_p$)

Parameter	**Definition**	**Value**	**Reference**
ρ_m	Density of monomer	1590 [kg/m^3]	Ref. 57, 59, 73
ρ_p	Density of polymer	1750 [kg/m^3]	
m	Consistency index	7.234	
n	Power law index	0.5088	
σ	Surface tension of the drop/air interface	0.039 [N/m]	
θ	Contact angle	20^0	
k_l	Thermal conductivity of drop	0.603 [W/m/K]	Ref. 74
C_{pl}	Heat capacity (at constant pressure) of the drop	4250 [J/kg/K]	Ref. 75

H_r	Heat of polymerization reaction	-50 [kJ/mol]	Ref. 58
E_p	Activation energy for the propagation reaction	29.7 [kJ/mol]	
E_t	Activation energy for the termination reaction	22.2 [kJ/mol]	
A_{p*}	Frequency factor for the propagation reaction for case 1 ($\tau_s << \tau_p$)	2.5×10^9 [L/mol/s]	
A_{t*}	Frequency factor for the termination reaction	10^{11} [L/mol/s]	

Appendix B

Here we show the distribution of the magnitude of the non-dimensional velocity gradient $\nabla^* U^* \left(= \frac{\nabla U}{U_0/R}\right)$ inside and around the droplets at various instances during the coalescence of the droplets for a Weber number of We = 0. In Fig. B1, we observe that the shear rate (or the velocity gradient) is higher at times immediately after the impact which will lead to lower effective viscosity. However, we observe a much smaller shear rates at later stages of spreading leading to a higher viscosity at these times. Such a behavior is typical in the spreading of shear-thinning liquid.[236]

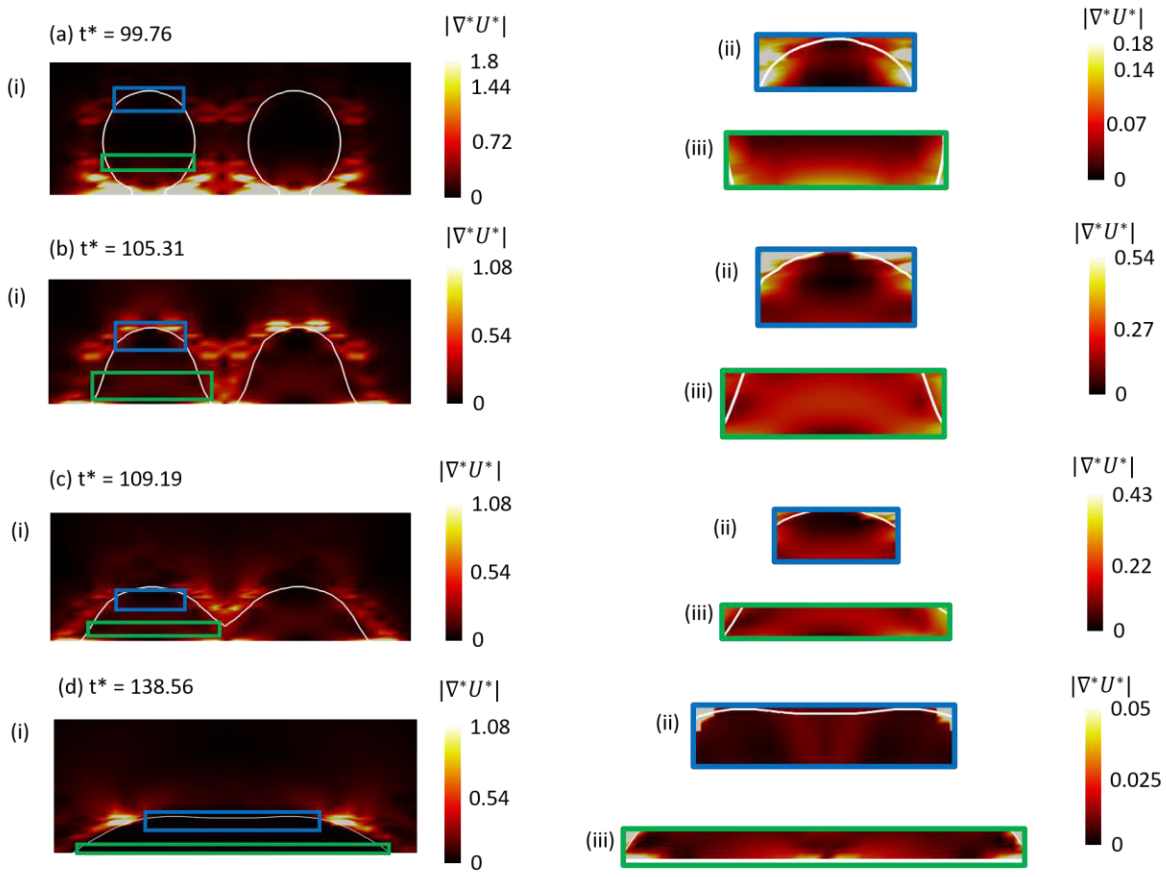

Figure B1: Variation of the magnitude of dimensionless velocity gradient ($|\nabla^* U^*|$) inside two polymeric and power-law obeying (with n=0.6) drops of radii 10 μm as well as inside the air in the immediate vicinity of the drops across a cross-section (i.e., the y-z plane) that passes through center of the drops (x=0) at different time instants (dimensionless) inside the coalescing drops for We=0. Here the dimensionless time is $t^* = \frac{t}{t_c}$, the dimensionless velocity gradient is $\nabla^* U^* = R\nabla(U/U_0)$ (where U_0=R/t_c is the characteristic velocity scale), and $t_c = \sqrt{\rho_1 R^3/\sigma}$ is the capillary time scale. Here, for different time instances, we show

distribution of the gradient over the entire drop in (i) and provide magnified views at locations near the top and bottom of the drop in (ii) and (iii) respectively.

Next, in order to properly estimate the mesh size required, we provide the plots to show the grid convergence of the study (see Fig. B2). For this purpose, we evaluate the evolution of the bridge height for the largest impact velocity that is studied here. From this figure, we can clearly observe that with number of cells as 5,625,000, the grid convergence is sufficiently obtained.

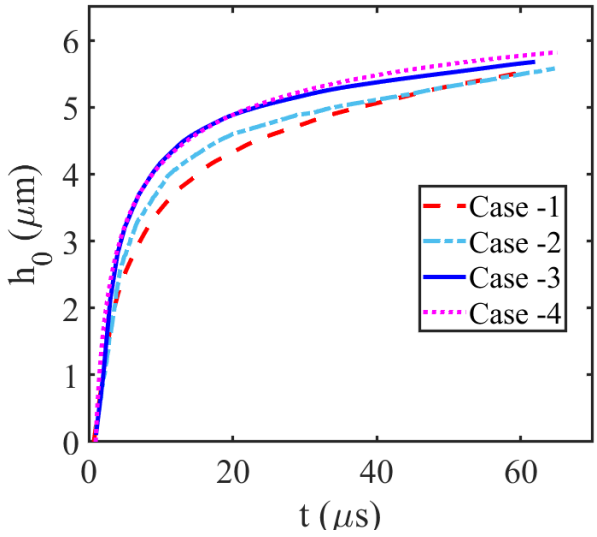

Figure B2: Figure showing the time evolution of the width of the bridge for different grid resolution. The number of cells for the four different cases are: Case 1: 1953125, Case 2: 2812500, Case 3: 5625000, Case 4: 1000000

Appendix C

C1. Grid convergence

In Fig. C1, we show the results of grid convergence study which was performed to obtain the optimum grid resolution for the problem. The evolution of the bridge width of the coalescing droplet over time was chosen as the parameter to study the grid convergence. This is chosen because the wall effects will be more apparent in the evolution of the bridge width. From this figure, we can clearly observe that with number of cells as 5,120,000, the grid convergence is sufficiently obtained.

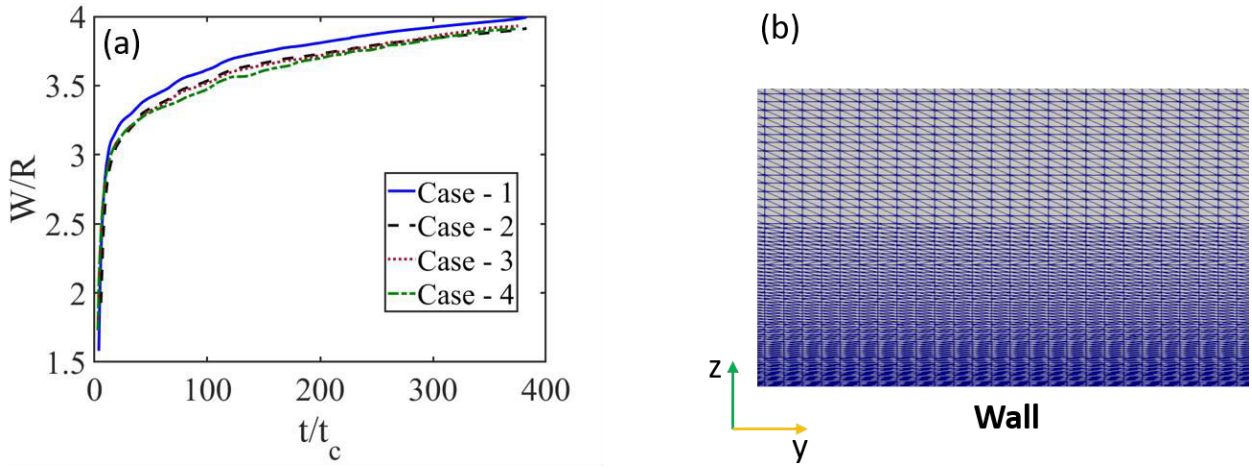

Figure C1: (a) Figure showing the time evolution of the width of the bridge for different grid resolution (denoted as different cases, namely, cases 1-4). The number of cells for the four different cases are: Case 1: 2560000, Case 2: 5120000, Case 3: 10240000, Case 4: 15360000. The grids near the walls are finer as shown in (b) and gradually reach a fixed

coarser value away from the wall. The grading and the size of the grid in z-direction is varied to obtain the grid convergence.

C2. Validation of the numerical model

In this section we provide the validation of our numerical model by comparing our findings with that provided in the numerical study by Borcia and Bestehorn.[140] In this study,[140] the authors investigated the coalescence dynamics of two droplets made of similar material but with different surface tension values (in other words all the parameters of the two drops were identical, except for their surface tension values). The comparison is done for 0.1 mm drops which are placed next to each other on a substrate with which the drops make a contact angle of 55°. We compare the drop profile obtained using our simulations with that provided in the study by Borcia et al. The snapshots presented in Fig. C2 show a good comparison.

Additionally, when viewed from a different direction, we see that the coalescence (for the case of the drops that are originally in partially wetted configurations) is characterized by the low-surface-tension drop *engulfing* the high-surface-tension drop (see Fig. C3): such an effect has been reported previously by Hack *et al.*[141] (studying the coalescence (without any substrate) of drops of different surface tension values) and provides us confidence in the validity of our simulation strategy.

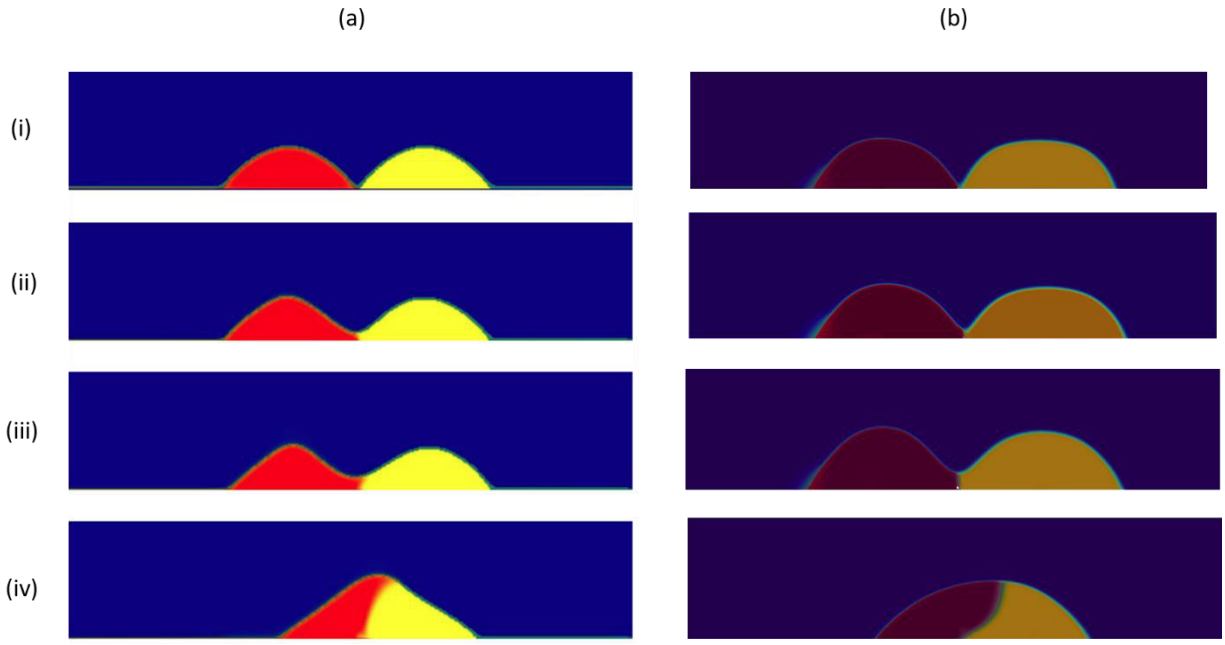

Figure C2*:* Snapshots showing the evolution of two drops of same material with same liquid properties but different surface tension values at time (i) t = 25 μs. (ii) t = 100 ms, (iii) t = 280 ms, and (iv) t = 600 ms. The subfigure (a) and (b) shows the snapshots of evolution of drops obtained from Borcia and Bestehorn[S1] and our simulation respectively. The properties used in this simulation are: density of the liquid drops, $\rho_l = 1000 kg/m^3$, density of the surrounding medium $\rho_s = 1\ kg/m^3$, kinematic viscosity of the liquid drops, $\nu_l = 10^{-5}\ m^2/s$, kinematic viscosity of the surrounding medium, $\nu_s = 10^{-5}\ m^2/s$, surface tension of drop-1 (left side), $\sigma_1 = 0.056\ N/m$, surface tension of drop-2 (right side), $\sigma_1 = 0.07\ N/m$. Figures in panel (a) have been reproduced from Borcia, R.; Bestehorn, M. Different behaviors of delayed fusion between drops with miscible liquids. *Phys. Rev. E* **2010**, *82*, 036312, DOI: 10.1103/PhysRevE.82.036312 (Reproduced with permission from reference 25. Copyright 2010, American Physical Society).

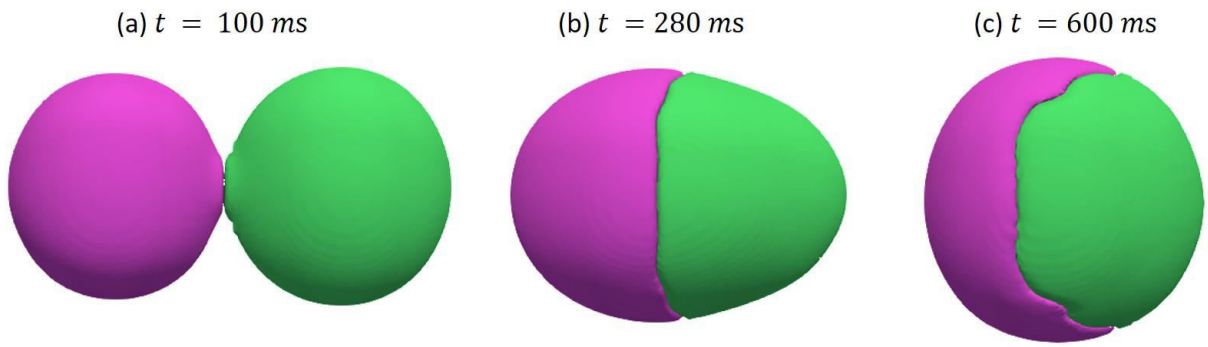

Figure C3*:* Snapshots showing the evolution of coalescence two drops of same material with same liquid properties but different surface tension values at time (a) t = 100 ms, (b) t = 280 ms, and (c) t = 600 ms. Properties used here are same as those mentioned in Fig. C2 (purple drop: left drop in Fig. C2; green drop: right drop in Fig. C2). Here, the top view of the coalescing droplets spreading on the substrate (i.e., same set-up as shown in Fig. C2) has been considered.

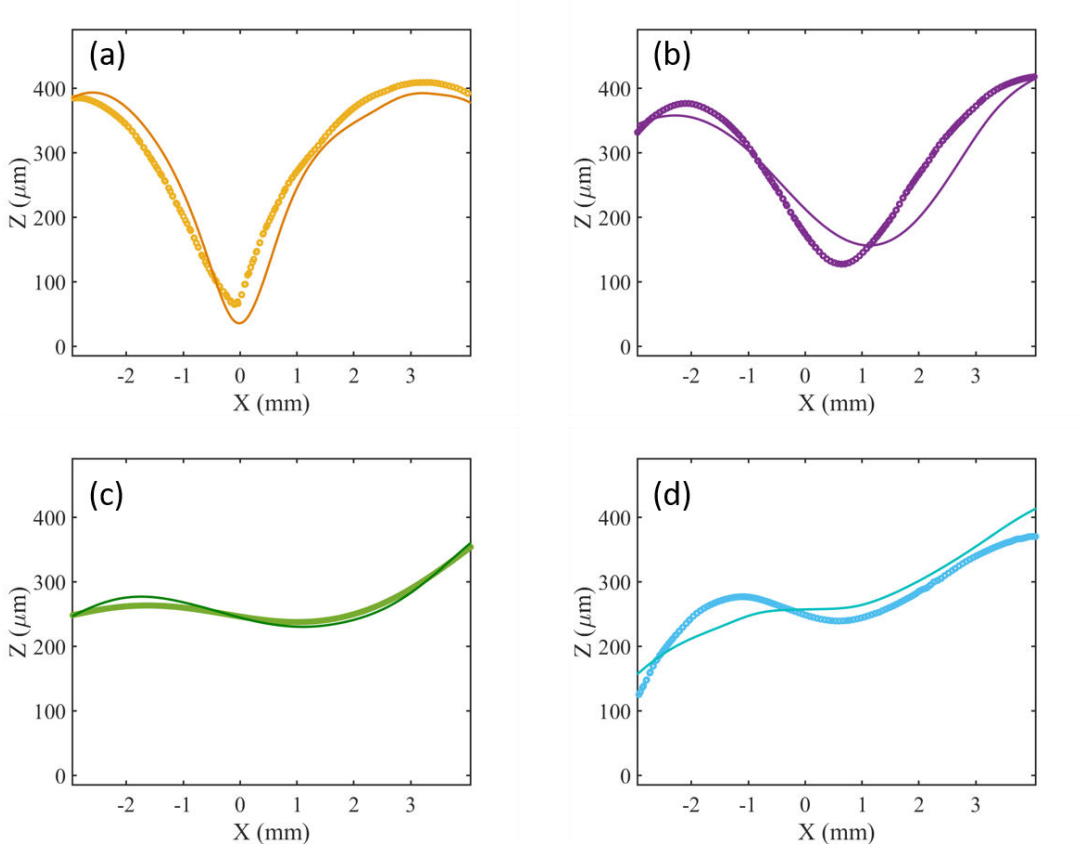

Figure C4: Comparison of the evolution of drop profiles (during the coalescence of two drops of different materials, namely drop 1: 45% 1,2-butanediol/water mixture and drop 2: 28% 1,2-butanediol/water mixture) obtained using our simulation (shown with circles) with that obtained in the experiments by Karpitschka and Riegler (the experimental results are shown by continuous lines).[136] The comparison has been shown for (a) t = 0 ms, (b) t = 320 ms, and (c) t = 810 ms, and (d) t = 1.4 s. The properties of the liquids of the two drops considered here are as follow: density of the liquid drops, $\rho_l = 1000 kg/m^3$ (both the drops), density of the surrounding medium $\rho_s = 1\ kg/m^3$, viscosity of the liquid drops, $\nu_{l1} = 2.3\ cP$, $\nu_{l1} = 4.35\ cP$, kinematic viscosity of the surrounding medium, $\nu_s = 10^{-5}\ m^2/s$, surface tension of drop-1 (left side), $\sigma_1 = 0.0354\ N/m$, surface tension of drop-2 (right side), $\sigma_2 = 0.0394\ N/m$.

Fig. C4 shows both qualitative and a reasonable quantitative match of the drop profiles (of two coalescing drops) obtained by our simulation with respect to the experimental observations recorded by Karpitschka and Riegler.[136] These two droplets are a drop of 45% 1,2-butanediol/water mixture and a drop of 28% 1,2-butanediol/water mixture. The liquids of these two drops have a surface tension difference of 4 mN/m. Of course, we find that there is some difference between the two profiles (profile obtained from our simulations and the experiments of Ref. C3) especially at later stages [see Fig. C4(d)]. This could be due to the uncertainty in the parameters due to the unavailability of information about (1) the contact angles of the two drops (average value of 16.5^0 as suggested in the study), (2) drop size (taken as R_1 = 1 mm and R_2 = 1.25 mm from the figure of fully spread droplet provided for the spreading radius in their work), and (3) distance between the drop centers at the point of release (from the figure of fully spread droplet).

Appendix D

D1. Validation of the numerical model

Here we aim to validate our VOF-based multiphase model. Currently, due to a lack of the experimental studies probing the *in-situ* photopolymerization of the spreading drop(s), we attempt to validate the model used in this study by comparing it against the findings from our previous computational study.[222] In that study,[222] we employed a different numerical model as compared to the present paper and investigated the dynamics of a single photocurable polymeric drop undergoing spreading in presence of *in-situ* photopolymerization. To test our present model, we use our present model to reproduce the results (provided in Ref. 222) of the spreading dynamics of a 10 μm polymeric drop (whose material properties are provided in Table 5.1) in the presence of in-situ photo-polymerization for the case where $\tau_p \sim \tau_s$ (see Fig. D1). The comparison confirms that there is an excellent match between the results provided in Ref. 222 and the results obtained using the VOF-based multiphase model used in this paper.

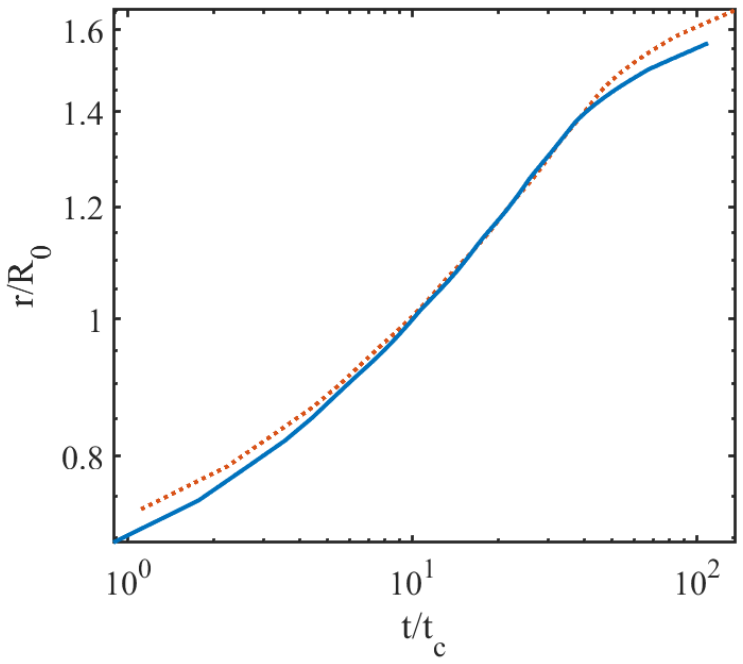

Figure D1: Comparison of the non-dimensional spreading radius of a 10 μm polymeric drop (properties of the drop have been provided in Table 5.1) in the presence of *in-situ* photopolymerization (for the case with $\tau_p \sim \tau_s$) generated by the VOF-based model used in this present study (this result is shown by solid blue line) with the corresponding results (shown by red dotted line) provided in the study by Sivasankar *et al.*[222] The dotted line been adapted with permission from Sivasankar, V. S.; Sachar, H. S.; Sinha, S.; Hines, D. R.; Das, S. 3D printed microdroplet curing: Unravelling the physics of on-spot photopolymerization. *ACS Appl. Polym. Mater.* **2020**, *2*, 966-976. Copyright (2020) American Chemical Society.

Bibliography

1. Schiller, G. J. (2015, March). Additive Manufacturing for Aerospace. In *2015 IEEE Aerospace Conference,* Big Sky, Montana, March 7-14, **2015**, pp. 1-8.
2. Dilberoglu, U. M.; Gharehpapagh, B.; Yaman, U.; Dolen, M. The Role of Additive Manufacturing in the Era of Industry 4.0. *Procedia Manuf.* **2017**, *11*, 545-554.
3. Sarvankar, S. G.; Yewale, S. N. Additive Manufacturing in Automobile Industry. *Int. J. Res. Aeronaut. Mech. Eng.* **2019**, *7*, 1-10
4. Chhaya, M. P.; Poh, P. S.; Balmayor, E. R.; Van Griensven, M.; Schantz, J. T.; Hutmacher, D. W. Additive Manufacturing in Biomedical Sciences and the Need for Definitions and Norms. *Expert Rev. Med. Devices* **2015**, *12*, 537-543.
5. Paolini, A.; Kollmannsberger, S.; Rank, E. Additive Manufacturing in Construction: A Review on Processes, Applications, and Digital Planning Methods. *Addit. Manuf.* **2019**, *30*, 100894.
6. Lu, B.; Lan, H.; Liu, H. Additive Manufacturing Frontier: 3D Printing Electronics. *Opto-Electron. Adv.* **2018**, *1*, 170004.
7. Sun, C.; Wang, Y.; McMurtrey, M. D.; Jerred, N. D.; Liou, F.; Li, J. Additive Manufacturing for Energy: A Review. *App. Energy* **2021**, *282*, 116041.
8. Lipton, J. I.; Cutler, M.; Nigl, F.; Cohen, D.; Lipson, H. Additive Manufacturing for the Food Industry. *Trends in food science & technology* **2015**, *43*, 114-123.
9. Pasandideh-Fard, M.; Chandra, S.; Mostaghimi, J. A Three-dimensional Model of Droplet Impact and Solidification. *Int. J. Heat Mass Transf.* **2002**, *45*, 2229-2242.

10. Bergmann, D.; Fritsching, U.; Bauckhage, K. A Mathematical Model for Cooling and Rapid Solidification of Molten Metal Droplets. *Int. J. Therm. Sci.* **2000**, *39*, 53-62.
11. Wang, C. H.; Tsai, H. L.; Wu, Y. C.; Hwang, W. S. Investigation of Molten Metal Droplet Deposition and Solidification for 3D Printing Techniques. *J. Micromech. Microeng.* **2016**, *26*, 095012.
12. Zhao, B.; Sivasankar, V. S.; Dasgupta, A.; Das, S. Ultrathin and Ultrasensitive Printed Carbon Nanotube-Based Temperature Sensors Capable of Repeated Uses on Surfaces of Widely Varying Curvatures and Wettabilities. *ACS Appl. Mater. Interfaces* **2021**, *13*, 10257-10270.
13. Zhao, B.; Sivasankar, V. S.; Subudhi, S. K.; Dasgupta, A.; Das, S. Printed Carbon Nanotube-Based Humidity Sensors Deployable on Surfaces of Widely Varying Curvatures. *ACS Appl. Nano Mater.* **2023***, 6*, 1459-1474.
14. Kamyshny, A.; Ben-Moshe, M.; Aviezer, S.; Magdassi, S. Ink-jet Printing of Metallic Nanoparticles and Microemulsions. *Macromol. Rapid Commun.* **2005**, *26*, 281-288.
15. Stieghorst, J.; Majaura, D.; Wevering, H.; Doll, T. Toward 3D Printing of Medical Implants: Reduced Lateral Droplet Spreading of Silicone Rubber Under Intense IR Curing. *ACS Appl. Mater. Interfaces* **2016**, *8*, 8239-8246.
16. Yu, X. J., Hu, R., Zhou, L. L., Wu, H., & Luo, X. B. Spreading and curing behaviors of a thermosetting droplet-silicone on a heated surface. *J. Harbin Institute Technol.* **2019**, *26*, 1-8.

17. De Ruiter, R.; Royon, L., Snoeijer, J. H.; Brunet, P. Drop Spreading and Gelation of Thermoresponsive Polymers. *Soft Matter* **2018**, *14*, 3096-3104.
18. Ngo, T. D.; Kashani, A.; Imbalzano, G.; Nguyen, K. T.; Hui, D. Additive Manufacturing (3D Printing): A Review of Materials, Methods, Applications and Challenges. *Compos. B. Eng.* **2018**, *143*, 172-196.
19. Gudapati, H.; Dey, M.; Ozbolat, I. A Comprehensive Review on Droplet-Based Bioprinting: Past, Present and Future. *Biomaterials* **2016**, *102*, 20-42.
20. Salary, R. R.; Lombardi, J.; Weerawarne, D.; Rao, P.; Poliks, M. D. A Computational Fluid Dynamics Investigation of Pneumatic Atomization, Aerosol Transport and Deposition in Aerosol Jet Printing Process. *J Micro. Nanomanuf.* **2021**, *9,* 010903.
21. Mette, A.; Richter, P. L.; Hörteis, M.; Glunz, S. W. Metal Aerosol Jet Printing for Solar Cell Metallization. *Prog. Photovolt. Res. Appl.* **2007**, *15*, 621-627.
22. Raje, P. V.; Murmu, N. C. (2014). A Review on Electrohydrodynamic Inkjet Printing Technology. *Int. J. Emerg. Tech. Adv. Eng.* **2014**, *4*, 174-183
23. Hoath, S. D. (Ed.). Fundamentals of Inkjet Printing: the Science of Inkjet and Droplets. John Wiley & Sons, **2016**.
24. Wadhwa, A. Run-Time Ink Stability in Pneumatic Aerosol Jet Printing Using a Split Stream Solvent Add Back System. Masters Thesis, Rochester Institute of Technology, Rochester, NY, **2015**. https://www.proquest.com/docview/1675025259?pqorigsite=gscholar&fromopenview=true (accessed 2023-03-03).

25. Zhao, B.; Sivasankar, V. S.; Subudhi, S. K.; Sinha, S.; Dasgupta, A.; Das, S. Applications, Fluid Mechanics, and Colloidal Science of Carbon-Nanotube-Based 3D Printable Inks. *Nanoscale* **2022**, *14*, 14858-14894.
26. Chen, G.; Gu, Y., Tsang, H.; Hines, D. R.; Das, S. The effect of droplet Sizes on overspray in aerosol-jet printing. *Adv. Eng. Mater.* **2018**, *20*, 1701084.
27. Friedrich, L.; Collino, R.; Ray, T.; Begley, M. Acoustic Control of Microstructures During Direct Ink Writing of Two-Phase Materials. *Sens. Actuator A Phys.* ***2017*** *268*, 213-221.
28. Guo, Q.; Ghadiri, R.; Weigel, T.; Aumann, A.; Gurevich, E. L.; Esen, C.; Medenbach, O.; Cheng, W.; Chichkov, B.; Ostendorf, A. Comparison of in Situ and ex Situ Methods for Synthesis of Two-Photon Polymerization Polymer Nanocomposites. *Polymers* **2014**, *6*, 2037−2050.
29. Haraguchi, K.; Takada, T. Synthesis and Characteristics of Nanocomposite Gels Prepared by In Situ Photopolymerization in an Aqueous System. *Macromolecules* **2010**, *43*, 4294−4299.
30. Choi, C-H.; Hwang, S.; Jeong, J-M.; Kang, S-M.; Kim, J.; Lee, C-S. Microfluidic Synthesis of Anisotropic Particles from Janus Drop by *in situ* Photopolymerization. *Biomed. Eng. Lett.* **2012**, *2*, 95−99.
31. Saito, Y.; Fukuri, N.; Senadeera, R.; Kitamura, T.; Wada, Y.; Yanagida, S. Solid State Dye Sensitized Solar Cells using in situ Polymerized PEDOTs as Hole Conductor. *Electrochem. Comm.* **2004**, *6*, 71−74.
32. Bella, F.; Sacco, A.; Salvador, G. P.; Bianco, S.; Tresso, E.; Pirri, C. F.; Bongiovanni, R. First Pseudohalogen Polymer Electrolyte for Dye-sensitized Solar

Cells Promising for in situ Photopolymerization. *J. Phys. Chem. C* **2013**, *117*, 20421-20430.

33. Pham, H. D.; Pham, V. H.; Oh, E. S.; Chung, J. S.; Kim, S. Synthesis of Polypyrrole-Reduced Graphene Oxide Composites by in-situ Photopolymerization and its Application as a Supercapacitor Electrode. *Korean J. Chem. Eng.* **2012**, *29*, 125−129.
34. Stepniak, I.; Andrzejewska, E.; Dembna, A.; Galinski, M. Characterization and Application of N-methyl-N-propylpiperidinium bis (trifluoromethanesulfonyl) imide Ionic Liquid–based gel Polymer Electrolyte prepared in situ by Photopolymerization Method in Lithium Ion Batteries. *Electrochim. Acta* **2014**, *121*, 27−33.
35. Kim, D-Y.; Lee, K. M.; White, T. J.; Jeong, K-U. Cholesteric Liquid Crystal Paints: In situ Photopolymerization of Helicoidally Stacked Multilayer Nanostructures for Flexible Broadband Mirrors. *NPG Asia Mater.* **2018**, *10*, 1061–1068.
36. Vigna, L.; Fasoli, A.; Cocuzza, M.; Pirri, F. C.; Bozano, L. D.; Sangermano, M. A Flexible, Highly Sensitive, and Selective Chemiresistive Gas Sensor Obtained by In Situ Photopolymerization of an Acrylic Resin in the Presence of MWCNTs. *Macromol. Mater. Eng.* **2019**, *304*, 1800453.
37. Su, P-G.; Peng, Y-T. Fabrication of a Room-temperature H_2S Gas Sensor based on PPy/WO_3 Nanocomposite Films by *in-situ* Photopolymerization. *Sens. Actuat. B* **2014**, *193*, 637–643.
38. Niu, Q.; Zeng, L.; Mu, X.; Nie, J.; Ma, G. Preparation and Characterization of Core-shell Nanofibers by Electrospinning Combined with *in situ* UV

Photopolymerization. *J. Ind. Eng. Chem.* **2016**, *34*, 337–343.

39. Kip, C.; Liu, S.; Fu, X.; Tuncel, A.; Lämmerhofer, M. In-situ Photopolymerized C4-functionalized Organosilicon Monoliths for Reversed-phase Protein Separation in Nano-liquid Chromatography. *Talanta* **2019***, 198*, 330–336.
40. LeValley, P. J.; Noren, B.; Kharkar, P. M.; Kloxin, A. M.; Gatlin, J. C.; Oakey, J. S. Fabrication of Functional Biomaterial Microstructures by in-situ Photopolymerization and Photodegradation. *ACS Biomater. Sci. Eng.* **2018**, *4*, 3078−3087.
41. Lin, R. Z.; Chen, Y. C.; Moreno-Luna, R.; Khademhosseini, A.; Melero-Martin, J. M. Transdermal Regulation of Vascular Network Bioengineering Using a Photopolymerizable Methacrylated Gelatin Hydrogel. *Biomater.* **2013**, *34*, 6785−6796.
42. Shinde, U. P.; Yeon, B.; Jeong, B. Recent Progress of in-situ Formed Gels for Biomedical Applications. *Prog. Polymer Sci.* **2013**, *38*, 672−701.
43. Nazar, R.; Ronchetti, S.; Roppolo, I.; Sangermano, M.; Bongiovanni, R. M. In-situ Synthesis of Polymer Embedded Silver Nanoparticles via Photopolymerization. *Macromol. Mater. Eng.* **2015**, *300*, 226-233.
44. Censi, R.; Di Martino, P.; Vermonden, T.; Hennink, W. E. Hydrogels for Protein Delivery in Tissue Engineering. *J. Control. Rel.* **2012**, *161*, 680-692.
45. Zang, L.; Qiu, J.; Yang, C.; Sakai, E. Preparation and Application of Conducting Polymer/Ag/clay Composite Nanoparticles formed by in situ UV-induced Dispersion Polymerization. *Sci. Rep.* **2016**, *6*, 20470.
46. Layani, M.; Wang, X.; Magdassi, S. Novel Materials for 3D Printing by

Photopolymerization. *Adv. Mater.* **2018**, *30*, e1706344.

47. Ligon, S. C.; Liska, R.; Stampfl, J.; Gurr, M.; Mülhaupt, R. Polymers for 3D Printing and Customized Additive Manufacturing. *Chem. Rev.* **2017**, *117*, 10212-10290.
48. Stansbury, J. W.; Idacavage, M. J. 3D Printing with Polymers: Challenges among Expanding Options and Opportunities. *Dent. Mater.* **2016**, *32*, 54-64.
49. Lee, J. Y.; An, J.; Chua, C. K. Fundamentals and Applications of 3D Printing for Novel Materials. *Appl. Mater. Today* **2017**, *7*, 120-133.
50. Liska, R.; Schuster, M.; Infuhr, R.; Turecek, C.; Fritscher, C.; Seidl, B.; Schmidt, V.; Kuna, L.; Lichtenegger, H. Photopolymers for Rapid Prototyping. *J. Coating. Tech. Res.* **2007***, 4*, 505-510.
51. Gu, Y.; Hines, D. R.; Yun, V.; Antoniak, M.; Das, S. Aerosol-Jet Printed Fillets for Well-Formed Electrical Connections between Different Leveled Surfaces. *Adv. Mater. Technol.* **2017**, *2*, 1700178.
52. Gu, Y.; Park, D.; Bowen, D.; Das, S.; Hines, D. R. Direct-Write Printed, Solid-Core Solenoid Inductors with Commercially Relevant Inductances. *Adv. Mater. Technol.* **2018**, *3*, 1800312.
53. Gu, Y.; Gutierrez, D.; Das, S.; Hines, D. R. Inkwells for On-demand Deposition Rate Measurement in Aerosol-jet based 3D Printing. *J. Micromech. Microeng.* **2017**, *27*, 097001.
54. Huang, Y.; Wu, H.; Xiao, L.; Duan, Y.; Zhu, H.; Bian, J.; Ye, D.; Yin, Z. Huang, Y.; Wu, H.; Xiao, L.; Duan, Y.; Zhu, H.; Bian, J.; Ye, D.; Yin, Z. Assembly and Applications of 3D Conformal Electronics on Curvilinear Surfaces. *Mater.*

Horizons **2019**, *9*, **6**, 642-683.

55. Hubert, P.; Johnston, A.; Poursartip, A.; Nelson, K. Cure Kinetics and Viscosity Models for Hexcel 8552 Epoxy Resin. *Int. SAMPE Symp. Exhibit.* **2001,** 2341-2354.
56. Saki, T. A. Reactive Melt Blending of Low-density Polyethylene with Poly (acrylic acid)." *Arab. J. Chem.* **2015**, *8*, 191-199.
57. Tang, Y. Stereolithography Cure Process Modeling. Ph.D. Dissertation, Georgia Institute of Technology, Atlanta, GA, **2005**. https://www.proquest.com/docview/305000048?pqorigsite=gscholar&fromopenview=true (accessed on 2023-03-03)
58. Odian, G. *Principles of Polymerization*. John Wiley & Sons, **2004**.
59. Goodner, M. D.; Bowman, C. N. Development of a Comprehensive Free Radical Photopolymerization Model Incorporating Heat and Mass Transfer Effects in Thick Films. *Chem. Eng. Sci.* **2002**, *57*, 887-900.
60. Morancho, J., Cadenato, A.; Fernández-Francos, X.; Salla, J.; Ramis, X. Isothermal Kinetics of Photopolymerization and Thermal Polymerization of bis-GMA/TEGDMA Resins. *J. Ther. Anal. Calorimet*. **2008**, 92, 513-522.
61. McCree, K. J. Test of Current Definitions of Photosynthetically Active Radiation against Leaf Photosynthesis Data. *J. Agric. Meteorol.* **1972**, *10*, 443– 453
62. Noble, D. R.; Kucala, A.; Martinez, M. J. A Conformal Decomposition Finite Element Method for Dynamic Wetting Applications. In ASME 2017, Fluids Engineering Division Summer Meeting, Waikoloa, HI, July 30 – August 3, 2017. American Society of Mechanical Engineers Digital Collection, USA, **2017**; Vol.

58059, pp. V01BT11A023. https://doi.org/10.1115/FEDSM2017-69378.

63. https://doc.comsol.com/5.4/doc/com.comsol.help.cfd/CFDModuleUsersGuide.pdf (accessed on 2023-03-03)
64. Venkatesan, J.; Ganesan, S. On the Navier-slip Boundary Condition for Computations of Impinging Droplets. In IEEE 2015, 22nd International Conference on High Performance Computing Workshops, Bengaluru, India, December 16 -19, 2015. IEEE, India, 2016; pp. 2-11. DOI: 10.1109/HiPCW.2015.10
65. Hossain, M. Modelling and Computation of Polymer Curing. Ph.D. Dissertation, Technical Faculty Erlangen, Erlangen, Germany, **2010**, https://www.proquest.com/docview/1962308791?pqorigsite=gscholar&fromopenview=true (accessed on 2023-03-03)
66. https://www.crystran.co.uk/optical-materials/silica-glass-sio2
67. de Beer, M. P., van der Laan, H. L., Cole, M. A., Whelan, R. J., Burns, M. A., & Scott, T. F. Rapid, Continuous Additive Manufacturing by Volumetric Polymerization Inhibition Patterning. *Sci. Adv*. **2019**, *5*, eaau8723.
68. Yamaguchi, T.; Wang, B. G.; Matsuda, E.; Suzuki, S.; Nakao, S. I. Prediction and Estimation of Solvent Diffusivities in Polyacrylate and Polymethacrylates. *J. Polymer Sci. Part B: Polymer Physics*. **2003**, 41, 1393-1400.
69. Capek, I. Photopolymerization of Acrylamide in the very Low Monomer Concentration Range. *Designed Mono. Polym.* **2016**, *19*, 290-296.

70. Courbin, L.; Bird, J. C.; Reyssat, M.; Stone, H. A. Dynamics of Wetting: From Inertial Spreading to viscous Imbibition. *J. Phys. Condens. Matter*, **2009**, *21*(46), 464127.

71. de Ruijter, M. J.; J. D. Coninck, Oshanin, G. Droplet Spreading: Partial Wetting Regime Revisited. *Langmuir* **1999**, *15*, 2209-2216.

72. Han, J.; Kim, C. Spreading of Boger fluid on Horizontal Surface. *J. Non-Newtonian Fluid Mech.* **2013**, *202*, 120-130.

73. Wang, X. D.; Zhang, Y.; Lee, D. J.; Peng, X. F. Spreading of Completely Wetting or Partially Wetting Power-law Fluid on Solid Surface. *Langmuir*, **2007**, *23*, 9258-9262.

74. Lee, W. Y.; Cho, Y. I.; Hartnett, J. P. Thermal Conductivity Measurements of non-Newtonian Fluids. *J. Heat Mass Transfer*, **1981**, *8*, 255-259.

75. Semmar, N.; Tanguier, J. L.; Rigo, M. O. Specific Heat of Carboxymethyl Cellulose and Carbopol Aqueous Solutions. *Thermochim. Acta*, **2003**, *402*, 225-235.

76. Tian, K.; Bae, J.; Bakarich, S. E.; Yang, C.; Gately, R. D.; Sprinks, G. M.; Panhuis, M.; Suo, Z.; Vlassak, J. J. 3D Printing of Transparent and Conductive Heterogeneous Hydrogel–Elastomer Systems**.** *Adv. Mater.* **2017**, *29*, 1604827**.**

77. Rahman, T.; Renaud, L.; Heo, D.; Renn, M.; Panat, R. Aerosol based Direct-write Micro-additive Fabrication Method for sub-mm 3D Metal-dielectric structures. *J. Micromech. Microeng.* **2015**, *25*, 107002.

78. Sun, H.; Kim, Y.; Kim, Y. C.; Park, I. K.; Suhr, J.; Byun, D.; Choi, H. R.; Kuk, K.; Baek, O. H.; Jung, Y. K.; Choi, H. J.; Kim, K. J.; Nam, J. D. Self-standing and

Shape-memorable UV-curing Epoxy Polymers for Three-dimensional (3D) Continuous-filament Printing. *J. Mater. Chem. C* **2018**, *6*, 2996-3003.

79. Gu, Y.; Park, D.; Gonya, S.; Jendrisak, J.; Das, S.; Hines, D. R. Direct-write Printed Broadband Inductors. *Additive Manuf.* **2019**, *30*, 100843.
80. Salary, R. R.; Lombardi, J. P.; Tootooni, M. S.; Donovan, R.; Rao, P. K.; Borgesen, P.; Poliks, M. D. Computational Fluid Dynamics Modeling and Online Monitoring of Aerosol Jet Printing Process. *ASME J. Manuf. Sci. Eng.* **2017**, *139*, 021015.
81. Secor, E. B. Principles of Aerosol Jet Printing. *Flex. Print. Electron.* **2018**, *3*, 035002**.**
82. Secor, E. B. Guided Ink and Process Design for Aerosol Jet Printing based on Annular Drying Effects. *Flex. Print. Electron.* **2018**, *3*, 035007.
83. Hernandez-Sanchez, J. F.; Lubbers, L. A.; Eddi, A.; Snoeijer, J. H. Symmetric and Asymmetric Coalescence of Drops on a Substrate. *Phys. Rev. Lett.* **2012**, 109, 184502.
84. Eggers, J.; Lister, J. R.; Stone, H. A. Coalescence of Liquid Drops. *J. Fluid Mech.* **1999**, 401, 293-310.
85. Hopper, R. W. Plane Stokes Flow Driven by Capillarity on a Free Surface. *J. Fluid Mech.* **1990**, 213, 349-375.
86. Thoroddsen, S. T.; Takehara, K.; Etoh, T. G. The coalescence speed of a pendent and a sessile drop. *J. Fluid Mech.* **2005**, 527, 85-114.
87. Aarts, D. G. A. L.; Lekkerkerker, H. N. W.; Guo, H.; Wegdam, G. H.; Bonn, D. Hydrodynamics of Droplet Coalescence. *Phys. Rev. Lett.* **2005**, 95, 164503.
88. Duchemin, L.; Eggers, J.; Josserand, C. Inviscid Coalescence of Drops, *J. Fluid*

Mech. **2003**, 487, 167-178.

89. Yao, W.; Maris, H. J.; Pennington, P.; Seidel, G. M. Coalescence of Viscous Liquid Drops. *Phys. Rev. E* **2005**, 71, 016309.
90. Sprittles, J. E.; and Shikhmurzaev, Y. D. Coalescence of Liquid Drops: Different Models versus Experiment. *Phys. Fluid.* **2012**, 24, 122105.
91. Kavehpour, H. P. Coalescence of Drops, *Annu. Rev. Fluid. Mech.* **2015**, 47, 245-268.
92. Paulsen, J. D.; Burton, J. C.; Nagel, S. R. Viscous to Inertial Crossover in Liquid Drop Coalescence. *Phys. Rev. Lett.*, 2011, **106**, 114501.
93. Anthony, C. R.; Harris, M. T.; Basaran, O. A. Initial Regime of Drop Coalescence. *Phys. Rev. Fluid.* **2020**, 5, 033608.
94. Paulsen, J. D.; Burton, J. C.; Nagel, S. R.; Appathuri, S.; Harris, M. T.; Basaran, O. A. The Inexorable Resistance of Inertia Determines the Initial Regime of Drop Coalescence. *Proc. Natl. Acad. Sci. USA* **2012**, 109, 6857-6861.
95. Sprittles, J. E.; Shikhmurzaev, Y. D.; Dynamics of Liquid Drops Coalescing in the Inertial Regime. *Phys. Rev. E* **2014**, 89, 063008.
96. Baroudi, L.; Kawaji, M.; Lee, T. Effects of Initial Conditions on the Simulation of Inertial Coalescence of Two Drops. *Comput. Math. Appl.* **2014**, 67, 282-289.
97. Xia, X.; He, C.; Zhang, P. Universality in the Viscous-to-Inertial Coalescence of Liquid Droplets. *Proc. Natl. Acad. Sci. USA* **2019**, 116, 23467-23472.
98. Fezzaa, K.; Wang, Y. Ultrafast X-Ray Phase-Contrast Imaging of the Initial Coalescence Phase of Two Water Droplets. *Phys. Rev. Lett.* **2008**, 100, 104501.
99. Ristenpart, W. D.; McCalla, P. M.; Roy, R. V.; Stone, H. A. Coalescence of

Spreading Droplets on a Wettable Substrate. *Phys. Rev. Lett.* **2006**, 97, 064501.

100. Burton, J. C.; Taborek, P. Role of Dimensionality and Axisymmetry in Fluid Pinch-Off and Coalescence. *Phys. Rev. Lett.* **2007**, 98, 224502.

101. Paulsen, J. D. Approach and Coalescence of Liquid Drops in Air. *Phys. Rev. E* **2013**, 88, 063010.

102. Sprittles, J. E.; Shikhmurzaev, Y. D.; A Parametric Study of the Coalescence of Liquid Drops in a Viscous Gas. *J. Fluid Mech.* **2019**, 753, 279-306.

103. Paulsen, J. D.; Carmigniani, R.; Kannan, A.; Burton, J. C.; Nagel, S. R. Coalescence of Bubbles and Drops in an Outer fluid. *Nat. Commun.* **2014,** 5, 1-7.

104. Oguz, H. N.; Prosperetti, A.; Surface-tension Effects in the Contact of Liquid Surfaces. *J. Fluid Mech.* **1989**, 203, 149-171.

105. Menchaca-Rocha, A.; Martínez-Dávalos, A.; Núñez, R.; Popinet, S.; Zaleski, S. Coalescence of Liquid Drops by Surface Tension. *Phys. Rev. E* **2001**, 63, 046309.

106. Case, S. C.; S. R. Nagel, S. R. Coalescence in Low-Viscosity Liquids. *Phys. Rev. Lett.* **2008**, 100, 084503.

107. Villermaux, E.; Bossa, B. Single-drop Fragmentation Determines Size Distribution of Raindrops. *Nature Phys.* **2009**, 5, 697-702.

108. Smith, P. L.; Musil, D. J.; Detwiler, A. G.; Ramachandran, R. Observations of Mixed-Phase Precipitation within a CaPE Thunderstorm. *J. Appl. Meteorol.* **1999**, 38, 145–155.

109. van Dongen, M. H. A.; van Loon, A.; Vrancken, R. J.; Bernards, J. P. C.; Dijksman, J. F. UV-Mediated Coalescence and Mixing of Inkjet Printed Drops. *Exp. Fluid.* **2014**, 55, 1744.

110. Klestova, A.; Sergeeva, E.; Vinogradov, A. V. Inkjet Printing in Liquid Media: Intra-Volumetric Drop Coalescence in Polymers. *Coatings* **2019**, 9, 275.

111. Wilkinson, N. J.; Smith, M. A. A.; Kay, R. W.; Harris, R. A. A Review of Aerosol Jet Printing—A Non-traditional Hybrid Process for Micro-manufacturing. *Int. J. Adv. Manuf. Technol.* **2019**, 105, 4599-4619.

112. Carrier, V.; Colin, A. Coalescence in Draining Foams. *Langmuir* **2003**, 19, 4535-4538.

113. Tcholakova, S.; Denkov, N. D.; Ivanov, I. B.; Campbell, B. Coalescence Stability of Emulsions Containing Globular Milk Proteins. *Adv. Colloid Interface Sci.* **2006**, 123, 259-293.

114. Mahdi, K.; Gheshlaghi, R.; Zahedi, G.; Lohi, A. Characterization and Modeling of a Crude Oil Desalting Plant by a Statistically Designed Approach. *J. Petrol. Sci. Eng.* **2008**, 61, 116-123.

115. Sundararaj U.; Macosko, C. W. Drop Breakup and Coalescence in Polymer Blends: The Effects of Concentration and Compatibilization. *Macromolecules* **1995**, 28, 2647-2657.

116. Varma, S. C.; Saha, A.; Mukherjee, S.; Bandopadhyay, A.; Kumar, A.; Chakraborty, S. Universality in coalescence of polymeric fluids. *Soft Matter*, **2020**, 16, 10921-10927.

117. Finotello, G.; De, S.; Vrouwenvelder, J. C. R.; Paddin, J. T.; Buist, K. A.; Jongsma, A.; Innings, F.; Kuipers, J. A. M. Experimental Investigation of non-Newtonian Droplet Collisions: The Role of Extensional Viscosity. *Exp. Fluid.* **2018**, 59, 113.

118. Verdier, C. Coalescence of Polymer Droplets: Experiments on Collision. *C. R.*

Acad. Sci. Paris. Series IV **2000**, 1, 119-126.

119. Lee, M. W.; Kang, D. K.; Yoon, S. S.; Yarin, A. L. Coalescence of Two Drops on Partially Wettable Substrates. *Langmuir* **2012**, 28, 3791-3798.
120. Clanet, C.; Béguin, C.; Richard, D.; Quéré, D. Maximal deformation of an impacting drop. *J. Fluid Mech.* **2004**, *517*, 199.
121. https://openfoam.org (accessed on 2023-03-03)
122. Brackbill, J. U.; Kothe, D. B.; Zemach, C. A Continuum Method for Modeling Surface Tension. *J. Comput. Phys.* **1992**, 100, 335-354.
123. Saha, A. A.; Mitra, S. K. Effect of Dynamic Contact Angle in a Volume of Fluid (VOF) Model for a Microfluidic Capillary Flow. *J. Colloid Interface Sci.* **2009**, 339, 461-480.
124. Gründing, D.; Smuda, M.; Antritter, T.; Fricke, M.; Rettenmaier, D.; Kummer, F.; Stephan, F., P.; Marschall, H.; Bothe, D. A Comparative Study of Transient Capillary Rise Using Direct Numerical Simulations. *Appl. Math. Model.* **2020**, 86, 142-165.
125. Sui, Y.; Maglio, M.; Spelt, P. D.; Legendre, D.; Ding, H. Inertial Coalescence of Droplets on a Partially Wetting Substrate. *Phys. Fluid.* **2013**, 25, 101701.
126. Kapur, N.; Gaskell, P. H. Morphology and Dynamics of Droplet Coalescence on a Surface. *Phys. Rev. E* **2007**, 75, 056315.
127. Eddi, A.; Winkels, K. G.; Snoeijer, J. H. Influence of Droplet Geometry on the Coalescence of Low Viscosity Drops. *Phys. Rev. Lett.* **2013**, 111, 144502.
128. Seevaratnam, G. K.; Suo, Y.; Ramé, E.; Walker, L. M.; Garoff, S. Dynamic Wetting of Shear Thinning Fluids. *Phys. Fluid.* **2007**, 19, 012103.

129. Johnson, D. B. The Onset of Effective Coalescence Growth in Convective Clouds. *Q. J. R. Meteorol. Soc.* **1993**, *119*, 925-933.

130. Nissanka, I. D.; Yapa, P. D. Calculation of Oil Droplet Size Distribution in Ocean Oil Spills: A Review. *Mar. Pollut. Bull.* **2018**, *135*, 723-734.

131. Kabalnov, A. S. Coalescence in Emulsions. *Modern Aspects of Emulsion Science* **1998**, 205-260.

132. Sivasankar, V. S.; Etha, S. A.; Hines, D. R.; Das, S. Coalescence of Microscopic Polymeric Drops: Effect of Drop Impact Velocities. *Langmuir* **2021**, *37*, 13512-13526.

133. Varma, S. C.; Saha, A.; Kumar, A. Coalescence of Polymeric Sessile Drops on a Partially Wettable Substrate. *Phys. Fluid.* **2021**, *33*, 123101.

134. Zawadzki, M.; Zawada, K.; Kowalczyk, S.; Plichta, A.; Jaczewski, J.; Zabielski, T. 3D Reactive Inkjet Printing of Aliphatic Polyureas Using In-Air Coalescence Technique. *RSC Adv.* **2022**, *12*, 3406-3415.

135. Zhang, M.; Zhang, H.; He, M.; Wang, L.; Yang, H.; Song, Y. Controlled Diffusion of Nanoparticles by Viscosity Gradient for Photonic Crystal with Dual Photonic Band gaps. *Nanotechnology* **2020**, *31*, 435604.

136. Karpitschka, S.; Riegler, H. Quantitative Experimental Study on the Transition Between Fast and Delayed Coalescence of Sessile Droplets with Different but Completely Miscible Liquids. *Langmuir* **2010**, *26*, 11823-11829.

137. Thoroddsen, S. T.; Qian, B., Etoh, T. G.; Takehara, K. The Initial Coalescence of Miscible Drops. *Phys. Fluid.* **2007**, *19*, 072110.

138. Riegler, H.; Lazar, P. Delayed Coalescence Behavior of Droplets with Completely Miscible Liquids. *Langmuir* **2008**, *24*, 6395-6398.

139. Borcia, R.; Bestehorn, M. Partial Coalescence of Sessile Drops with Different Miscible Liquids. *Langmuir* **2013**, *29*, 4426-4429.

140. Borcia, R.; Bestehorn, M. Different Behaviors of Delayed Fusion Between Drops with Miscible Liquids. *Phys. Rev. E* **2010**, *82*, 036312.

141. Hack, M. A.; Vondeling, P.; Cornelissen, M.; Lohse, D.; Snoeijer, J. H.; Diddens, C.; Segers, T. Asymmetric Coalescence of Two Droplets with Different Surface Tensions is Caused by Capillary Waves. *Phys. Rev. Fluid.* **2021**, *6*, 104002.

142. Blanchette, F. Simulation of Mixing within Drops due to Surface Tension Variations. *Phys. Rev. Lett.* **2010**, *105*, 074501.

143. Sellier, M.; Nock, V.; Verdier, C. Self-Propelling, Coalescing Droplets. *Int. J. Multiphase Flow* **2011**, *37*, 462-468.

144. Sellier, M.; Nock, V.; Gaubert, C.; Verdier, C. Droplet Actuation Induced by Coalescence: Experimental Evidences and Phenomenological Modeling. *Eur. Phys. J. Spec. Top.* **2013**, *219*, 131-141.

145. Castrejón-Pita, J. R.; Kubiak, K. J.; Castrejón-Pita, A. A.; Wilson, M. C. T.; Hutchings, I. M. Mixing and Internal Dynamics of Droplets Impacting and Coalescing on a Solid Surface. *Phys. Rev. E* **2013**, *88*, 023023.

146. Jehannin, M.; Charton, S.; Karpitschka, S.; Zemb, T.; Möhwald, H.; Riegler, H. Periodic Precipitation Patterns During Coalescence of Reacting Sessile Droplets. *Langmuir* **2015**, *31*, 11484-11490.

147. Sykes, T. C.; Castrejón-Pita, A. A.; Castrejón-Pita, J. R.; Harbottle, D.; Khatir, Z.; Thompson, H. M.; Wilson, M. C. Surface Jets and Internal Mixing During the Coalescence of Impacting and Sessile Droplets. *Phys. Rev. Fluid.* **2020**, 5, 023602.

148. Focke, C.; Kuschel, M.; Sommerfeld, M.; Bothe, D. Collision Between High and Low Viscosity Droplets: Direct Numerical Simulations and Experiments. *Int. J. Multiphase Flow* **2013**, 56, 81-92.

149. Karpitschka, S.; Riegler, H. Sharp Transition Between Coalescence and Non-Coalescence of Sessile Drops. *J. Fluid Mech.* **2014**, 743.

150. Karpitschka, S.; Riegler, H. Noncoalescence of Sessile Drops from Different but Miscible Liquids: Hydrodynamic Analysis of the Twin Drop Contour as a Self-stabilizing Traveling Wave. *Phys. Rev. Lett.* **2012**, 109, 066103.

151. Borcia, R.; Menzel, S.; Bestehorn, M.; Karpitschka, S.; Riegler, H. Delayed Coalescence of Droplets with Miscible Liquids: Lubrication and Phase Field Theories. *Eur. Phys. J. E* **2011**, *34*, 1-9.

152. Borcia, R.; Bestehorn, M. Numerical Simulations on Delayed Coalescence of Droplets in Confined Geometries. *AIP Conf. Proc.* **2010**, *1203*, pp 1221-1226.

153. Blanchette, F.; Messio, L.; Bush, J. W. The Influence of Surface Tension Gradients on Drop Coalescence. *Phys. Fluid.* **2009**, *21*, 072107.

154. Alhareth, A. A.; Thoroddsen, S. T. Partial Coalescence of a Drop on a Larger-Viscosity Pool. *Phys. Fluid.* **2020**, *32*, 122115.

155. Kim, H.; Lee, J.; Kim, T. H.; Kim, H. Y. Spontaneous Marangoni Mixing of Miscible Liquids at a Liquid–Liquid–Air Contact Line. *Langmuir* **2015**, *31*, 8726-8731.

156. Sweet, E.; Mehta, R.; Xu, Y.; Jew, R.; Lin, R.; Lin, L. Finger-powered Fluidic Actuation and Mixing via MultiJet 3D Printing. *Lab Chip* **2020**, *20*, 3375-3385.

157. Sochol, R. D.; Sweet, E.; Glick, C. C.; Venkatesh, S.; Avetisyan, A.; Ekman, K. F.; Raulinaitis, A.; Tsai, A.; Wienkers, A.; Korner, K.; Hanson, K. 3D Printed Microfluidic Circuitry via Multijet-based Additive Manufacturing. *Lab Chip* **2016**, *16*, 668-678.

158. Hassan, I.; Selvaganapathy, P. R. A Microfluidic Printhead with Integrated Hybrid Mixing by Sequential Injection for Multimaterial 3D Printing. *Additive Manuf.* **2022**, *50*, 102559.

159. Kokkinis, D.; Schaffner, M.; Studart, A. R. Multimaterial Magnetically Assisted 3D Printing of Composite Materials. *Nat. Commun.* **2015**, *6*, 1-10.

160. Lim, J. M.; Lee, H. J.; Kim, H. W.; Lee, J. Y.; Yoo, J.; Park, K. W.; Lee, C. K.; Hong, Y. T.; Lee, S. Y. Dual Electrospray-assisted Forced Blending of Thermodynamically Immiscible Polyelectrolyte Mixtures. *J. Membr. Sci.* **2015**, *481*, 28-35.

161. Hirt, C. W.; Nichols, B. D. Volume of Fluid (VOF) Method for the Dynamics of Free Boundaries. *J. Comput. Phys.* **1981**, *39*, 201-225.

162. Nichols, B. D.; Hirt, C. W.; Hotchkiss, R. S. *SOLA-VOF:* A Solution Algorithm for Transient Fluid Flow with Multiple Free Boundaries. *Los Alamos National Laboratory* **1980**, LA-8355.

163. Xu, Y.; Fan, S.; Liu, Y.; Zhou, X.; Liu, X.; Yang, Z.; Liu, L.; Liu, J. Analysis of Silt Interaction with Water in an Estuary. *J Nat. Gas Sci. Eng.* **2016**, *35*, 1270-1276.

164. Mohammadi, E.; Narayanaswamy, R.; King, A. A Study of the Phase Change in Three Phase Environment. *Australasian Fluid Mechanics Conference* **2018**.

165. Belsak, G.; Bajt, S.; Beyerlein, K. R.; Sarler, B. Numerical Simulations of Micro Jets Produced with a Double Flow Focusing Nozzle. In *COUPLED VII: Proceedings of the VII International Conference on Computational Methods for Coupled Problems in Science and Engineering* **2017**, 1239-1248, CIMNE.

166. Rodríguez-Ocampo, P. E.; Ring, M.; Hernández-Fontes, J. V.; Alcérreca-Huerta, J. C.; Mendoza, E.; Silva, R. CFD Simulations of Multiphase Flows: Interaction of Miscible Liquids with Different Temperatures. *Water* **2020**, *12*, 2581.

167. Rodríguez-Ocampo, P. E.; Ring, M.; Hernández-Fontes, J. V.; Alcérreca-Huerta, J. C.; Mendoza, E.; Gallegos-Diez-Barroso, G.; Silva, R. A 2D Image-Based Approach for CFD Validation of Liquid Mixing in a Free-Surface Condition. *J. Appl. Fluid Mech.* **2020**, *13*, 1487-1500.

168. Oberthuer, D.; Knoška, J.; Wiedorn, M. O.; Beyerlein, K. R.; Bushnell, D. A.; Kovaleva, E. G.; Heymann, M.; Gumprecht, L.; Kirian, R. A.; Barty, A.; Mariani, V.; Tolstikova, A.; Adriano, L.; Awel, S.; Barthelmess, M.; Dörner, K.; Xavier, P. L.; Yefanov, O.; James, D. R.; Nelson, G.; Wang, D.; Calvey, G.; Chen, Y.; Schmidt,

A.; Szczepek, M.; Frielingsdorf, S.; Lenz, O.; Snell, E.; Robinson, P. J.; Šarle, B.; Belšak, G.; Maček, M.; Wilde, F.; Aquila, A.; Boutet, S.; Liang, M.; Hunter, M. S.; Scheerer, P.; Lipscomb, J. D.; Weierstall, U.; Kornberg, R. D.; Spence, J. C. H.; Pollack, L.; Chapman, H. N.; Bajt, S. Double-flow Focused Liquid Injector for Efficient Serial Femtosecond Crystallography. *Sci. Rep.* **2017**, *7*, 1-12.

169. Zhang, Y.; Lyu, L.; Li, P. An Optimized Volume of Fluid Method for Modelling Three-dimensional Debris Flows. Implementation in OpenFOAM, Validation, and Application in the Aiwa Watershed, Beijing. *Comput. Geotech.* **2022**, *144*, 104651.
170. Seric, I.; Afkhami, S.; Kondic, L. Direct Numerical Simulation of Variable Surface Tension Flows Using a Volume-of-fluid Method. *J. Comput. Phys.* **2018**, 352, 615-636.
171. Adami, S.; Hu, X. Y.; Adams, N. A. A Conservative SPH Method for Surfactant Dynamics. *J. Comput. Phys.* **2010**, *229*, 1909-1926.
172. Ma, C.; Bothe, D. Direct Numerical Simulation of Thermocapillary Flow Based on the Volume of Fluid Method. *Int. J. Multiphase Flow* **2011**, *37*, 1045-1058.
173. Rieber, M. Numerische Modellierung der Dynamik Freier Grenzflachen in Zweiphasenstromungen. *Fortschritt-Berichte VDI: Reihe 7, Stromungstechnik* **2004**, *459*.
174. Colinet, P.; Legros, J. C.; Velarde, M. G. *Nonlinear Dynamics of Surface-tension-driven Instabilities*; Wiley-VCH: Berlin, **2001**.
175. Nepomnyashchy, A. A.; Velarde, M. G.; Colinet, P. *Interfacial Phenomena and Convection*; CRC Press, **2001**.

176. Dee, G. T.; Sauer, B. B. The Surface Tension of Polymer Blends: Theory and Experiment. *Macromolecules* **1993**, *26*, 2771-2778.

177. Kano, Y.; Akiyama, S. Estimation of Surface Tension and Surface Segregation of Poly (Ethyl Acrylate)/Poly (Vinylidene Fluoride-co-hexafluoro Acetone) Blends. *Polymer* **1996**, *37*, 4497-4503.

178. Chandra, M. V.; Karthikeyan, S.; Selvasekarapandian, S.; Pandi, D. V.; Monisha, S.; Packiaseeli, S. A. Characterization of High Ionic Conducting PVAc–PMMA Blend-based Polymer Electrolyte for Electrochemical Applications. *Ionics* **2016**, *22*, 2409-2420.

179. Berberovic, E. Investigation of Free-surface Flow Associated with Drop Impact: Numerical Simulations and Theoretical Modeling. Ph.D. dissertation, Technische Universität, Berlin, Germany, **2010**.

180. Deshpande, S. S.; Anumolu, L.; Trujillo, M. F. Evaluating the Performance of the Two-phase Flow Solver InterFoam. *Comput. Sci. Discov.* **2012**, *5*, 014016.

181. Larsen, B. E.; Fuhrman, D. R.; Roenby, J. Performance of InterFoam on the Simulation of Progressive Waves. *Coast. Eng. J.* **2019**, *61*, 380-400.

182. Malekzadeh, S.; Roohi, E. Investigation of Different Droplet Formation Regimes in a T-junction Microchannel Using the VOF Technique in OpenFOAM. *Microgravity Sci. Technol.* **2015**, *27*, 231-243.

183. Renardy, M.; Renardy, Y.; Li, J. Numerical Simulation of Moving Contact Line Problems Using a Volume-of-Fluid Method. *J. Comput. Phys.* **2001**, *171*, 243-263.

184. Rosengarten, G.; Harvie, D. J. E.; Cooper-White, J. Contact Angle Effects on Microdroplet Deformation Using CFD. *Appl. Math. Model.* **2006**, *30*, 1033-1042.

185. Fukai, J.; Shiiba, Y.; Yamamoto, T.; Miyatake, O.; Poulikakos, D.; Megaridis, C. M.; Zhao, Z. Wetting Effects on The Spreading of a Liquid Droplet Colliding with a Flat Surface: Experiment and Modeling. *Phys. Fluid.* **1995**, *7*, 236-247.

186. Castonguay, S.; Gervais, T. A Simple Static Contact Angle-Based Mesh-Dependency Correction for 3D Capillary Flow Simulations. *Comput. Fluid.* **2021**, *228*, 105060.

187. Hou, H.; Yuan, Z.; Hu, Z.; Gao, S.; Wu, X. Effects of The Surface Tension Gradient and Viscosity on Coalescence-Induced Droplet Jumping on Superamphiphobic Surfaces. *Phys. Fluid.* **2021**, *33*, 112101.

188. Yonemoto, Y.; Kunugi, T. Experimental and Theoretical Investigation of Contact-Angle Variation for Water–Ethanol Mixture Droplets on a Low-Surface-Energy Solid. *Int. J. Heat Mass Transf.* **2016**, *96*, 614-626.

189. Waghmare, P. R.; Mitra, S. K. Contact Angle Hysteresis of Microbead Suspensions. *Langmuir* **2010**, *26*, 17082-17089.

190. https://www.sigmaaldrich.com/US/en/product/aldrich/387932 (accessed on 2023-03-03)

191. Shen, Z.; Simon, G. P.; Cheng, Y. B. Nanocomposites of Poly (Methyl Methacrylate) and Organically Modified Layered Silicates by Melt Intercalation. *J. Appl. Polym. Sci.* **2004**, *92*, 2101-2115.

192. Agarwal, S. H.; Porter, R. S. Concentration Dependence of Rheology for Poly (Vinyl Acetate) Solutions. *J. Rheol.* **1981**, *25*, 171-191.

193. Cheng, B.; Zhou, C.; Yu, W.; Sun, X. Evaluation of Rheological Parameters of Polymer Melts in Torque Rheometers. *Polym. Test.* **2001**, *20*, 811-818.

194. E. McCafferty and J.P. Wightman, *In Apparent and Microscopic Contact Angles*, J. Drelich, J.S. Laskowski, and K.L. Mittal, eds., VSP, Utrecht, The Netherlands, **2000**, p. 149-170.

195. Wu, S. Surface and Interfacial Tensions of Polymer Melts. II. Poly (Methyl Methacrylate), Poly (N-Butyl Methacrylate), and Polystyrene. *J. Phys. Chem.* **1970**, *74*, 632-638.

196. Carbone, M. G. P.; Tammaro, D.; Manikas, A. C.; Paterakis, G.; Di Maio, E.; Galiotis, C. Wettability of Graphene by Molten Polymers. *Polymer* **2019**, *180*, 121708.

197. Sun, D. L.; Tao, W. Q. A Coupled Volume-of-fluid and Level Set (VOSET) Method for Computing Incompressible Two-Phase Flows. *Int. J. Heat Mass Transf.* **2010**, *53*, 645-655.

198. Sussman, M.; Fatemi, E.; Smereka, P.; Osher, S. An Improved Level Set Method for Incompressible Two-Phase Flows. *Comput. Fluid.* **1998**, *27*, 663-680.

199. Nourgaliev, R. R.; Wiri, S.; Dinh, N. T.; Theofanous, T. G. On Improving Mass Conservation of Level Set by Reducing Spatial Discretization Errors. *Int. J. Multiphase Flow* **2005**, *31*, 1329-1336.

200. Sussman, M.; Smereka, P.; Osher, S. A Level Set Approach for Computing Solutions to Incompressible Two-Phase Flow. *J. Comput. Phys.* **1994**, *114*, 146-159.

201. Sussman, M.; Fatemi, E. An Efficient, Interface-Preserving Level Set Redistancing Algorithm and its Application to Interfacial Incompressible Fluid Flow. *SIAM J. Sci. Comput.* **1999**, *20*, 1165-1191.

202. Adalsteinsson, D.; Sethian, J. A. The Fast Construction of Extension Velocities in Level Set Methods. *J. Comput. Phys.* **1999**, *148*, 2-22.

203. Silva, M. F.; Campos, J. B.; Miranda, J. M.; Araújo, J. D. Numerical Study of Single Taylor Bubble Movement Through a Microchannel Using Different CFD Packages. *Processes* **2020**, *8*, 1418.

204. Vachaparambil, K. J.; Einarsrud, K. E. Comparison of Surface Tension Models for the Volume of Fluid Method. *Processes* **2019**, *7*, 542.

205. Chen, J. Y.; Gao, P.; Xia, Y. T.; Li, E. Q.; Liu, H. R.; Ding, H. Early Stage of Delayed Coalescence of Soluble Paired Droplets: A Numerical Study. *Phys. Fluid.* **2021**, *33*, 092005.

206. Parihar, R. S.; Setti, S. G.; Sahu, R. K. Recent Advances in the Manufacturing Processes of Functionally Graded Materials: A Review. *Sci. Eng. Composite Mater.* **2016**, *25*, 309-336.

207. Li, Y.; Feng, Z.; Hao, L.; Huang, L.; Xin, C.; Wang, Y.; Bilotti, E.; Essa, K.; Zhang, H.; Li, Z.; Yan, F.; Peijs, T. A Review on Functionally Graded Materials and Structures via Additive Manufacturing: From Multi-Scale Design to Versatile Functional Properties. *Adv. Mater. Technol.* **2020**, *5*, 1900981.

208. Daling, P. S.; Mackay, D.; Mackay, N.; Brandvik, P. J. (1990). Droplet Size Distributions in Chemical Dispersion of Oil Spills: Towards a Mathematical Model. *Oil and Chemical Pollution* **1990**, *7*, 173-198.

209. Dickinson, E.; Williams, A. Orthokinetic Coalescence of Protein-Stabilized Emulsions. *Colloids Surf. A Physicochem. Eng.***1994**, *88*, 317-326.

210. Danner, T.; Schubert, H. Coalescence Processes in Emulsions. In *Food colloids: fundamentals of Formulation;* Dickinson, E; Miller, R., Eds., Royal Society of Chemistry, **2001**, *258*, 116-124.

211. Hines, D. R.; Gu, Y.; Martin, A. A.; Li, P.; Fleischer, J.; Clough-Paez, A.; Stackhouse, G.; Das, S. Considerations of Aerosol-Jet Printing for the Fabrication of Printed Hybrid Electronic Circuits. *Addit. Manuf.* **2021**, *47*, 102325.

212. De Gans, B. J.; Duineveld, P. C.; Schubert, U. S. Inkjet Printing of Polymers: State of the Art And Future Developments. *Adv. Mater.* **2004**, *16*, 203-213.

213. Kamp, J.; Villwock, J.; Kraume, M. Drop Coalescence in Technical Liquid/Liquid Applications: A Review on Experimental Techniques and Modeling Approaches. *Rev. Chem. Eng.* **2017**, *33*, 1-47.

214. Hack, M. A.; Tewes, W.; Xie, Q.; Datt, C.; Harth, K.; Harting, J.; Snoeijer, J. H. Self-similar Liquid Lens Coalescence. *Phys. Rev. Lett.* **2020**, *124*, 194502.

215. Sarojini KG, K.; Dhar, P.; Varughese, S.; Das, S. K. Coalescence Dynamics of PEDOT: PSS Droplets Impacting at Offset on Substrates for Inkjet Printing. *Langmuir* **2016**, *32*, 5838-5851.

216. Pawar, N. D.; Bahga, S. S.; Kale, S. R.; Kondaraju, S. Symmetric and Asymmetric Coalescence of Droplets on a Solid Surface in The Inertia-Dominated Regime. *Phys. Fluids* **2019**, *31*, 092106.

217. Varma, S. C.; Rajput, A. S.; Kumar, A. Rheocoalescence: Relaxation Time Through Coalescence of Droplets. *Macromolecules* **2022**, *55*, 6031-6039.

218. Sivasankar, V. S.; Hines, D. R.; Das, S. Numerical Study of the Coalescence and Mixing of Drops of Different Polymeric Materials. *Langmuir* **2022**, *38*, 14084-14096.

219. Dekker, P. J.; Hack, M. A.; Tewes, W.; Datt, C.; Bouillant, A.; Snoeijer, J. H. When Elasticity Affects Drop Coalescence. *Phys. Rev. Lett.* **2022**, *128*, 028004.

220. Yue, P.; Feng, J. J.; Liu, C.; Shen, J. Diffuse-interface Simulations of Drop Coalescence and Retraction in Viscoelastic Fluids. *J. Non-Newton. Fluid Mech.* **2005**, *129*, 163-176.

221. Pawar, A. B.; Caggioni, M.; Hartel, R. W.; Spicer, P. T. Arrested Coalescence of Viscoelastic Droplets with Internal Microstructure. *Faraday Discuss.* **2012**, *158*, 341-350.

222. Sivasankar, V. S.; Sachar, H. S.; Sinha, S.; Hines, D. R.; Das, S. 3D Printed Microdroplet Curing: Unravelling the Physics of On-Spot Photopolymerization. *ACS Appl. Polym. Mater.* **2020**, *2*, 966-976.

223. Sung, Y. L.; Garan, J.; Hu, Z.; Shan, X.; Shih, W. C. Modeling The Surface Of Fast-Cured Polymer Droplet Lenses For Precision Fabrication. *Appl. Opt.* **2018**, *57*, 10342-10347.

224. Varma, S. C.; Dasgupta, D.; Kumar, A. Elasticity Can Affect Droplet

Coalescence. *Phys. Fluids* **2022**, *34*, 093112.

225. Vlnieska, V.; Gilshtein, E.; Kunka, D.; Heier, J.; Romanyuk, Y. E. Aerosol Jet Printing of 3D Pillar Arrays from Photopolymer Ink. *Polymers* **2022**, *14*, 3411-4322.

226. Yi, C.; Fedderwitz, R.; Park, D.; Ding, C.; Lu, G. Q.; Fleischer, J.; Li, P.; Kofinas, P.; Das, S.; Hines, D. R. Fully Printed Resonance-Free Broadband Conical Inductors Using Engineered Magnetic Inks. *Addit. Manuf.* **2021**, *44*, 102034.

227. Seipel, S.; Yu, J.; Periyasamy, A. P.; Viková, M.; Vik, M.; Nierstrasz, V. A. Inkjet Printing and UV-LED Curing of Photochromic Dyes for Functional and Smart Textile Applications. *RSC Adv.* **2018**, *8*, 28395-28404.

228. Sung, Y. L.; Jeang, J.; Lee, C. H.; Shih, W. C. Fabricating Optical Lenses By Inkjet Printing And Heat-Assisted in-situ Curing of Polydimethylsiloxane for Smartphone Microscopy. *J. Biomed. Opt.* **2015**, *20*, 047005

229. Ferrer, P. M.; Causon, D. M.; Qian, L.; Mingham, C. G.; Ma, Z. H. (2016). A Multi-Region Coupling Scheme for Compressible and Incompressible Flow Solvers for Two-Phase Flow in a Numerical Wave Tank. *Comput. Fluids* **2016**, *125*, 116-129.

230. Guan, H.; Wang, J.; Wei, Z.; Wu, C. Numerical Analysis of the Interaction of 3D Compressible Bubble Clusters. Appl. Math. Mech. **2019**, *40*, 1181-1196.

231. Wu, M.; Cubaud, T.; Ho, C. M. Scaling Law in Liquid Drop Coalescence Driven by Surface Tension. *Phys. Fluids* **2004**, *16*, L51-L54.

232. Yuan, X.; Ferrer-Campos, R.; Garcés-Pineda, F. A.;Villa, K. Molecular Imprinted BiVO4 Microswimmers for Selective Target Recognition and Removal. *Small* **2023**, 2207303.

233. Nicholls, D.; DeVerse, A.; Esplin, R. S.; Castaneda, J.; Loyd, Y.; Nair, R.; Voinescu, R.; Zhou, C.; Wang, W.; Gibbs, J. G. Shape-dependent Motion of Structured Photoactive Microswimmers. *ACS Appl. Mat. Interfaces* **2018**, *10*, 18050-18056.

234. Zhang, X.; Chen, Z.; Li, Y.; Li, X.; Li, R.; Zhang, J.; Imran, M.; Gao, Y. Magnetic and Photoactive Colloidal Shuttles for Active Cargo Transportation. *JCIS Open* **2023**, *9*, 100071.

235. Song, H.; Chen, D. L.; Ismagilov, R. F. Reactions in Droplets in Microfluidic Channels. *Angew. Chem. Int. Ed.* **2006**, *45*, 7336-7356.

236. Dechelette, A.; Sojka, P. E.; Wassgren, C. R. Non-Newtonian Drops Spreading on a Flat Surface. *J. Fluids Eng.* **2010**, 132, 101302.